AN EXPERIMENTAL AND THEORETICAL STUDY OF RADIATIVE EXTINCTION OF DIFFUSION FLAMES

FINAL REPORT
NASA GRANT # NAG3 - 1460
December, 1995

Prepared

by

ARVIND ATREYA
Department of Mechanical Engineering and Applied Mechanics
The University of Michigan, Ann Arbor MI 48109 - 2125
Telephone: (313) 647 4790; Fax: (313) 647 3170

for

NASA Microgravity Science & Applications Division
NASA Project Monitor: Mr. Kurt R. Sacksteder; Lewis Research Center
Combustion Science Program; Program Scientist: Dr. Merrill King

AN EXPERIMENTAL AND THEORETICAL STUDY OF RADIATIVE EXTINCTION OF DIFFUSION FLAMES

(NASA GRANT#: NAG3-1460)

CONTENTS

EXECUTIVE SUMMARY

The objective of this research was to experimentally and theoretically investigate the radiation-induced extinction of gaseous diffusion flames in μg. The μg conditions were required because radiation-induced extinction is generally not possible in *1-g* but is highly likely in μg. In *1-g*, the flame-generated particulates (e.g. soot) and gaseous combustion products that are responsible for flame radiation, are swept away from the high temperature reaction zone by the buoyancy-induced flow and a steady state is developed. In μg, however, the absence of buoyancy-induced flow which transports the fuel and the oxidizer to the combustion zone and removes the hot combustion products from it enhances the flame radiation due to: (i) transient build-up of the combustion products in the flame zone which increases the gas radiation, and (ii) longer residence time makes conditions appropriate for substantial amounts of soot to form which is usually responsible for most of the radiative heat loss. Numerical calculations conducted during the course of this work show that even non-radiative flames continue to become "weaker" (diminished burning rate per unit flame area) due to reduced rates of convective & diffusive transport. Thus, it was anticipated that radiative heat loss may eventually extinguish the already "weak" μg diffusion flame. While this hypothesis appears convincing and our numerical calculations support it, experiments for a long enough μg time could not be conducted during the course of this research to provide an experimental proof. Space shuttle experiments on candle flames [Dietrich, Ross and T'ien, 1995] show that in an infinite ambient atmosphere, the hemispherical candle flame in μg will burn indefinitely. It was hoped that radiative extinction can be experimentally shown by the aerodynamically stabilized gaseous diffusion flames where the fuel supply rate was externally controlled. While substantial progress toward this goal was made during this project, identifying the experimental conditions for which radiative extinction occurs, for various fuels, requires further study.

To investigate radiation-induced extinction, spherical geometry was used for the μg experiments for the following reasons: (i) It reduces the complexity by making the problem one-dimensional. Thus, it is convenient for both experimental measurements and theoretical modeling. (ii) The spherical diffusion flame completely encloses the soot which is formed on the fuel rich side of the reaction zone. This increases the importance of flame radiation because now both soot and gaseous combustion products co-exist inside the high temperature spherical diffusion flame. It also increases the possibility of radiative extinction due to soot crossing the high temperature reaction zone. (iii) For small fuel injection velocities, as is usually the case for a pyrolyzing solid, the diffusion controlled flame in μg around the pyrolyzing solid naturally develops spherical symmetry. Thus, spherical diffusion flames are of interest to fires in μg and identifying conditions (ambient atmosphere, fuel flow rate, fuel type, fuel additives, etc.) where radiation-induced extinction occurs was considered important for spacecraft fire safety.

During the course of this research, it was also found that the absence of buoyant flows in μg and the resulting long reactant residence times significantly change the thermochemical environment and hence the flame chemistry. Thus, for realistic theoretical models, knowledge of the formation and oxidation rates of soot and other combustion products in the thermochemical environment existing under μg conditions was essential. This requires detailed optical and gas chromatographic measurements that are not easily possible under μg conditions. Thus, supplementary *1-g* experiments with detailed chemical measurements were conducted. The

spherical burner, however, was not suitable for these detailed *1-g* experiments due to the complex buoyancy-induced flow field generated around it. Thus, a one-dimensional counterflow diffusion flame was used. At low strain rates, with the diffusion flame on the fuel side of the stagnation plane, conditions similar to the μg case are created -- soot is again forced through the high temperature reaction zone. Furthermore, high concentration of combustion products in the sooting zone can be easily obtained by adding appropriate amounts of CO_2 and H_2O to the fuel and/or the oxidizer streams. These *1-g* experiments were used to support the development of detailed chemistry transient models that include soot formation and oxidation for both μg and *1-g* cases.

To understand the radiative-extinction process and to explain the experimental results, transient numerical models for both μg and *1-g* cases were developed. These models include simplified one-step chemistry and gas radiation. Soot formation and oxidation and soot radiation was included only for the transient *1-g* case along with the simplified one-step chemistry. Within the assumptions, both the μg and *1-g* models predicted radiative extinction of diffusion flames due to gas radiation. While this was very encouraging, detailed chemistry and transport properties need to be included in these models. This was done only for the *1-g* steady-state counterflow diffusion flame both with & without enhanced H_2O concentrations. The *1-g* experiments were particularly important for validating these models because for cases where flame extinction does not occur, a steady state is predicted. This steady-state condition was directly compared with the detailed experimental measurements.

The research conducted during the course of this project was published in the following articles:

1. *Atreya, A., Wichman, I., Guenther, M., Ray, A. and Agrawal, S.* "An Experimental and Theoretical Study of Radiative Extinction of Diffusion Flames," Second International Microgravity Combustion Workshop, Cleveland, OH, NASA Conference Publication 10113, September, 1992.
2. *Atreya, A. and Agrawal, S.* "Effect of Radiative Heat Loss on Diffusion Flames in Quiescent Microgravity Atmosphere," Annual Conference on Fire Research, NIST, October, 1993.
3. *Atreya, A., and Agrawal, S.*, "Extinction of Moving Diffusion Flames in a Quiescent Microgravity Environment due to CO_2/H_2O/Soot Radiative Heat Losses," First ISHMT-ASME Heat and Mass Transfer Conference, 1994.
4. *Atreya, A, Agrawal, S., Sacksteder, K., and Baum, H.*, "Observations of Methane and Ethylene Diffusion Flames Stabilized around a Blowing Porous Sphere under Microgravity Conditions," AIAA paper # 94-0572, 1994.
5. *Atreya, A., Agrawal, S., Shamim, T., Pickett, K., Sacksteder, K. R. and Baum, H. R.* "Radiant Extinction of Gaseous Diffusion Flames," 3rd International Microgravity Conference, April, 1995.
6. *Pickett, K., Atreya, A., Agrawal, S., and Sacksteder, K.*, "Radiation from Unsteady Spherical Diffusion Flames in Microgravity," AIAA paper # 95-0148, January 1995.
7. *Atreya, A. and Agrawal, S.*, "Effect of Radiative Heat Loss on Diffusion Flames in Quiescent Microgravity Atmosphere," *Combustion & Flame*, (accepted for publication), 1995.
8. *Atreya, A., Agrawal, S., Sacksteder, K. R., and Baum, H. R.* "Unsteady Gaseous Spherical Diffusion Flames in Microgravity - Part A: Expansion Rate" being prepared for submission

to Combustion and Flame.

9. *Atreya, A., Agrawal, S., Pickett, K., Sacksteder, K. R., and Baum, H. R.* "Unsteady Gaseous Spherical Diffusion Flames in Microgravity - Part B: Radiation, Temperature and Extinction" being prepared for submission to Combustion and Flame.
10 *Shamim, T., and Atreya, A.*, "A Study of the Effects of Flame Radiation on Transient Extinction of Strained Diffusion Flames," Joint Technical Meeting of Combustion Institute, paper: 95S-104 pp.553, 1995. Currently being prepared for submission to Combustion and Flame.
11 *Shamim, T., and Atreya, A.*, "Numerical Simulations of Radiative Extinction of Unsteady Strained Diffusion Flames," Symposium on Fire and Combustion Systems, ASME IMECE, November, 1995.
12 *Atreya, A. and Zhang, C.*, "Experiments and Correlations of Soot Formation and Oxidation in Methane Counterflow Diffusion Flames," submitted to International Symposium on Combustion, Not accepted, currently being revised for submission to Combustion and Flame.
13 *Zhang, C. and Atreya, A.* "Measurements of Soot Volume Fraction Profiles in Counterflow Diffusion Flames Using a Transient Thermocouple Response Technique," Submitted to The International Symposium on Combustion, Not accepted, currently being revised for submission to Combustion and Flame.
14 *Atreya, A., Zhang, C., Kim, H. K., Shamim, T. and Suh, J.* "The Effect of Changes in the Flame Structure on Formation and Destruction of Soot and NO_x in Radiating Diffusion Flames," Accepted for publication in the Twenty-Sixth (International) Symposium on Combustion, 1996.
15 *Shamim, T. and Atreya, A.* "Dynamic Response of Radiating Flamelets Subject to Variable Reactant Concentrations," Proceedings of the Central Section of the Combustion Institute, 1996. The corresponding paper "Transient Response of a Radiating Flamelet to Changes in Global Stoichiometric Conditions." is being prepared for submission to Combustion and Flame.
16 *Crompton, T. and Atreya, A.* "The Effect of Water on Radiative Laminar Hydrocarbon Diffusion Flames - Part A: Experimental Results," being prepared for submission to Combustion Science and Technology.
17 *Suh, J. and Atreya, A.* "The Effect of Water on Radiative Laminar Hydrocarbon Diffusion Flames - Part B: Theoretical Results," being prepared for submission to Combustion Science and Technology. Also published in the proceedings of the International Conference on Fire Research and Engineering, Sept, 1995.
18 *Suh, J. and Atreya, A.*, "The Effect of Water Vapor on Radiative Counterflow Diffusion Flames," Symposium on Fire and Combustion Systems, ASME IMECE, Nov. 1995.
19 *Zhang, C, Atreya, A., Kim, H. K., Suh, J. and Shamim, T,* "The Effect of Flame Structure on Soot Inception, Growth and Oxidation in Counterflow Diffusion Flames," Proceedings of the Central Section of the Combustion Institute, 1996.
20 *Zhang, C, Atreya, A., Shamim, T, Kim, H. K. and Suh, J.*, "Measurements of OH, CH, C_2 and PAH in Laminar Counterflow Diffusion Flames," Proceedings of the Central Section of the Combustion Institute, 1996.

NOTE: Most of the above papers are presented in the Appendices of this report.

RESEARCH RESULTS

1. INTRODUCTION AND OBJECTIVES

The absence of buoyancy-induced flows in μg and the resulting increase in the reactant residence time significantly alters the fundamentals of many combustion processes. Substantial differences between *1-g* and μg flames have been reported in experiments on candle flames [1, 2], flame spread over solids [3, 4], droplet combustion [5, 6] and others. These differences are more basic than just in the visible flame shape. Longer residence times and higher concentration of combustion products in the flame zone create a thermochemical environment which changes the flame chemistry and the heat and mass transfer processes. Processes such as flame radiation (and its interaction with the flame chemistry), that are often ignored under normal gravity, become very important and sometimes even controlling. This is particularly true for conditions at extinction of a μg diffusion flame. As an example, consider the droplet burning problem. The visible flame shape is spherical under μg versus a teardrop shape under *1-g*. Since most models of droplet combustion utilize spherical symmetry, excellent agreement with the experiments is anticipated. However, μg experiments show that a soot shell is formed between the flame and the evaporating droplet of a sooty fuel [5, 6]. This soot shell alters the heat and mass transfer between the droplet and its flame resulting in significant changes in the burning rate and the propensity for flame extinction.

Under *1-g*, the buoyancy-generated flow, which may be characterized by the strain rate, assists the diffusion process to transport the fuel and the oxidizer to the combustion zone and remove the hot combustion products from it. These are essential functions for the survival of the flame which needs fuel and oxidizer. Numerical calculations [7] show that even flames with no heat loss become "weak" (diminished burning rate per unit flame area) in the absence of flow or zero strain rate. Thus, as the strain rate (or the flow rate) is increased, the diffusion flame which is "weak" at low strain rates is initially "strengthened" and eventually it may be "blown-out." The computed flammability boundaries show that such a reversal in material flammability occurs at strain rates around 5 sec^{-1} [8]. Also, model calculations of zero strain rate transient diffusion flames show that even gas radiation is sufficient to extinguish the flame [7]. Yet, the literature substantially lacks a systematic study of low strain rate, radiation-induced, extinction of diffusion flames. Experimentally, this can only be accomplished under microgravity conditions.

The lack of buoyant flow in μg also enhances the flame radiation due to: (i) build-up of combustion products in the flame zone which increases the gas radiation, and (ii) longer residence times make conditions appropriate for substantial amounts of soot to form which is usually responsible for most of the radiative heat loss. Thus, it is anticipated that radiative heat loss may eventually extinguish the already "weak" μg diffusion flame. While this is a convincing hypothesis, space shuttle experiments on candle flames show that in an infinite ambient atmosphere, the hemispherical candle flame in μg will burn indefinitely [1]. It was our goal to experimentally and theoretically find conditions under which radiative extinction occurs for aerodynamically stabilized gaseous diffusion flames. Identifying these conditions (ambient atmosphere, fuel flow rate, fuel type, fuel additives, etc.) is important for spacecraft fire safety. *Thus, the objective of this research was to experimentally and theoretically investigate the*

radiation-induced extinction of gaseous diffusion flames in μg and determine the effect of flame radiation on the "weak" μg diffusion flame. Scientifically, this requires understanding the interaction of flame radiation with flame chemistry.

To experimentally investigate radiation-induced extinction, spherical geometry was used for *μg* for the following reasons: (i) It reduces the complexity by making the problem one-dimensional. Thus, it is convenient for both experimental measurements and theoretical modeling. (ii) The spherical diffusion flame completely encloses the soot which is formed on the fuel rich side of the reaction zone. This increases the importance of flame radiation because now both soot and gaseous combustion products co-exist inside the high temperature spherical diffusion flame. It also increases the possibility of radiative extinction due to soot crossing the high temperature reaction zone. (iii) For small fuel injection velocities, as is usually the case for a pyrolyzing solid, the diffusion controlled flame in *μg* around the pyrolyzing solid naturally develops spherical symmetry. Thus, spherical diffusion flames are of interest to fires in *μg*.

To theoretically investigate the radiation-induced extinction limits, knowledge of the rates of production and destruction of soot and other combustion products in the thermochemical environment existing under *μg* conditions is essential. This requires detailed optical and gas chromatographic measurements that are not easily possible under *μg* conditions. Thus, supplementary *1-g* experiments with detailed chemical measurements were conducted. The spherical burner, however, is not suitable for these detailed *1-g* experiments due to the complex buoyancy-induced flow field generated around it. Thus, a one-dimensional counterflow diffusion flame was used. At low strain rates, with the diffusion flame on the fuel side of the stagnation plane, conditions similar to the *μg* case are created -- soot is again forced through the high temperature reaction zone. Furthermore, high concentration of combustion products in the sooting zone was easily obtained by adding appropriate amounts of CO_2 and H_2O to the fuel and/or the oxidizer streams. These *1-g* experiments supported the development of detailed chemistry transient models for both *μg* and *1-g* cases. Interestingly, understanding the effect of increased concentration of combustion products on sooting diffusion flames is also important for several *1-g* applications. For example, many furnaces and engines use exhaust gas recirculation for pollutant control. Similarly, oxidizing soot by forcing it through the reaction zone is an excellent method of controlling soot emissions, if the flame is not extinguished. The effect of increased water vapor concentration on sooty diffusion flames is also important for water mist fire suppression technology. Thus, the fundamental knowledge generated during this research has wide spread *1-g* applications in addition to helping develop a fire safe *μg* environment.

2. PREVIOUS RESEARCH

An extensive review on *μg* combustion has recently been published by Law and Faeth [9]. Thus, only relevant aspects are summarized here. In the literature, propagation and extinction of premixed flames (both under *μg* and *1-g* conditions) has received much more attention than diffusion flames. Some excellent work on premixed flames may be found in references [9-14]. Relatively fewer studies on mechanisms of diffusion flame extinction are available [8, 15-20]. Of these, even fewer have included flame radiation as the extinction mechanism [19, 20]. This is not surprising, because under *1-g* conditions flame radiation does not extinguish diffusion flames. Even in very sooty diffusion flames, the excess particulates are simply ejected from the

flame tip (where it is locally extinguished) and convected away by the buoyant flow field. Typically, in *1-g*, extinction is caused by high strain rates generated by buoyant or forced flows and has been a subject of numerous studies (see for e.g., [21]). However, in μg, strain rates are very low and excess flame-generated particles and products of combustion become efficient radiators of chemical energy and may cause radiative-extinction. To the best of author's knowledge, to-date there is no systematic study of the radiative-extinction hypothesis; although numerical models supporting it have recently been presented [7, 22-25]. Much related work in this area is currently underway by Drs. T. Kashiwagi, H. Baum, J. T'ein, H. Ross, K. Sacksteder, F. Willams, C. Law, G. M. Faeth, C. Avedisian, S. Bhattacharjee and R. Altenkirch. Their work is described in Refs. [9, 26-28] and the references cited therein. **In summary**: *Combustion research prior to this work had focused primarily on problems that may be characterized by moderate to high strain rates. Combustion products do not accumulate near the reaction zone at these strain rates and soot is not produced in significant quantities. Thus, flame radiation was justifiably ignored and few studies that investigate the effect of flame radiation on extinction are available in the literature. Furthermore, low strain rates available under μg conditions, open a much less investigated fundamental branch of combustion science, i.e., - understanding the interaction of flame radiation with flame chemistry in addition to the limit phenomenon of radiation-induced flame extinction.*

Counterflow diffusion flames (used in the *1-g* supporting experiments) have been extensively used in the past to study the extinction phenomena due to high strain rates and inert gas dilution (Tsuji, Sheshadri, Law and others, see for e.g. [29-31]). However, despite their obvious 1-D advantages, they have rarely been used to study particulate formation in flames and have never been used to investigate radiative extinction at low strain rates. The primary reason for this is that particulate formation is associated with long residence times - or low strain rates - and such flames are very difficult to stabilize under *1-g* conditions. The buoyant high-temperature gases in the combustion zone alter the flow field until the ideal counterflow ceases to exist. To overcome the buoyancy effect, flow rates of fuel and oxidizer are increased, which in turn reduces the residence times and the particulate formation rate. Thus, despite the obvious advantage of 1-D species and temperature fields, many investigators have been forced to use more complicated co-flow or Parker-Wolfhard burners to study soot formation rates. *We designed a special low-strain-rate, high-temperature and controlled composition, 1-D counterflow diffusion flame burner to enable reproducing the thermochemical environment present under μg conditions and to measure the thermal, chemical and sooting structure of radiating diffusion flames.*

3. EXPERIMENTAL APPARATUS

Microgravity Experiments

The μg experiments were conducted in the 2.2 sec drop tower at the NASA Lewis Research Center. The experimental drop-rig used is shown in Figure 1. It consists of a test chamber, burner, igniter, gas cylinders, solenoid and metering valves, thermocouples with signal processors, photodiodes with electronics, video camera, computer and batteries to power the computer and the solenoid valves. The spherical burner (1.9 cm in diameter) was constructed from a porous ceramic material. Two gas cylinders (150 cc & 500 cc) charged with various gases between 15 to 45 psig were used to supply the fuel to the porous spherical burner. Typical

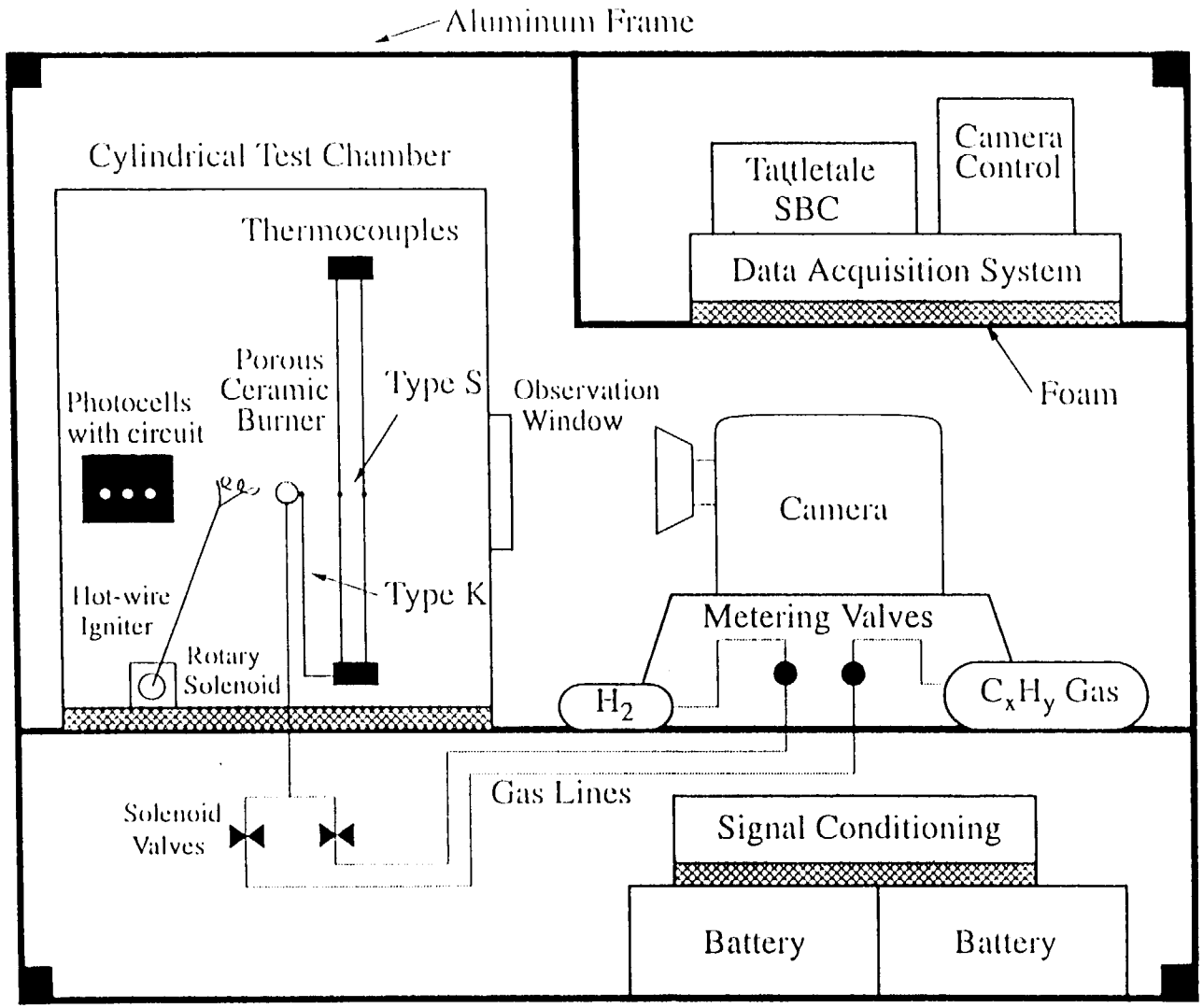

Schematic of 2.2 Second Drop Tower Apparatus

gas flow rates used were in the range of 3-25 cm^3/s. Flow rates to the burner were controlled by a needle valve and a gas solenoid valve was used to open and close the gas line to the burner upon computer command. An igniter was used to establish a diffusion flame. After ignition the igniter was quickly retracted from the burner and secured in a catching mechanism by a computer-controlled rotary solenoid. This was necessary for two reasons (i) The igniter provides a heat sink and will quench the flame (ii) Upon impact with the ground (after 2.2 sec) the vibrating igniter may damage the porous burner.

As shown in the figure, the test chamber has a 5" diameter Lexan window which enables the camera to photograph the spherical diffusion flame. The flame growth was recorded either by a 16mm color movie camera or by a color CCD camera which was connected to a video recorder by a fiber-optic cable during the drop. Since the flow may change with time, it was calibrated for various settings of the needle valve for all gases. A soap bubble flow meter was used for this purpose. An in-line pressure transducer was used to obtain the transient flow rates. Changes in the cylinder pressure during the experiment along with the pressure-flow rate calibration, provides the transient volumetric flow rates. However, the flow rates during the experiments were found to be nearly constant.

Ground-Based Counterflow Diffusion Flame Experiments

The *1-g* ground-based supporting experiments were performed in the counterflow diffusion flame apparatus schematically shown in Figure 2 (for further details see Ref.[32-34]). In this apparatus, an axis-symmetric diffusion flame was stabilized between the two preheated fuel and oxidizer streams in a specially-constructed ceramic burner. Two streams of gases which can be electrically preheated impinge against each other to form a stable stagnation plane, which lies approximately at the center of the burner gap. Upon ignition, a flat axis-symmetric diffusion flame roughly 8cm in diameter was established above the stagnation plane. All measurements are taken along the axial streamline. Co-flowing nitrogen was introduced along the outer edge of the burner to eliminate oxidizer entrainment and to extinguish the flame in the outer jacket. Methane, ethylene, oxygen, nitrogen, helium and carbon dioxide used during the experiments are obtained from chemical purity gas cylinders and their flow rates are measured using calibrated critical flow orifices. Water vapor was generated by passing a stream of inert gas (helium or nitrogen) through a distilled water saturater maintained at a specified temperature. To determine the detailed diffusion flame structure, very low strain rates ($\approx$ 6-8 sec^{-1}) were employed in order to increase the reactant residence time as much as possible and thus obtain a thick reaction zone convenient for measurements. The inert gases in the fuel and/or oxidizer streams were also substituted by various amounts of CO_2 and H_2O to simulate increased concentration of combustion products in the reaction zone. Experimental measurements consisted of: (i) temperature profile, (ii) profiles of stable gases, light hydrocarbons (up to benzene) and PAH, (iii) profiles of laser light scattering, extinction, and fluorescence across the flame, (iv) Laser induced fluorescence for OH profile measurements, and (v) spatially resolved spectral radiative emission profiles.

As shown in the figure, is a beam of argon-ion laser operating at 350/514/1090nm. This beam was modulated by a mechanical chopper and then directed by a collimating lens to the center of the burner. This beam was used for classical light scattering and extinction measurements. A photomultiplier tube and a photodiode were used to detect the scattered and

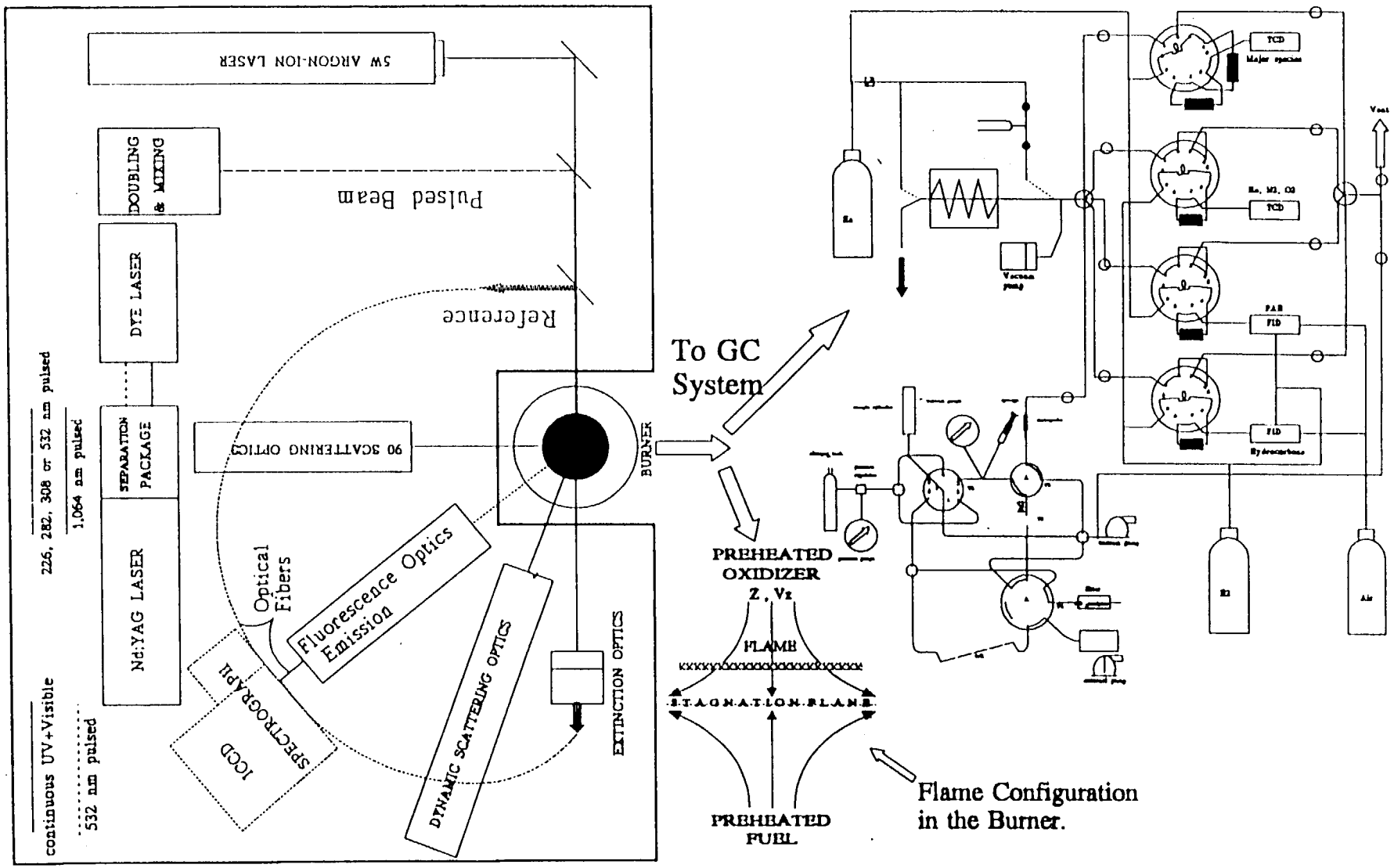

SCHEMATIC OF THE 1-g COUNTERFLOW DIFFUSION FLAME APPARATUS

transmitted signals respectively. These signals are processed by a lock-in amplifier interfaced with a microcomputer. The extinction coefficient was experimentally corrected for gas absorption by subtracting the extinction coefficient of a reference flame. This reference flame is carefully chosen by slightly reducing the fuel and the oxidizer concentrations such that soot scattering is reduced to less than 0.5% of the original flame. Emission from soot particles was not observed from this blue-yellow "scattering limit" flame. Laser-induced broadband fluorescence (LIF) measurement were made by operating the laser at 350/488nm and detecting the fluorescence intensity at 514±10nm. This signal was taken proportional to the PAH concentration. In the subsequent data reduction, the soot aerosol was assumed monodispersed with a complex refractive index of 1.57-0.56i. OH measurements were made by using a pulsed UV laser to excite the molecules and detecting the fluorescence by an ICCD spectrograph. This spectrograph was also used to make spatially resolved measurements of radiative emission.

Temperatures were measured by 0.076mm diameter Pt/Pt-10%Rh thermocouples. The thermocouples were coated with SiO_2 to prevent possible catalytic reactions on the platinum surface. They were traversed across the flame in the direction of decreasing temperature at a rate fast enough to avoid soot deposition and slow enough to obtain negligible transient corrections. For radiation corrections, separate experiments were performed to determine the emissivity of the SiO_2 coating as a function of temperature. The maximum radiation correction was found to be 150K. The temperature measurements were repeatable to within ±25K. Chemical species concentrations in the flame were obtained by an uncooled quartz microprobe and a gas chromatograph. A 70 μm sampling probe was used for most of the analysis except for the heavily sooting flame where a larger (90 μm) probe was used. This probe was positioned radially along the streamlines to minimize the flow disturbance. Concentrations of stable gases (H_2, CO_2, O_2, N_2, CH_4, CO and H_2O), light hydrocarbons (up to C_6) and PAH were measured. This data was reduced via. a model to obtain the production and destruction rates of various species.

4. RESEARCH RESULTS

As discussed above, radiation-induced extinction was investigated in *μg* using spherical diffusion flames and the supporting *1-g* experiments were conducted using counterflow diffusion flames. The purpose of the supporting *1-g* experiments was to quantify the detailed thermal, chemical and sooting structure of low strain rate radiative diffusion flames in the thermochemical environment encountered under *μg* conditions. The data from *1-g* experiments was needed for the development of detailed chemistry transient models for both *μg* and *1-g* cases. In this section, first a theoretical formulation for transient radiative diffusion flames is discussed to show the relationship between *1-g* and *μg* parts of the study. Next, progress on the *μg* experiments is described followed by the progress on the *1-g* experiments. Several papers have been published during the course of this research. These are presented in the Appendices.

4.1 *Transient Radiative Diffusion Flames*

Since we are interested in radiative-extinction and the processes that induce it, the theoretical formulation must be transient. Also, eventually detailed chemistry and transport properties must be included to better understand the interaction between radiation and chemistry that leads to the limit phenomenon of radiative extinction. To this end, we are linking the Sandia Chemkin code

with our transient programs. The steady-state version of the Sandia Chemkin code with detailed chemistry and transport properties has been successfully implemented (see Appendices). For the transient problem, however, initially the simplest case with *constant pressure ideal gas reactions & Le=1* is considered. Also, an *overall one-step reaction* was assumed. This is represented by:

$\nu_F F + \nu_O O \rightarrow \sum_{i=1}^{N-2} \nu_i P_i$; with q°, the standard heat of reaction, given by:

$q^\circ = h_F^\circ M_F \nu_F + h_O^\circ M_O \nu_O - \sum_{i=1}^{N-2} h_i^\circ M_i \nu_i$ and Q = q°/$M_F\nu_F$ is the heat released per unit mass of fuel. Within these assumptions, we may write the following governing equations for any geometrical configuration (spherical or counterflow) [14]. Numerical solution of these equations for the transient counterflow case is presented in the Appendices.

Mass Conservation: $$\frac{\partial \rho}{\partial t} + \vec{\nabla}\cdot(\rho\vec{v}) = 0 \qquad (1)$$

Species Conservation: $$\rho\frac{\partial Y_i}{\partial t} + \rho\vec{v}\cdot\vec{\nabla}Y_i - \vec{\nabla}\cdot(\rho D\vec{\nabla}Y_i) = w_i \qquad (2)$$

Energy Conservation: $$\rho\frac{\partial h^s}{\partial t} + \rho\vec{v}\cdot\vec{\nabla}h^s - \vec{\nabla}\cdot(\rho D\vec{\nabla}h^s) = -\sum_i h_i^\circ w_i - \vec{\nabla}\cdot(\vec{q}_r) - Q_s\dot{m}_{s_o}''' \qquad (3)$$

Ideal Gas: $$\rho T = \rho_\infty T_\infty \qquad (4)$$

Here, the symbols have their usual definitions with ρ = density, T = temperature, v = velocity, Y_i = mass fraction of species i, h^s = sensible enthalpy, w_i = mass production or destruction rate per unit volume of species i and D = diffusion coefficient. The last three terms in Equ (3) respectively are: the chemical heat release rate due to gas phase combustion, the radiative heat loss rate per unit volume and the chemical heat released due to soot oxidation. The above equations, however, are insufficient for our problem because soot volume fraction must be known as a function of space and time to determine the radiative heat loss. To enable describing soot in a simple manner [Note: initially, a very simple soot model was considered], we define the mass fraction of atomic constituents as follows: $\xi_j = \sum_i \left(M_j\nu_i^j/M_i\right)Y_i$, where M_i is the molecular weight of species i, M_j is the atomic weight of atom j and ν_i^j is the number of atoms of kind j in specie i. Assuming that the only atomic constituents present in the hydrocarbon flame are C, H, O & Inert and with $Y_{soot} \equiv \Phi \equiv \rho_s f_v/\rho$ (where: ρ_s= soot density & f_v= soot volume fraction), we obtain: $\xi_C + \xi_H + \xi_O + \xi_I + \rho_s f_v/\rho = 1$. Defining $\xi_C + \xi_H = \xi_F$ and $Z_F = \xi_F/Y_{F_\infty}$, we obtain $Z = \left[(\xi_F)_{F_\infty} Z_F + \rho_s f_v/\rho\right]$ as the conserved scalar for a sooty flame. This yields the following soot conservation equation:

Soot Conservation: $$\rho\frac{\partial \Phi}{\partial t} + \rho\vec{v}\cdot\vec{\nabla}(\Phi) - \vec{\nabla}\cdot[\rho D_s\vec{\nabla}(\Phi)] = \dot{m}_{s_p}''' - \dot{m}_{s_o}''' = \dot{m}_{net}''' \qquad (5)$$

The corresponding fuel equation becomes:

Fuel Conservation:
$$\rho\frac{\partial Z_F}{\partial t} + \rho\vec{v}\cdot\vec{\nabla}(Z_F) - \vec{\nabla}\cdot[\rho D\vec{\nabla}(Z_F)] = -\frac{1}{Y_{F\infty}}(\dot{m}'''_{S_p} - \dot{m}'''_{S_o}) = -\frac{\dot{m}'''_{net}}{Y_{F\infty}} \qquad (6)$$

The oxygen conservation equation for Z_O defined as $Z_O = \xi_O/Y_{O\infty}$ is obtained as:

Oxygen Conservation:
$$\rho\frac{\partial Z_O}{\partial t} + \rho\vec{v}\cdot\vec{\nabla}(Z_O) - \vec{\nabla}\cdot[\rho D\vec{\nabla}(Z_O)] = 0 \qquad (7)$$

Under conditions of small soot loading, the soot terms in the energy and the fuel conservation equations (3) & (6), may be ignored. Thus, Equ.(6) may be considered homogeneous to a good approximation and becomes similar to Equ. (7). Thus, Φ calculated from the soot equation can be used to determine the radiative heat loss term in the energy equation.

The above formulation requires a description of soot formation ($\dot{m}'''_{S_p}$) and oxidation ($\dot{m}'''_{S_o}$) terms. To experimentally determine these terms, measurements of soot volume fraction, soot number density, temperature, velocity and species profiles were needed. These measurements were not possible under μg conditions. Thus, a supporting *1-g* experiment that can determine these terms in an enhanced combustion products environment (simulated μg) was used. The most convenient *1-g* experimental configuration is one that simplifies the above PDE's to ODE's. One such flame configuration is the counterflow diffusion flame which was used to determine $\dot{m}'''_{S_p}$ and $\dot{m}'''_{S_o}$. [The counterflow diffusion flame apparatus used for these experiments had the following additional advantages: (i) Its special construction enabled obtaining strain rates as low as 6 sec^{-1}. This increases the reactant residence time and yields a thick reaction zone convenient for determining the detailed thermal, chemical and sooting structure of the diffusion flame. (ii) The reactants were preheated and the desired mixture with combustion products was created to match the μg thermochemical environment. (iii) The optical and gas chromatographic equipment was used to make spatially resolved profile measurements of: temperature; stable gases; light hydrocarbons (up to benzene); PAH; laser light scattering and extinction for soot; laser induced fluorescence for OH & PAH; and spectral radiative emission. These flame structure measurements are presented in the Appendices and were used for developing detailed chemistry models for *1-g* and μg cases. (iv) Some flames were also established on the fuel side of the stagnation plane. This enables soot to oxidize as it approaches the reaction zone and makes the flames very radiative.]

4.2 *Progress on μg Experiments*

(A spherical diffusion flame supported by a low heat capacity porous gas burner)

Significant progress has been made on both experimental and theoretical parts of the μg research despite the fact that radiative extinction could not be experimentally proven due to short μg times. The accomplishments are briefly summarized below and the papers are presented in the Appendices:

1. *Atreya, A, Agrawal, S., Sacksteder, K., and Baum, H.*, "Observations of Methane and Ethylene Diffusion Flames Stabilized around a Blowing Porous Sphere under Microgravity Conditions," AIAA paper # 94-0572, 1994. APPENDIX B
2. *Pickett, K., Atreya, A., Agrawal, S., and Sacksteder, K.*, "Radiation from Unsteady Spherical Diffusion Flames in Microgravity," AIAA paper # 95-0148, January 1995. APPENDIX C
3. *Atreya, A., Agrawal, S., Shamim, T., Pickett, K., Sacksteder, K. R. and Baum, H. R.* "Radiant Extinction of Gaseous Diffusion Flames," 3rd International Microgravity Conference, April, 1995. APPENDIX D
4. *Atreya, A., Agrawal, S., Sacksteder, K. R., and Baum, H. R.* "Unsteady Gaseous Spherical Diffusion Flames in Microgravity - Part A: Expansion Rate" being prepared for submission to Combustion and Flame.
5. *Atreya, A., Agrawal, S., Pickett, K., Sacksteder, K. R., and Baum, H. R.* "Unsteady Gaseous Spherical Diffusion Flames in Microgravity - Part B: Radiation, Temperature and Extinction" being prepared for submission to Combustion and Flame.

The above experimental and theoretical work is briefly described below:

μg Experimental Work: The *μg* experiments were conducted in the 2.2 sec drop tower at the NASA Lewis Research Center. A low heat capacity porous spherical burner was used to produce an aerodynamically stabilized gaseous spherical diffusion flame [It is important to note that such flames are very difficult to obtain even in *μg* and considerable time and effort was devoted toward obtaining these flames]. Several *μg* experiments under ambient pressure and oxygen concentration conditions, were performed with methane (less sooty), ethylene (sooty), and acetylene (very sooty) for flow rates ranging from 4 to 28 cm^3/s. Two ignition methods were used for these experiments: (i) The burner was ignited in *1-g* with the desired fuel flow rate and the package was dropped within one second after ignition. This method is suitable only for very low flow rates. (ii) The burner was ignited in *1-g* with the lowest possible flow rate (~2.5 cm^3/s) to make a very small flame and create the smallest possible disturbance. The flow was then switched to the desired flow rate in *μg* just after the commencement of the drop. However, in all the experiments with different fuels and flow rates, radiative extinction was not observed. It appears that longer *μg* time may be required. The following measurements were made during the *μg* experiments:

1. The *flame radius* was measured from photographs taken by a color CCD camera. Image processing was used to determine both the flame radius and the relative image intensity. A typical sequence of photographs is shown in Appendices B & C.
2. The *flame radiation* was measured by three photodiodes with different spectral absorptivities. The first photodiode essentially measures the blue & green radiation, the second photodiode captures the yellow, red & near infra-red radiation, and the third photodiode is for infra-red radiation from 0.8 to 1.8 μm. Results of these measurements are presented in Appendices C & D.
3. The *flame temperature* was measured by two S-type thermocouples and the sphere surface temperature was measured by a K-type thermocouple. In both cases 0.003" diameter wire was used. The measured temperatures were later corrected for time response and radiation. The temperature results are also presented in Appendices C & D.

It was interesting to note that for all fuels (methane, ethylene and acetylene), initially the flame is blue (non-sooty) but becomes bright yellow (sooty) under μg conditions (see the progressive flame growth for methane in Appendix B). Later, as the μg time progresses, the flame grows in size and becomes orange and less luminous and the soot luminosity seems to disappear. A possible explanation for this observed behavior is suggested by the theoretical calculations of Refs. [7, 24 & Appendix E]. As can be seen from Fig. 6 of Appendix E, the soot volume fraction first quickly increases and later decreases as the local concentration of combustion products increases. Essentially, further soot formation is inhibited by the increase in the local concentration of the combustion products and soot oxidation is enhanced [Refs. 32-35]. Also, the high temperature reaction zone moves away from the existing soot leaving behind a relatively cold (non-luminous) soot shell (soot-shell was visible for ethylene flames). Thus, at the onset of μg conditions, initially a lot of soot is formed in the vicinity of the flame front resulting in bright yellow emission. As the flame grows, several events reduce the flame luminosity: (i) The high concentration of combustion products left behind by the flame front inhibits the formation of new soot and promotes soot oxidation. (ii) The primary reaction zone, seeking oxygen, moves away from the soot region and the soot is pushed toward cooler regions by thermophoresis. Both these effects increase the distance between the soot layer and the reaction zone. (iii) The dilution and radiative heat losses caused by the increase in the concentration of the combustion products reduces the flame temperature which in turn reduces the soot formatión rate and the flame luminosity.

It was further observed that, for the same fuel flow rate, methane flames eventually become blue (non-sooty) in approximately one second, ethylene flames became blue toward the end of the μg time (i.e. ~2 sec) while acetylene flames remained luminous yellow throughout the 2.2 sec μg time (although the intensity was significantly reduced as seen by the photodiode measurements in Figure 2). This is because of the higher sooting tendency of acetylene which enables soot formation to persist for a longer time. Thus, acetylene soot remains closer to the high temperature reaction zone for a longer time making the average soot temperature higher and the distance between the soot and the reaction layers smaller. Eventually, as is evident from Figure 2, even the acetylene flames will become blue in μg. From Figure 2 we note that the peak infrared, visible and UV radiation intensities occur at about 0.1 sec which almost corresponds to the location of the first thermocouple whose output is plotted in Figures 3 & 4 as Tgas(1). From the temperature measurements presented in Figures 3 & 4, we note that: (i) The flame radiation significantly reduces the flame temperature (compare the peaks of the second thermocouple [Tgas(2)] with those of the first [Tgas(1)] for both ethylene and acetylene) by approximately 300K for ethylene and 500K for acetylene. (In fact, the acetylene flame seems to be close to extinction at this instant.) (ii) The temperature of the acetylene flame is about 200K lower than the ethylene flame at the first thermocouple location. (iii) The final gas temperature is also about 100K lower for the acetylene flame, which is consistent with larger radiative heat loss. Thus, it seems that a higher fuel flow rate and/or a sootier fuel and/or an enhanced CO_2 & H_2O atmosphere will radiatively extinguish the flame.

The data from the photodiodes was further reduced to obtain the total soot mass and the average temperature of the soot layer. This is plotted in Figures 5 & 6. These figures show that the average acetylene soot shell temperature is higher than the average ethylene soot shell temperature. The total soot mass produced by acetylene peaks at 0.2 seconds which corresponds

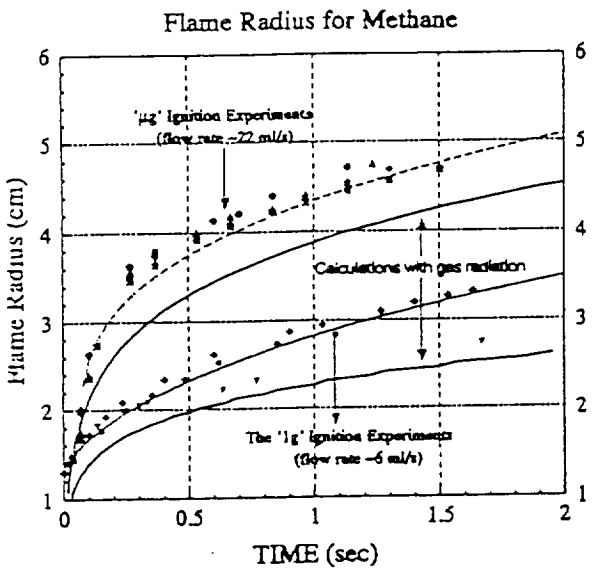

Figure 1

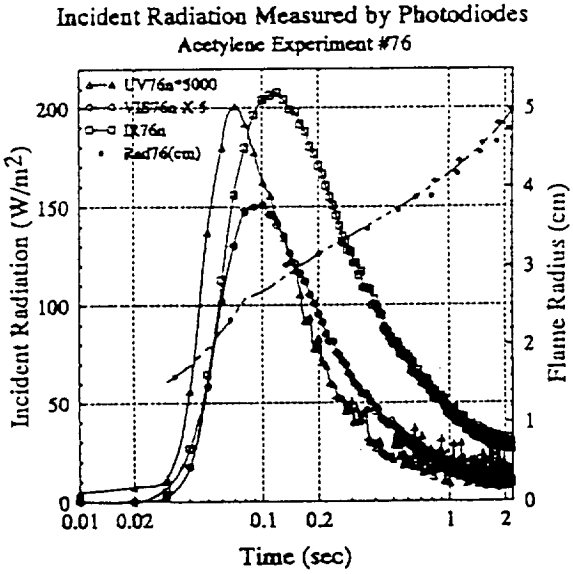

Figure 2

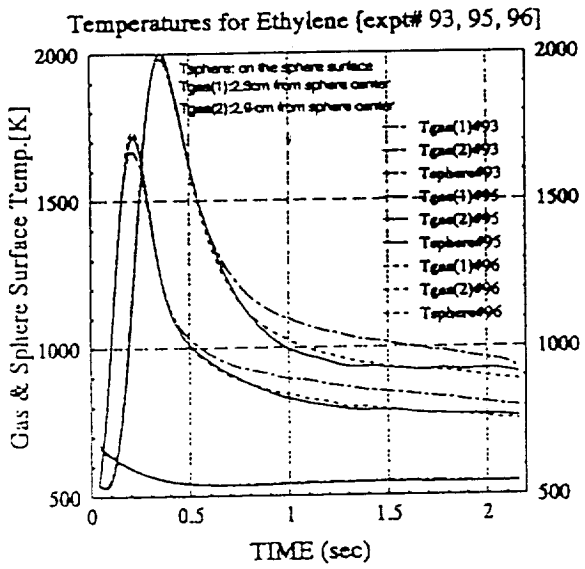

Figure 3

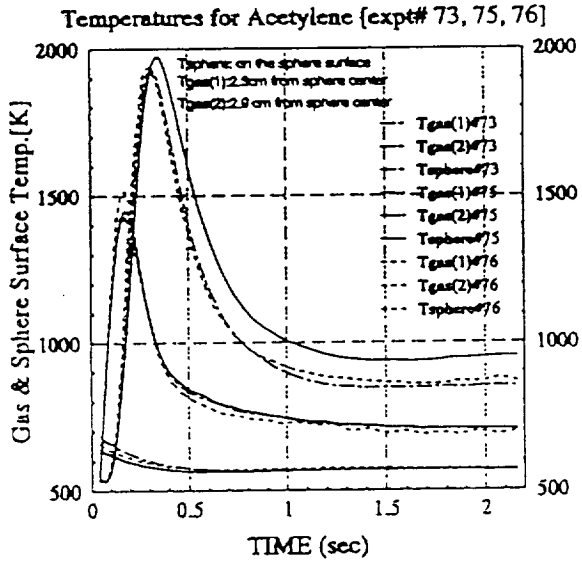

Figure 4

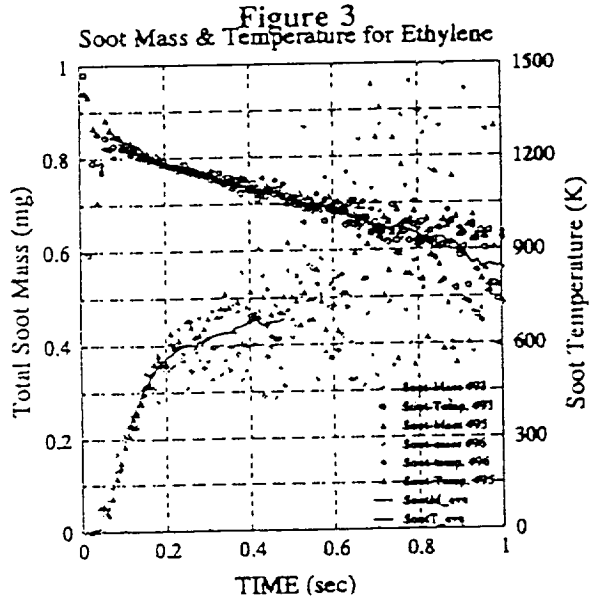

Figure 5

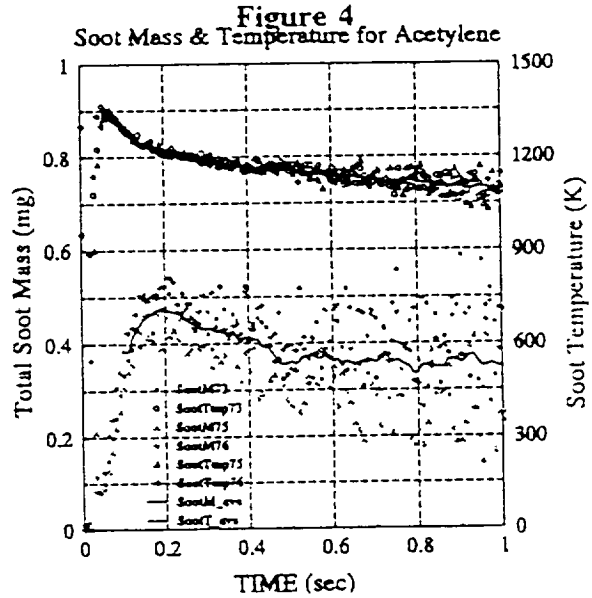

Figure 6

to the peak of the first thermocouple [Tgas(1)], explaining the large drop in temperature. Also, the acetylene soot shell is cooling more slowly than the ethylene soot shell which is consistent with the above discussion regarding the photographic observations. Thus, for ethylene the reaction layer is moving away faster from the soot layer than for acetylene. This is also consistent with the fact that ethylene soot mass becomes nearly constant but the acetylene soot mass reduces due to oxidation. Finally, the rate of increase in the total soot mass (i.e. the soot production rate) should be related to the sooting tendency of a given fuel. This corresponds to the slope of the soot mass curves in Figures 5 & 6. Clearly, the slope for acetylene is higher.

Figure 1 shows the measured and calculated flame radius for methane flames plotted against μg time. Two sets of data are shown: (i) low flow rate flames where the flame was ignited in *1-g* and the package was dropped, and (ii) high fuel flow rate flames that were ignited in μg. This data was obtained both by visually measuring the radius of the outer faint blue flame region from the photographs, and by using video image processing and defining the radius by a threshold intensity. The two methods of determining the flame radius were within the experimental scatter. Since, methane is the least radiative flame, it is expected that a model with only gas radiation (i.e. without soot radiation) may compare favorably. Model calculations are also shown in Figure 1 (these will be discussed later). The flame radius measurements show a substantial change in the growth rate from initially being roughly proportional to $t^{1/2}$ to eventually (after radiative heat loss) being proportional to $t^{1/5}$.

μg Modeling Work: As a first step, it was of interest to see if the transient expansion of μg spherical diffusion flames could be predicted without including soot and flame radiation and in the limit of infinite reaction rates. This simple model was very informative and was presented in Ref.[36] & NASA Technical Memorandum 106766. Thus, our more recent work with a second order overall finite rate reaction and gas radiation is described here. The gas radiation model and other reaction rate constants used were identical to those described in Appendix A & E. Equations (1) through (4) for the 1-D spherical case were numerically solved assuming Le =1 and $\rho^2 D$ = constant. Boundary conditions at R = R_i were:

$$at\ R=R_i:\ T=T_\infty;\ Y_F=1;\ Y_O=0;\ Y_P=0;\ \textit{and Fuel injection rate} = \dot{M}(t) = 4\pi R_i^2 (\rho v)_{@R_i}$$

where R_i was taken as 0.15 cm, and $as\ R \to \infty$: $T=T_\infty$; $Y_F=0$; $Y_O=Y_{O_\infty}$; $Y_P=Y_{P_\infty}$. Also, initial spatial distribution of temperature and species based on infinite reaction rate solution was assumed.

Model calculations for four cases are shown in Figures 7, 8 and 9. The four cases were: (i) Case 1 - No flame radiation & fuel flow rate = 22 cm^3/s of methane; (ii) Case 2 - same as case 1 but with gas radiation; (iii) Case 3 - same as case 2 but with increased ambient product concentration, Y_{P_∞}= 0.2 instead of zero; (iv) Case 4 - same as case 2 but with a step change in fuel flow rate from 2 cm^3/s until flame radius of 1.3 cm and 22 cm^3/s thereafter. Figure 7a shows several calculated flame radii for different fuel flow rates for both with and without flame radiation. Clearly, the flame radius increases with the fuel flow rate and decreases substantially due to gas radiation. Essentially, as the gas inside the spherical flame looses heat via radiation, its temperature falls and its density increases. Thus, the spherical flame collapses as is evident from Figures 8 and 9 which are time sequences of gas density and velocity. Figure 9 actually shows that there is a reversal in the gas velocities near the flame zone due to the collapsing

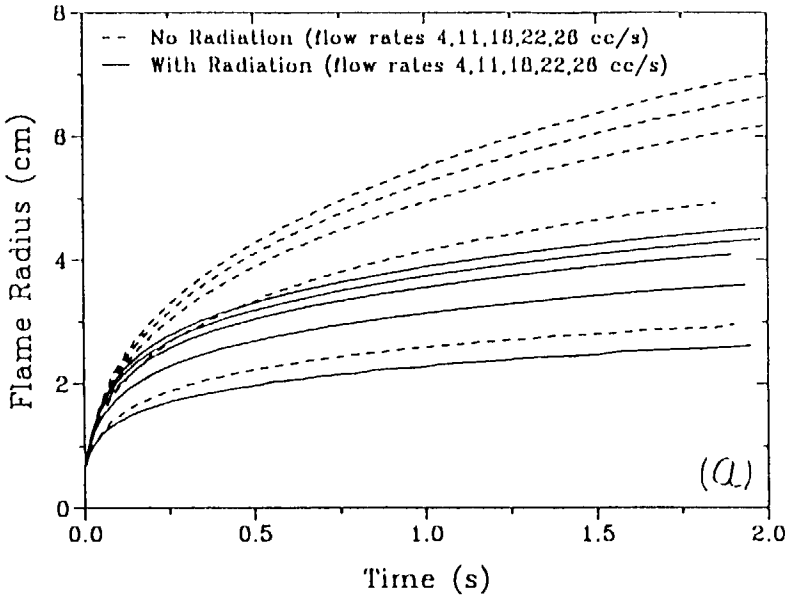

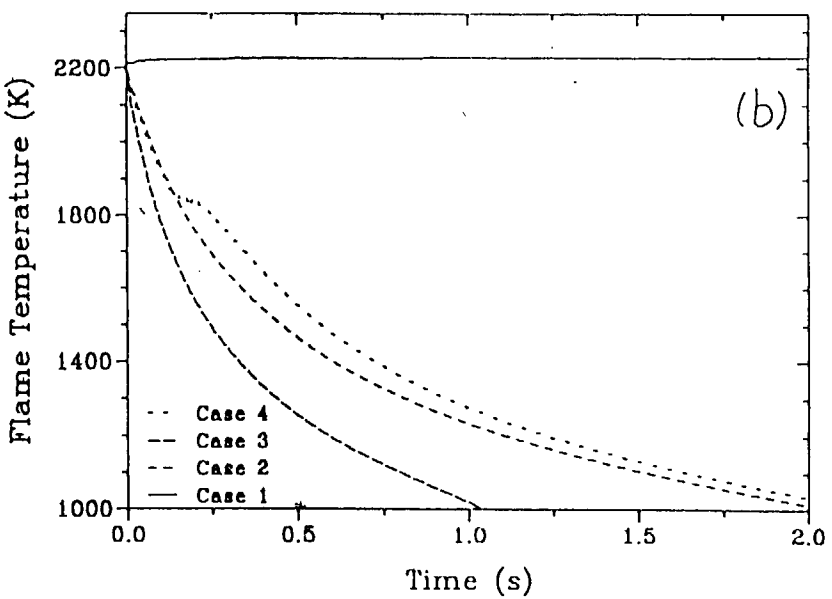

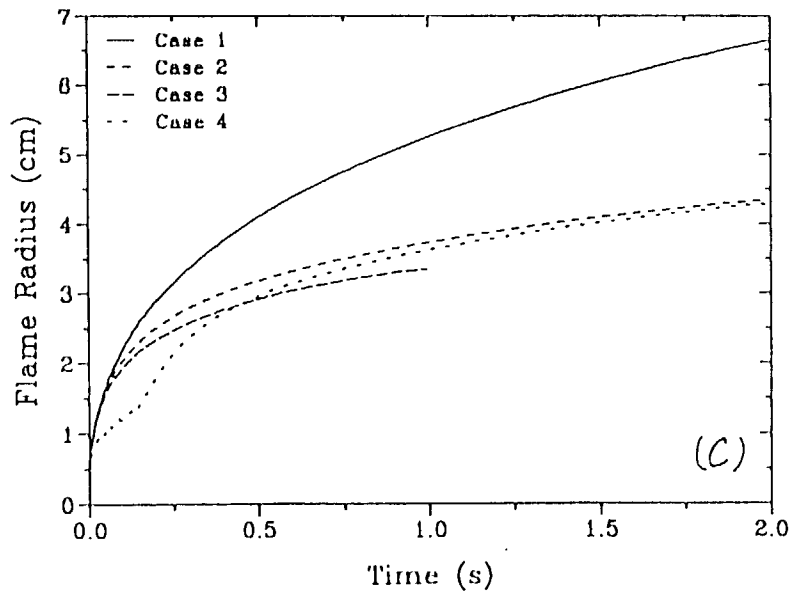

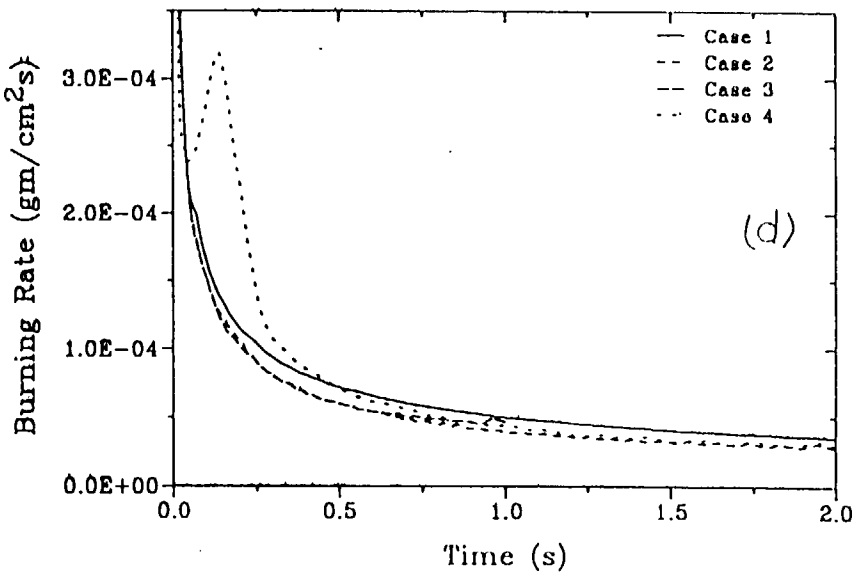

Case 1: No Radiation; Case2: With Gas Radiation

Case 3: With Rad. & Ypl=0.2; Case 4: With Rad. & Fuel Flow Step Change

Figure 7 (a, b, c & d)

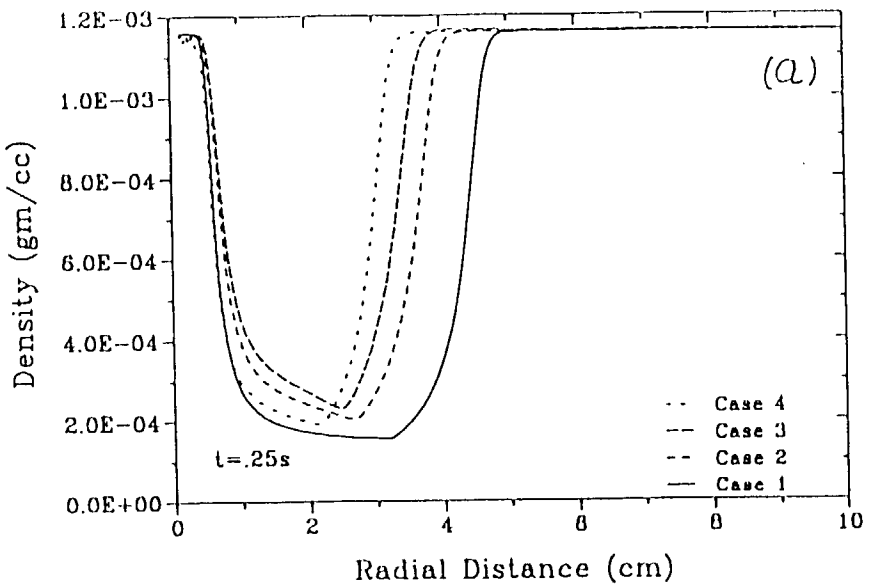

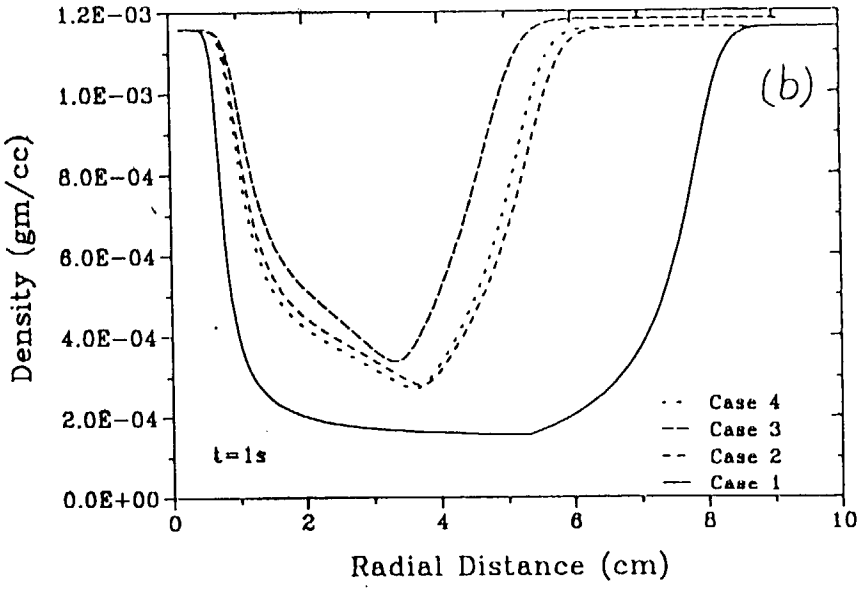

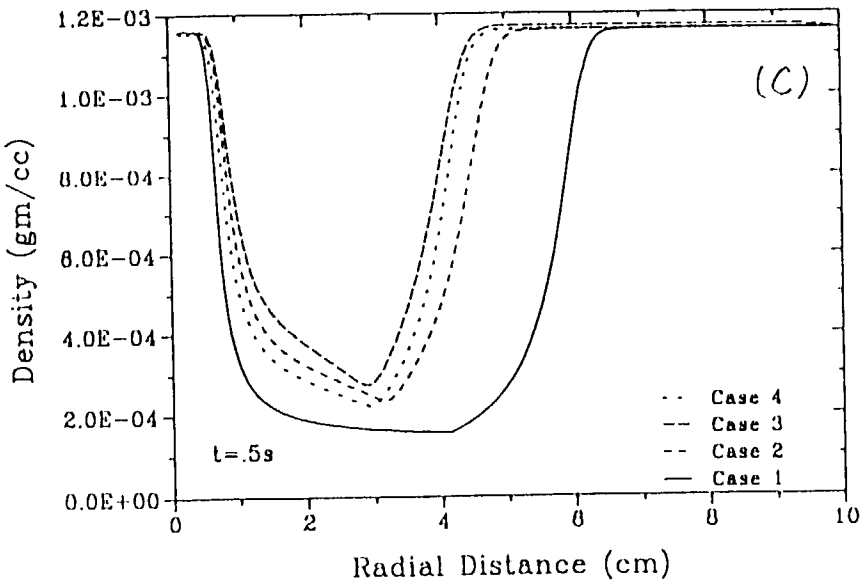

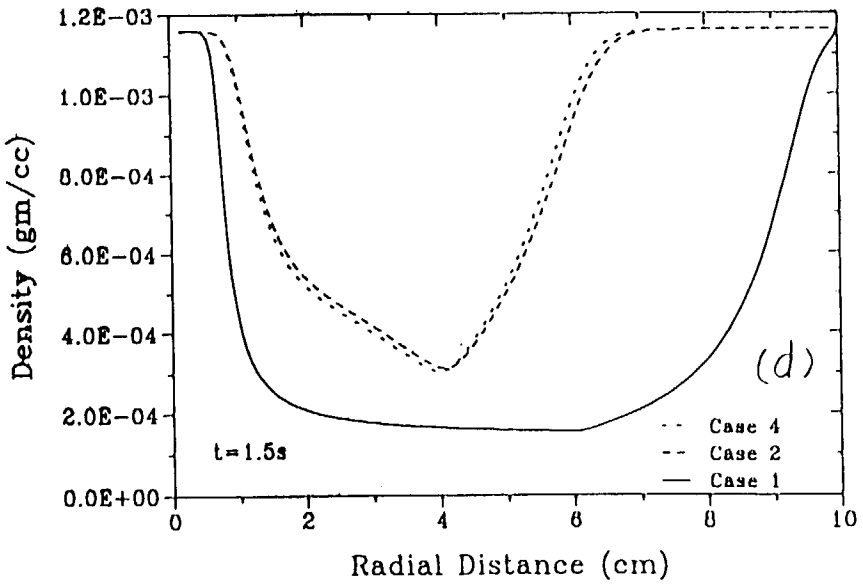

Case 1: No Radiation; Case2: With Gas Radiation

Case 3: With Rad. & Ypl=0.2; Case 4: With Rad. & Fuel Flow Step Change

Figure 8 (a, b, c & d)

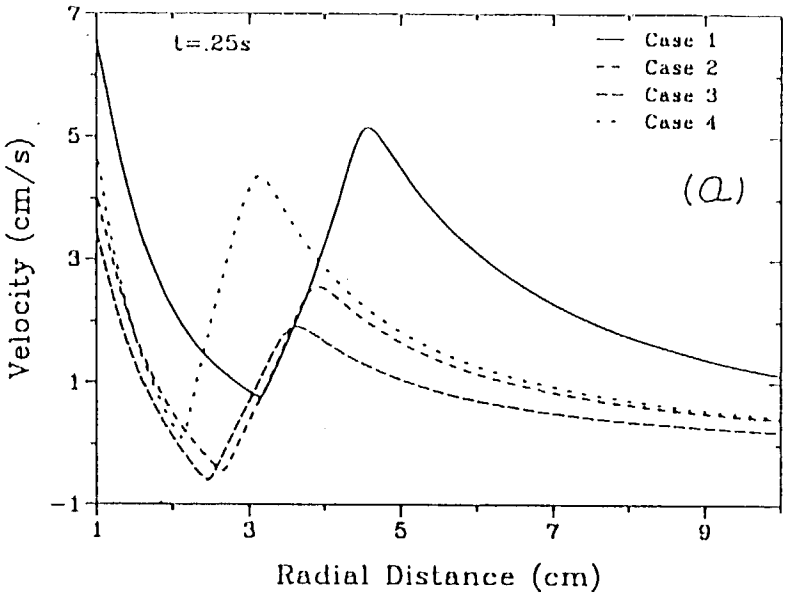

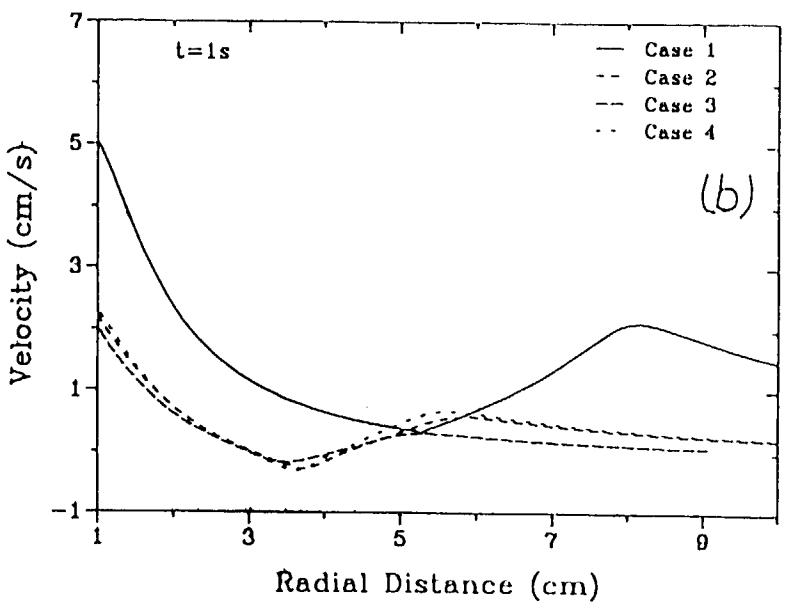

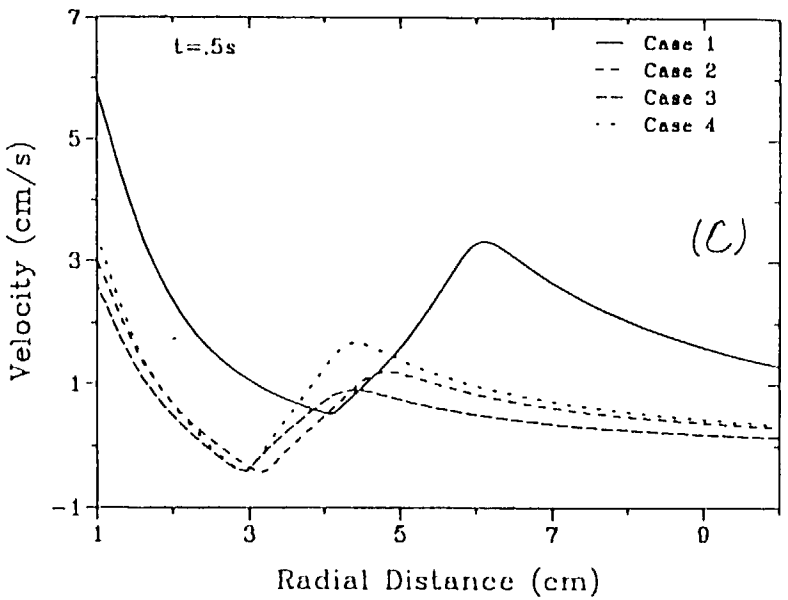

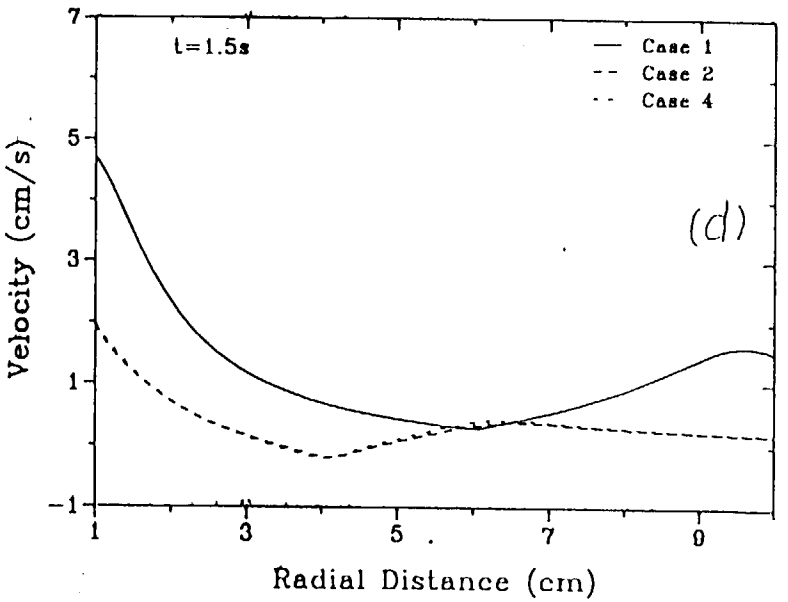

Case 1: No Radiation; Case2: With Radiation

Case 3: With Rad. & Ypl=0.2; Case 4: With Rad. & Fuel Flow Step Change

Figure 9 (a, b, c & d)

spherical flame. However, the net flame radius still increases, albeit slowly. Figure 7b shows that for Case 3 the flame temperature falls below 1000K within 1 second. Thus, radiative extinction is possible for certain atmospheres. Also, as seen from Figure 7d, the burning rate per unit area decreases as the flame expands and radiation contributes to decrease it further.

4.3 *Progress on 1-g Experiments*

(An axis-symmetric low strain rate counterflow diffusion flame)

Significant progress has been made on both experimental and theoretical parts of the *1-g* which may be briefly summarized as follows:

a) Theoretical modeling of zero strain rate transient diffusion flame with radiation (Ref. 7).
   - *Atreya, A., and Agrawal, S.*, "Extinction of Moving Diffusion Flames in a Quiescent Microgravity Environment due to CO_2/H_2O/Soot Radiative Heat Losses," First ISHMT-ASME Heat and Mass Transfer Conference, 1994. (Appendix A)
   - *Atreya, A. and Agrawal, S.*, "Effect of Radiative Heat Loss on Diffusion Flames in Quiescent Microgravity Atmosphere," *Combustion & Flame*, (accepted for publication), 1995. (Appendix E)

b) Theoretical modeling of finite strain rate transient counterflow diffusion flame with radiation (Refs. 24, 25).
   - *Shamim, T., and Atreya, A.*, "A Study of the Effects of Flame Radiation on Transient Extinction of Strained Diffusion Flames," Joint Technical Meeting of Combustion Institute, paper: 95S-104 pp.553, 1995. Currently being prepared for submission to Combustion and Flame. (Appendix F)
   - *Shamim, T., and Atreya, A.*, "Numerical Simulations of Radiative Extinction of Unsteady Strained Diffusion Flames," Symposium on Fire and Combustion Systems, ASME IMECE, November, 1995. (Appendix G)
   - *Shamim, T. and Atreya, A.* "Dynamic Response of Radiating Flamelets Subject to Variable Reactant Concentrations," Proceedings of the Central Section of the Combustion Institute, 1996. The corresponding paper "Transient Response of a Radiating Flamelet to Changes in Global Stoichiometric Conditions." is being prepared for submission to Combustion and Flame. (Appendix L & O)

c) Experimental work on counterflow diffusion flames to determine the soot formation and oxidation rates (Refs. 32, 33).
   - *Atreya, A. and Zhang, C.*, "Experiments and Correlations of Soot Formation and Oxidation in Methane Counterflow Diffusion Flames," submitted to International Symposium on Combustion, Not accepted, currently being revised for submission to Combustion and Flame. (Appendix H)
   - *Zhang, C. and Atreya, A.* "Measurements of Soot Volume Fraction Profiles in Counterflow Diffusion Flames Using a Transient Thermocouple Response Technique," Submitted to The International Symposium on Combustion, Not accepted, currently being revised for submission to Combustion and Flame. (Appendix I)
   - *Atreya, A., Zhang, C., Kim, H. K., Shamim, T. and Suh, J.* "The Effect of Changes in the Flame Structure on Formation and Destruction of Soot and NO_x in Radiating Diffusion

Flames," Accepted for publication in the Twenty-Sixth (International) Symposium on Combustion, 1996. (Appendix J)

- *Zhang, C, Atreya, A., Kim, H. K., Suh, J. and Shamim, T,* "The Effect of Flame Structure on Soot Inception, Growth and Oxidation in Counterflow Diffusion Flames," Proceedings of the Central Section of the Combustion Institute, 1996. (Appendix M)
- *Zhang, C, Atreya, A., Shamim, T, Kim, H. K. and Suh, J.*, "Measurements of OH, CH, C_2 and PAH in Laminar Counterflow Diffusion Flames," Proceedings of the Central Section of the Combustion Institute, 1996. (Appendix N)

d) Detailed chemistry simulation of the effect of enhanced water vapor concentration on radiative counterflow diffusion flames.
   - *Crompton, T. and Atreya, A.* "The Effect of Water on Radiative Laminar Hydrocarbon Diffusion Flames - Part A: Experimental Results," being prepared for submission to Combustion Science and Technology.
   - *Suh, J. and Atreya, A.* "The Effect of Water on Radiative Laminar Hydrocarbon Diffusion Flames - Part B: Theoretical Results," being prepared for submission to Combustion Science and Technology. Also published in the proceedings of the International Conference on Fire Research and Engineering, Sept, 1995.
   - *Suh, J. and Atreya, A.*, "The Effect of Water Vapor on Radiative Counterflow Diffusion Flames," Symposium on Fire and Combustion Systems, ASME IMECE, Nov. 1995. (Appendix K)

Experiments on counterflow diffusion flames were conducted to determine the soot particle formation and oxidation rates. This geometry was adopted for the ground-based experiments and modeling because it provides a constant strain rate flow field which is one-dimensional in temperature and species concentrations. The strain rate is directly related to the imposed flow velocity and the one-dimensionality of this flame simplifies experimental measurements and analysis. As noted earlier in Section 4.1, this is the simplest flame for experimentally determining the RHS of Equ. (5). Two types of counterflow diffusion flames are being investigated: (1) A low-strain-rate diffusion flame which lies on the oxidizer side of the stagnation plane. Here, all the soot produced is convected away from the flame toward the stagnation plane. Thus, soot formation is the dominant process. (2) A low-strain-rate diffusion flame which lies on the fuel side of the stagnation plane. Here, all the soot produced is convected into the diffusion flame. This enhances flame radiation as the soot is oxidized. The second configuration is especially relevant to the μg experiments. The experimental results for the flame on the oxidizer side of the stagnation plane are described in Ref. [32] and a soot formation model developed based on these results is being prepared for publication (Ref. [33]).

To theoretically investigate the extinction limits of diffusion flames, first a simple case of zero strain rate one-dimensional diffusion flame with flame radiation was examined [Ref. 7]. Next strained diffusion flame calculations with flame radiation were conducted. These are presented in the Appendices. As a first step, constant properties, one-step irreversible reaction and unity Lewis number were assumed. The equations were numerically integrated to examine the conditions under which radiation-induced extinction occurs. The soot formation and oxidation rates were obtained from the counterflow diffusion flame experiments. Surprisingly, calculations show that extinction occurs due to gas radiation as in the spherical diffusion flame case.

5. REFERENCES

1. *Dietrich, D. L., Ross, H. D. and T'ien, J. S.* "Candle Flames in Microgravity," Third Microgravity Combustion Workshop, Cleveland, Ohio, April, 1995.
2. *Ross, H. D., Sotos, R. G. and T'ien, J. S.*, Combustion Science and Technology, Vol. 75, pp. 155-160, 1991.
3. *T'ien, J. S., Sacksteder, K. R., Ferkul, P. V. and Grayson, G. D.* "Combustion of Solid Fuels in very Low Speed Oxygen Streams," Second International Microgravity Combustion Workshop," NASA Conference Publication, 1992.
4. *Ferkul, P., V.*, "A Model of Concurrent Flow Flame Spread Over a Thin Solid Fuel," NASA Contractor Report 191111, 1993.
5. *Avedisian, C., T.* "Multicomponent Droplet Combustion and Soot Formation in Microgravity," Third Microgravity Combustion Workshop, Cleveland, Ohio, April, 1995.
6. *Jackson, G., S., Avedisian, C., T. and Yang, J., C.*, Int. J. Heat Mass Transfer., Vol.35, No. 8, pp. 2017-2033, 1992.
7. *Atreya, A. and Agrawal, S.*, "Effect of Radiative Heat Loss on Diffusion Flames in Quiescent Microgravity Atmosphere," *Combustion & Flame*, (accepted for publication), 1995.
8. *T'ien, J. S.*, Combustion and Flame, Vol. 80, pp. 355-357, 1990.
9. *Law, C. K. and Faeth, G. M.*, Prog. Energy Combust. Sci., Vol. 20, 1994, pp. 65-116.
10. *Buckmaster, J., Gessman, R., and Ronney, P.*, Twenty-Fourth (International) Symposium on Combustion, The Combustion Institute, 1992.
11. *Ronney, P.D., and Wachman, H.Y.*, "Effect of Gravity on Laminar Premixed Gas Combustion I: Flammability Limits and Burning Velocities," Comb. & Flame,62,pp.107-119(1985).
12. *Ronney, P.D.*, "Effect of Gravity on Laminar Premixed Gas Combustion II: Ignition and Extinction Phenomena," Comb. & Flame,62,pp.121- 133(1985).
13. *Ronney, P.D.*, "On the Mechanisms of Flame Propagation Limits and Extinguishment Processes at Microgravity," 22nd Symposium(Int'l) on Combustion, The Combustion Institute, Pittsburgh, 1989.
14. *Williams, F.A.*, Combustion Theory, Benjamin/Cummings Publishing Co., 2nd Ed.(1985).
15. *Fendell, F.E.*, J. Fluid Mech.,21,pp. 281-303 (1965).
16. *Linan, A.*, Acta Astronautica, Vol. 1, pp. 1007-1039, 1974.
17. *Linan, A. and Crespo, A.*, Combustion Science and Technology, Vol. 14, pp. 95-117,1976.
18. *T'ien, J.S.*, "Diffusion Flame Extinction at Small Stretch Rate: the Mechanism of Radiative Heat Loss," Comb.& Flame, 65, pp.31-34(1986).
19. *Sohrab, S.H., Linan, A., and Williams, F.A.*, "Asymptotic Theory of Diffusion Flame Extinction with Radiant Heat Loss from the Flame Zone," Comb. Sci. Tech.,27,pp.143-154(1982).
20. *Chao, B. H., Law, C. K. and T'ien, J. S.*, Twenty-Third (International) Symposium on Combustion, The Combustion Institute, pp. 523-531, 1990.
21. *Seshadri, K. and Williams, F. A.*,Intl. J. Heat Mass Transfer 21, 251 (1978).
22. *Chao, B. H., Law, C. K.*, 1993, "Asymptotic Theory of Flame Extinction with Surface Radiation," Combustion & Flame, Vol. 92, pp. 1-24.
23. *Kaplan, C. R., Baek, S. W., Oran, E. S., and Ellzey, J. L.*, "Dynamics of a Strongly Radiating Unsteady Ethylene Jet Diffusion Flame," Combustion & Flame, Vol. 96, pp. 1-21, 1994.
24. *Shamim, T., and Atreya, A.*, "A Study of the Effects of Radiation on Transient Extinction of Strained Diffusion Flames," Joint Technical Meeting of Combustion Institute, paper 95S-104 pp. 553-558, 1995.
25. *Shamim, T., and Atreya, A.*, "Numerical Simulations of Radiative Extinction of Unsteady Strained Diffusion Flames," Symposium on Fire and Combustion Systems, ASME IMECE Conference, 1995.
26. *Ross, H. D.*, Proceedings of the Third International Microgravity Combustion Workshop," NASA Conference Publication, Cleveland, April 1995.
27. *Ross, H. D.*, Proceedings of the Second International Microgravity Combustion Workshop," NASA Conference Publication, Cleveland, 1992.
28. Microgravity Science and Applications, Program Tasks and Bibliography for 1992, NASA Technical Memorandum 4469, March, 1993.
29. *Ishizuka, S., and Tsuji, H.*, "An Experimental Study of the Effect of Inert Gases on Extinction of Laminar Diffusion Flames,"18th Symposium (Int'l) on Combustion, The Combustion Institute, Pittsburgh

pp.695-703(1981).
30. *Ishizuka, S., Miyasaka, K., and Law, C.K.*, "Effects of Heat Loss, Preferential Diffusion, and Flame Stretch on Flame-Front Instability and Extinction of Propane-Air Mixtures," Comb.& Flame,45,pp. 293-308(1982).
31. *Tsuji, H.*, "Counterflow Diffusion Flames," Prog. Energy & Comb. Sci.,8,93 (1982).
32. *Zhang, C., Atreya, A. and Lee, K.*, Twenty-Fourth (International) Symposium on Combustion, The Combustion Institute, pp. 1049-1057, 1992.
33. *Atreya, A. and Zhang, C.*, "A Global Model of Soot Formation derived from Experiments on Methane Counterflow Diffusion Flames," in preparation for submission to Combustion and Flame.
34. *Atreya, A.*, "Formation and Oxidation of Soot in Diffusion Flames," Annual Technical Report, GRI-91/0196, Gas Research Institute, November, 1991.
35. *Atreya, A., Kim, H. K., Zhang, C., Agrawal, A., Suh, J., Serauskas, R. V. and Kezerle, J.*, "Measurements and Modeling of Soot, NOx and Trace Organic Compounds in Radiating Flamelets," International Gas Research Conference, 1995.
36. *Atreya, A, Agrawal, S., Sacksteder, K., and Baum, H.*, "Observations of Methane and Ethylene Diffusion Flames Stabilized around a Blowing Porous Sphere under Microgravity Conditions," AIAA paper # 94-0572, January 1994.
37. *Pickett, K., Atreya, A., Agrawal, S., and Sacksteder, K.*, "Radiation from Unsteady Spherical Diffusion Flames in Microgravity," AIAA paper # 95-0148, January 1995.

APPENDIX A

Extinction of a Moving Diffusion Flame in a Quiescent Microgravity Environment due to CO_2/H_2O/Soot Radiative Heat Losses

First ISHMT-ASME Heat Transfer Conference paper

By

A. Atreya and S. Agrawal

EXTINCTION OF A MOVING DIFFUSION FLAME IN A QUIESCENT MICROGRAVITY ENVIRONMENT DUE TO CO_2/H_2O/SOOT RADIATIVE HEAT LOSSES

Arvind Atreya and Sanjay Agrawal

Combustion and Heat Transfer Laboratory
Department of Mechanical Engineering and Applied Mechanics
The University of Michigan
Ann Arbor, MI 48109

Corresponding Author

Prof. Arvind Atreya
Department of Mechanical Engineering and Applied Mechanics
The University of Michigan
Ann Arbor, MI 48109

Phone: (313)-747-4790
Fax : (313)-747-3170

Submitted to the First ISHMT-ASME Heat and Mass Transfer Conference,
January 5-7, 1994, Bombay, India

EXTINCTION OF A MOVING DIFFUSION FLAME IN A QUIESCENT MICROGRAVITY ATMOSPHERE DUE TO CO_2/H_2O/SOOT RADIATIVE HEAT LOSSES

ARVIND ATREYA AND SANJAY AGRAWAL

Combustion and Heat Transfer Laboratory
Department of Mechanical Engineering and Applied Mechanics
The University of Michigan
Ann Arbor, MI 48109-2125

ABSTRACT

In this paper we present the results of a theoretical calculation for radiation-induced extinction of a one-dimensional unsteady diffusion flame in a quiescent microgravity environment. The model formulation includes both gas and soot radiation. Soot volume fraction is not a priori assumed, instead it is produced and oxidized according to temperature and species dependent formation and oxidation rates. Thus, soot volume fraction and the resulting flame radiation varies with space and time. Three cases are considered (i) a non-radiating flame, (ii) a scarcely sooty flame, and (iii) a very sooty flame. For a non-radiating flame, the maximum flame temperature remains constant and it does not extinguish. However, the reaction rate decreases as $t^{-1/2}$ making the flame "weaker." For radiating flames, the flame temperature decreases due to radiative heat loss for both cases resulting in extinction. The decrease in the reaction rate for radiating flames is also much faster than $t^{-1/2}$. Surprisingly, gas radiation has a larger effect on the flame temperature in this configuration. This is because combustion products accumulate in the high temperature reaction zone. This accumulation of combustion products also reduces the soot concentration via oxidation by OH radicals. At early times, before a significant increase in the concentration of combustion products, large amount of soot is formed and radiation from soot is also very large. However, this radiative heat loss does not cause a local depression in the temperature profile because it is offset by the heat release due to soot oxidation. These results are consistent with the experiments and provide considerable insight into radiative cooling of sooty flames. This work clearly shows that radiative-extinction of diffusion flames can occur in a microgravity environment.

INTRODUCTION

The absence of buoyancy-induced flows in a microgravity environment and the resulting increase in the reactant residence time significantly alters the fundamentals of many combustion processes. Substantial differences between normal gravity and microgravity flames have been reported during droplet combustion[1], flame spread over solids[2], candle flames[3] and others. These differences are more basic than just in the visible flame shape. Longer residence time and higher

concentration of combustion products create a thermochemical environment which changes the flame chemistry. Processes such as soot formation and oxidation and ensuing flame radiation, which are often ignored under normal gravity, become very important and sometimes controlling. As an example, consider the droplet burning problem. The visible flame shape is spherical under microgravity versus a teardrop shape under normal gravity. Since most models of droplet combustion utilize spherical symmetry, excellent agreement with experiments is anticipated. However, microgravity experiments show that a soot shell is formed between the flame and the evaporating droplet of a sooty fuel[1]. This soot shell alters the heat and mass transfer between the droplet and its flame resulting in significant changes in the burning rate and the propensity for flame extinction. This change in the nature of the process seems to have occurred because of two reasons: (i) soot formed could not be swept out of the flame due to the absence of buoyant flows, and (ii) soot formation was enhanced due to an increase in the residence time.

Recently, some very interesting observations of candle flames under various atmospheres in microgravity have been reported[3]. It was found that for the same atmosphere, the burning rate per unit wick surface area and the flame temperature were considerably reduced in microgravity as compared with normal gravity. Also, the flame (spherical in microgravity) was much thicker and further removed from the wick. It thus appears that the flame becomes "weaker" in microgravity due to the absence of buoyancy generated flow which serves to transport the oxidizer to the combustion zone and remove the hot combustion products from it. The buoyant flow, which may be characterized by the strain rate, assists the diffusion process to execute these essential functions for the survival of the flame. Thus, the diffusion flame is "weak" at very low strain rates and as the strain rate increases the flame is initially "strengthened" and eventually it may be "blown out." The computed flammability boundaries[4] show that such a reversal in material flammability occurs at strain rates around 5 sec^{-1}.

The above experimental observations suggest that flame radiation will substantially influence diffusion flames under microgravity conditions, particularly the conditions at extinction. This is because, flame radiation at very low or zero strain rates is enhanced due to: (i) high concentration of combustion products in the flame zone which increases the gas radiation, and (ii) low strain rates provide sufficient residence time for substantial amounts of soot to form which is usually responsible for most of the radiative heat loss. This radiative heat loss may extinguish the already "weak" diffusion flame. Thus, the objective of this work is to theoretically investigate the reason why the diffusion flame becomes "weak" under microgravity conditions and determine the effect of flame radiation on this "weak" diffusion flame. This will lead to radiation-induced extinction limits. This work is important for spacecraft fire safety.

THE MODEL PROBLEM

We note that the problem at hand is inherently transient and to study the effect of flame radiation we must focus on the reaction zone. Also, since the reaction zone is usually thin compared with other characteristic dimensions of the flame, its basic structure is essentially independent of the flame shape. Thus, we consider a simple model problem consisting of an unsteady one-dimensional diffusion flame (*with flame radiation*) initiated at the interface of two quiescent half spaces of fuel and oxidizer at time t=0. Zero gravity, constant properties, one-step

irreversible reaction and unity Lewis number are assumed. A novel feature of the formulation presented below is that soot volume fraction is not a priori specified to determine the ensuing flame radiation. Instead, soot is produced and oxidized according to the temperature and species concentration dependent formation and oxidation rates. Thus, the soot volume fraction and its location within the flame evolve as a function of space and time. The soot formation and oxidation rates used here are obtained from the counterflow diffusion flame experiments and models of Refs. 5 and 6. A large activation energy asymptotic analysis of this problem *without flame radiation* may be found in Ref. 7. A schematic of the physical problem along with the imposed boundary conditions is presented in Figure 1 and the corresponding equations are:

Continuity:

$$\frac{\partial \rho}{\partial t} + \frac{\partial (\rho v)}{\partial x} = 0 \qquad (1)$$

where ρ is the density, t the time and v the velocity normal to the fuel-oxidizer interface induced by volumetric expansion.

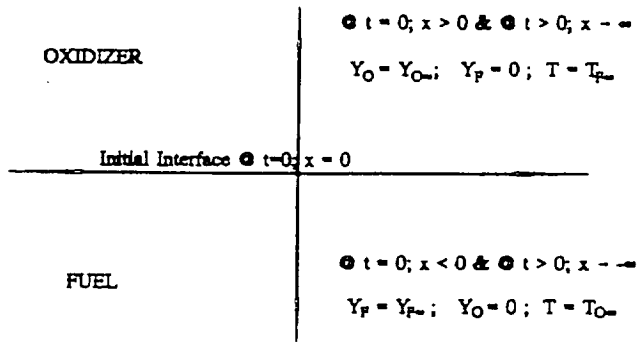

Figure 1 : Schematic of the Model Problem

Species Conservation:

$$\rho \frac{\partial Y_F}{\partial t} + \rho v \frac{\partial Y_F}{\partial x} = \frac{\partial}{\partial x}\left(\rho D \frac{\partial Y_F}{\partial x}\right) - w_g - \left(\dot{m}'''_{s_p} - \dot{m}'''_{s_o} \right) \qquad (2)$$

$$\rho \frac{\partial Y_O}{\partial t} + \rho v \frac{\partial Y_O}{\partial x} = \frac{\partial}{\partial x}\left(\rho D \frac{\partial Y_O}{\partial x}\right) - \nu w_g \qquad (3)$$

$$\rho \frac{\partial Y_P}{\partial t} + \rho v \frac{\partial Y_P}{\partial x} = \frac{\partial}{\partial x}\left(\rho D \frac{\partial Y_P}{\partial x}\right) + (1+\nu) w_g \qquad (4)$$

Symbols used in the above equations are defined in the nomenclature. The reaction rate, w_g, is modelled by a second order Arrhenius expression. Preexponential factor and the activation energy are chosen for methane undergoing a one-step irreversible reaction $F + \nu O \rightarrow (1+\nu) P$; where ν is the mass-based stoichiometric coefficient. Fuel depleted as a result of soot formation, though usually small, is also included in the model via the term $(\dot{m}'''_{sp} - \dot{m}'''_{so})$, which is zero when negative.

Energy Conservation:

$$\rho\frac{\partial T}{\partial t} + \rho v\frac{\partial T}{\partial x} = \frac{\partial}{\partial x}\left(k\frac{\partial T}{\partial x}\right) + Q_g w_g + Q_s\left(\dot{m}_{s_o}''' - \dot{m}_{s_p}'''\right) - \nabla\cdot Q_r \quad (5)$$

In this equation, the source terms include heat released by the primary reaction and soot oxidation and heat lost via flame radiation. The soot oxidation term is clearly zero when negative. Emission approximation is used to describe the radiative heat flux from the flame. Thus, $\nabla\cdot Q_r = 4\sigma T^4(a_{pg}+a_{ps})$ where, a_{pg} *and* a_{ps} are Planck mean absorption coefficients for combustion products (CO_2, H_2O) and soot respectively. Planck mean absorption coefficients for combustion products were obtained from Ref. 8 and for soot we have used $a_{ps} = 11.86\, f_v T\ cm^{-1}$ obtained from Ref. 9.

Soot Conservation:

$$\rho\frac{\partial \phi}{\partial t} + \rho v\frac{\partial \phi}{\partial x} = \left(\dot{m}_{s_p}''' - \dot{m}_{s_o}'''\right), \quad where, \quad \phi = \frac{f_v \rho_s}{\rho} \quad (6)$$

Here, both production and oxidative destruction of soot are considered, but soot diffusion is ignored. A simplified equation for the net soot production rate (production - oxidation) is taken from Refs. 6 & 7. Also, average number density is used to avoid including the soot nucleation rate equation. The net mass production rate of soot per unit volume is thus described by:

$$\dot{m}_{s_p}''' - \dot{m}_{s_o}''' = A_p f_v^{2/3}\left(\xi_F - \frac{3}{8}\xi_O\right)\exp\left(-E_s/RT\right), \quad where\ \xi_j \equiv \sum_{i=1}^{n}\left[\frac{M_j \nu_i^j}{W_i}\right] Y_i \quad (7)$$

In this equation, the combined atomic mass fraction of carbon and hydrogen is taken to represent the hydrocarbon fuel according to $\xi_F = \xi_C + \xi_H$, where the subscripts F, C & H denote fuel, carbon and hydrogen respectively. Finally, the boundary conditions, as depicted in Figure 1, are: $Y_o = Y_{o\infty}$, $T = T_\infty$, $Y_F = 0$ *at* $t=0$, $x > 0$ *&* *at* $t > 0$, $x \to \infty$ and $Y_F = Y_{F\infty}$, $Y_o = 0$, $T = T_\infty$ *at* $t = 0$, $x < 0$ *&* *at* $t > 0$, $x \to -\infty$.

The incompressible form of the above equations is obtained by using Howarth transformation $z = \int_0^x \frac{\rho(x', t)}{\rho_\infty} dx'$, where x = 0 defines the location of the material surface that coincides at t = 0 with the original fuel-oxidizer interface. As a result of this choice, v = 0 at x = 0. Assuming $\rho^2 D = \rho_\infty^2 D_\infty$ and defining the reaction rate as $w_g = A_g \rho^2 Y_F Y_O \exp(-E_g/RT)$ we obtain:

$$\frac{\partial Y_F}{\partial t} = D_\infty \frac{\partial^2 Y_F}{\partial z^2} - \frac{w_g}{\rho} - A_p f_v^{2/3} \left(\xi_F - \frac{3}{8}\xi_O\right) \exp\left(-E_s/RT\right) \qquad (8)$$

$$\frac{\partial Y_O}{\partial t} = D_\infty \frac{\partial^2 Y_O}{\partial z^2} - \nu \rho A_g Y_F Y_O \exp\left(-E_g/RT\right) \qquad (9)$$

$$\frac{\partial Y_P}{\partial t} = D_\infty \frac{\partial^2 Y_P}{\partial z^2} + (1+\nu)\, \rho A_g Y_F Y_O \exp\left(-E_g/RT\right) \qquad (10)$$

$$\frac{\partial T}{\partial t} = D_\infty \frac{\partial^2 T}{\partial z^2} + \frac{Q_g w_g}{\rho C_p} + \frac{Q_s}{C_p}\left(\frac{\partial \phi}{\partial t}\right) - \frac{4\sigma T^4 a_{ps}}{\rho C_p} - \frac{4\sigma T^4 a_{pg}}{\rho C_p} \qquad (11)$$

$$\text{where;} \quad \frac{\partial \phi}{\partial t} = \frac{A_p}{\rho} f_v^{2/3} \left(\xi_F - \frac{3}{8}\xi_O\right) \exp\left(-E_s/RT\right) \qquad (12)$$

SOLUTION:

Analytical Solution

For infinitely fast gas-phase reactions and no flame radiation a simple, well known, analytical solution is obtained.

$$\eta = \frac{\beta - \beta_{-\infty}}{\beta_\infty - \beta_{-\infty}} = \frac{1}{2} erfc\left(\frac{z}{2\sqrt{D_\infty t}}\right) \qquad (13)$$

Here, $\beta = Y_F - Y_O/\nu$ and $\beta = Y_F + C_p T/Q_g$ are the Schvab-Zeldovich variables. The flame lies at the location $\eta_{fl} = 1/(1+\nu Y_{F\infty}/Y_{O\infty})$. Thus, for unity equivalence ratio (E=1) based on free stream concentrations, the flame lies at $z = 0$. For non-unity equivalence ratios [fuel rich (E>1) or fuel lean (E<1) conditions] the flame will travel as $\sqrt{t}$ in either direction. This is evident from Equ. (13) by simply substituting $\eta = \eta_{fl}$. The three possible cases are plotted in Fig. 2 for methane. The constants used are[10]: for $Q_g = 47465\ J/gm\ of\ fuel$, $C_p = 1.3\ J/gmK$, $T_\infty = 295\ K$, $\nu = 4$, $\rho_\infty = 1.16 \times 10^{-3}\ gm/cm^3$, and $D_\infty = 0.226\ cm^2/sec$. The flame conditions are: (a) $Y_{O\infty} = 0.5$, $Y_{F\infty} = 0.125$. (b) $Y_{O\infty} = 0.5$, $Y_{F\infty} = 0.0625$. (c) $Y_{O\infty} = 0.25$, $Y_{F\infty} = 0.125$. For case (b) the flame travels towards the fuel side because of excess oxygen (Fig. 2b). Similarly, for case (c) it travels towards the oxygen side because of excess fuel (Fig. 2c). However, for case (a) the

equivalence ratio is unity and hence the flame is stationary. It simply becomes thicker with time (Fig. 2a).

Numerical Solution

The above equations were numerically integrated by using a finite difference Crank-Nickolson method where previous time step values were used to evaluate the nonlinear reaction terms. Care was taken to start the diffusion flame with minimum disturbance. Ideally, the problem must be started such that the two half spaces of fuel and oxidizer, as illustrated in Fig. 1, begin a self-sustaining reaction at t=0. This ignition of the reactants may be spontaneous or induced by a pilot. For high activation energy, spontaneous ignition will take a long time during which the reactants will diffuse into one other developing a thick premixed zone which will burn prior to establishing a diffusion flame. This will change the character of the proposed problem. Thus, ignition was forced (piloted) by artificially making the fuel-oxidizer interface temperature as the adiabatic flame temperature. Only Eqs. (8-10) were solved during this period. Ignition was assumed when the reaction rate at the interfacial node becomes maximum (i.e. $dw_g/dt = 0$). After this instant, the interfacial node was not artificially maintained at the adiabatic flame temperature because the combustion process becomes self-sustaining and all the equations described above are used. For the calculations presented below, the time taken to ignite was 4×10^{-6} sec. A uniform grid with grid size $\Delta z=3\times10^{-3}$ cm and a time-step of $\Delta t=1\times10^{-6}$ sec was used. Typical calculation for 0.4 seconds physical time took 5 hours on a Sun Sparkstation.

To limit the computational domain which extends from $+\infty$ to $-\infty$, the analytical solution presented above was used to compute the temperature at the desired final time (0.4 sec in the present case). The location from the origin where the temperature first becomes equal to ambient (within machine error) was used to apply boundary conditions at infinity in the numerical calculations. This was further confirmed by checking the space derivatives ($\partial T/\partial x$) at these boundaries during the calculations. Since initial soot volume fraction is zero, the governing equation (Eq. 12) will produce a trivial solution if explicit or implicit finite difference methods are used. Thus, for first step, an implicit integral method was used to obtain the soot volume fraction. At the end of the first time step the soot volume fraction is of the order 10^{-80}. It is important to note that Equ. (12) can self-initiate soot formation despite the absence of a soot nucleation model.

For the calculations presented below, we have used the following data: for gas reactions[10]: $\rho A_g=3.56\times10^{9}$ sec^{-1}, $E_g=122$ KJ/mole. For soot reactions we have used[5,6] $A_p=10^{6}$ gm/cm^{3}sec for Case 1 and 10^{7} gm/cm^{3}sec for Case 2, $E_s=150$ KJ/mole, $\rho_s=1.86$ gm/cm^3. We assume that soot oxidizes to CO releasing heat $Q_s=9$ KJ/gm of soot.

RESULTS AND DISCUSSION

Results of calculations for three cases are presented here. These are labeled as Cases 0,1&2 in Figure 3. Case 0 is the base case with finite reaction rates but without soot formation and flame radiation. Case 1 represents a barely sooting flame and Case 2 represents a highly sooting flame. As noted above, A_p for Case 2 is increased ten times over Case 1. Based on our

previous work (Refs.5&6), A_p for most hydrocarbon fuels is expected to fall between Cases 1&2.

Let us first consider the overall results. Figure 3 shows that in the absence of external flow (i.e., zero strain rate) and without soot formation and flame radiation (Case 0), the peak flame temperature becomes constant while the reaction rate decreases as $t^{1/2}$ and the reaction zone thickness increases [note: in Fig.3 the ordinate has been multiplied by $t^{1/2}$]. Since the maximum flame temperature remains constant, extinction does not occur. However, for Cases 1 & 2, the peak flame temperature decreases with time faster than $t^{1/2}$ and eventually extinction (as identified by some pre-defined temperature limit) will occur. This *(radiation-induced extinction)* is also evident from Figure 4 where the temperature profiles at different times are plotted for Cases 1 & 2. Clearly, the flame temperature decreases due to flame radiation and the flame thickness increases because of diffusion.

The net amount of soot formed as a function of space and time is shown in Figure 5. The soot volume fraction for Case 1 is two orders of magnitude smaller than for Case 2. Physically, Case 1 represents a barely sooting blue flame and Case 2 represents a fairly sooty blue-yellow-orange flame. However, despite the differences in the magnitude of the soot volume fraction for the two cases, it first increases and later decreases with time and its spatial distribution shifts toward the fuel side for both cases. This decrease in the soot volume fraction occurs because of two reasons: (i) A reduction in the flame temperature due to radiation reduces the soot formation rate, and (ii) A buildup in the concentration of CO_2 and H_2O near the high-temperature reaction zone, increases the OH radical concentration which reduces the formation of soot precursors and assists in soot oxidation (see Refs.6 & 7). This increased OH radical concentration is also responsible for shifting the soot profile toward the fuel side.

The effect of soot formation on flame radiation is shown in Figure 6. Here, radiation from both combustion products and soot is plotted as a function of space and time. As expected, soot radiation for Case 2 is substantially larger than for Case 1 while the gas radiation is approximately the same [Note: the scales of the two figures are different]. This soot radiation decreases with time because both the soot volume fraction and the flame temperature decrease. The effect of soot radiation is to reduce the peak flame temperature by about 100K (see Fig.3) with the difference diminishing with increasing time. Surprisingly, as seen in Fig. 3, the effect of gas radiation on the peak flame temperature is much larger and increases with time, becoming 1000K at 0.4 sec. This is because at zero strain rates the combustion products accumulate in the high temperature reaction zone. As noted above, these combustion products are also responsible for the reduction in the soot volume fraction.

Another interesting observation is that despite the large asymmetry introduced by soot radiation at initial times (Fig. 6), Figure 4 shows that the temperature profiles are essentially symmetrical. This implies that the heat lost via soot radiation [5th term of Eq. (11)] approximately equals the heat produced via soot oxidation [4th term of Eq. (11)]. Since both occur at the same location, a discernible local depression in the temperature profile is not observed. This fact is experimentally substantiated by our low strain rate counterflow diffusion flame experiments (Ref. 6 & 7). It is also consistent with the observation that radiation from a soot particle at these high temperatures will quickly quench the particle unless its temperature is maintained via some local heat release. In the present case, this heat release is due to soot

oxidation. Thus, a portion of the fuel that is converted into soot oxidizes at a location different from the main reaction zone and nearly all the heat released during this process is radiated away. The remaining fuel is oxidized at the main reaction zone resulting in a lower heat release and hence a reduced peak flame temperature. This is the justification for including the last term in Eq. (8) and the 4th term in Eq. (11). These terms account for fuel consumption and heat released due to net soot formation (or oxidation) and provide valuable new insight into the mechanism of radiative cooling of sooty flames.

The above conclusion is also clear from Figure 7 which shows the spatial distribution of soot and temperature for Cases 1 & 2 at 0.2 seconds after ignition. Note that while the peak temperature is about 75K lower for Case 2, the profile is nearly symmetrical about the origin for both cases despite the sharp & narrow soot peaks on the fuel side. Also note that the magnitude of the soot peak (soot peak for Case 2 is about two orders of magnitude larger than for Case 1) had a negligible effect on the symmetry of the temperature profile. Figure 7 is also qualitatively very similar to our low strain rate counterflow diffusion flame experimental measurements.

Finally, we note that emission approximation was used in the flame radiation formulation. Since the reaction zone thickness is of the order of a few centimeters, self-absorption of radiation may become important and in some cases it may alter the extinction limit.

CONCLUSIONS:

This paper presents the results of a theoretical calculation for radiation-induced extinction of a one-dimensional unsteady diffusion flame in a quiescent microgravity environment. The model formulation includes both gas and soot radiation. Soot volume fraction is not a priori assumed, instead it is produced and oxidized according to temperature and species dependent formation and oxidation rates. Thus, soot volume fraction and the resulting flame radiation varies with space and time. Three cases are considered (i) a non-radiating flame, (ii) a scarcely sooty flame, and (iii) a very sooty flame. For a non-radiating flame, the maximum flame temperature remains constant and it does not extinguish. However, the reaction rate decreases as $t^{-1/2}$ making the flame "weaker." For radiating flames, the flame temperature decreases due to radiative heat loss for both cases resulting in extinction. The decrease in the reaction rate for radiating flames is also much faster than $t^{-1/2}$. Surprisingly, gas radiation has a larger effect on the flame temperature in this configuration. This is because combustion products accumulate in the high temperature reaction zone. This accumulation of combustion products also reduces the soot concentration via oxidation by OH radicals. At early times, before a significant increase in the concentration of combustion products, large amount of soot is formed and radiation from soot is also very large. However, this radiative heat loss does not cause a local depression in the temperature profile because it is offset by the heat release due to soot oxidation. These results are consistent with the experiments and provide considerable insight into radiative cooling of sooty flames. This work clearly shows that radiative-extinction of diffusion flames can occur in a microgravity environment. In the present model self-absorption of the radiation was neglected which in some cases may alter the extinction limits because of relatively thick reaction zone [O(cms)] . Further work is required.

ACKNOWLEDGEMENTS:

Financial support for this work was provided by NASA under the contract number NAG3-1460, NSF under the contract number CBT-8552654, and GRI under the contract number GRI-5087-260-1481. We are also indebted to Dr. Kurt Sacksteder of NASA Lewis and Drs. Thomas R. Roose & James A. Kezerle of GRI for their help.

REFERENCES

1. *Jackson, G., S., Avedisian, C., T. and Yang, J., C.*, Int. J. Heat Mass Transfer., Vol.35, No. 8, pp. 2017-2033, 1992.
2. *Ferkul, P., V.*, "A Model of Concurrent Flow Flame Spread Over a Thin Solid Fuel," NASA Contractor Report 191111, 1993.
3. *Ross, H. D., Sotos, R. G. and T'ien, J. S.*, Combustion Science and Technology, Vol. 75, pp. 155-160, 1991.
4. *T'ien, J. S.*, Combustion and Flame, Vol. 80, pp. 355-357, 1990.
5. *Zhang, C., Atreya, A. and Lee, K.*, Twenty-Fourth (International) Symposium on Combustion, The Combustion Institute, pp. 1049-1057, 1992.
6. *Atreya, A. and Zhang, C.*, "A Global Model of Soot Formation derived from Experiments on Methane Counterflow Diffusion Flames," in preparation for submission to Combustion and Flame.
7. *Linan, A. and Crespo, A.*, Combustion Science and Technology, Vol. 14, pp. 95-117.
8. *Abu-Romia, M. M and Tien, C. L.*, J. Heat Transfer, 11, pp. 32-327, 1967
9. *Seigel, R. and Howell, J. R.*, "Thermal Radiation Heat Transfer", Hemisphere Publishing Corporation, 1991.
10. *Tzeng, L. S.*, PhD Thesis, Michigan State University, East Lansing, MI, USA, 1990.

NOMENCLATURE

a	*Planck mean absorption coefficient*
A	*Frequency Factor*
C_p	*Specific heat*
D	*Diffusion Coefficient*
E	*Activation Energy*
f_v	*Soot volume fraction*
k	*Thermal conductivity*
$\dot{m}'''_{s_g}$	*Soot surface growth rate*
$\dot{m}'''_{s_o}$	*Soot oxidation rate*
M	*Atomic weight*
Q_r	*Radiative heat flux*
Q	*Heat of combustion per unit mass*
t	*Time*
T	*Temperature*
v	*Velocity*
w	*Reaction rate*
W	*Molecular weight*
x	*Distance*
Y	*Mass fraction*
z	*Density distorted coordinate*

GREEK

α	*Thermal diffusivity*
β	*Schvab-Zeldovich variable*
ν	*Mass based stoichiometric coefficient; number of moles*
ϕ	*Soot mass fraction*
ρ	*Density*
ξ	*Variable defined in Eq.(7)*

Subscripts

F	*Fuel*
g	*Gas*
o	*Oxygen*
P	*Products (H_2O, CO_2)*
s	*Soot*
∞	*Free stream*

FIGURE CAPTIONS

Figure 1: Schematic of the Model Problem

Figure 2: Analytical solution. Temperature distribution as a function of distance for various equivalence ratios. (a) Equivalence ratio (E) is unity (b) $E < 1$ (c) $E > 1$.

Figure 3: Maximum reaction rate and temperature as a function of time. Note that reaction rate is multiplied with $t^{1/4}$.

Figure 4: Numerical solution. Temperature distribution as a function of distance at various instants. (a) Case 1, less sooty flame, (b) Case 2, very sooty flame.

Figure 5: Soot volume fraction as a function of distance at various instants. (a) Case 1, less sooty flame, (b) Case 2, very sooty flame.

Figure 6: Radiative Heat Loss as a function of distance at various instants. (a) Case 1, less sooty flame, (b) Case 2, very sooty flame.

Figure 7: Soot volume fraction and Temperature distribution at $t = 0.2$ seconds. (a) Case 1, less sooty flame, (b) Case 2, very sooty flame.

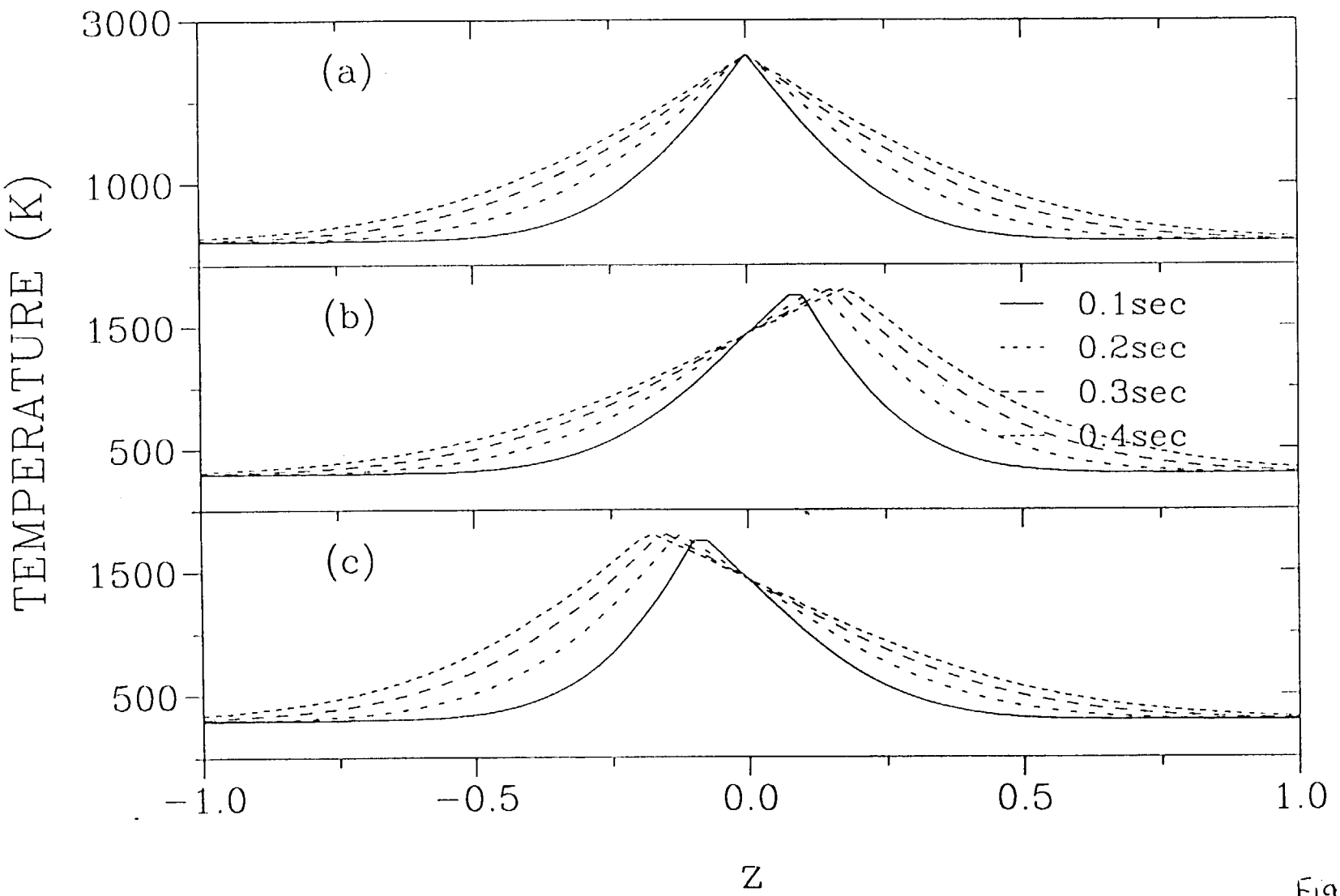
TEMPERATURE (K)
3000
1000
(a)
1500
500
(b)
0.1sec
0.2sec
0.3sec
0.4sec
1500
500
(c)
−1.0
−0.5
0.0
0.5
1.0
Z

Fig 2

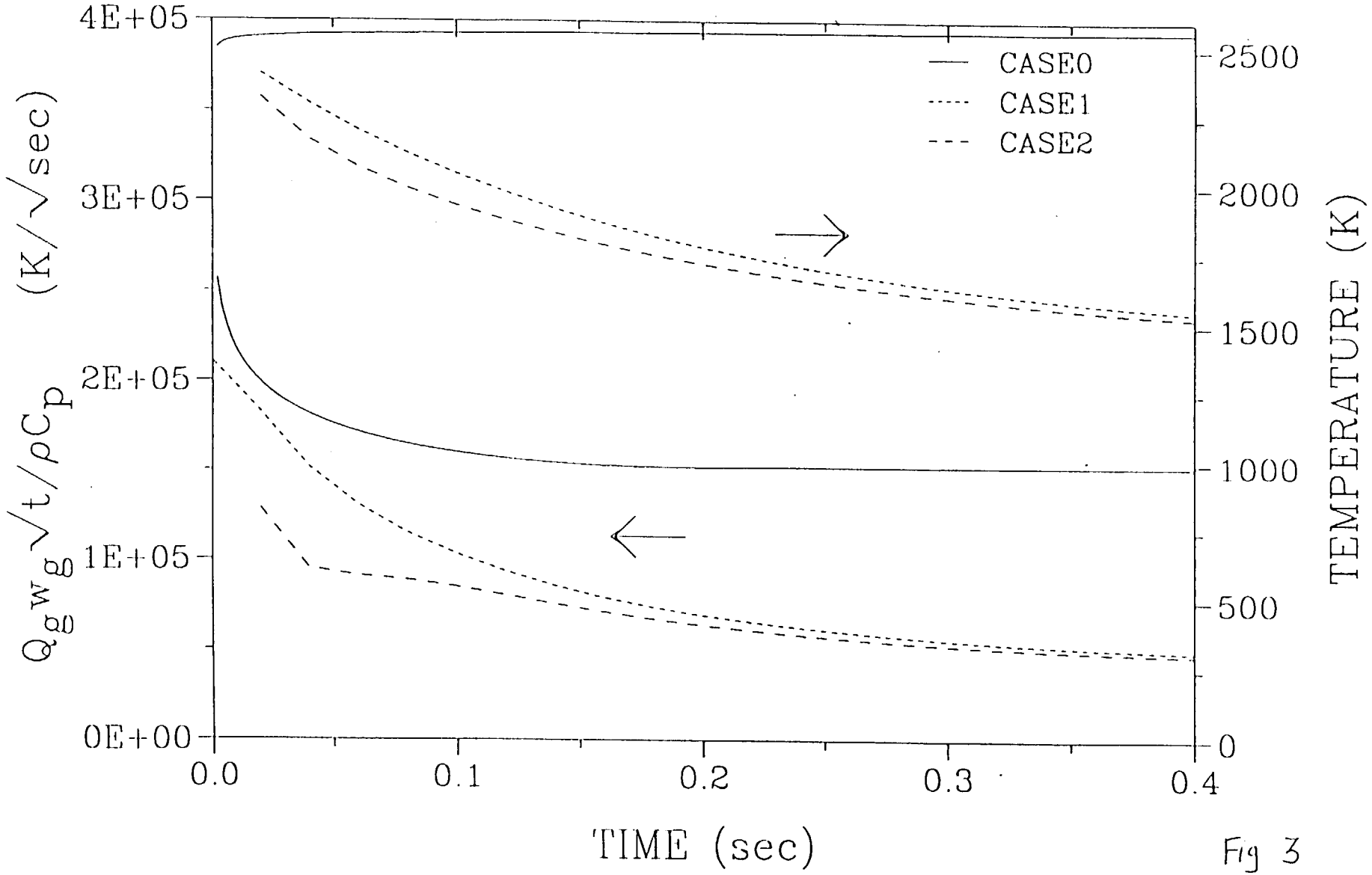
4E+05
3E+05
2E+05
1E+05
0E+00
$Q_g w_g \sqrt{t}/\rho C_p$ (K/√sec)
0.0
0.1
0.2
0.3
0.4
TIME (sec)
2500
2000
1500
1000
500
0
TEMPERATURE (K)
CASE0
CASE1
CASE2

Fig 3

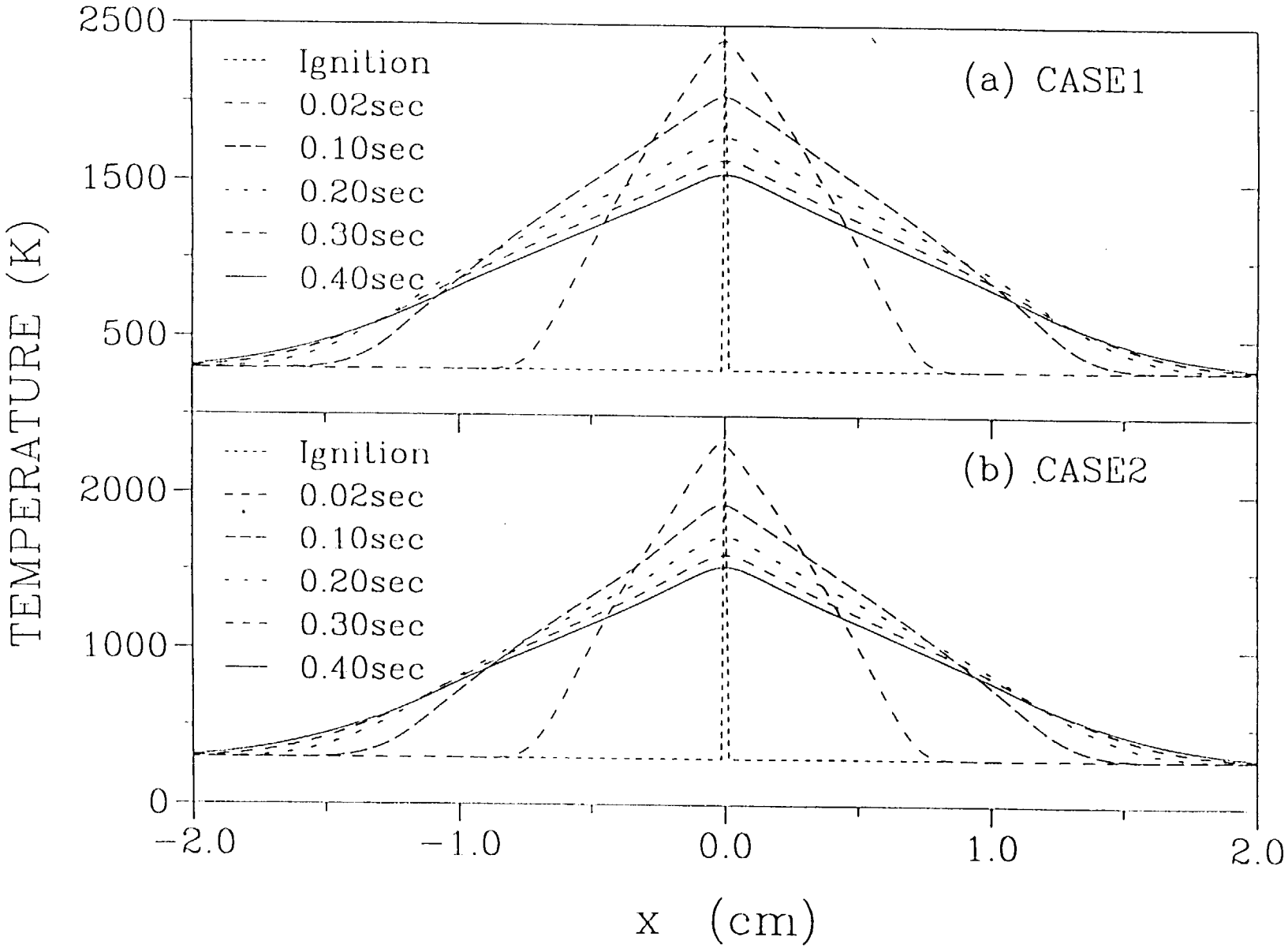
2500
1500
500
2000
1000
0
TEMPERATURE (K)
Ignition
0.02sec
0.10sec
0.20sec
0.30sec
0.40sec
(a) CASE1
Ignition
0.02sec
0.10sec
0.20sec
0.30sec
0.40sec
(b) CASE2
−2.0
−1.0
0.0
1.0
2.0
x (cm)

Fig 4

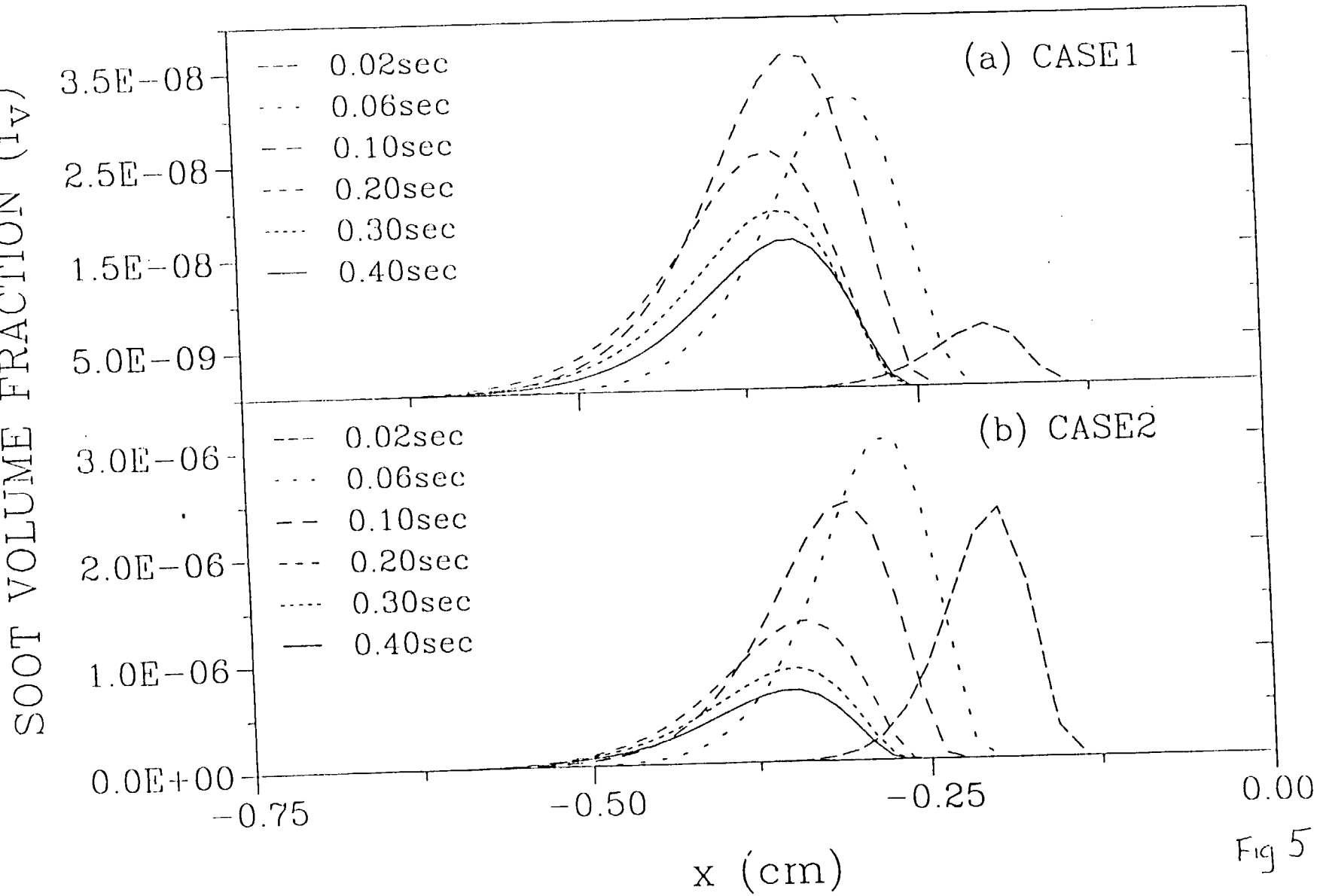
SOOT VOLUME FRACTION (f_V)
3.5E-08
2.5E-08
1.5E-08
5.0E-09
3.0E-06
2.0E-06
1.0E-06
0.0E+00
0.02sec
0.06sec
0.10sec
0.20sec
0.30sec
0.40sec
(a) CASE1
(b) CASE2
-0.75
-0.50
-0.25
0.00
x (cm)

Fig 5

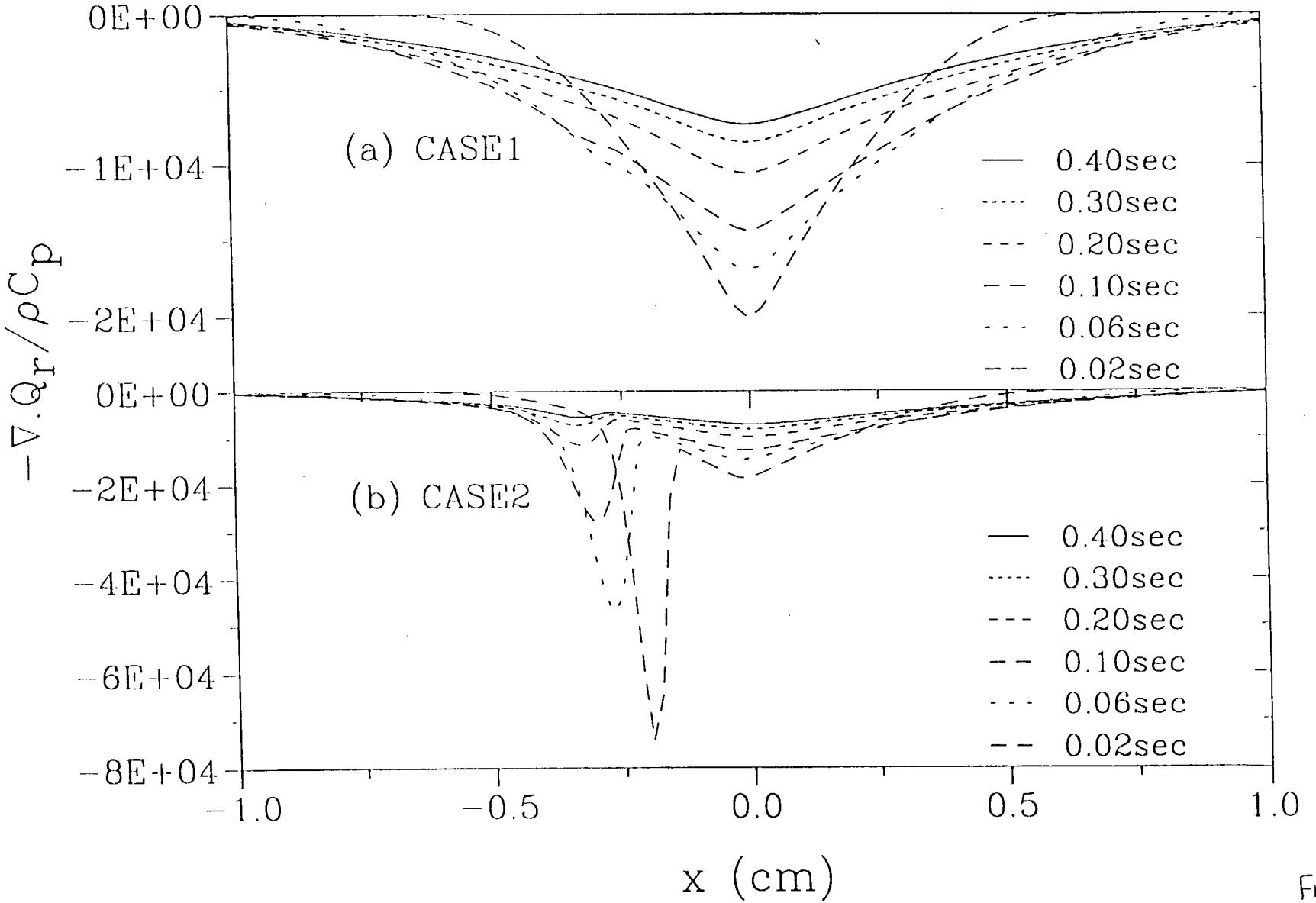
0E+00
-1E+04
-2E+04
0E+00
-2E+04
-4E+04
-6E+04
-8E+04
-1.0
-0.5
0.0
0.5
1.0
x (cm)
$-\nabla \cdot Q_r / \rho C_p$
(a) CASE1
(b) CASE2
0.40sec
0.30sec
0.20sec
0.10sec
0.06sec
0.02sec

Fig. 6

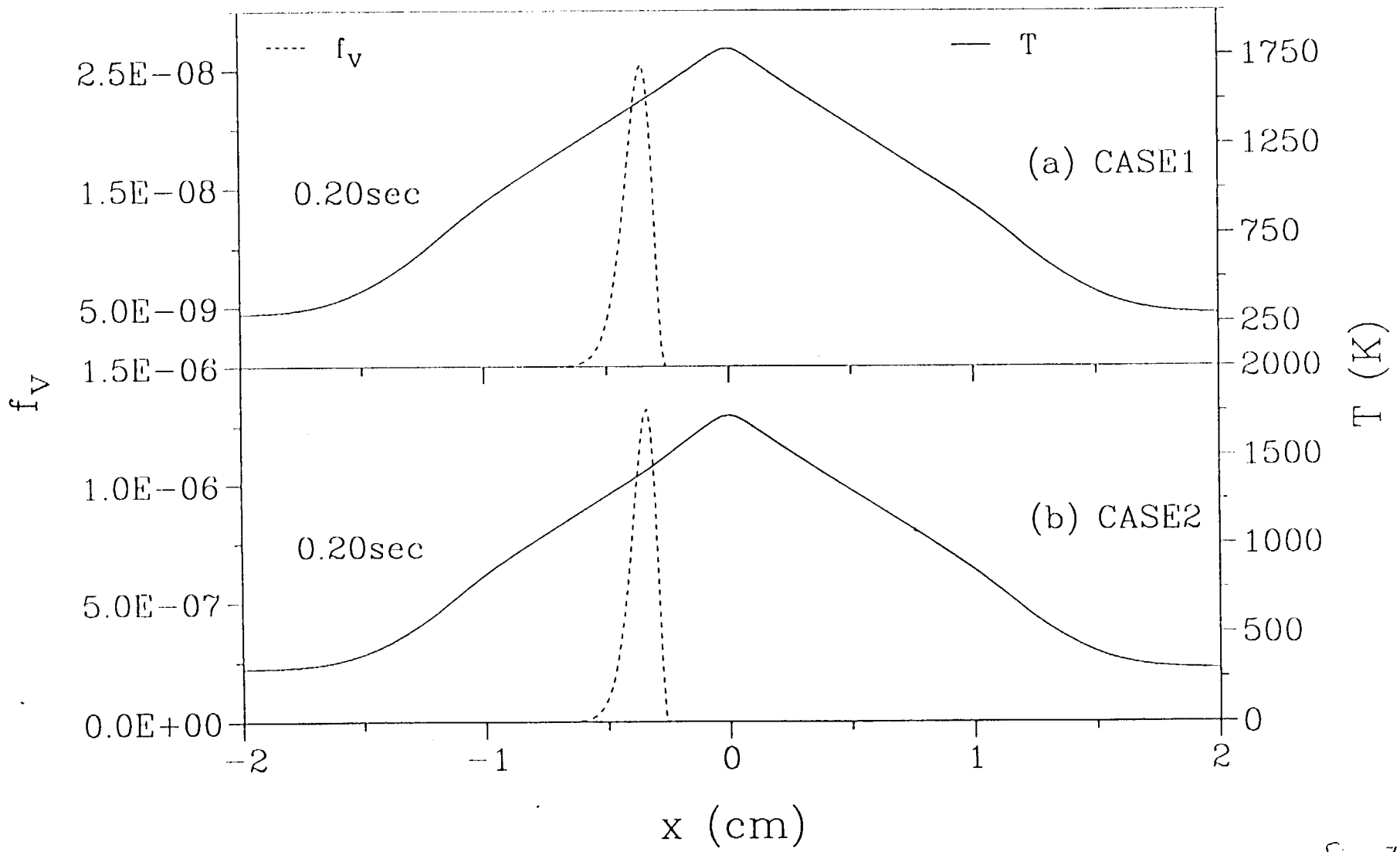
f_v
T
2.5E-08
1.5E-08
5.0E-09
1.5E-06
1.0E-06
5.0E-07
0.0E+00
1750
1250
750
250
2000
1500
1000
500
0
0.20sec
(a) CASE1
0.20sec
(b) CASE2
-2
-1
0
1
2
x (cm)
T (K)

Fig. 7

APPENDIX B

Observations of Methane and Ethylene Diffusion Flames Stabilized Around a Blowing Porous Sphere under Microgravity Conditions

32nd Aerospace Sciences Meeting (AIAA 94-0572) paper

By

Atreya, A, Agrawal, S., Sacksteder, K., and Baum, H.

AIAA 94-0572

Observations of Methane and Ethylene Diffusion Flames Stabilized Around a Blowing Porous Sphere under Microgravity Conditions

A. Atreya and S. Agrawal
Department of Mechanical Engineering
and Applied Mechanics
The University of Michigan
Ann Arbor, MI 48109-2125

K. R. Sacksteder
Microgravity Combustion Research
NASA Lewis Research Center
Cleveland, OH 44135

H. R. Baum
National Institute of Standards and Technology
Gaithersburg, MD 20899

32nd Aerospace Sciences Meeting & Exhibit
January 10-13, 1994 / Reno, NV

OBSERVATIONS OF METHANE AND ETHYLENE DIFFUSION FLAMES STABILIZED AROUND A BLOWING POROUS SPHERE UNDER MICROGRAVITY CONDITIONS

Arvind Atreya and Sanjay Agrawal
Combustion and Heat Transfer Laboratory
Department of Mechanical Engineering and Applied Mechanics
The University of Michigan, Ann Arbor, MI 48109-2125

Kurt R. Sacksteder
Microgravity Combustion Research
NASA Lewis Research Center
Cleveland, OH 44135

Howard R. Baum
National Institute of Standards and Technology
Gaithersburg, MD 20899

Abstract

This paper presents the experimental and theoretical results for expanding methane and ethylene diffusion flames in microgravity. A small porous sphere made from a low-density and low-heat-capacity insulating material was used to uniformly supply fuel at a constant rate to the expanding diffusion flame. A theoretical model which includes soot and gas radiation is formulated but only the problem pertaining to the transient expansion of the flame is solved by assuming constant pressure infinitely fast one-step ideal gas reaction and unity Lewis number. This is a first step toward quantifying the effect of soot and gas radiation on these flames. The theoretically calculated expansion rate is in good agreement with the experimental results. Both experimental and theoretical results show that as the flame radius increases, the flame expansion process becomes diffusion controlled and the flame radius grows as $\sqrt{t}$. Theoretical calculations also show that for a constant fuel mass injection rate a quasi-steady state is developed in the region surrounded by the flame and the mass flow rate at any location inside this region equals the mass injection rate.

I. Introduction

The absence of buoyancy-induced flows in a microgravity environment and the resulting increase in the reactant residence time significantly alters the fundamentals of many combustion processes. Substantial differences between normal gravity and microgravity flames have been reported during droplet combustion[1], flame spread over solids[2,3], candle flames[4] and others. These differences are more basic than just in the visible flame shape. Longer residence time and higher concentration of combustion products create a thermochemical environment which changes the flame chemistry. Processes such as soot formation and oxidation and ensuing flame radiation, which are often ignored under normal gravity, become very important and sometimes controlling. As an example, consider the droplet burning problem. The visible flame shape is spherical under microgravity versus a teardrop shape under normal gravity. Since most models of droplet combustion utilize spherical symmetry, excellent agreement with experiments is anticipated. However, microgravity experiments show that a soot shell is formed between the flame and the evaporating droplet of a sooty fuel[1]. This soot shell alters the heat and mass transfer between the droplet and its flame resulting in significant changes in the burning rate and the propensity for flame extinction. This change in the nature of the process seems to have occurred because of two reasons: (i) The soot formed could not be swept out of the flame due to the absence of buoyant flows. Instead, it was forced to go through the high temperature reaction zone increasing the radiative heat losses, and (ii) soot formation was enhanced due to an increase in the reactant residence time.

Recently, some very interesting observations of candle flames under various atmospheres in microgravity have been reported[4]. It was found that for the same atmosphere, the burning rate per unit wick surface area and the flame temperature were considerably reduced in microgravity as compared with normal gravity. Also, the flame (spherical in microgravity) was much thicker and further removed from the wick. It thus appears that the flame becomes "weaker" in microgravity due to the absence of buoyancy generated flow which serves to transport the oxidizer to the combustion zone and remove the hot combustion products from it. The buoyant flow, which may be characterized by the strain rate, assists the diffusion process to execute these essential functions for

the survival of the flame. Thus, the diffusion flame is "weak" at very low strain rates and as the strain rate increases the flame is initially "strengthened" and eventually it may be "blown-out." The computed flammability boundaries[5] show that such a reversal in material flammability occurs at strain rates around 5 sec^{-1}. Model calculations for a zero strain rate *1-D* diffusion flame show that even gas radiation is sufficient to extinguish the flame[6].

The above observations suggest that flame radiation will substantially influence diffusion flames under microgravity conditions, particularly the conditions at extinction. This is because, flame radiation at very low or zero strain rates is enhanced due to: (i) high concentration of combustion products in the flame zone which increases the gas radiation, and (ii) low strain rates provide sufficient residence time for substantial amounts of soot to form which is usually responsible for most of the radiative heat loss. It is anticipated that this radiative heat loss may extinguish the already "week" diffusion flame.

To investigate the possibility of radiation-induced extinction limits under microgravity conditions, spherical geometry is chosen. This is convenient for both experiments and theoretical modeling. In this work, a porous spherical burner is used to produce spherical diffusion flames in μg. Experiments conducted with this burner on methane (less sooty) and ethylene (sooty) diffusion flames are described in the next section. A general theoretical model for transient radiative diffusion flames is then formulated and calculations are presented for the transient expansion of the spherical diffusion flame. These calculations are compared with the experimental measurements in the discussion section. This work is the first necessary step toward investigating radiative-extinction of spherical diffusion flames.

II. Experimental Apparatus and Results

The μg experiments were conducted in the 2.2 sec drop tower at the NASA Lewis Research Center. The experimental drop-rig used is schematically shown in Color Plate 1. It consists of a test chamber, burner, igniter, gas cylinder, solenoid valve, camera, computer and batteries to power the computer and the solenoid valves. The spherical burner (1.9 cm in diameter) is constructed from a low density and low heat capacity porous ceramic material. A 150 cc gas cylinder at approximately 46.5 psig is used to supply the fuel to the porous spherical burner. Typical gas flow rates used were in the range of 3-15 cm^3/s. Flow rates to the burner are controlled by a needle valve and a gas solenoid valve is used to open and close the gas line to the burner upon computer command. An igniter is used to establish a diffusion flame. After ignition the igniter is quickly retracted from the burner and secured in a catching mechanism by a computer-controlled rotary solenoid. This was necessary for two reasons (i) The igniter provides a heat sink and will quench the flame (ii) Upon impact with the ground (after 2.2 sec) the vibrating igniter may damage the porous burner.

As shown in the Color Plate 1, the test chamber has a 5" diameter Lexan window which enables the camera to photograph the spherical diffusion flame. The flame growth can be recorded either by a 16mm color movie camera or by a color CCD camera which is connected to a video recorder by a fiber-optic cable during the drop. Since the fuel flow may change with time, it had to be calibrated for various settings of the needle valve for both methane and ethylene. A soap bubble flow meter was used to calibrate the flow for various constant gas cylinder pressures. Constant pressures were obtained by connecting the cylinder to the main 200 lb gas cylinder using a quick-disconnect. An in-line pressure transducer was used to obtain the transient flow rates. Changes in the cylinder pressure during the experiment along with the pressure-flow rate calibration, provides the transient volumetric flow rates. These are shown plotted in Figure 1.

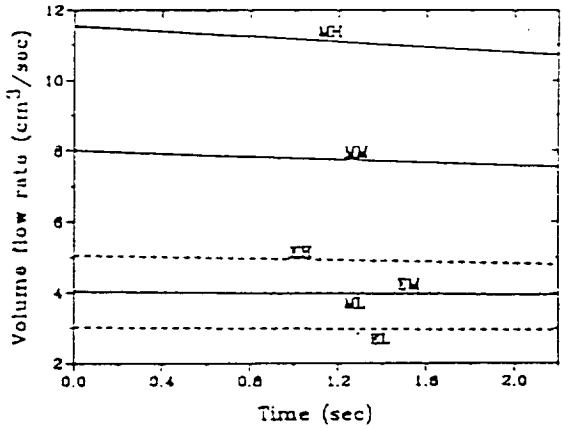

Figure 1: Volume flow rates versus time.

In Figure 1, the letters "M" and "E" represent methane and ethylene respectively and the letters "L", "M" and "H" represent low, medium and high flow rates. Thus, MM implies medium flow rate of methane. Note that low flow rate for methane is nearly equal to the medium flow rate of ethylene. For these experiments, the gas velocity at the burner wall was between 0.25-1 cm/sec.

The porous spherical burner produced a nearly spherical diffusion flame in microgravity. Some observed

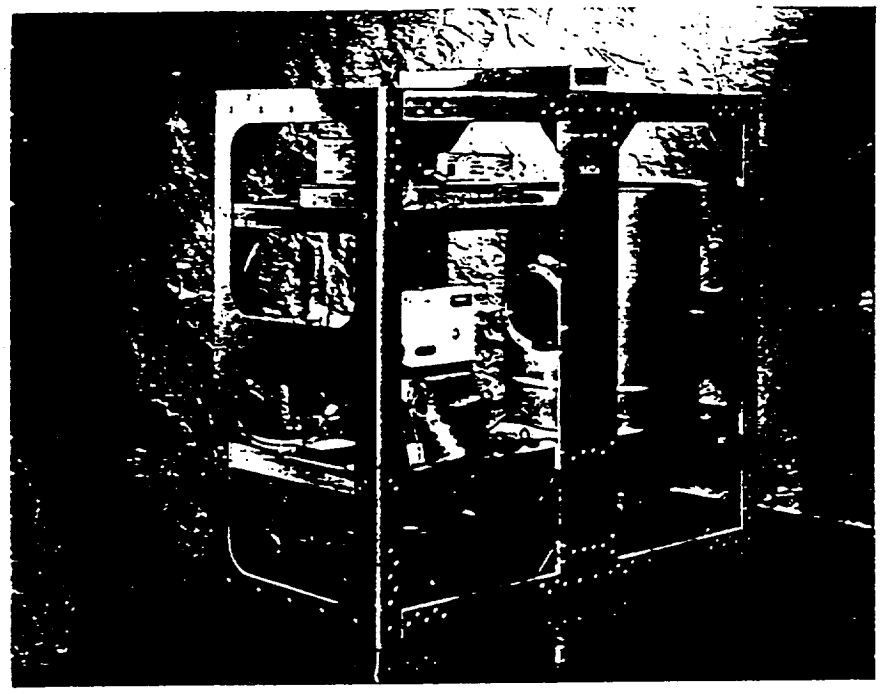

Picture of the microgravity spherical diffusion flame apparatus

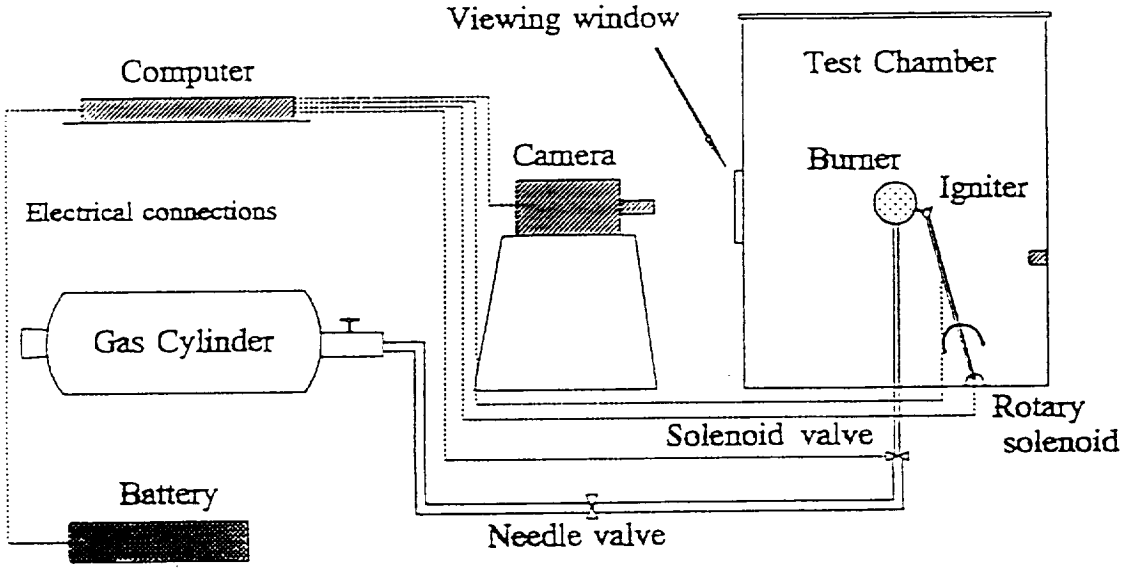

Schematic of the microgravity spherical diffusion flame apparatus

COLOR PLATE 1

disturbances are attributed to slow large-scale air motion inside the test chamber. Several microgravity experiments were performed under ambient pressure and oxygen concentration conditions for different flow rates of methane and ethylene (as shown in Fig. 1). Methane was chosen to represent a non-sooty fuel and ethylene was chosen to represent a moderately sooty fuel. In these experiments, ignition was always initiated in 1-g just prior to the drop. The package was typically dropped within one second after ignition. The primary reason for not igniting in μg was the loss of time in heating the igniter wire and in stabilizing the flame after the initial ignition disturbances. Some photographs from these experiments are shown in the Color Plate 2.

The flame radius measured from such photographs along with the model predictions (to be discussed later) are shown in Fig. 2. As expected, for the same flow rates it was found that ethylene flames were much sootier and smaller. Immediately after dropping the package, the flame shape changed from a teardrop shape (see Color Plate 2) to a spherical shape (although it was not always completely spherical, probably because of slow large-scale air motion persisting inside the test chamber). The photographs shown in the Color Plate 2 are for medium flow rates of methane and low flow rates of ethylene. For the data presented in Fig. 2, an average flame radius determined from the photographs was used.

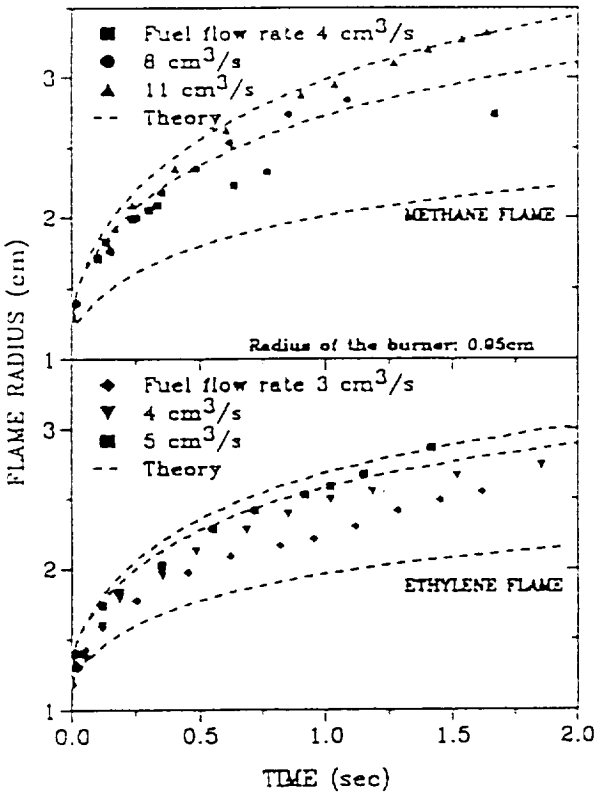

Figure 2: Flame radius versus time

It is interesting to note that for both methane and ethylene (see the progressive flame growth in Color Plate 2), initially and in 1-g (e.g. photographs 'e' & 'f') the flame is nearly blue (non-sooty) but becomes bright yellow (sooty) immediately after the onset of μg conditions. Later, as the μg time progresses, the flame grows in size and becomes orange and less luminous and the soot seems to disappear. A possible explanation for this observed behavior is suggested by the theoretical calculations of Ref. 6. The soot volume fraction first quickly increases and later decreases as the local concentration of combustion products increases. Essentially, further soot formation is inhibited by the increase in the local concentration of the combustion products [Ref.7,8] and soot oxidation is enhanced. Thus, at the onset of μg conditions, initially a lot of soot is formed in the vicinity of the flame front (the outer faint blue envelope) resulting in bright yellow emission. As the flame grows, several events reduce the flame luminosity: (i) The soot is pushed toward cooler regions by thermophoresis. In fact, for sootier fuels this leads to the formation of a soot shell. (ii) The high concentration of combustion products left behind by the flame front inhibits soot formation and promotes soot oxidation. (iii) The dilution and radiative heat losses caused by the increase in the concentration of combustion products reduces the flame temperature which in turn reduces the soot formation rate and the flame luminosity.

Figure 2 shows the average measured flame radius for methane and ethylene μg diffusion flames plotted against time. This is the radius of the outer faint blue region of the flame as measured from the photographs. To a good approximation this may be considered as the flame front location. Thus, as a first step, it will be interesting and important to determine if the transient expansion of the μg spherical diffusion flame can be theoretically predicted without considering soot formation and oxidation kinetics and flame radiation.

III. Model Formulation

As noted above, the spherical diffusion flames are expanding and changing their luminosity with time. Thus, the general theoretical formulation must be transient and must include flame radiation. For the simplest case of *constant pressure ideal gas reactions with Le=1*, we may write the following governing equations for any geometrical configuration (spherical or counterflow geometry):

Mass Conservation:

$$\frac{\partial \rho}{\partial t} + \nabla \cdot (\rho \vec{v}) = 0 \qquad (1)$$

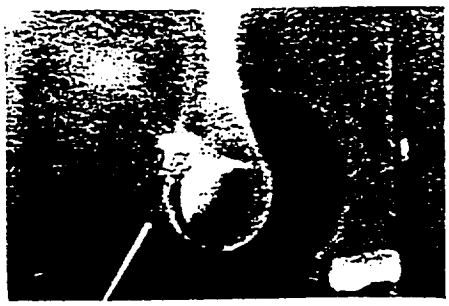

(a)

1-g flame

(b)

0.0667sec into μg

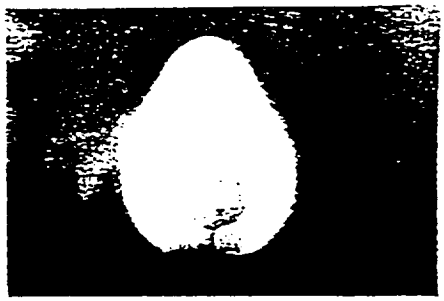

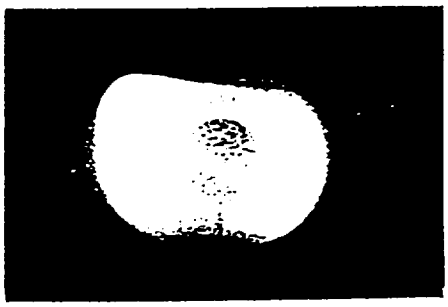

(c)

0.3333sec into μg

(d)

0.6667sec into μg

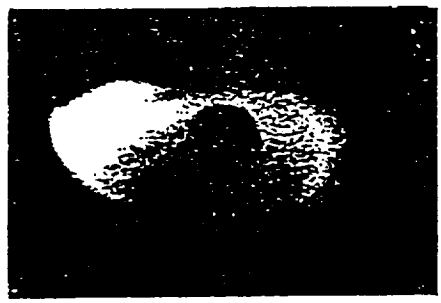

METHANE FLAME, FUEL FLOW RATE 8 cm^3/sec

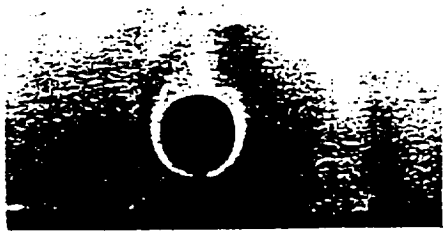

(e)

1-g flame

(f)

0.0667sec into μg

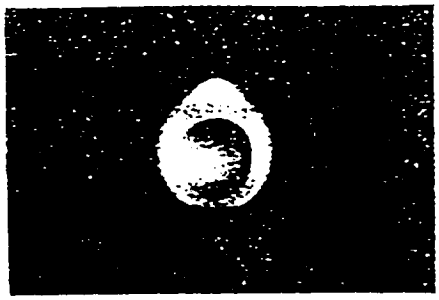

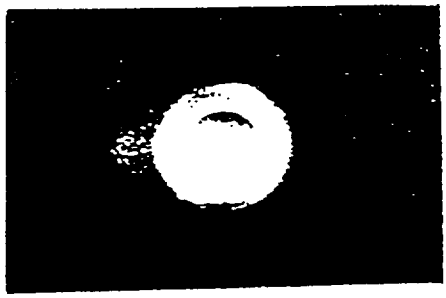

(g)

0.1667sec into μg

(h)

0.5667sec into μg

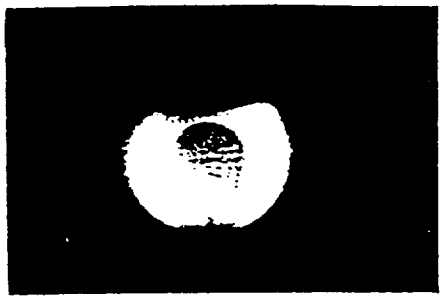

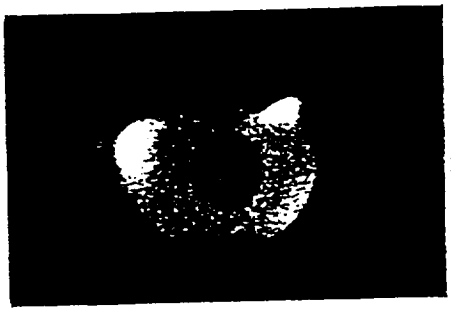

(i)

1.233sec into μg

(j)

1.667sec into μg

ETHYLENE FLAME, FUEL FLOW RATE 3 cm^3/sec COLOR PLATE 2

Energy Conservation:

$$\rho\frac{\partial h'}{\partial t}+\rho\vec{v}\cdot\nabla h'-\nabla\cdot(\rho D\nabla h')$$
$$=-\sum_i h_i^{\circ}W_i-Q_r\dot{m}_{s_v}^{'''}-\nabla\cdot\vec{q}_r \qquad (2)$$

Constant Pressure Ideal Gas:

$$\rho T=\rho_{\infty}T_{\infty} \quad or \quad \rho h'=const. \qquad (3)$$

Here, the symbols have their usual definitions with ρ = density, T = temperature, v = velocity, Y_i = mass fraction of species i, h' = sensible enthalpy, w_i = mass production or destruction rate per unit volume of species i and D = diffusion coefficient. The last three terms in Equ (2) respectively are: the chemical heat release rate due to gas phase combustion, chemical heat released due to soot oxidation and the radiative heat loss rate per unit volume. The above equations, however, are insufficient for our problem because the soot volume fraction must be known as a function of space and time to determine the radiative heat loss. To enable describing soot volume fraction in a simple manner, we define the mass fraction of atomic constituents as follows: $\xi_j=\sum_i\left(M_j\nu_i^j/M_i\right)Y_i$, where M_i is the molecular weight of species i, M_j is the atomic weight of atom j and ν_i^j is the number of atoms of kind j in specie i. Assuming that the only atomic constituents present in the hydrocarbon flame are C, H, O & Inert and with $Y_{soot}\equiv\Phi\equiv\rho_s f_v/\rho$ (where: ρ_s= soot density & f_v = soot volume fraction), we obtain: $\xi_C+\xi_H+\xi_O+\xi_I+\rho_s f_v/\rho=1$. Defining $\xi_C+\xi_H=\xi_F$ and $Z_F=\xi_F/Y_{F-}$ and $Z_O=\xi_O/Y_{\infty-}$, we obtain $Z=\left[(\xi_F)_{F-}Z_F+\rho_s f_v/\rho\right]$ as the conserved scalar for a sooty flame. This yields the following soot, fuel and oxidizer conservation equations in terms of their scalar variables:

Soot Conservation:

$$\rho\frac{\partial\Phi}{\partial t}+\rho\vec{v}\cdot\nabla(\Phi)-\nabla\cdot[\rho D_s\nabla(\Phi)]$$
$$=\dot{m}_{s_g}^{'''}-\dot{m}_{s_v}^{'''}=\dot{m}_{net}^{'''} \qquad (4)$$

Fuel Conservation:

$$\rho\frac{\partial Z_F}{\partial t}+\rho\vec{v}\cdot\nabla(Z_F)-\nabla\cdot[\rho D\nabla(Z_F)]$$
$$=-\frac{1}{Y_{F-}}(\dot{m}_{s_g}^{'''}-\dot{m}_{s_v}^{'''})=-\frac{\dot{m}_{net}^{'''}}{Y_{F-}} \qquad (5)$$

Oxygen Conservation:

$$\rho\frac{\partial Z_O}{\partial t}+\rho\vec{v}\cdot\nabla(Z_O)-\nabla\cdot[\rho D\nabla(Z_O)]=0 \qquad (6)$$

Under conditions of small soot loading, the soot terms in the fuel and energy conservation equations can be ignored except when studying radiative extinction. Thus, Equ (5) may be considered homogeneous to a good approximation. Also, as a first crude approximation, the heat lost by flame radiation may be subtracted from the heat of combustion in the form of a radiative fraction. Thus, the energy equation (Equ(2)) can also be made homogeneous if written in terms of the total enthalpy [$h=\sum_i Y_i(h_i^{\circ}+h_i')$]. This approach may be adequate for calculating the observed expansion rate of the spherical diffusion flames, but it is completely inadequate for predicting radiative extinction. However, the great mathematical advantage of this approach is that it makes Eqs. (2, 4, 5, & 6) identical and only one conserved scalar equation need be considered. As a first step, it is of interest to see how well the transient expansion of the µg spherical diffusion flames be predicted without rigorously considering soot and gas radiation. This will also help in quantifying the effect of soot and gas radiation by comparison with more detailed calculations. Re-writing the above equations in spherical coordinates, we get:

Mass Conservation:

$$\frac{\partial\rho}{\partial t}+\frac{1}{r^2}\frac{\partial}{\partial r}(r^2\rho v)=0 \qquad (7)$$

Fuel Conservation:

$$\rho\frac{\partial Z}{\partial t}+\rho v\frac{\partial Z}{\partial r}-\frac{1}{r^2}\frac{\partial}{\partial r}\left(r^2\rho D\frac{\partial Z}{\partial r}\right)=0 \qquad (8)$$

These two equations along with the ideal gas law at constant pressure, Equ.(3), are sufficient to describe the transient growth of non-radiative spherical diffusion flames and are expected to approximate this growth in the presence of flame radiation. It is also assumed that a fast one-step overall reaction occurs at the flame surface. This is represented by: $\nu_F F+\nu_O O\rightarrow\sum_{i=1}^{N-2}\nu_i P_i$; with q° as the standard heat of reaction and $Q=q^{\circ}/M_F\nu_F$ the heat released per unit mass of fuel. Clearly, $q^{\circ}=h_F^{\circ}M_F\nu_F+h_O^{\circ}M_O\nu_O-\sum_{i=1}^{N-2}h_i^{\circ}M_i\nu_i$. The corresponding initial and boundary conditions for a sphere of radius 'R' blowing fuel gases at a rate $\dot{M}(t)$ are discussed below and illustrated in Figure 3.

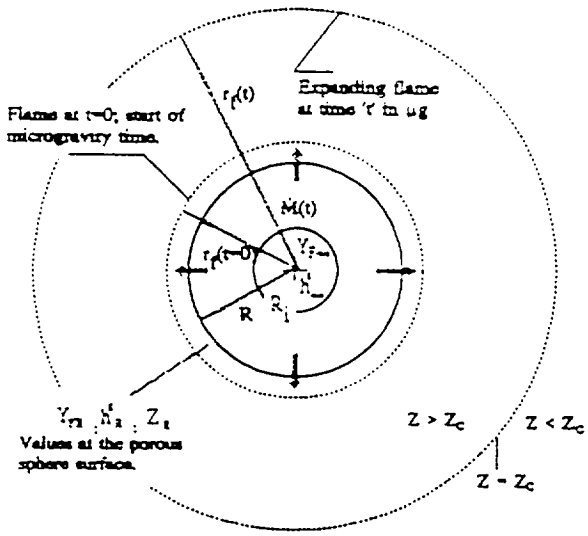

Figure 3: Schematic of the Model Problem

Continuity, fuel mass fraction and energy conservation at the surface of the sphere yield:

$$\frac{\dot{M}(t)}{4\pi R^2} = (\rho v)_{@R} \tag{9a}$$

$$\frac{\dot{M}(t)}{4\pi R^2}(Y_{F-} - Y_{FR}) = -\rho D\left(\frac{\partial Y_F}{\partial r}\right)_{@R} \tag{9b}$$

$$\frac{\dot{M}(t)}{4\pi R^2}(h'_- - h'_R) = -\rho D\left(\frac{\partial h'}{\partial r}\right)_{@R} \tag{9c}$$

Here, Y_{F-} & h'_- are the fuel mass fraction and enthalpy of the incoming fuel stream and Y_{FR} and h'_R are the corresponding values at the outer surface of the sphere. The ambient values of fuel and oxidizer enthalpies are taken to be equal *i.e.* $h^s_- = h^s_{F-} = h^s_{O-}$ and $Z \equiv 1$ & $\rho \equiv \rho_\infty$ for ambient conditions on the fuel side and $Z \equiv 0$ & $\rho \equiv \rho_\infty$ for ambient conditions on the oxidizer side. Now, for high fuel injection rates, $Y_{F-} = Y_{FR}$; $h'_- = h'_R$ and $Z_R = 1$ and the corresponding diffusion terms in Equs. 9b & 9c become zero. For a given mass injection rate [$\dot{M}(t)$], these conditions are also satisfied as $R \to 0$. Thus, for a point fuel source, the boundary conditions at the source are simplified. Other initial and boundary conditions are: At t=0, Z(r,0); ρ(r,0) & v(r,0) are the spatial distributions corresponding to the flame at t=0, as shown in Figure 3. Also, at the flame surface [$r = r_f(t)$] $Z = Z_c = (1 + Y_{F-} M_O \nu_O / Y_{O-} M_F \nu_F)^{-1}$, and as $r \to \infty$, $Z \to 0$; $v \to 0$ & $h' \to h'_-$. All other variables can be easily obtained in terms of Z by utilizing the linear relationships between the conserved scalars [Ref.10]. For constant pressure ideal gas reactions these linear relationships yield:

For $R \le r < r_f(t)$:

$$\rho = \rho_\infty \left(1 + \frac{(1-z) Q Y_{F-} Z_c}{h'_- (1 - Z_c)}\right)^{-1} \tag{10}$$

$$v = \frac{\dot{M}(t)}{4\pi r^2 \rho_\infty} - \frac{D}{\rho}\frac{\partial \rho}{\partial r}$$

$$+ \frac{\dot{M}(t)}{4\pi r^2 \rho_\infty} \frac{Q Z_c}{h'_-}\left(Y_{FR} - Y_{F-}\frac{(Z_R - Z_c)}{(1 - Z_c)}\right) \tag{11}$$

These equations, along with Equ. (8), are sufficient to provide all the distributions in the region between the porous sphere and the flame. In Equ. (11), the first term on the right hand side represents the injection velocity and the second term accounts for the increase in the velocity due to the decrease in density. The third term is identically zero if the distribution of Y_F within the porous sphere (r<R) is identical to that in the gas i.e. $Y_F = Y_{F-}(Z - Z_c)/(1 - Z_c)$. Note at r=R, $Y_F = Y_{FR}$ and $Z = Z_R$. Also note that the third term becomes zero for high injection velocities and small 'R' since $Z_R \to 1$ & $Y_{FR} \to Y_{F-}$. In Equ. (11), ρ and $(\partial \rho / \partial r)$ can be expressed entirely in terms of Z through Equ. (10). Thus, Equ. (8) along with the appropriate boundary conditions is sufficient to determine Z(r,t).

At the flame surface $r = r_f(t)$:

At the flame surface, the $Z^{(-)} = Z^{(+)} = Z_c$ and all its derivatives are continuous. Here, '-' represents the fuel side and '+' represents the air side. Also, $T(r_f^-, t) = T(r_f^+, t) = T_f$; $\rho(r_f^-, t) = \rho(r_f^+, t) = \rho_f$ and $v(r_f^-, t) = v(r_f^+, t) = v_f$. Other jump conditions at the flame surface are obtained from species and energy balances as follows (assuming $Le = 1$ & $D = D_t$):

$$\left(\frac{\partial Y_F}{\partial r}\right)_{(r_f^-, t)} = -\left(\frac{M_F \nu_F}{M_O \nu_O}\right)\left(\frac{\partial Y_O}{\partial r}\right)_{(r_f^+, t)} \tag{12}$$

$$\left(\frac{\partial h'}{\partial r}\right)_{(r_f^-, t)} - \left(\frac{\partial h'}{\partial r}\right)_{(r_f^+, t)} = -Q\left(\frac{\partial Y_F}{\partial r}\right)_{(r_f^-, t)} \tag{13}$$

In terms of Z, both Equs. (12) & (13) are identically satisfied if the first derivatives of Z are equal at the flame surface. Thus, for the solution of Equ. (8) in

the domain $r > r_f$, we only need to find expressions for ρ and v in terms of Z.

For $r_f(t) < r < \infty$:

$$\rho = \rho_\infty \left(1 + \frac{\nu Q Y_{F-}}{h'_-}\right)^{-1} \qquad (14)$$

$$v = \frac{r_f^2(1-Z_c)}{r^2 Z_c}\left[\frac{v_f}{(1-Z_c)} - \frac{\dot{M}(t)}{4\pi r_f^2 \rho_\infty} - \frac{\dot{M}(t) Q Z_c}{4\pi r_f^2 \rho_\infty h'_-}\left(Y_{FR} - Y_{F-}\left(\frac{Z_R - Z_c}{1-Z_c}\right)\right)\right] - \frac{D}{\rho}\frac{\partial \rho}{\partial r} \qquad (15)$$

In the derivation of Equ. (15), gas velocity and density at the flame front are made continuous i.e. $v(r_f^+, t) = v(r_f^-, t) = v_f$, and $\rho(r_f^+, t) = \rho(r_f^-, t) = \rho_f$. Thus, v_f in Equ. (15) can be obtained from Equ. (11). Once again, the third term inside the bracket of Equ (15) becomes zero for reasons discussed above. Equs. (14), (15) and (8) along with the boundary conditions are sufficient to determine $Z(r,t)$ for $r > r_f$.

IV Solution

Before discussing the solution procedure, let us examine the porous sphere used in the experiments. This sphere is quite small (19 mm dia.) and is constructed from a high porosity, low density and low heat capacity insulating material. Thus, its capacity to store heat and mass is negligible compared to the fuel injection rate which is injected inside the sphere (see Fig. 3). Hence, conditions inside the material of the sphere equilibrate on a time scale much shorter than the flame expansion time i.e. convection balances diffusion for any variable under consideration that can be described by an equation similar to Equ. (8). Neglecting radiation from the surface of the sphere, conservation conditions yield equations identical to Equs. 9(a) and 9(b) where ambient conditions are assumed to exist near the center of the sphere. Physically, the only purpose the porous sphere serves is to provide a radially uniform flow and it does not participate in energy and species balances because of its low storage capacity. Thus, the boundary conditions at the source can be applied at an arbitrarily small radius 'R' (chosen for numerical convenience) such that $Y_{F-} = Y_{FR}$; $h'_- = h'_R$ and $Z_R = 1$. This considerably simplifies Eqs. (11) & (15).

Equation (8), with Eqs. (10) & (11) for the fuel side and Eqs. (14) & (15) for the air side were numerically solved using the method of lines. A computer package entitled DSS2 was employed for this purpose. The calculated results for the flame location are shown plotted by dotted lines in Fig. 2. Property values used were those for air ($\rho_\infty = 1.16 \times 10^{-3}$ gm/cm^3, D_∞ = 0.226 cm^2/s, T_∞ =298K, Cp =1.35 J/kgK) and the diffusion coefficient was assumed to vary as $T^{3/2}$ as predicted by kinetic theory of gases. Heat of combustion (Q) and mass based stoichiometric coefficient (v) used for methane and ethylene were Q=47465 J/gm and v=4 and Q=47465 J/gm and v=3.429 respectively. No assumptions other than those stated above were made to match the experimental data. Initial spatial distribution of Z(r,0) required for the flame at the start of μg time (i.e. at t=0) was taken as:

$$Z(r,0) = erfc\left(\frac{(r-R)\,erfc^{-1}(Z_c)}{(r_f - R)}\right) \qquad (16)$$

V Results and Discussion

Figure 2 shows the average radius of the outer faint blue regions for both methane and ethylene μg diffusion flames plotted against time. This radius was measured from the photographs. As stated above, the corresponding calculated results for the flame location are shown plotted with dotted lines. Given the approximations made in the model and the experimental errors, the comparison between the experimental and predicted flame radius is quite encouraging.

Numerical calculations also yield the instantaneous velocity and density profiles around the porous sphere during the flame expansion. These are shown plotted in Figures 4 & 5. Starting from the porous

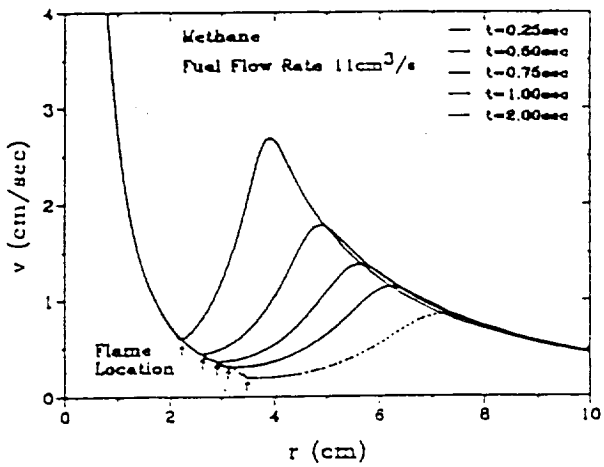

Figure 4: Radial velocity distribution at various instants

sphere (r=0.95), the gas velocity drops sharply and becomes a minimum at the flame location ($r=r_f$). Surprisingly, the mass flow rate at any location $r < r_f$ is found to be equal to the mass injection rate (i.e. $4\pi\rho v r^2 = \dot{M}(t)$). This implies that a similarity exists in the normalized coordinate $r/r_f(t)$ in the region $r < r_f(t)$. The density profiles in this region (Fig. 5) also show a similarity. Further reflection shows that this is to be

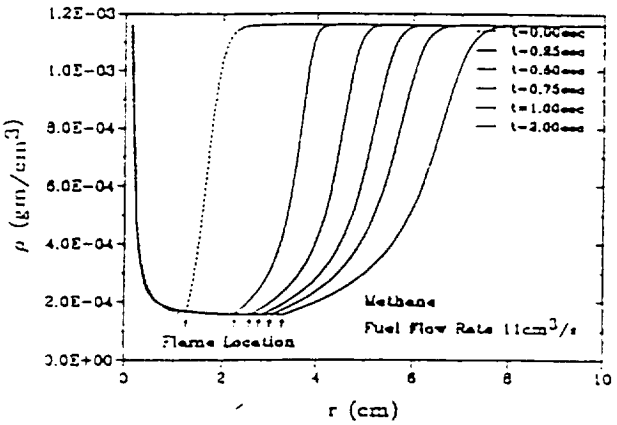

Figure 5: Radial density distribution at various instants

expected. In this problem, a constant temperature (adiabatic flame temperature) spherical flame is propagating outward starting from a small radius. In the spherical geometry, heat loss from the region surrounded by the flame is not possible. Thus, the only heat required by this region from the flame (in the absence of radiation) is to heat the injected mass $\dot{M}(t)$ to the flame temperature. Since, the injected mass is taken to be constant with time, a quasi steady state is developed. This is also observed in the density gradients at the flame on the fuel side (which are constant and are proportional to the temperature gradients). Applying a simple energy balance over the region $r \le r_f$, we obtain:

$$\frac{\dot{M}(t)}{4\pi r_f^2 \rho_f} = \frac{\dot{M}(t)}{4\pi r_f^2 \rho_\infty} - \frac{D}{\rho_f}\left(\frac{\partial \rho}{\partial r}\right)_{r_f} = v_f \qquad (17)$$

Using Equ. (11) we find that at the flame $v_f = \dot{M}(t)/4\pi\rho_f r_f^2$. It is important to note that this is possible only because the injection rate is not varying with time.

VI Conclusions

In this work, experimental and theoretical results for expanding methane and ethylene diffusion flames in microgravity are presented. A small porous sphere made from a low-density and low-heat-capacity insulating material was used to uniformly supply fuel at a constant rate to the expanding diffusion flame. A theoretical model which includes soot and gas radiation is formulated but only the problem pertaining to the transient expansion of the flame is solved by assuming constant pressure infinitely fast one-step ideal gas reaction and unity Lewis number. This is a first step toward quantifying the effect of soot and gas radiation on these flames. The theoretically calculated expansion rate is in good agreement with the experimental results. Both experimental and theoretical results show that as the flame radius increases, the flame expansion process becomes diffusion controlled and the flame radius grows as $\sqrt{t}$. Theoretical calculations also show that for a constant fuel mass injection rate a quasi-steady state is developed in the region surrounded by the flame and the mass flow rate at any location inside this region equals the mass injection rate.

Acknowledgements: We would like to thank Mr. Mark Guether for his initial work on the Drop Rig. This project is supported by NASA under contract no. NAG3-1460.

References

1 *Jackson, G., S., Avedisian, C., T. and Yang, J., C.,* Int. J. Heat Mass Transfer., Vol.35, No. 8, pp. 2017-2033, 1992.

2.*T'ien, J. S., Sacksteder, K. R., Ferkul, P. V. and Grayson, G. D.* "Combustion of Solid Fuels in very Low Speed Oxygen Streams." Second International Microgravity Combustion Workshop," NASA Conference Publication, 1992.

3.*Ferkul, P., V.*, "A Model of Concurrent Flow Flame Spread Over a Thin Solid Fuel," NASA Contractor Report 191111, 1993.

4.*Ross, H. D., Sotos, R. G. and T'ien, J. S.*, Combustion Science and Technology, Vol. 75, pp. 155-160, 1991.

5.*T'ien, J. S.*, Combustion and Flame, Vol. 80, pp. 355-357, 1990.

6.*Atreya, A. and Agrawal, S.*, "Effect of Radiative Heat Loss on Diffusion Flames in Quiescent Microgravity Atmosphere," Accepted for publication in Combustion and Flame, 1993.

7.*Zhang, C., Atreya, A. and Lee, K.*, Twenty-Fourth (International) Symposium on Combustion, The Combustion Institute, pp. 1049-1057, 1992.

8.*Atreya, A. and Zhang, C.*, "A Global Model of Soot Formation derived from Experiments on Methane Counterflow Diffusion Flames," in preparation for submission to Combustion and Flame.

9.*Atreya, A.*, "Formation and Oxidation of Soot in Diffusion Flames," Annual Technical Report, GRI-91/0196, Gas Research Institute, November, 1991.

10.*Williams, F. A.*, "Combustion Theory," The Benjamin/Cummings Publishing Company, pp 73-76, 1985.

APPENDIX C

Radiation from Unsteady Spherical Diffusion Flames in Microgravity

33nd Aerospace Sciences Meeting (AIAA 95-0148) paper

By

Pickett, K., Atreya, A., Agrawal, S., and Sacksteder, K. R.

AIAA 95-0148

Radiation From Unsteady Spherical Diffusion Flames In Microgravity

K. Pickett, A. Atreya and S. Agrawal
Department of Mechanical Engineering
and Applied Mechanics
The University of Michigan
Ann Arbor, MI 48109-2125

K. R. Sacksteder
Microgravity Combustion Research
NASA Lewis Research Center
Cleveland, OH 44135

33rd Aerospace Sciences Meeting and Exhibit
January 9-12, 1995 / Reno, NV

RADIATION FROM UNSTEADY SPHERICAL DIFFUSION FLAMES IN MICROGRAVITY

Kent Pickett, Arvind Atreya and Sanjay Agrawal
Combustion and Heat Transfer Laboratory
Department of Mechanical Engineering and Applied Mechanics
The University of Michigan, Ann Arbor, MI 48109-2125

Kurt R. Sacksteder
Microgravity Combustion Research
NASA Lewis Research Center
Cleveland, OH 44135

Abstract

This paper presents the experimental results of flame temperature and radiation for expanding spherical diffusion flames in microgravity. A small porous sphere madé from a low-density and low-heat-capacity insulating material was used to uniformly supply fuel, at a nearly constant rate, to the expanding spherical diffusion flame. Three gaseous fuels methane, ethylene and acetylene were used with fuel flow rates ranging from 12 to 28 ml/sec. Time histories of the radius of the spherical diffusion flame, its temperature and the radiation emitted by it were measured. The objective is to quantify the effect of soot and gas radiation on these diffusion flames. The experimental results show that as the flame radius increases, the flame expansion process becomes diffusion controlled and the flame radius grows roughly as $\sqrt{t}$. While previous theoretical calculations for non-radiative flames show that for a constant fuel mass injection rate a quasi-steady state is developed inside the region surrounded by the flame, current experimental results show a substantial reduction in the temperature and flame luminosity with time.

I. Introduction

The absence of buoyancy-induced flows in a microgravity environment and the resulting increase in the reactant residence time significantly alters the fundamentals of many combustion processes. Substantial differences between normal gravity and microgravity flames have been reported during droplet combustion[1], flame spread over solids[2,3], candle flames[4] and others. These differences are more basic than just in the visible flame shape. Longer residence time and higher concentration of combustion products create a thermochemical environment which changes the flame chemistry. Processes such as soot formation and oxidation and ensuing flame radiation, which are often ignored under normal gravity, become very important and sometimes controlling. As an example, consider the droplet burning problem. The visible flame shape is spherical under microgravity versus a teardrop shape under normal gravity. Since most models of droplet combustion utilize spherical symmetry, excellent agreement with experiments is anticipated. However, microgravity experiments show that a soot shell is formed between the flame and the evaporating droplet of a sooty fuel[1]. This soot shell alters the heat and mass transfer between the droplet and its flame resulting in significant changes in the burning rate and the propensity for flame extinction. This change in the nature of the process seems to have occurred because of two reasons: (i) The soot formed could not be swept out of the flame due to the absence of buoyant flows. Instead, it was forced to go through the high temperature reaction zone increasing the radiative heat losses, and (ii) soot formation was enhanced due to an increase in the reactant residence time.

Recently, some very interesting observations of candle flames under various atmospheres in microgravity have been reported[4]. It was found that for the same atmosphere, the burning rate per unit wick surface area and the flame temperature were considerably reduced in microgravity as compared with normal gravity. Also, the flame (spherical in microgravity) was much thicker and further removed from the wick. It thus appears that the flame becomes "weaker" in microgravity due to

the absence of buoyancy generated flow which serves to transport the oxidizer to the combustion zone and remove the hot combustion products from it. The buoyant flow, which may be characterized by the strain rate, assists the diffusion process to execute these essential functions for the survival of the flame. Thus, the diffusion flame is "weak" at very low strain rates and as the strain rate increases the flame is initially "strengthened" and eventually it may be "blown-out." The computed flammability boundaries[5] show that such a reversal in material flammability occurs at strain rates around 5 sec^{-1}. Model calculations for a zero strain rate *1-D* diffusion flame show that even gas radiation is sufficient to extinguish the flame[6].

The above observations suggest that flame radiation will substantially influence diffusion flames under microgravity conditions, particularly the conditions at extinction. This is because, flame radiation at very low or zero strain rates is enhanced due to: (i) high concentration of combustion products in the flame zone which increases the gas radiation, and (ii) low strain rates provide sufficient residence time for substantial amounts of soot to form which is usually responsible for most of the radiative heat loss. It is anticipated that this radiative heat loss may extinguish the already "week" diffusion flame.

To investigate the possibility of radiation-induced extinction limits under microgravity conditions, spherical geometry is chosen. This is convenient for both experiments and theoretical modeling. In this work, a porous spherical burner is used to produce spherical diffusion flames in μg. Experiments conducted with this burner on methane (less sooty), ethylene (sooty), and acetylene (very sooty) diffusion flames are described in the next section. This work is a continuation of the work reported in Ref. [11] and provides the necessary insight and measurements needed for modeling radiative-extinction of spherical diffusion flames.

II. Experimental Apparatus and Results

The μg experiments were conducted in the 2.2 sec drop tower at the NASA Lewis Research Center. The experimental drop-rig used is schematically shown in Figure 1. It consists of a test chamber, burner, igniter, gas cylinder, solenoid valve, camera, computer and batteries to power the computer and the solenoid valves. The spherical burner (2.18 cm in diameter) is constructed from a low density and low heat capacity porous ceramic material. A 500 cc gas cylinder at approximately 15 psig is used to supply the fuel to the porous spherical burner. Typical gas flow rates used were in the range of 12 -28 cm^3/s. Flow rates to the burner are controlled by a needle valve and a gas solenoid valve is used to open and close the gas line to the burner upon computer command. An igniter is used to establish a diffusion flame. After ignition the igniter is quickly retracted from the burner and secured in a catching mechanism by a computer-controlled rotary solenoid. This was necessary for two reasons (i) The igniter provides a heat sink and will quench the flame (ii) Upon impact with the ground (after 2.2 sec) the vibrating igniter may damage the porous burner.

As shown in the Figure 1, the test chamber has a 5" diameter Lexan window which enables the camera to photograph the spherical diffusion flame. The flame growth can be recorded either by a 16mm color movie camera or by a color CCD camera which is connected to a video recorder by a fiber-optic cable during the drop. Since the fuel flow may change with time, it had to be calibrated for various

FUEL	Start flow rate (ml/s)	End flow rate (ml/s)
METHANE		
High	27.8	24.2
Medium	23.5	20.5
Low	18.9	17.2
ETHYLENE		
High	21.2	18.2
Medium	16.9	14.9
Low	13.5	11.9
ACETYLENE		
High	20.2	18.7
Medium	18.0	17.0
Low	16.3	15.7

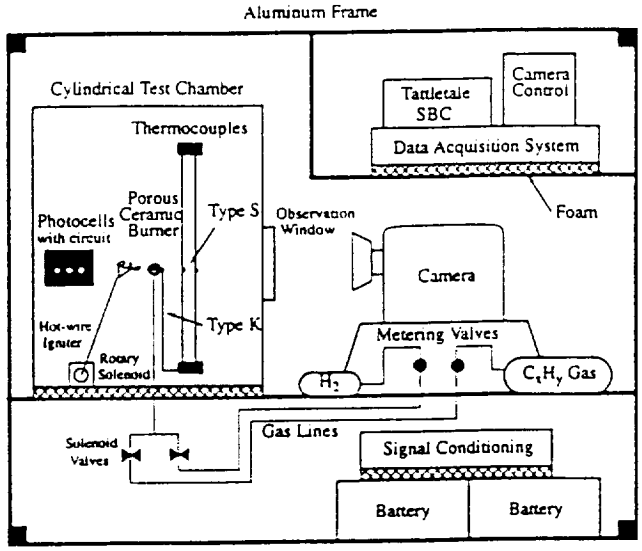

Figure 1 Schematic of Experimental Drop-rig

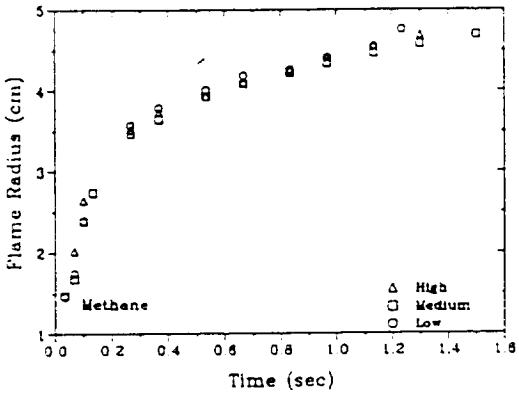

Fig 2(a) Methane Flame

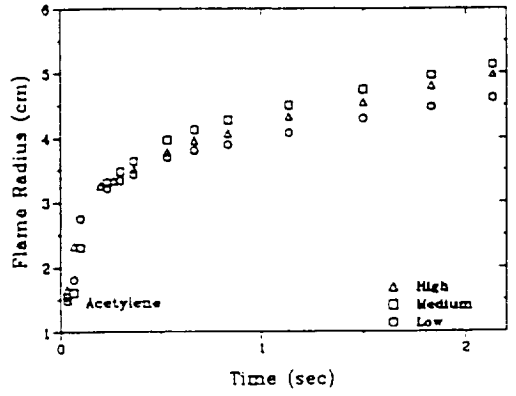

Fig 2(c) Acetylene Flame

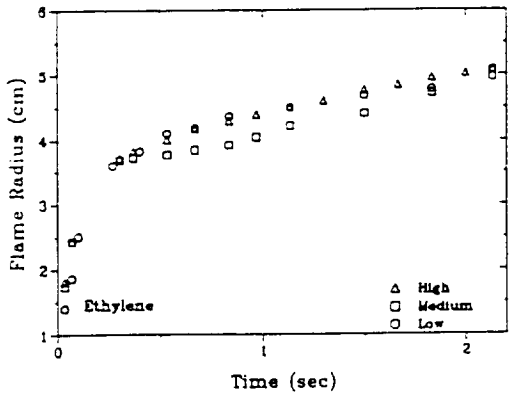

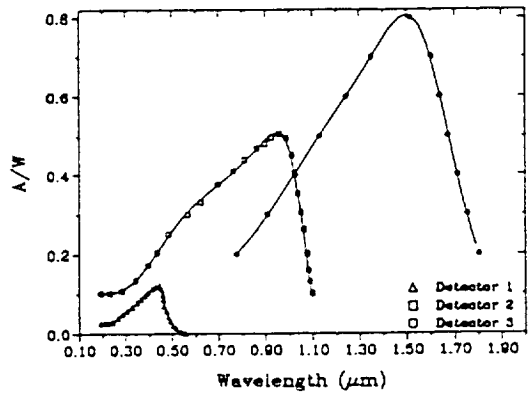

Fig 2(b) Flame radius as a function of time; Fig 3: Calibration curves for photodiodes Ethylene Flame

settings of the needle valve for all fuels. A soap bubble flow meter was used to calibrate the flow for various constant gas cylinder pressures. Constant pressures were obtained by connecting the cylinder to the main 200 lb gas cylinder using a quick-disconnect. An in-line pressure transducer was used to obtain the transient flow rates. Changes in the cylinder pressure during the experiments change the volumetric fuel flow rates slightly. These are shown in Table 1 for the experiments reported here.

The porous spherical burner produced a nearly spherical diffusion flame in microgravity. Some observed disturbances are attributed to slow large-scale air motion inside the test chamber and non-uniform fuel injection from the burner. Several microgravity experiments were performed under ambient pressure and oxygen concentration conditions for different flow rates of methane, ethylene and acetylene (as listed in Table. 1). Methane was chosén to represent a non-sooty fuel, ethylene was chosen to represent a moderately sooty fuel and acetylene was chosen to represent a very sooty fuel. In these experiments, ignition of a very low flow rate of H_2 was initiated in1-g and the flow was switched to the desired flow rate of the given fuel in μg just after the commencement of the drop. The package was typically dropped within one second after the establishment of the H_2 flame. Photographs of these experiments are shown in the Color Plates 1, 2 & 3.

The flame radius measured from these photographs are shown in Fig. 2. For the same flow rates it was found that ethylene and acetylene flames were much sootier and smaller. The flame shape is not always completely spherical because of the fuel injection non-uniformities and slow large-scale air motion persisting inside the test chamber. The photographs shown in the Color Plates 1, 2 & 3 are for methane, ethylene and acetylene respectively. For the data presented in Fig. 2, an average flame radius determined from the photographs was used.

It is interesting to note that for all the fuels (see the progressive flame growth in the Color Plates) initially the flame is nearly blue (non-sooty) but becomes bright yellow (sooty) under μg conditions. Later, as the μg time progresses, the flame grows in size and becomes orange and less luminous and the soot seems to disappear. (A soot-shell is also visible in the ethylene photographs.) A possible explanation for this observed behavior is suggested by the theoretical calculations of Ref. 6. The soot volume fraction first quickly increases and later decreases as the local concentration of combustion products increases. Essentially, further soot formation is inhibited by the increase in the local concentration of the combustion products [Ref.7,8] and soot oxidation is enhanced. Thus, at the onset of μg conditions, initially a lot of soot is formed in the vicinity of the flame front (the outer faint blue envelope) resulting in bright yellow emission. As the flame grows, several events reduce the flame luminosity: (i) The soot is pushed toward cooler regions by thermophoresis. In fact, for sootier fuels this leads to the formation of a soot shell. (ii) The high concentration of combustion products left behind by the flame front inhibits soot formation and promotes soot oxidation. (iii) The dilution and radiative heat losses caused by the increase in the concentration of combustion products reduces the flame temperature which in turn reduces the soot formation rate and the flame luminosity. This effect is clearly evident from the incident radiation measured by the three photodiodes and shown in Figures 5, 7 & 8. The photodiodes are not spectrally flat. As shown in Figure 3, detector 1 essentially measures the blue & green radiation, detector 2 primarily captures the yellow, red & near infra-red radiation, and detector 3 is for infra-red radiation up to 1.8 μm.

Our previous calculations [11] for non-radiating spherical diffusion flames (schematically shown in Figure 10), show that the temperature and therefore the density becomes nearly uniform inside

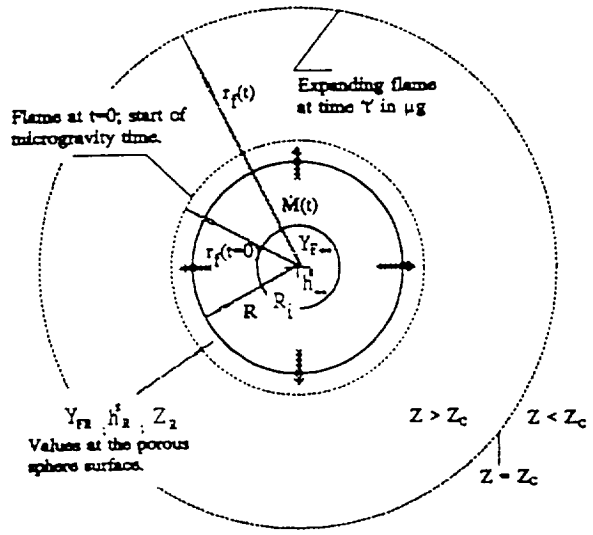

Figure 10: Schematic of the Model Problem

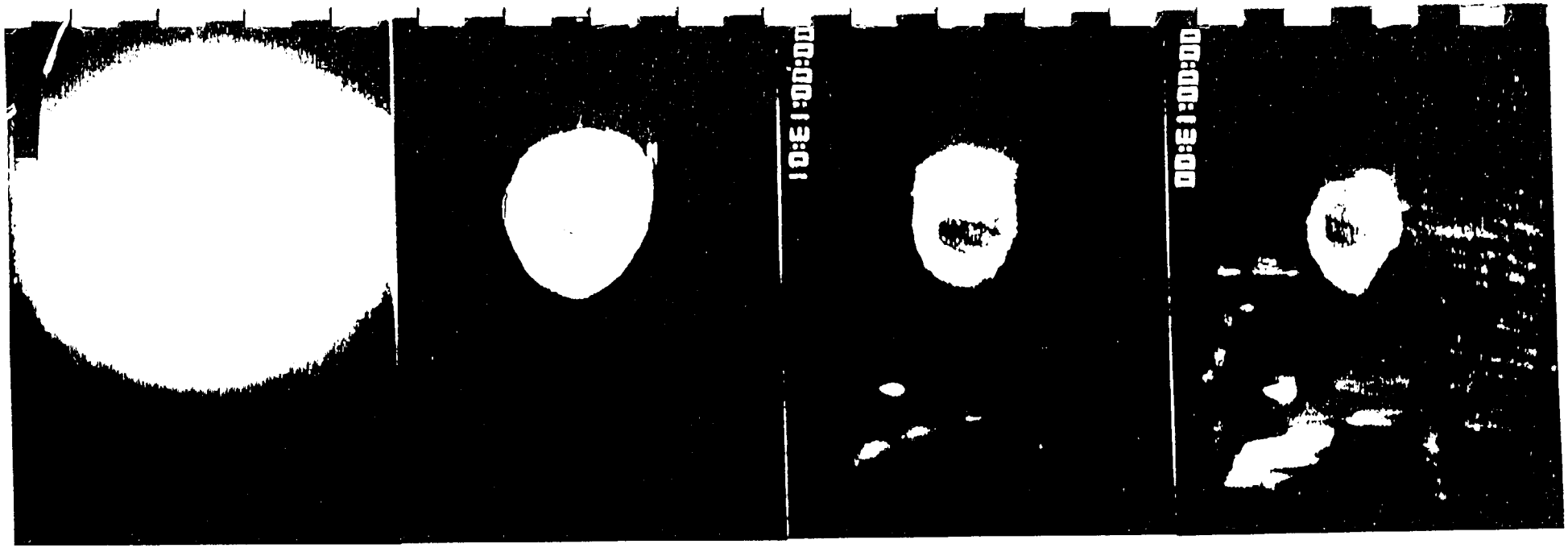

(d) (c) (b) (a)

PLATE 1 - Methane Flames: (a) 0.033 sec after microgravity onset, (b) 0.067 sec, (c) 0.10 sec, (d) 0.37 sec, (e) 0.57 sec, (f) 0.67 sec, (g) 0.90 sec, and (h) 0.97 sec. (Medium flow rate)

(h) (g) (f) (e)

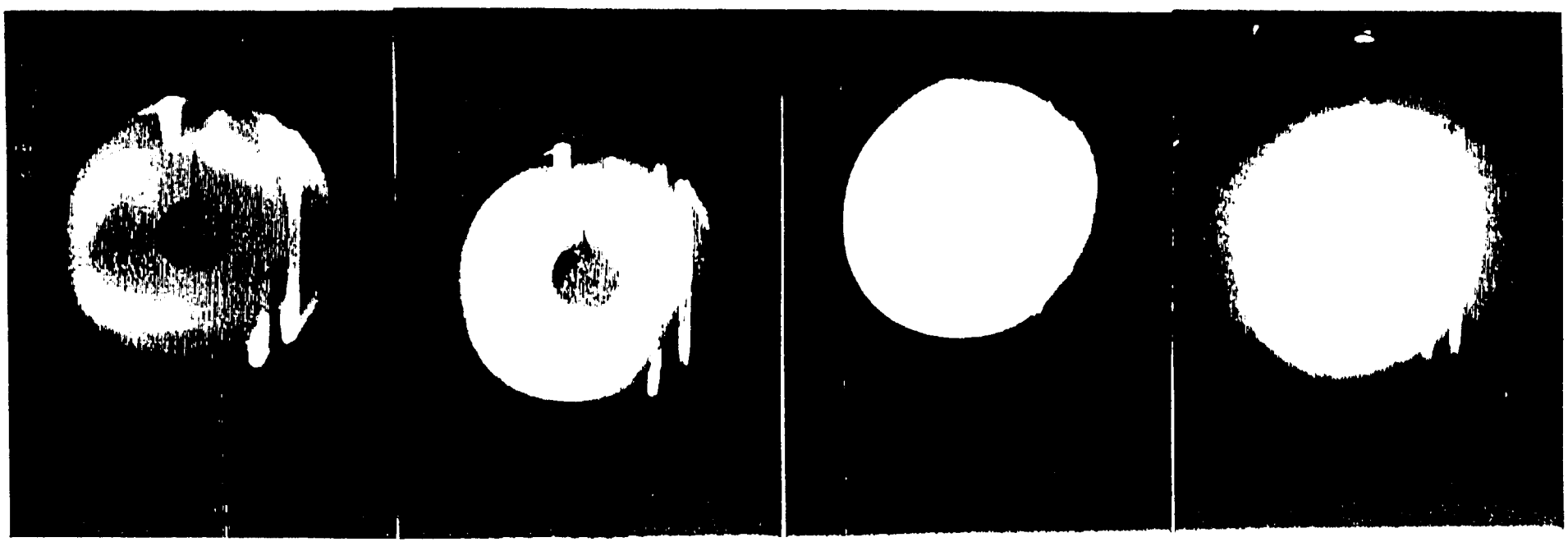

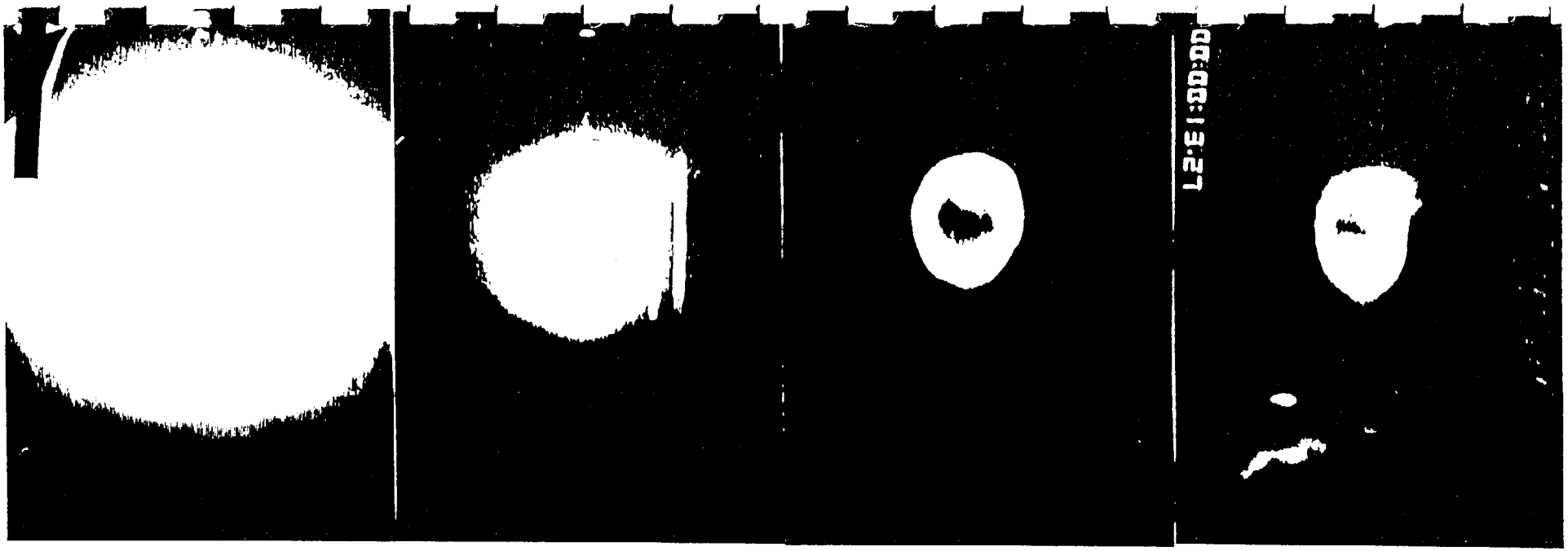

(d) (c) (b) (a)

PLATE 2 - Ethylene Flames: (a) 0.033 sec after microgravity onset, (b) 0.067 sec, (c) 0.133 sec, (d) 0.33 sec, (e) 1.07 sec, (f) 1.20 sec, (g) 1.37 sec, and (h) 1.80 sec. (High flow rate)

(h) (g) (f) (e)

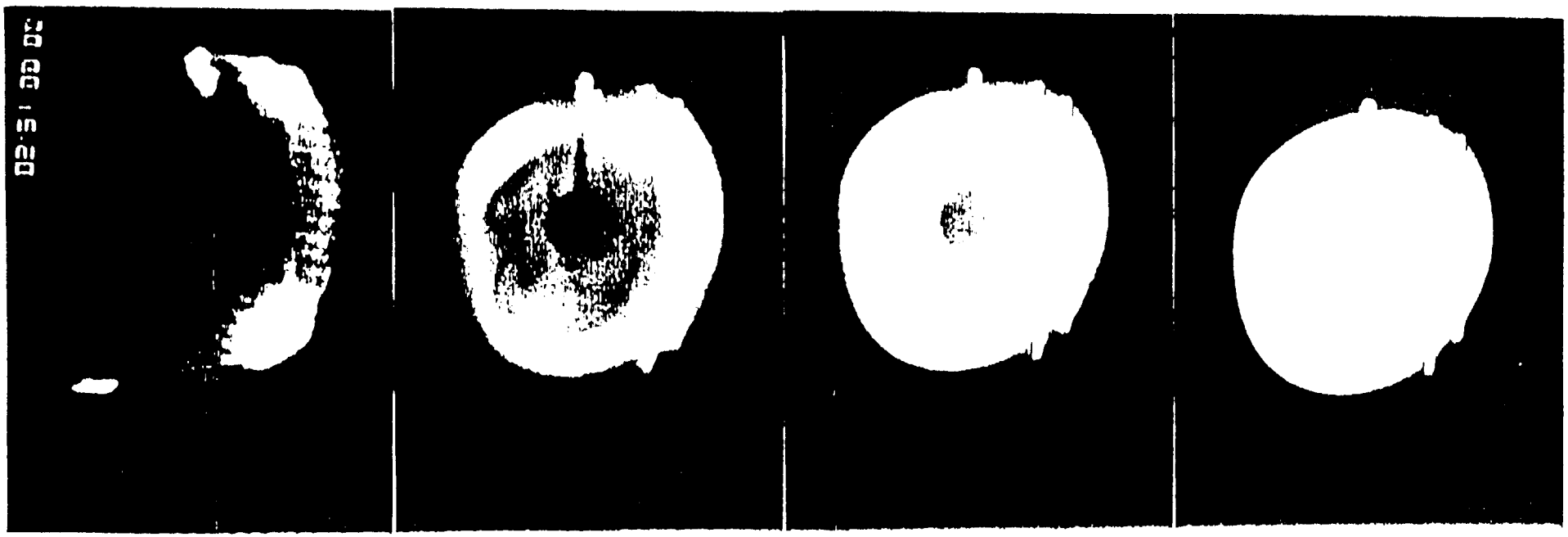

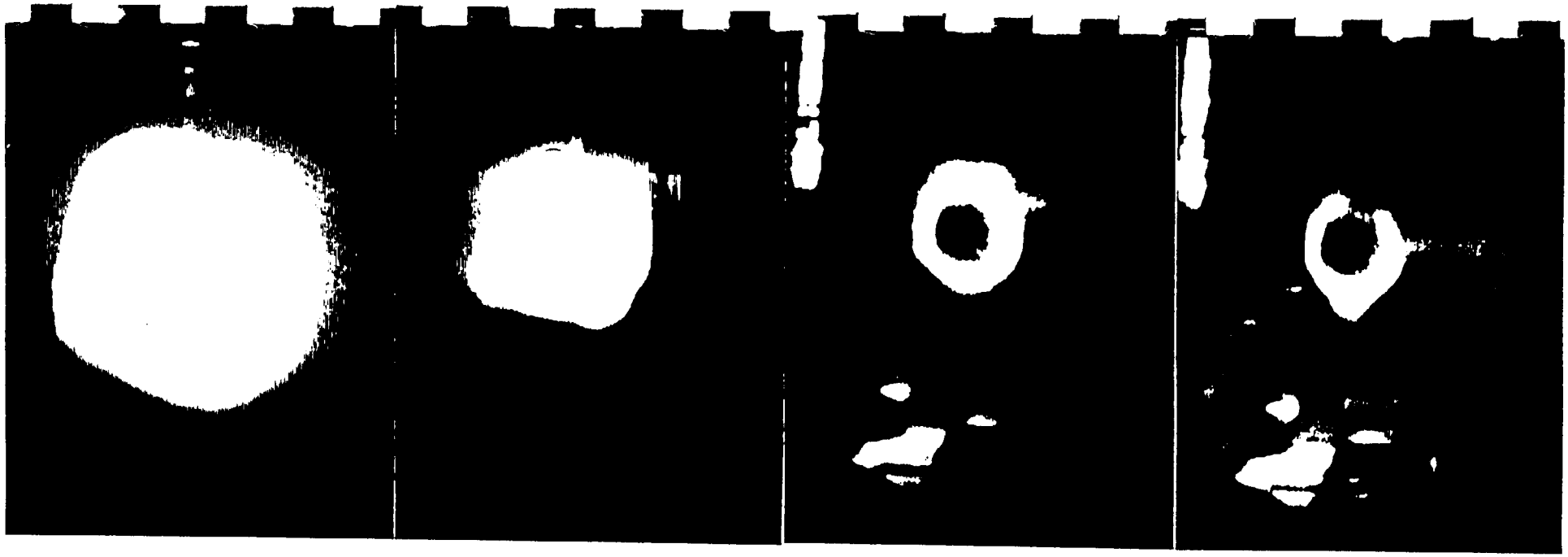

(d) (c) (b) (a)

PLATE 3 - Acetylene Flames: (a) 0.033 sec after microgravity onset, (b) 0.067 sec, (c) 0.10 sec, (d) 0.20 sec, (e) 0.37 sec, (f) 0.50 sec, (g) 1.90 sec, and (h) 2.13 sec. (High flow rate)

(h) (g) (f) (e)

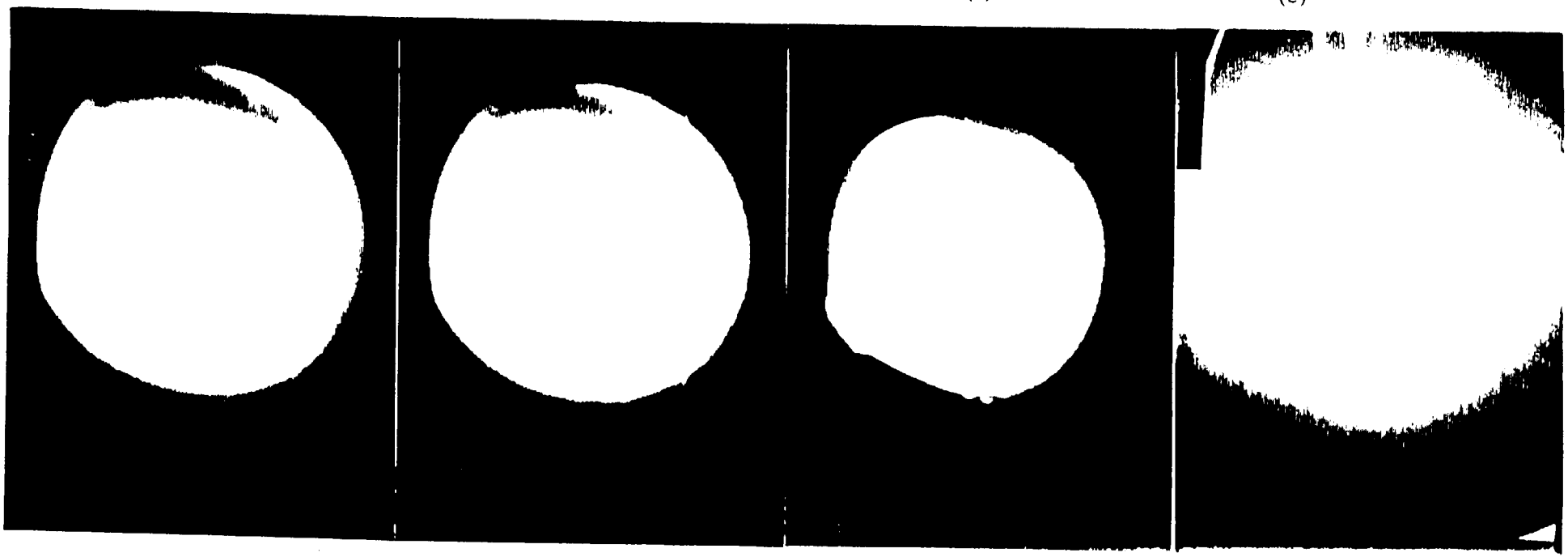

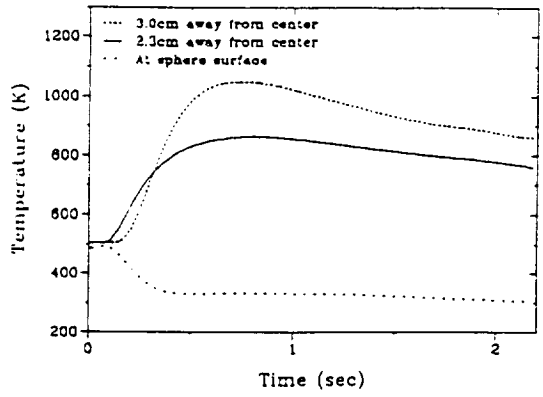

(a) Low Flow Rate

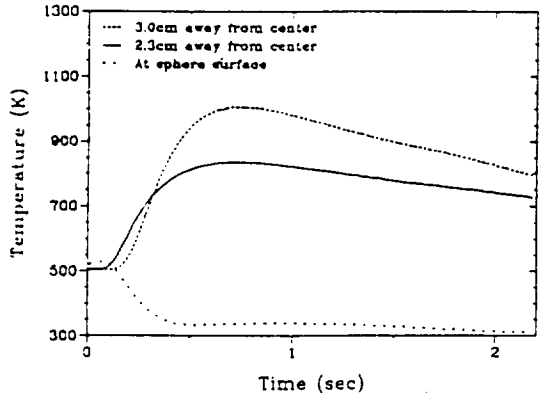

(b) Medium Flow Rate

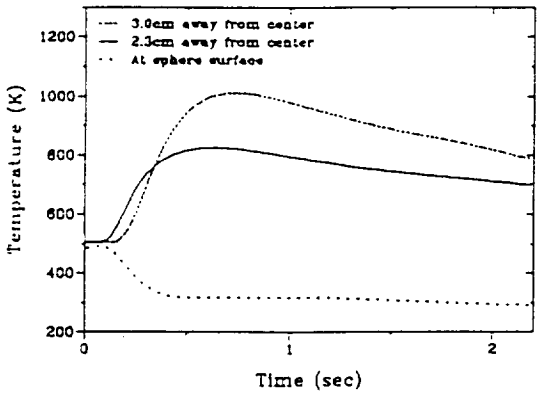

(c) High Flow Rate

Fig 4: Flame Temperatures for Methane

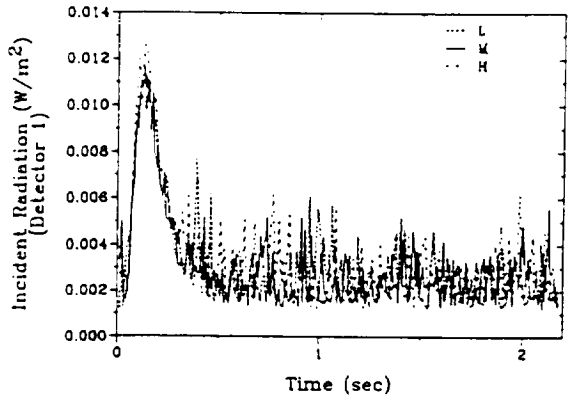

(a) Detector 1

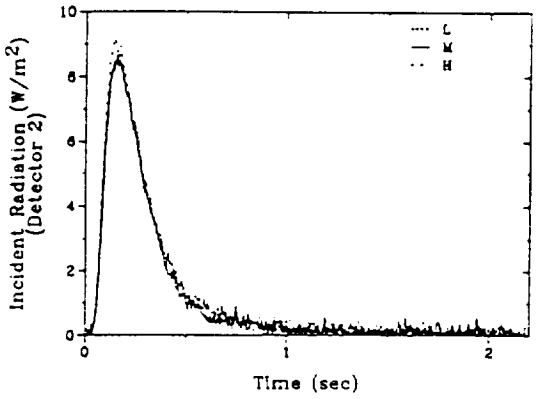

(b) Detector 2

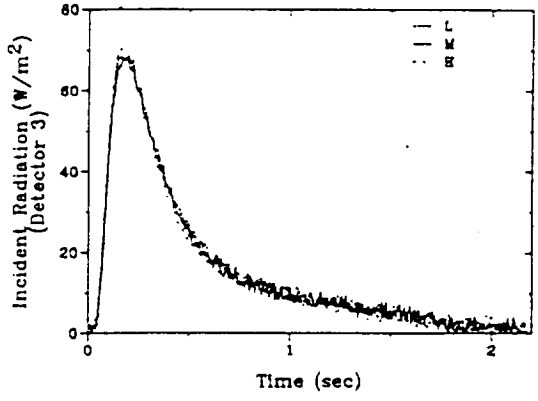

(c) Detector 3

Fig 5: Incidence radiation detected by photodiodes

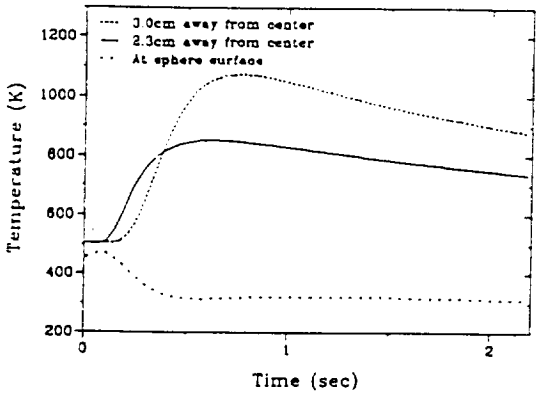

(a) Low Flow Rate

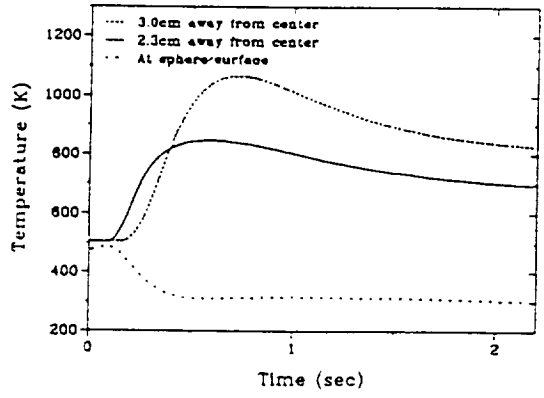

(b) Medium Flow Rate

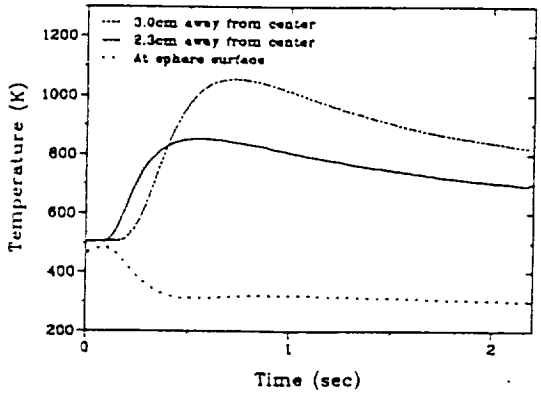

(c) High Flow Rate

Fig 6: Flame Temperatures for Ethylene

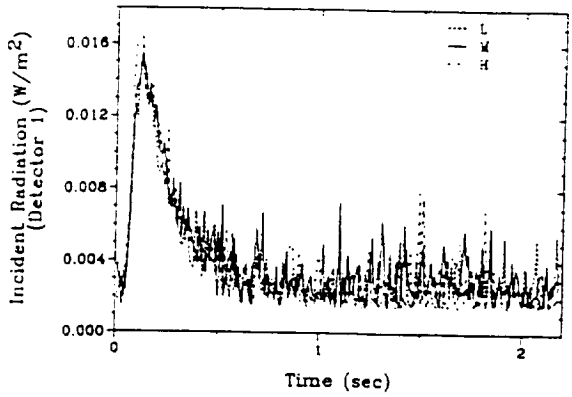

(a) Detector 1

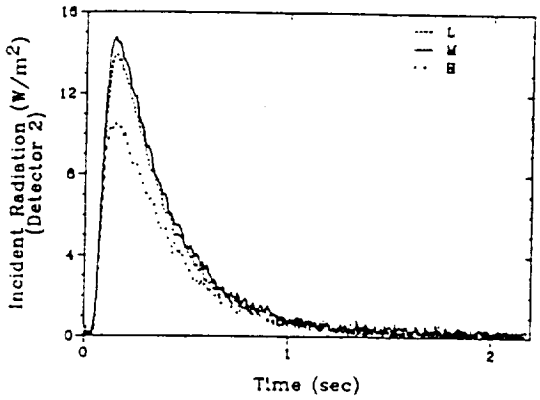

(b) Detector 2

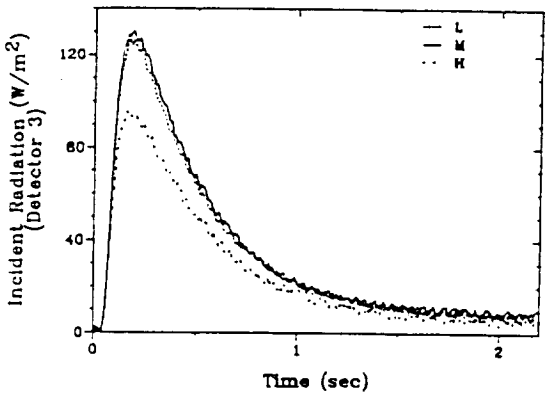

(c) Detector 3

Fig 7: Incidence radiation detected by photodiodes

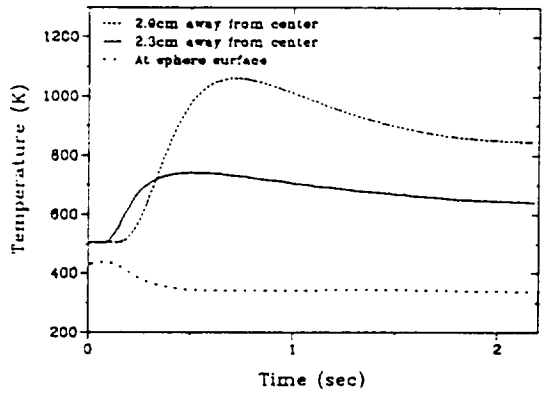

(a) Low Flow Rate

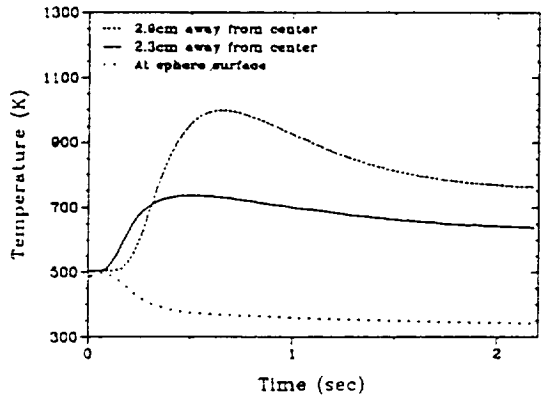

(b) Medium Flow Rate

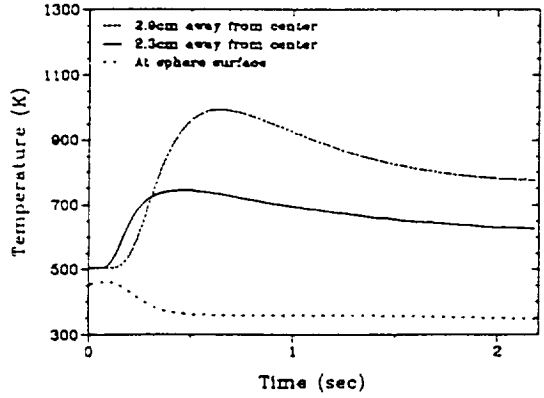

(c) High Flow rate

Fig 8: Flame Temperatures for Acetylene

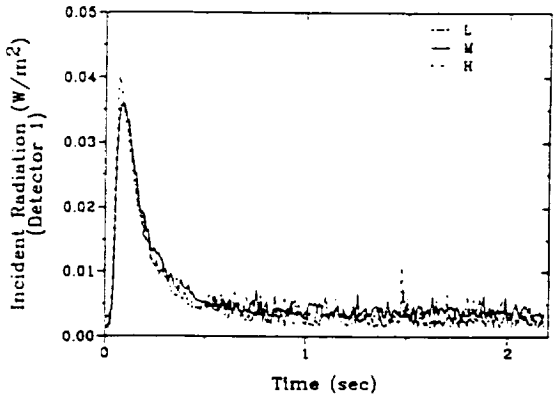

(a) Detector 1

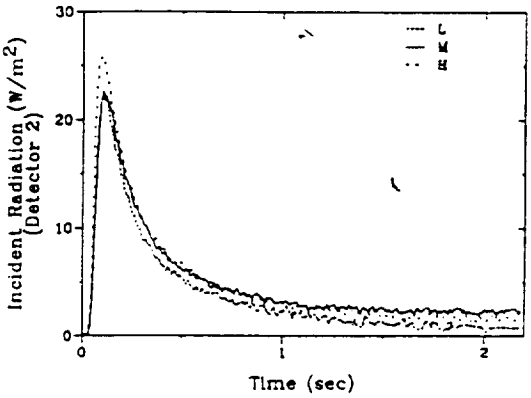

(b) Detector 2

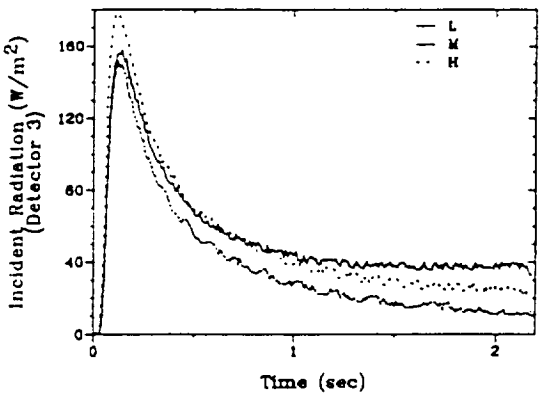

(c) Detector 3

Fig 9: Incidence radiation detected by photodiodes

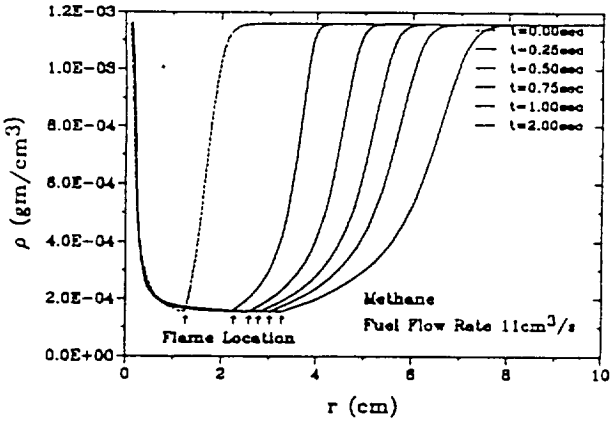

Figure 11: Radial density distribution at various instants

the flame. The density profiles in this region (Fig. 11) also show a similarity. In the theoretical problem, a constant temperature (adiabatic flame temperature) spherical flame is propagating outward starting from a small radius. In the spherical geometry, heat loss from the region surrounded by the flame is not possible. Thus, the only heat required by this region from the flame (in the absence of radiation) is to heat the injected mass to the flame temperature. Since, the injected mass is taken to be constant with time, a quasi steady state is developed. This is also observed in the density gradients at the flame on the fuel side (which are constant and are proportional to the temperature gradients). However, the experimentally measured temperature profiles (see Figures 4, 6 & 8) show a substantial drop in the temperature profile. This is due to radiative heat loss.

VI Conclusions

In this work, experimental results for expanding methane, ethylene and acetylene diffusion flames in microgravity are presented. A small porous sphere made from a low-density and low-heat-capacity insulating material was used to uniformly supply fuel at a constant rate to the expanding diffusion flame. Three gaseous fuels methane, ethylene and acetylene were used. Time histories of the radius of the spherical diffusion flame, its temperature and the radiation emitted by it were measured. The experimental results show that as the flame radius increases, the flame expansion process becomes diffusion controlled and the flame radius grows roughly as $\sqrt{t}$. While previous theoretical calculations for non-radiative flames show that for a constant fuel mass injection rate a quasi-steady state is developed inside the region surrounded by the flame, current experimental results show a substantial reduction in the temperature and flame luminosity with time.

Acknowledgements: This project is supported by NASA under contract no. NAG3-1460.

References

1.*Jackson, G., S., Avedisian, C., T. and Yang, J., C.*, Int. J. Heat Mass Transfer., Vol.35, No. 8, pp. 2017-2033, 1992.

2.*T'ien, J. S., Sacksteder, K. R., Ferkul, P. V. and Grayson, G. D.* "Combustion of Solid Fuels in very Low Speed Oxygen Streams," Second International Microgravity Combustion Workshop," NASA Conference Publication, 1992.

3.*Ferkul, P., V.*, "A Model of Concurrent Flow Flame Spread Over a Thin Solid Fuel," NASA Contractor Report 191111, 1993.

4.*Ross, H. D., Sotos, R. G. and T'ien, J. S.*, Combustion Science and Technology, Vol. 75, pp. 155-160, 1991.

5.*T'ien, J. S.*, Combustion and Flame, Vol. 80, pp. 355-357, 1990.

6.*Atreya, A. and Agrawal, S.*, "Effect of Radiative Heat Loss on Diffusion Flames in Quiescent Microgravity Atmosphere," Accepted for publication in Combustion and Flame, 1993.

7.*Zhang, C., Atreya, A. and Lee, K.*, Twenty-Fourth (International) Symposium on Combustion, The Combustion Institute, pp. 1049-1057, 1992.

8.*Atreya, A. and Zhang, C.*, "A Global Model of Soot Formation derived from Experiments on Methane Counterflow Diffusion Flames," in preparation for submission to Combustion and Flame.

9.*Atreya, A.*, "Formation and Oxidation of Soot in Diffusion Flames," Annual Technical Report, GRI-91/0196, Gas Research Institute, November, 1991.

10.*Williams, F. A.*, "Combustion Theory," The Benjamin/Cummings Publishing Company, pp 73-76, 1985.

11. *Atreya, A, Agrawal, S., Sacksteder, K., and Baum, H.*, "Observations of Methane and Ethylene Diffusion Flames Stabilized around a Blowing Porous Sphere under Microgravity Conditions," AIAA paper # 94-0572, January 1994.

APPENDIX D

Radiant Extinction of Gaseous Diffusion Flames

3rd International Microgravity Conference, April, 1995 paper

By

Atreya, A., Agrawal, S., Shamim, T., Pickett, K., Sacksteder, K. R. and Baum, H. R.

RADIANT EXTINCTION OF GASEOUS DIFFUSION FLAMES

Arvind Atreya, Sanjay Agrawal, Tariq Shamim & Kent Pickett
University of Michigan; Ann Arbor, MI 48109

Kurt R. Sacksteder
NASA Lewis Research Center; Cleveland, OH 44135

Howard R. Baum
NIST, Gaithersburg, MD 20899

INTRODUCTION

The absence of buoyancy-induced flows in microgravity significantly alters the fundamentals of many combustion processes. Substantial differences between normal-gravity and microgravity flames have been reported during droplet combustion[1], flame spread over solids[2,3], candle flames[4] and others. These differences are more basic than just in the visible flame shape. Longer residence time and higher concentration of combustion products create a thermochemical environment which changes the flame chemistry. Processes such as flame radiation, that are often ignored under normal gravity, become very important and sometimes even controlling. This is particularly true for conditions at extinction of a μg diffusion flame.

Under normal-gravity, the buoyant flow, which may be characterized by the strain rate, assists the diffusion process to transport the fuel & oxidizer to the combustion zone and remove the hot combustion products from it. These are essential functions for the survival of the flame which needs fuel & oxidizer. Thus, as the strain rate is increased, the diffusion flame which is "weak" (reduced burning rate per unit flame area) at low strain rates is initially "strengthened" and eventually it may be "blown-out." Most of the previous research on diffusion flame extinction has been conducted at the high strain rate "blow-off" limit. The literature substantially lacks information on low strain rate, radiation-induced, extinction of diffusion flames. At the low strain rates encountered in μg, flame radiation is enhanced due to: (i) build-up of combustion products in the flame zone which increases the gas radiation, and (ii) low strain rates provide sufficient residence time for substantial amounts of soot to form which further increases the flame radiation. It is expected that this radiative heat loss will extinguish the already "weak" diffusion flame under certain conditions. Identifying these conditions (ambient atmosphere, fuel flow rate, fuel type, etc.) is important for spacecraft fire safety. Thus, the objective of this research is to experimentally and theoretically investigate the radiation-induced extinction of diffusion flames in μg and determine the effect of flame radiation on the "weak" μg diffusion flame.

RESEARCH APPROACH

To investigate radiation-induced extinction, spherical and counterflow geometries are chosen for μg & *1-g* respectively for the following reasons: Under μg conditions, a spherical burner is used to

produce a spherical diffusion flame. This forces the combustion products (including soot which is formed on the fuel side of the diffusion flame) into the high temperature reaction zone and may cause radiative-extinction under suitable conditions. Under normal-gravity conditions, however, the buoyancy-induced flow field around the spherical burner is complex and unsuitable for studying flame extinction. Thus, a one-dimensional counterflow diffusion flame is chosen for *1-g* experiments and modeling. At low strain rates, with the diffusion flame on the fuel side of the stagnation plane, conditions similar to the μg case are created -- the soot is again forced through the high temperature reaction zone. The *1-g* experiments are primarily used to determine the rates of formation and oxidation of soot in the thermochemical environment present under μg conditions. These rates are necessary for modeling purposes. Transient numerical models for both μg and *1-g* cases are being developed to provide a theoretical basis for the experiments. These models include soot formation and oxidation and flame radiation and will help quantify the low-strain-rate radiation-affected diffusion flame extinction limits.

RESULTS

Significant progress has been made on both experimental and theoretical parts of this research. This may be summarized as follows:

1) Experimental and theoretical work on determining the expansion rate of the μg spherical diffusion flame. Preliminary results were presented at the AIAA conference (Ref. 5).
2) Theoretical modeling of zero strain rate transient diffusion flame with radiation (Ref. 6).
3) Experimental and theoretical work for determining the radiation from the μg spherical diffusion flame. Preliminary results were presented at the AIAA conference (Ref. 7).
4) Theoretical modeling of finite strain rate transient counterflow diffusion flame with radiation (Ref 8).
5) Experimental work on counterflow diffusion flames to determine the soot formation and oxidation rates (Ref. 9).

The above experimental and theoretical work is briefly summarized in the remainder of this section.

Experimental Work: The μg experiments were conducted in the 2.2 sec drop tower at the NASA Lewis Research Center and the counterflow diffusion flame experiments (not described here) were performed at UM. For the μg experiments, a porous spherical burner was used to produce nearly spherical diffusion flames. Several experiments, under ambient pressure and oxygen concentration conditions, were performed with methane (less sooty), ethylene (sooty), and acetylene (very sooty) for flow rates ranging from 4 to 28 cm^3/s. These fuel flow rates were set by a needle valve and a solenoid valve was used to open and close the gas line to the burner upon computer command. Two ignition methods were used for these experiments: (i) The burner was ignited in *1-g* with the desired fuel flow rate and the package was dropped within one second after ignition. (ii) The burner was ignited in *1-g* with a very low flow rate of H_2 and the flow was switched to the desired flow rate of the given fuel in μg just after the commencement of the drop. Following measurements were made during the μg experiments:

i) The *flame radius* was measured from photographs taken by a color CCD camera. Image processing was used to determine both the flame radius and the relative image intensity. Sample photographs are shown in Photos E1 to E3 for ethylene and A1 to A3 for acetylene.
ii) The *flame radiation* was measured by the three photodiodes with different spectral absorptivities. The first photodiode essentially measures the blue & green radiation, the second photodiode captures the yellow, red & near infra-red radiation, and the third photodiode is for infra-red radiation from 0.8 to 1.8 μm.
iii) The *flame temperature* was measured by two S-type thermocouples and the sphere surface temperature was measured by a K-type thermocouple. In both cases 0.003" diameter wire was used. The measured temperatures were later corrected for time response and radiation.

It is interesting to note that for both ethylene and acetylene (see the progressive flame growth in the Color Photos) initially the flame is blue (non-sooty) but becomes bright yellow (sooty) under μg conditions. Later, as the *μg* time progresses, the flame grows in size and becomes orange and less luminous and the soot luminosity seems to disappear. A possible explanation for this observed behavior is suggested by the theoretical calculations of Ref. 6 & 8. The soot volume fraction first quickly increases and later decreases as the local concentration of combustion products increases. Essentially, further soot formation is inhibited by the increase in the local concentration of the combustion products and soot oxidation is enhanced [Ref.9,10]. Also, the high temperature reaction zone moves away from the already present soot leaving behind a relatively cold (non-luminous) soot shell. (A soot-shell is clearly visible in the ethylene Photo E2.) Thus, at the onset of μg conditions, initially a lot of soot is formed in the vicinity of the flame front (the outer faint blue envelope in the photographs) resulting in bright yellow emission. As the flame grows, several events reduce the flame luminosity: (i) The high concentration of combustion products left behind by the flame front inhibits the formation of new soot and promotes soot oxidation. (ii) The primary reaction zone, seeking oxygen, moves away from the soot region and the soot is pushed toward cooler regions by thermophoresis. Both these effects increase the distance between the soot layer and the reaction zone. (iii) The dilution and radiative heat losses caused by the increase in the concentration of the combustion products reduces the flame temperature which in turn reduces the soot formation rate and the flame luminosity.

Upon further observation, we note that the ethylene flames become blue toward the end of the *μg* time while the acetylene flames remain luminous yellow (although the intensity is significantly reduced as seen by the photodiode measurements in Figure 2). This is because of the higher sooting tendency of acetylene which enables soot formation to persist for a longer time. Thus, acetylene soot remains closer to the high temperature reaction zone for a longer time making the average soot temperature higher and the distance between the soot and the reaction layers smaller. Eventually, as is evident from Figure 2, even the acetylene flames will become blue in *μg*. From Figure 2 we note that the peak radiation intensity occurs at about 2.5 cm flame radius which corresponds to a time of about 0.2 seconds. This is almost the location of the first thermocouple whose output is plotted in Figures 3 & 4 as Tgas(1). From the temperature measurements presented in Figures 3 & 4, we note that: (i) The flame radiation significantly reduces the flame temperature (compare the peaks of the second thermocouple with those of the first for both fuels) by approximately 300K for ethylene and 500K for acetylene. (In fact, the acetylene flame seems to be on the threshold of extinction at this instant.) (ii) The temperature of the acetylene flame is about 200K lower than the ethylene flame at the first thermocouple location. (iii) The final gas temperature is also about 100K lower for the acetylene flame, which is consistent with larger radiative heat loss.

The data from the photodiodes is further reduced to obtain the total soot mass and the average temperature of the soot layer. This is plotted in Figures 5 & 6. These figures show that the average acetylene soot layer temperature is higher than the average ethylene soot layer temperature. The total soot mass produced by acetylene peaks at 0.2 seconds which corresponds to the peak of the first thermocouple, explaining the large drop in temperature. Also, the acetylene soot layer is cooling more slowly than the ethylene soot layer which is consistent with the above discussion regarding the photographic observations. Thus, for ethylene the reaction layer is moving away faster from the soot layer than in the case of acetylene. This is also consistent with the fact that ethylene soot mass becomes nearly constant but the acetylene soot mass reduces due to oxidation. Finally, the rate of increase in the total soot mass (i.e. the soot production rate) should be related to the sooting tendency of a given fuel. This corresponds to the slope of the soot mass curve in Figures 5 & 6. Clearly, the slope for acetylene is higher.

The flame radius measurements, presented in Figure 1, show a substantial change in the growth rate from initially being roughly proportional to $t^{1/2}$ to eventually (after significant radiative heat loss) being

proportional to $t^{1/5}$. In Ref. 5, we had developed a model for the expansion rate of non-radiating flames which is currently being modified to include the effects of radiant heat loss.

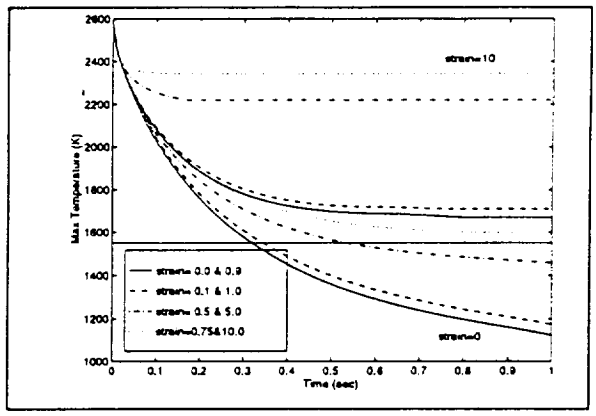

Reduction in Maximum Flame Temperature with Radiation (T_∞=295K, $Y_{F\infty}$=0.125, $Y_{O\infty}$=0.5)

Theoretical Work: Due to lack of space, only our most recent theoretical work is summarized here. In this work, to quantify the low-strain-rate radiation-induced diffusion flame extinction limits, a computational model has been developed for an unsteady counterflow diffusion flame. So far, only the radiative heat loss from combustion products (CO_2 and H_2O) have been considered in the formulation. The computations show a significant reduction in the flame temperature due to radiation. The adjacent figure shows the time variations of the maximum flame temperature for various values of the strain rates. This plot shows that for flames with strain rates less than 1 s^{-1}, the effect of gas radiation is sufficient to cause extinction. These results agree with our earlier study [6] at zero strain rate where gas radiation was also found to be sufficient to cause extinction. Clearly, additional radiation due to soot will extinguish the flames at higher strain rates.

Acknowledgements: This project is supported by NASA under contract no. NAG3-1460.

REFERENCES

1. *Jackson, G., S., Avedisian, C., T. and Yang, J., C.*, Int. J. Heat Mass Transfer., Vol.35, No. 8, pp. 2017-2033, 1992.

2. *T'ien, J. S., Sacksteder, K. R., Ferkul, P. V. and Grayson, G. D.* "Combustion of Solid Fuels in very Low Speed Oxygen Streams," Second International Microgravity Combustion Workshop," NASA Conference Publication, 1992.

3. *Ferkul, P., V.*, "A Model of Concurrent Flow Flame Spread Over a Thin Solid Fuel," NASA Contractor Report 191111, 1993.

4. *Ross, H. D., Sotos, R. G. and T'ien, J. S.*, Combustion Science and Technology, Vol. 75, pp. 155-160, 1991.

5. *Atreya, A, Agrawal, S., Sacksteder, K., and Baum, H.*, "Observations of Methane and Ethylene Diffusion Flames Stabilized around a Blowing Porous Sphere under Microgravity Conditions," AIAA paper # 94-0572, January 1994.

6. *Atreya, A. and Agrawal, S.*, "Effect of Radiative Heat Loss on Diffusion Flames in Quiescent Microgravity Atmosphere," Accepted for publication in Combustion and Flame, 1993.

7. *Pickett, K., Atreya, A., Agrawal, S., and Sacksteder, K.*, "Radiation from Unsteady Spherical Diffusion Flames in Microgravity," AIAA paper # 95-0148, January 1995.

8. *Shamim, T., and Atreya, A.* "A Study of the Effects of Radiation on Transient Extinction of Strained Diffusion Flames," Central States Combustion Institute Meeting, 1995.

9. *Atreya, A. and Zhang, C.*, "A Global Model of Soot Formation derived from Experiments on Methane Counterflow Diffusion Flames," in preparation for submission to Combustion and Flame.

10. *Zhang, C., Atreya, A. and Lee, K.*, Twenty-Fourth (International) Symposium on Combustion, The Combustion Institute, pp. 1049-1057, 1992.

11. *Atreya, A.*, "Formation and Oxidation of Soot in Diffusion Flames," Annual Technical Report, GRI-91/0196, Gas Research Institute, November, 1991.

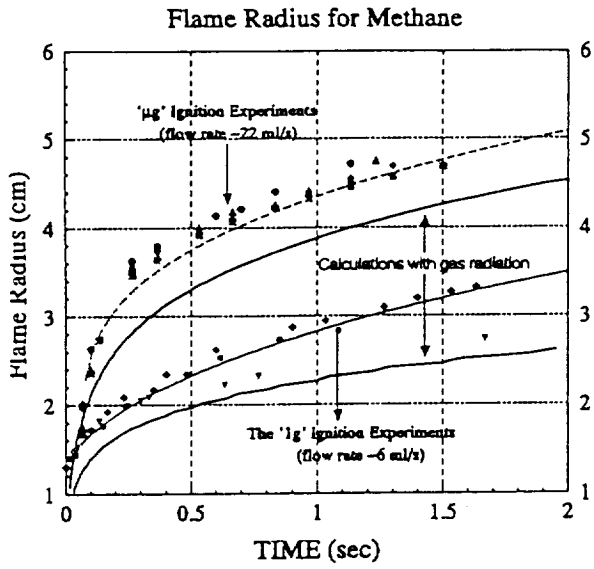

Figure 1

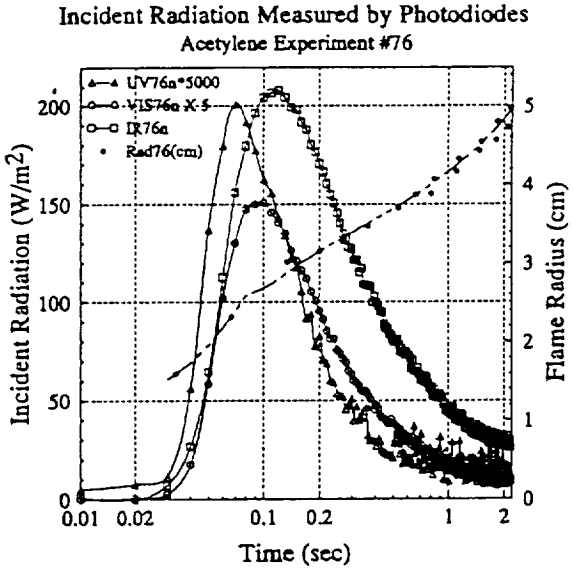

Figure 2

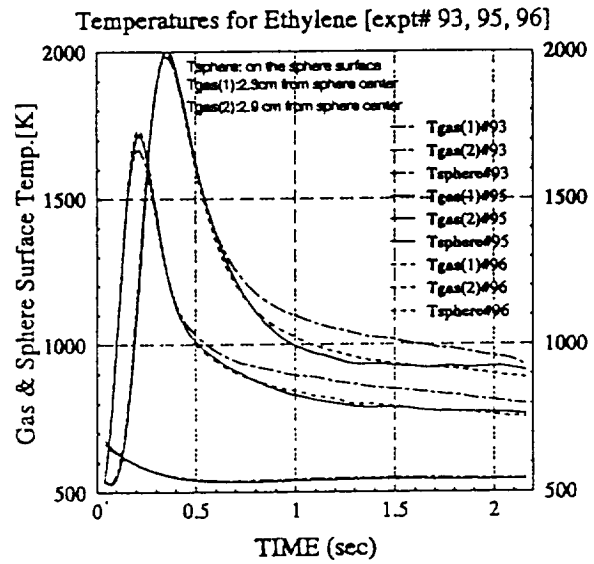

Figure 3

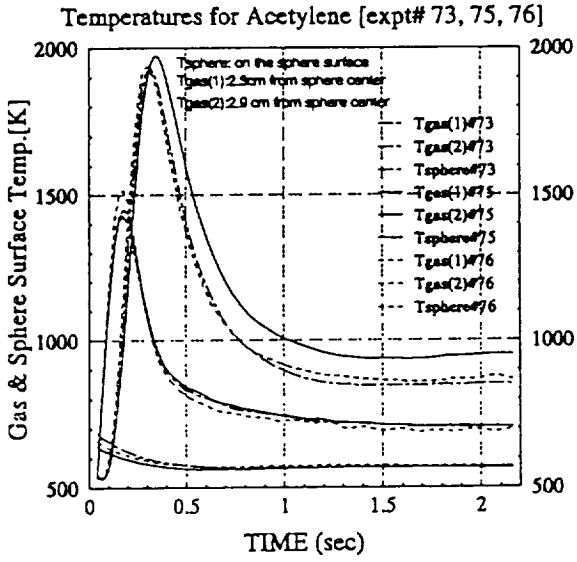

Figure 4

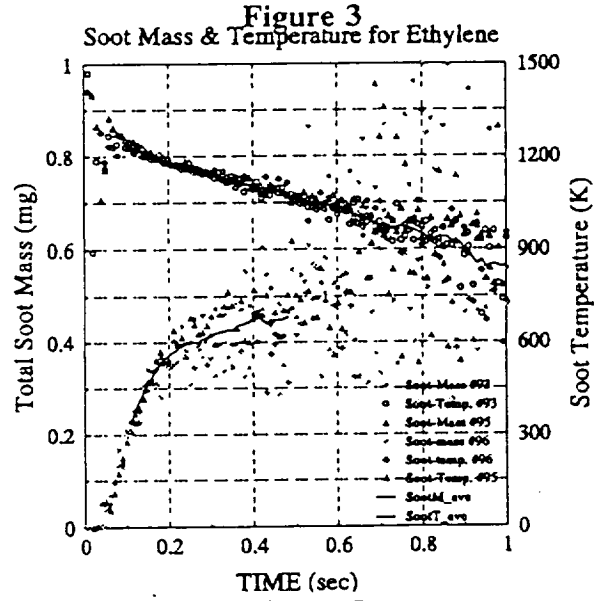

Figure 5

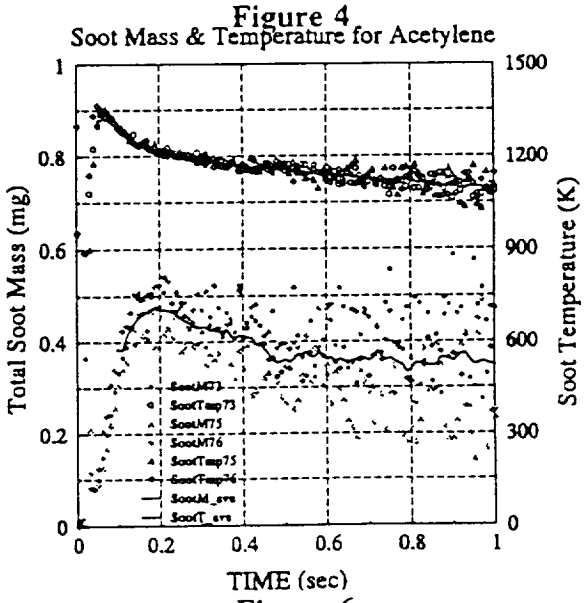

Figure 6

APPENDIX E

Effect of Radiative Heat Loss on Diffusion Flames in Quiescent Microgravity Atmosphere

Combustion and Flame paper

By

Atreya, A. and Agrawal, S.

1994

EFFECT OF RADIATIVE HEAT LOSS ON DIFFUSION FLAMES IN QUIESCENT MICROGRAVITY ATMOSPHERE

ARVIND ATREYA AND SANJAY AGRAWAL

Combustion and Heat Transfer Laboratory
Department of Mechanical Engineering and Applied Mechanics
The University of Michigan, Ann Arbor, MI 48109 USA

In this paper we present the results of a theoretical calculation for radiation-induced extinction of a one-dimensional unsteady diffusion flame in a quiescent microgravity environment. The model formulation includes both gas and soot radiation. Soot volume fraction is not a priori assumed, instead it is produced and oxidized according to temperature and species dependent formation and oxidation rates. Thus, soot volume fraction and the resulting flame radiation varies with space and time. Three cases are considered (i) a non-radiating flame, (ii) a scarcely sooty flame, and (iii) a very sooty flame. For a non-radiating flame, the maximum flame temperature remains constant and it does not extinguish. However, the reaction rate decreases as $t^{1/4}$ making the flame "weaker." For radiating flames, the flame temperature decreases due to radiative heat loss for both cases resulting in extinction. The decrease in the reaction rate for radiating flames is also much faster than $t^{1/4}$. Surprisingly, gas radiation has a larger effect on the flame temperature in this configuration. This is because combustion products accumulate in the high temperature reaction zone. This accumulation of combustion products also reduces the soot concentration via oxidation by OH radicals. At early times, before a significant increase in the concentration of combustion products, large amount of soot is formed and radiation from soot is also very large. However, this radiative heat loss does not cause a local depression in the temperature profile because it is offset by the heat release due to soot oxidation. These results are consistent with the experiments and provide considerable insight into radiative cooling of sooty flames. This work clearly shows that radiative-extinction of diffusion flames can occur in a quiescent microgravity environment.

NOMENCLATURE

a	*Planck mean absorption coefficient*
A	*Frequency Factor*
C_p	*Specific heat*
D	*Diffusion Coefficient*
E	*Activation Energy*
f_v	*Soot volume fraction*
k	*Thermal conductivity*
$\dot{m}_s'''$	*Soot surface growth rate*
$\dot{m}_o'''$	*Soot oxidation rate*
M	*Atomic weight*

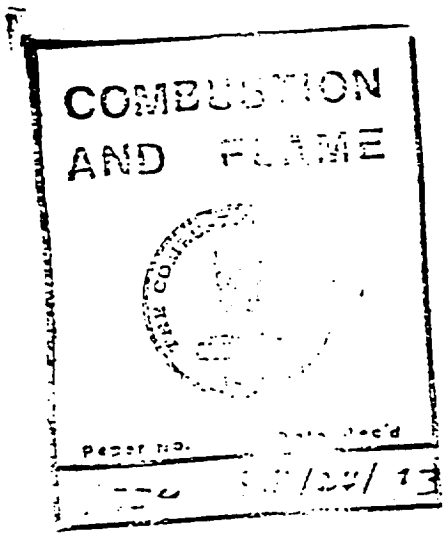

Q_r *Radiative heat flux*
Q *Heat of combustion per unit mass*
t *Time*
T *Temperature*
v *Velocity*
w *Reaction rate*
W *Molecular weight*
x *Distance*
Y *Mass fraction*
z *Density distorted coordinate*

Greek

α *Thermal diffusivity*
β *Schvab-Zeldovich variable*
ν *Mass based stoichiometric coefficient; number of moles*
ϕ *Soot mass fraction*
ρ *Density*
ξ *Variable defined in Eq. (7)*

Subscripts

F *Fuel*
g *Gas*
o *Oxygen*
P *Products (H_2O, CO_2)*
s *Soot*
∞ *Free stream*

INTRODUCTION

The absence of buoyancy-induced flows in a microgravity environment and the resulting increase in the reactant residence time significantly alters the fundamentals of many combustion processes. Substantial differences between normal gravity and microgravity flames have been reported during droplet combustion[1], flame spread over solids [2], candle flames [3] and others. These differences are more basic than just in the visible flame shape. Longer residence time and higher concentration of combustion products create a thermochemical environment which changes the flame chemistry. Processes such as soot formation and oxidation and ensuing flame radiation, which are often ignored under normal gravity, become very important and sometimes controlling. As an example, consider the droplet burning problem. The visible flame shape is spherical under microgravity versus a teardrop shape under normal gravity. Since most models of droplet combustion utilize spherical symmetry, excellent agreement with experiments is anticipated. However, microgravity experiments show that a soot shell is formed between the flame and the evaporating droplet of a sooty fuel [1]. This soot shell alters the heat and mass transfer between the droplet and its flame resulting in significant changes in the burning rate and the propensity for flame extinction. This change in the nature of the process seems to have occurred because of two reasons: (i) soot formed could not be swept out of the flame due to the absence of

buoyant flows, and (ii) soot formation was enhanced due to an increase in the residence time.

Recently, some very interesting observations of candle flames under various atmospheres in microgravity have been reported [3]. It was found that for the same atmosphere, the burning rate per unit wick surface area and the flame temperature were considerably reduced in microgravity as compared with normal gravity. Also, the flame (spherical in microgravity) was much thicker and further removed from the wick. It thus appears that the flame becomes "weaker" in microgravity due to the absence of buoyancy generated flow which serves to transport the oxidizer to the combustion zone and remove the hot combustion products from it. The buoyant flow, which may be characterized by the strain rate, assists the diffusion process to execute these essential functions for the survival of the flame. Thus, the diffusion flame is "weak" at very low strain rates and as the strain rate increases the flame is initially "strengthened" and eventually it may be "blown out." The computed flammability boundaries [4] show that such a reversal in material flammability occurs at strain rates around 5 sec^{-1}.

The above experimental observations suggest that flame radiation will substantially influence diffusion flames under microgravity conditions, particularly the conditions at extinction. This is because, flame radiation at very low or zero strain rates is enhanced due to: (i) high concentration of combustion products in the flame zone which increases the gas radiation, and (ii) low strain rates+ provide sufficient residence time for substantial amounts of soot to form which is usually responsible for most of the radiative heat loss. This radiative heat loss may extinguish the already "weak" diffusion flame. Thus, the objective of this work is to theoretically investigate the reason why the diffusion flame becomes "weak" under microgravity conditions and determine the effect of flame radiation on this "weak" diffusion flame. This will lead to radiation-induced extinction limits. This work is important for spacecraft fire safety.

THE MODEL PROBLEM

We note that the problem at hand is inherently transient with finite rate kinetics and flame (gas and soot) radiation. Thus, to study the effect of flame radiation on the reaction zone, we must focus on the simplest possible (planar) geometry. While no attempt is made to model the spherical flame geometry around a fuel droplet in microgravity, the work of Law [5] suggests that the present results are representative. This is to be expected because the reaction zone is usually thin compared with other characteristic dimensions of the flame, rendering the basic flame structure essentially independent of the flame shape. Thus, we consider a simple model problem consisting of an unsteady one-dimensional diffusion flame (*with flame radiation*) initiated at the interface of two quiescent half spaces of fuel and oxidizer at time t=0. Zero gravity, constant properties, one-step irreversible reaction and unity Lewis number are assumed. A novel feature of the formulation presented below is that soot volume fraction is not a priori specified to determine the ensuing flame radiation. Instead, soot is produced and oxidized according to the temperature and species concentration dependent formation and oxidation rates. Thus, the soot volume fraction and its location within the flame evolve as a function of space and time. The simplest possible (but realistic) soot formation and oxidation model obtained from counterflow diffusion flame experiments of Ref. 6 is used here to simplify the analysis. A large activation energy asymptotic analysis of this problem *without soot formation and flame radiation* may be found in Ref. 7. A schematic of the physical problem along with the imposed boundary

conditions is presented in Figure 1 and the corresponding equations are:

Continuity:

$$\frac{\partial \rho}{\partial t} + \frac{\partial (\rho v)}{\partial x} = 0 \qquad (1)$$

where ρ is the density, t the time and v the velocity normal to the fuel-oxidizer interface induced by volumetric expansion.

Species Conservation:

$$\rho \frac{\partial Y_F}{\partial t} + \rho v \frac{\partial Y_F}{\partial x} = \frac{\partial}{\partial x}\left(\rho D \frac{\partial Y_F}{\partial x}\right) - w_g - \left(\dot{m}_{g_p}''' - \dot{m}_{g_o}''' \right) \qquad (2)$$

$$\rho \frac{\partial Y_O}{\partial t} + \rho v \frac{\partial Y_O}{\partial x} = \frac{\partial}{\partial x}\left(\rho D \frac{\partial Y_O}{\partial x}\right) - \nu w_g \qquad (3)$$

$$\rho \frac{\partial Y_P}{\partial t} + \rho v \frac{\partial Y_P}{\partial x} = \frac{\partial}{\partial x}\left(\rho D \frac{\partial Y_P}{\partial x}\right) + (1+\nu) w_g \qquad (4)$$

Symbols used in the above equations are defined in the nomenclature. The reaction rate, w_g, is modelled by a second order Arrhenius expression. Preexponential factor and the activation energy are chosen for methane undergoing a one-step irreversible reaction $F + \nu O \rightarrow (1+\nu) P$; where ν is the mass-based stoichiometric coefficient. Fuel depleted as a result of soot formation, though usually small, is also included in the model via the term $(\dot{m}_{s_p}''' - \dot{m}_{s_o}''')$, which is zero when negative.

Energy Conservation:

$$\rho \frac{\partial C_p T}{\partial t} + \rho v \frac{\partial C_p T}{\partial x} = \frac{\partial}{\partial x}\left(k \frac{\partial C_p T}{\partial x}\right) + Q_g w_g + Q_s \left(\dot{m}_{s_o}''' - \dot{m}_{s_p}''' \right) - \nabla \cdot Q_r \qquad (5)$$

In this equation, the source terms include heat released by the primary reaction and soot oxidation and heat lost via flame radiation. The soot oxidation term is clearly zero when negative. Emission approximation is used to describe the radiative heat flux from the flame. Thus, $\nabla \cdot Q_r = 4\sigma T^4 (a_{pg} + a_{ps})$ where, a_{pg} and a_{ps} are Planck mean absorption coefficients for combustion products (CO_2, H_2O) and soot respectively. Planck mean absorption coefficients for

combustion products were obtained from Ref. 8 and for soot we have used $a_{ps} = 11.86\, f_v T\ cm^{-1}$ obtained from Ref. 9.

Soot Conservation:

$$\rho \frac{\partial \phi}{\partial t} + \rho v \frac{\partial \phi}{\partial x} = (\dot{m}_{s_p}''' - \dot{m}_{s_o}''') \quad , \qquad where, \quad \phi = \frac{f_v \rho_s}{\rho} \tag{6}$$

Here, both production and oxidative destruction of soot are considered, but the thermophoretic soot diffusion is ignored for simplicity. Note that the thermophoretic soot diffusion coefficient is substantially smaller than the corresponding gas diffusion coefficients. While ignoring soot diffusion will introduce an error in the location of the soot zone relative to the peak flame temperature, this error is expected to be small and of the same order of magnitude as that introduced by assuming unit Lewis number, constant properties, equal diffusion coefficients for all gases and one step chemical reactions. Thus, this assumption is made to enable simplifications such as : $\rho^2 D = const.$ A simplified equation for the net soot production rate (production - oxidation) is taken from Refs. 6 & 10. Also, average number density is used to avoid including the soot nucleation rate equation. The net mass production rate of soot per unit volume is thus described by:

$$\dot{m}_{s_p}''' - \dot{m}_{s_o}''' = A_p f_v^{2/3} \left(\xi_F - \frac{3}{8}\xi_O\right) \exp\left(-E_s/RT\right) ; \qquad where\ \xi_j \equiv \sum_{i=1}^{n} \left[\frac{M_j \nu_i^j}{W_i}\right] Y_i \tag{7}$$

In this equation, the combined atomic mass fraction of carbon and hydrogen is taken to represent the hydrocarbon fuel according to $\xi_F = \xi_C + \xi_H$, where the subscripts F, C & H denote fuel, carbon and hydrogen respectively. Finally, the boundary conditions, as depicted in Figure 1, are: $Y_o = Y_{o_\infty}$, $T = T_\infty$, $Y_F = 0$ *at* $t=0$, $x > 0$ *&* *at* $t > 0$, $x \to \infty$ and $Y_F = Y_{F_\infty}$, $Y_o = 0$, $T = T_-$ *at* $t = 0$, $x < 0$ *&* *at* $t > 0$, $x \to -\infty$.

The incompressible form of the above equations is obtained by using Howarth transformation $z = \int_0^x \frac{\rho(x', t)}{\rho_-} dx'$, where x = 0 defines the location of the material surface that coincides at t = 0 with the original fuel-oxidizer interface. As a result of this choice, v = 0 at x = 0. Assuming $\rho^2 D = \rho_-^2 D_-$ and defining the reaction rate as $w_g = A_g \rho^2 Y_F Y_O \exp(-E_g/RT)$, we obtain:

$$\frac{\partial Y_F}{\partial t} = D_- \frac{\partial^2 Y_F}{\partial z^2} - \frac{w_g}{\rho} - \frac{A_p}{\rho} f_v^{2/3} \left(\xi_F - \frac{3}{8}\xi_O\right) \exp\left(-E_s/RT\right) \tag{8}$$

$$\frac{\partial Y_O}{\partial t} = D_\infty \frac{\partial^2 Y_O}{\partial z^2} - \nu \rho A_g Y_F Y_O \exp(-E_g/RT) \tag{9}$$

$$\frac{\partial Y_F}{\partial t} = D_\infty \frac{\partial^2 Y_F}{\partial z^2} + (1+\nu) \rho A_g Y_F Y_O \exp(-E_g/RT) \tag{10}$$

$$\frac{\partial T}{\partial t} = D_\infty \frac{\partial^2 T}{\partial z^2} + \frac{Q_g W_g}{\rho C_p} + \frac{Q_s}{C_p}\left(\frac{\partial \phi}{\partial t}\right) - \frac{4\sigma T^4 a_{ps}}{\rho C_p} - \frac{4\sigma T^4 a_{pg}}{\rho C_p} \tag{11}$$

$$\text{where;} \quad \frac{\partial \phi}{\partial t} = \frac{A_p}{\rho} f_v^{2/3} \left(\xi_F - \frac{3}{8}\xi_O\right) \exp(-E_s/RT) \tag{12}$$

SOLUTION

Analytical Solution

For infinitely fast gas-phase reactions and no flame radiation, a simple, well known, analytical solution is obtained.

$$\eta = \frac{\beta - \beta_{-\infty}}{\beta_\infty - \beta_{-\infty}} = \frac{1}{2} erfc\left(\frac{z}{2\sqrt{D_\infty t}}\right) \tag{13}$$

Here, $\beta = Y_F - Y_O/\nu$ and $\beta = Y_F + C_p T/Q_g$ are the Schvab-Zeldovich variables. The flame lies at the location $\eta_{fl} = 1/(1+\nu Y_{F\infty}/Y_{O\infty})$. Thus, for unity equivalence ratio (E=1) based on free stream concentrations, the flame lies at $z = 0$. For non-unity equivalence ratios [fuel rich (E>1) or fuel lean (E<1) conditions] the flame will travel as $\sqrt{t}$ in either direction. This is evident from Equ. (13) by simply substituting $\eta = \eta_{fl}$. The three possible cases are plotted in Fig. 2 for methane. The constants used are [11]: for $Q_g = 47465$ J/gm of fuel $C_p = 1.3$ J/gmK, $T_\infty = 295$ K, $\nu = 4$., $\rho_\infty = 1.16 \times 10^{-3}$ gm/cm^3, and $D_\infty = 0.226$ cm^2/sec. The flame conditions are: (a) $Y_{O\infty} = 0.5$, $Y_{F\infty} = 0.125$. (b) $Y_{O\infty} = 0.5$, $Y_{F\infty} = 0.0625$. (c) $Y_{O\infty} = 0.25$, $Y_{F\infty} = 0.125$. For case (b) the flame travels towards the fuel side because of excess oxygen (Fig. 2b). Similarly, for case (c) it travels towards the oxygen side because of excess fuel (Fig. 2c). However, for case (a) the equivalence ratio is unity and hence the flame is stationary. It simply becomes thicker with time (Fig. 2a).

Numerical Solution

The above equations were numerically integrated by using a finite difference Crank-

Nickolson method where previous time step values were used to evaluate the nonlinear reaction terms. Care was taken to start the diffusion flame with minimum disturbance. Ideally, the problem must be started such that the two half spaces of fuel and oxidizer, as illustrated in Fig. 1, begin a self-sustaining reaction at t=0. This ignition of the reactants may be spontaneous or induced by a pilot. For high activation energy, spontaneous ignition will take a long time during which the reactants will diffuse into one other developing a thick premixed zone which will burn prior to establishing a diffusion flame. This will change the character of the proposed problem. Thus, ignition was forced (piloted) by artificially making the fuel-oxidizer interface temperature as the adiabatic flame temperature. Only Eqs. (8-10) were solved during this period. Ignition was assumed when the reaction rate at the interfacial node becomes maximum (i.e. $d\dot{w}_g/dt = 0$). After this instant, the interfacial node was not artificially maintained at the adiabatic flame temperature because the combustion process becomes self-sustaining and all the equations described above are used. For the calculations presented below, the time taken to ignite was 4×10^{-4} sec. A uniform grid with grid size $\Delta z=3\times10^{-3}$ cm and a time-step of $\Delta t=1\times10^{-4}$ sec was used. Typical calculation for 0.4 seconds physical time took 5 hours on a Sun Sparkstation.

To limit the computational domain which extends from $+\infty$ to $-\infty$, the analytical solution presented above was used to compute the temperature at the desired final time (0.4 sec in the present case). The location from the origin where the temperature first becomes equal to ambient (within machine error) was used to apply boundary conditions at infinity in the numerical calculations. This was further confirmed by checking the space derivatives ($\partial T/\partial x$) at these boundaries during the calculations. Since initial soot volume fraction is zero, the governing equation (Eq. 12) will produce a trivial solution if explicit or implicit finite difference methods are used. Thus, for first step, an implicit integral method was used to obtain the soot volume fraction. At the end of the first time step the soot volume fraction is of the order 10^{-80}. It is important to note that Eq. (12) can self-initiate soot formation despite the absence of a soot nucleation model.

For the calculations presented below, we have used the following data: for gas reactions [11]: $\rho A_g=3.56\times10^9$ sec^{-1}, $\mathcal{E}_g=122$ KJ/mole. For soot reactions we have used[6,10] $A_p=10^4$ gm/cm^{3}sec for Case 1 and 10^7 gm/cm^{3}sec for Case 2, $\mathcal{E}_s=150$ KJ/mole, $\rho_s=1.86$ gm/cm^3. We assume that soot oxidizes to CO releasing heat $Q_s=9$ KJ/gm of soot.

RESULTS AND DISCUSSION

Results of calculations for three cases are presented here. These are labeled as Cases 0,1&2 in Figure 3. Case 0 is the base case with finite reaction rates but without soot formation and flame radiation. Case 1 represents a barely sooting flame and Case 2 represents a highly sooting flame. As noted above, A_p for Case 2 is increased ten times over Case 1. Based on our previous work (Refs.6&10), A_p for most hydrocarbon fuels is expected to fall between Cases 1&2.

Let us first consider the overall results. Figure 3 shows that in the absence of external flow (i.e., zero strain rate) and without soot formation and flame radiation (Case 0), the peak flame temperature becomes constant while the reaction rate decreases as $t^{-1/2}$ and the reaction zone

thickness increases [note: in Fig.3 the ordinate has been multiplied by $t^{1/2}$]. Since the maximum flame temperature remains constant, extinction does not occur. However, for Cases 1 & 2, the peak flame temperature decreases with time faster than $t^{1/2}$ and eventually extinction (as identified by some pre-defined temperature limit) will occur. This *(radiation-induced extinction)* is also evident from Figure 4 where the temperature profiles at different times are plotted for Cases 1 & 2. Clearly, the flame temperature decreases due to flame radiation and the flame thickness increases because of diffusion.

The net amount of soot formed as a function of space and time is shown in Figure 5. The soot volume fraction for Case 1 is two orders of magnitude smaller than for Case 2. Physically, Case 1 represents a barely sooting blue flame and Case 2 represents a fairly sooty blue-yellow-orange flame. However, despite the differences in the magnitude of the soot volume fraction for the two cases, it first increases and later decreases with time and its spatial distribution shifts toward the fuel side for both cases. This decrease in the soot volume fraction occurs because of two reasons: (i) A reduction in the flame temperature due to radiation reduces the soot formation rate, and (ii) A buildup in the concentration of CO_2 and H_2O near the high-temperature reaction zone, increases the OH radical concentration which reduces the formation of soot precursors and assists in soot oxidation (see Refs.6 & 10). This increased OH radical concentration is also responsible for shifting the soot profile toward the fuel side.

The effect of soot formation on flame radiation is shown in Figure 6. Here, radiation from both combustion products and soot is plotted as a function of space and time. As expected, soot radiation for Case 2 is substantially larger than for Case 1 while the gas radiation is approximately the same [Note: the scales of the two figures are different]. This soot radiation decreases with time because both the soot volume fraction and the flame temperature decrease. The effect of soot radiation is to reduce the peak flame temperature by about 100K (see Fig.3) with the difference diminishing with increasing time. Surprisingly, as seen in Fig. 3, the effect of gas radiation on the peak flame temperature is much larger and increases with time, becoming 1000K at 0.4 sec. This is because at zero strain rates the combustion products accumulate in the high temperature reaction zone. As noted above, these combustion products are also responsible for the reduction in the soot volume fraction.

Another interesting observation is that despite the large asymmetry introduced by soot radiation at initial times (Fig. 6), Figure 4 shows that the temperature profiles are essentially symmetrical. This implies that the heat lost via soot radiation [5th term of Eq. (11)] approximately equals the heat produced via soot oxidation [4th term of Eq. (11)]. Since both occur at the same location, a discernible local depression in the temperature profile is not observed. This fact is experimentally substantiated by our low strain rate counterflow diffusion flame experiments. Figure 7 shows the measured soot volume fraction and flame temperature. The fuel and oxidizer concentrations and the strain rate for this flames are 22.9%, 32.6% and 8 sec^{-1} respectively. Absence of local temperature depression is also consistent with the observation that radiation from a soot particle at these high temperatures will quickly quench the particle unless its temperature is maintained via some local heat release. In the present case, this heat release is due to soot oxidation. Thus, a portion of the fuel that is converted into soot oxidizes at a location different from the main reaction zone and nearly all the heat released during this process is radiated away. The remaining fuel is oxidized at the main reaction zone

resulting in a lower heat release and hence a reduced peak flame temperature. This is the justification for including the last term in Eq.-(8) and the 4th term in Eq.-(11). These terms account for fuel consumption and heat released due to net soot formation (or oxidation) and provide valuable new insight into the mechanism of radiative cooling of sooty flames.

The above conclusion is also clear from Figure 8 which shows the spatial distribution of soot and temperature for Cases 1 & 2 at 0.2 seconds after ignition. Note that while the peak temperature is about 75K lower for Case 2, the profile is nearly symmetrical about the origin for both cases despite the sharp & narrow soot peaks on the fuel side. Also note that the magnitude of the soot peak (soot peak for Case 2 is about two orders of magnitude larger than for Case 1) had a negligible effect on the symmetry of the temperature profile. Figure 8 is also qualitatively very similar to our low strain rate counterflow diffusion flame experimental measurements as shown in Fig. 7. The conclusions of this paper will not be altered with the inclusion of thermophoretic soot diffusion. As the soot moves away from the high temperature reaction zone toward the cooler regions of the flame, its contribution to flame radiation drops relative to gaseous radiation. Thus, the importance of gaseous radiation increases. However, thermophoresis may result in the formation of a soot-plane similar to the soot-shell observed in spherical geometry. This will indeed be quite interesting to observe.

Finally, we note that emission approximation was used in the flame radiation formulation. Since the reaction zone thickness is of the order of a few centimeters, self-absorption of radiation may become important and in some cases it may alter the extinction limit.

CONCLUSIONS

This paper presents the results of a theoretical calculation for radiation-induced extinction of a one-dimensional unsteady diffusion flame in a quiescent microgravity environment. The model formulation includes both gas and soot radiation. Soot volume fraction is not a priori assumed, instead it is produced and oxidized according to temperature and species dependent formation and oxidation rates. Thus, soot volume fraction and the resulting flame radiation varies with space and time. Three cases are considered (i) a non-radiating flame, (ii) a scarcely sooty flame, and (iii) a very sooty flame. For a non-radiating flame, the maximum flame temperature remains constant and it does not extinguish. However, the reaction rate decreases as $t^{-1/2}$ making the flame "weaker." For radiating flames, the flame temperature decreases due to radiative heat loss for both cases resulting in extinction. The decrease in the reaction rate for radiating flames is also much faster than $t^{-1/2}$. Surprisingly, gas radiation has a larger effect on the flame temperature in this configuration. This is because the combustion products accumulate in the high temperature reaction zone. This accumulation of combustion products also reduces the soot concentration via oxidation by OH radicals. At early times, before a significant increase in the concentration of combustion products, large amount of soot is formed and radiation from soot is also very large. However, this radiative heat loss does not cause a local depression in the temperature profile because it is offset by the heat release due to soot oxidation. These results are consistent with the experiments and provide considerable insight into radiative cooling of sooty flames. This model, while approximate with several assumptions, clearly shows that radiative-extinction of diffusion flames can occur in a microgravity environment. In the present model self-absorption of the radiation is also neglected. In some cases this may alter the

extinction limits because of the development of a thick reaction zone.

ACKNOWLEDGEMENTS

Financial support for this work was provided by NASA under the contract number NAG3-1460, NSF under the contract number CBT-8552654, and GRI under the contract number GRI-5087-260-1481. We are also indebted to Dr. Kurt Sacksteder of NASA Lewis and Dr. Jim Kezerle of GRI for their help. Mr. Anjan Ray helped in conducting the experiments.

REFERENCES

1. Jackson, G., S., Avedisian, C., T. and Yang, J., C., *Int. J. Heat Mass Transfer.*, 35(8):2017-2033 (1992).
2. Ferkul, P., V., A Model of Concurrent Flow Flame Spread Over a Thin Solid Fuel, NASA Contractor Report 191111, 1993.
3. Ross, H. D., Sotos, R. G. and T'ien, J. S., *Comb. Sci. Tech.*, 75:155-160 (1991)
4. T'ien, J. S., *Combust. Flame*, 80:355-357 (1990).
5. Law, C.K., *Combust. Flame*, 24:89-98 (1975).
6. Zhang, C., Atreya, A. and Lee, K., *Twenty-Fourth (International) Symposium on Combustion*, The Combustion Institute, 1992, pp. 1049-1057.
7. Linan, A. and Crespo, A., *Comb. Sci. Tech.*, 14:95-117 (1976).
8. Abu-Romia, M. M and Tien, C. L., *J. Heat Transfer*, 11:32-327 (1967).
9. Seigel, R. and Howell, J. R., Thermal Radiation Heat Transfer, Hemisphere Publishing Corporation, 1991.
10. Atreya, A. and Zhang, C., "A Global Model of Soot Formation derived from Experiments on Methane Counterflow Diffusion Flames," in preparation for submission to *Combustion and Flame*.
11. Tzeng, L. S., Theoretical Investigation of Piloted Ignition of Wood, PhD Thesis, Dept. Mech. Engg., Michigan State University, East Lansing, MI, USA, 1990.

FIGURE CAPTIONS

Figure 1: Schematic of the Model Problem

Figure 2: Analytical solution. Temperature distribution as a function of distance for various equivalence ratios. (a) Equivalence ratio (E) is unity (b) E < 1 (c) E > 1.

Figure 3: Maximum reaction rate and temperature as a function of time. Note that reaction rate is multiplied with $t^{1/2}$.

Figure 4: Numerical solution. Temperature distribution as a function of distance at various instants. (a) Case 1, less sooty flame, (b) Case 2, very sooty flame.

Figure 5: Soot volume fraction as a function of distance at various instants. (a) Case 1, less sooty flame, (b) Case 2, very sooty flame.

Figure 6: Radiative Heat Loss as a function of distance at various instants. (a) Case 1, less sooty flame, (b) Case 2, very sooty flame.

Figure 7: Soot volume fraction and Temperature distribution at t = 0.2 seconds. (a) Case 1, less sooty flame, (b) Case 2, very sooty flame.

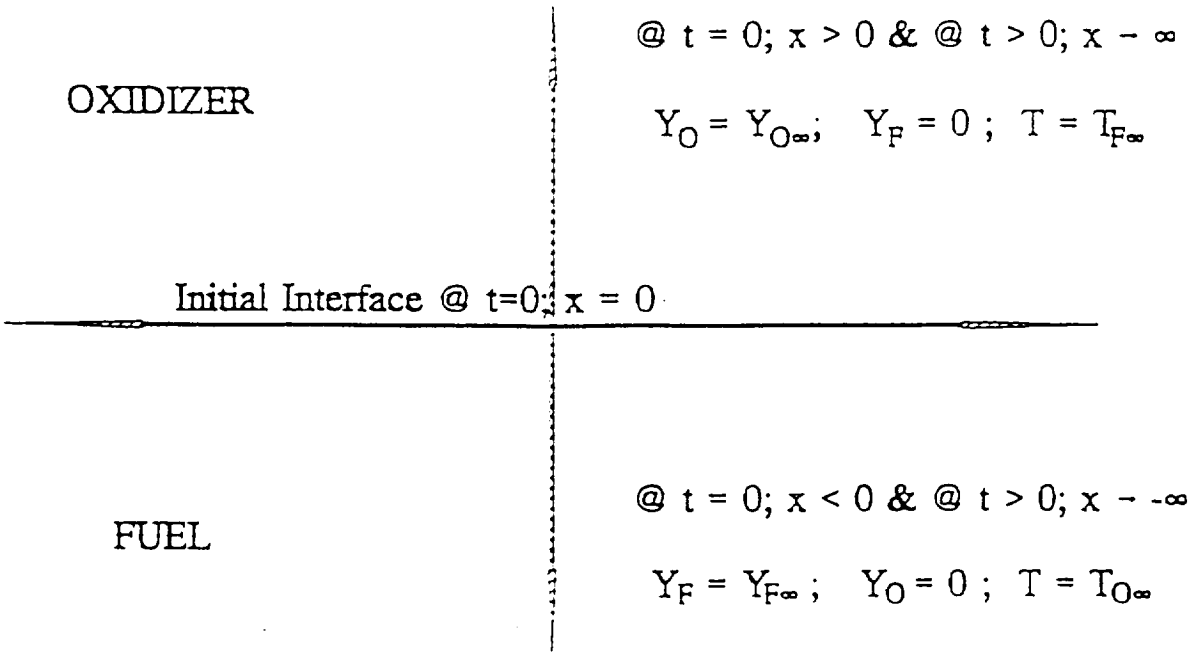

Figure 1 : Schematic of the Model Problem

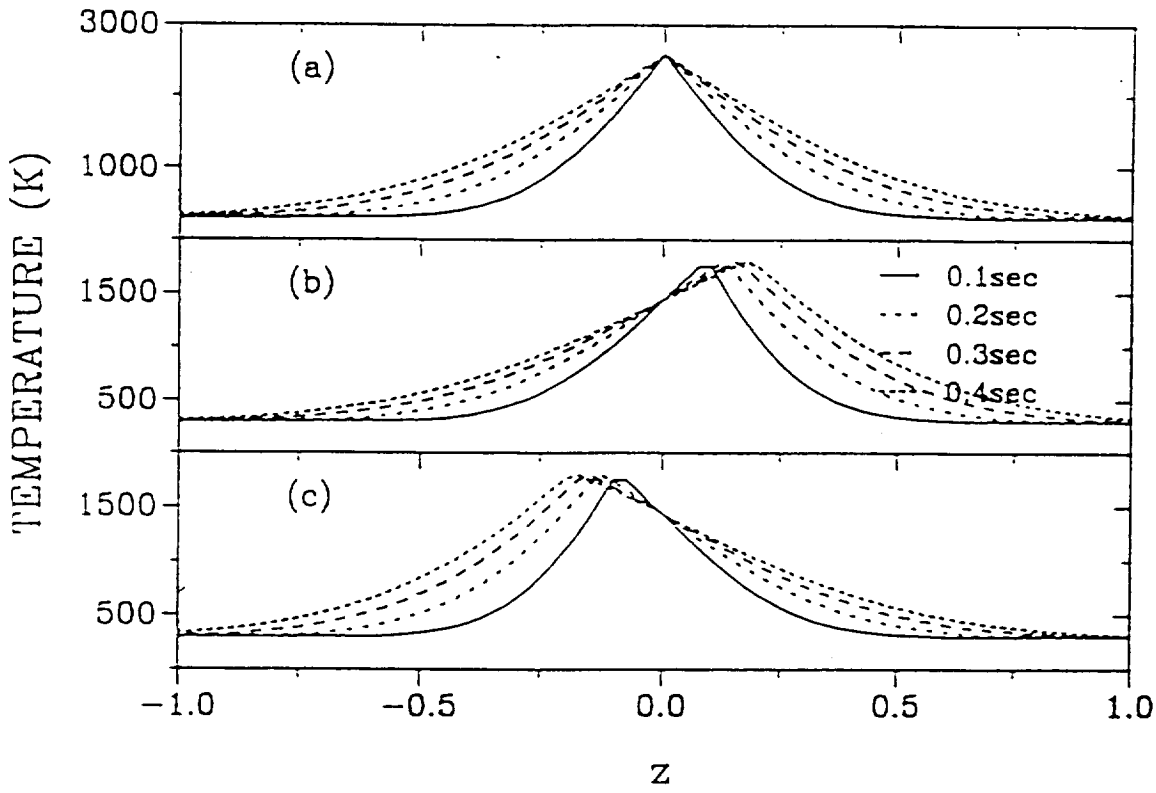

Figure 2: Analytical solution. Temperature distribution as a function of distance for various equivalence ratios. (a) Equivalence ratio (E) is unity (b) E < 1 (c) E > 1

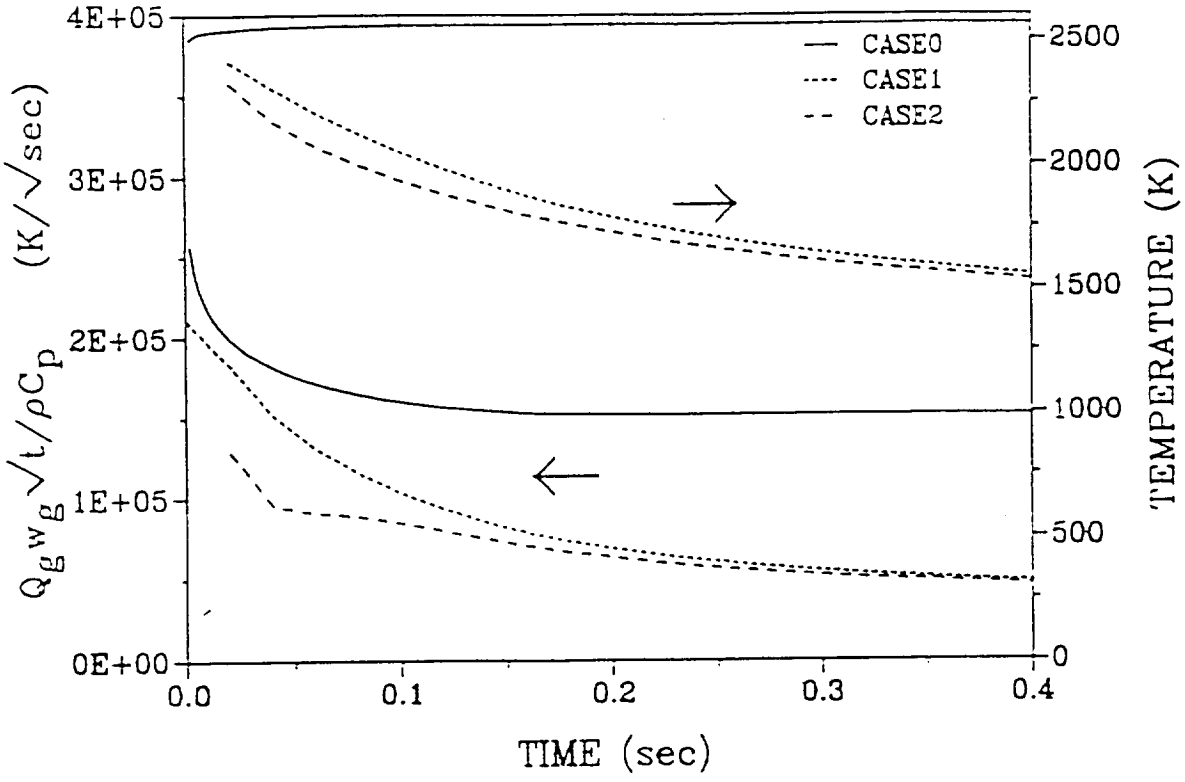

Figure 3: Maximum reaction rate and temperature as a function of time. Note that reaction rate is multiplied with $t^{1/2}$

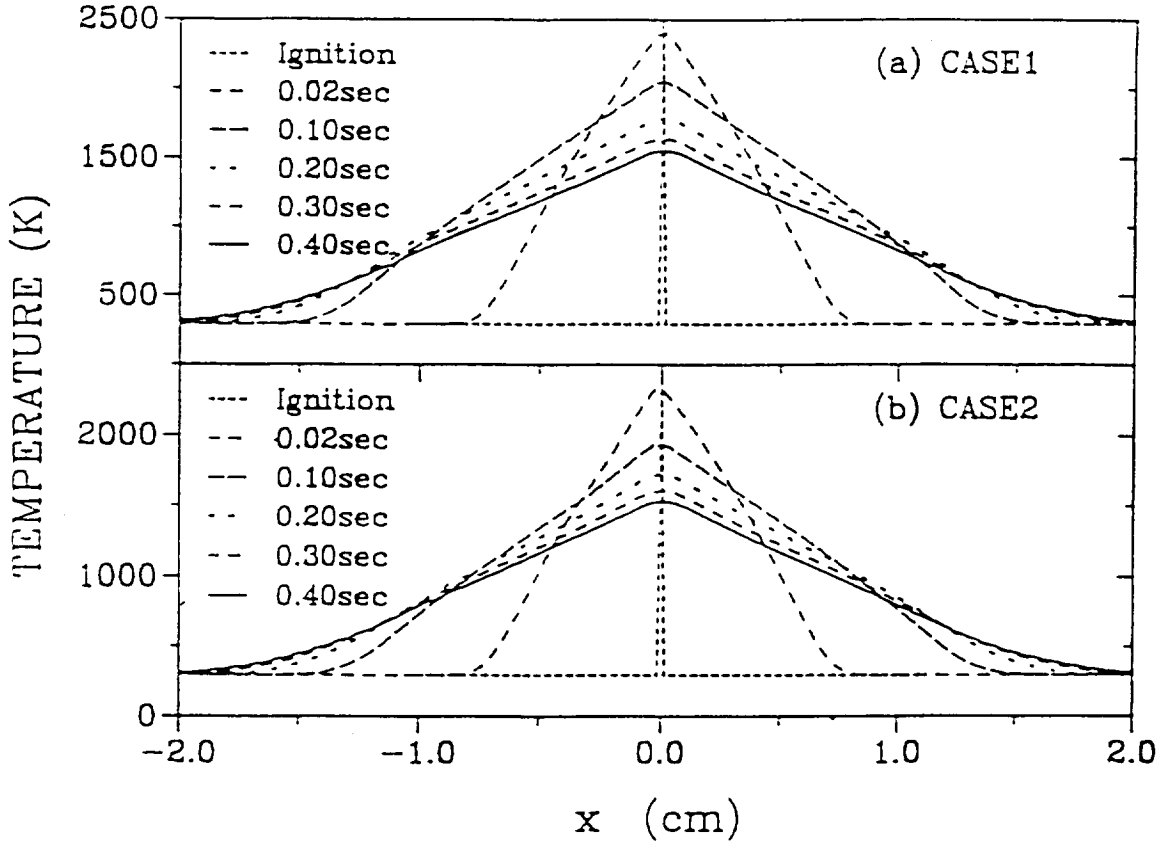

Figure 4: Numerical solution. Temperature distribution as a function of distance at various instants. (a) Case 1, less sooty flame, (b) Case 2, very sooty flame

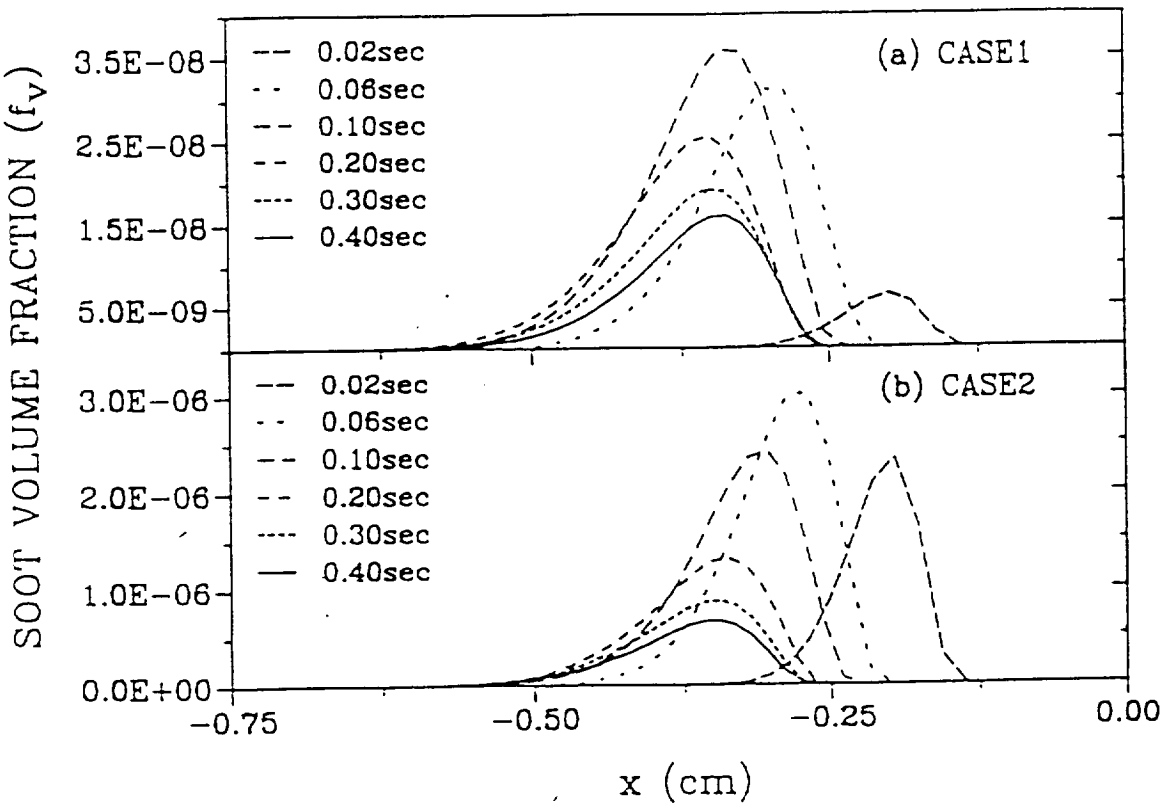

Figure 5: Soot volume fraction as a function of distance at various instants. (a) Case 1, less sooty flame, (b) Case 2, very sooty flame

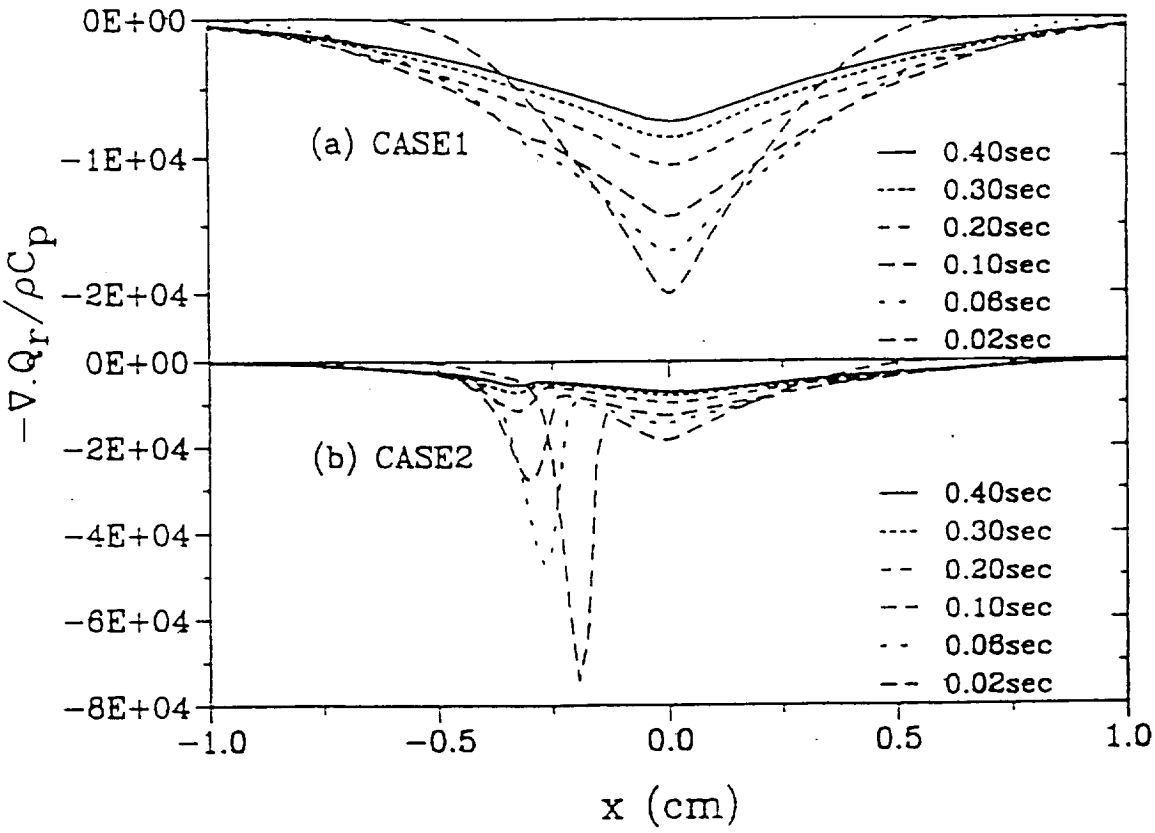

Figure o: Radiative heat loss as a function of distance at various instants. (a) Case 1, less sooty flame, (b) Case 2, very sooty flame

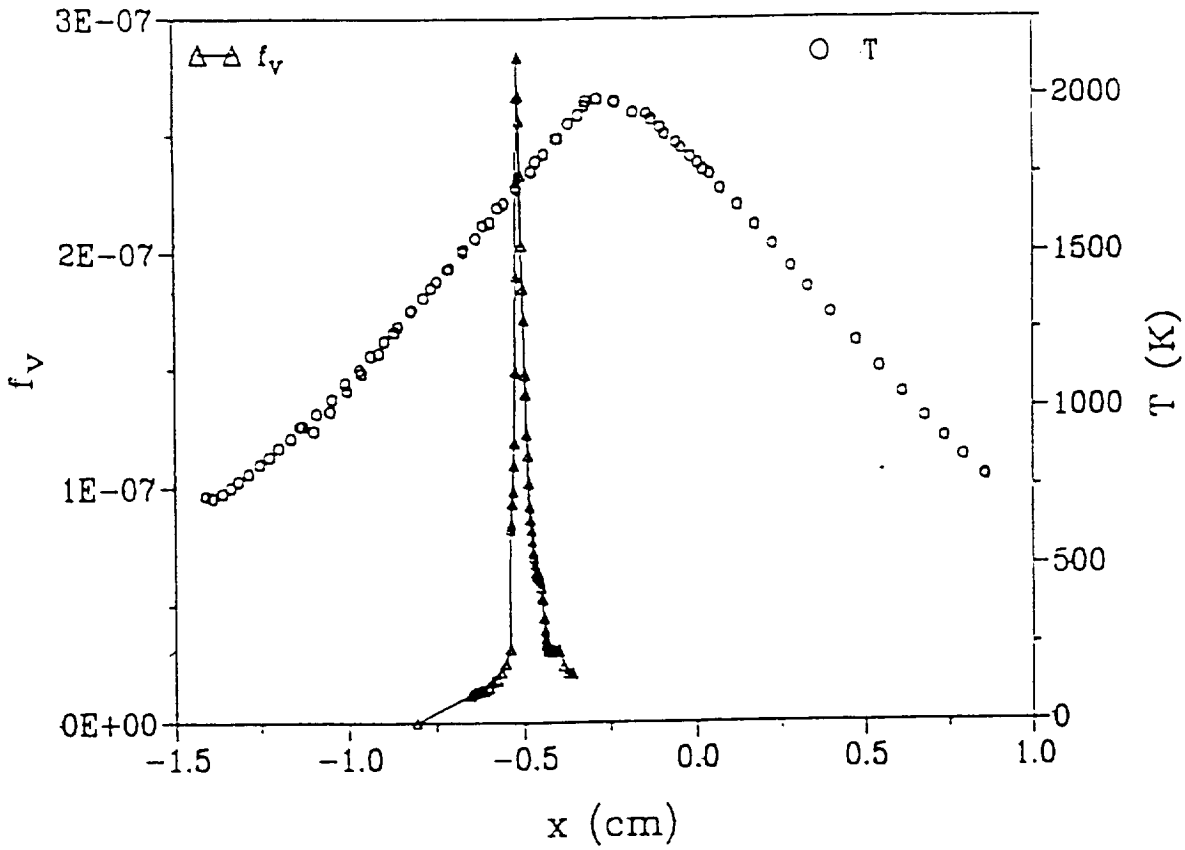

Figure 7: Soot volume fraction and temperature distribution (experimental results)

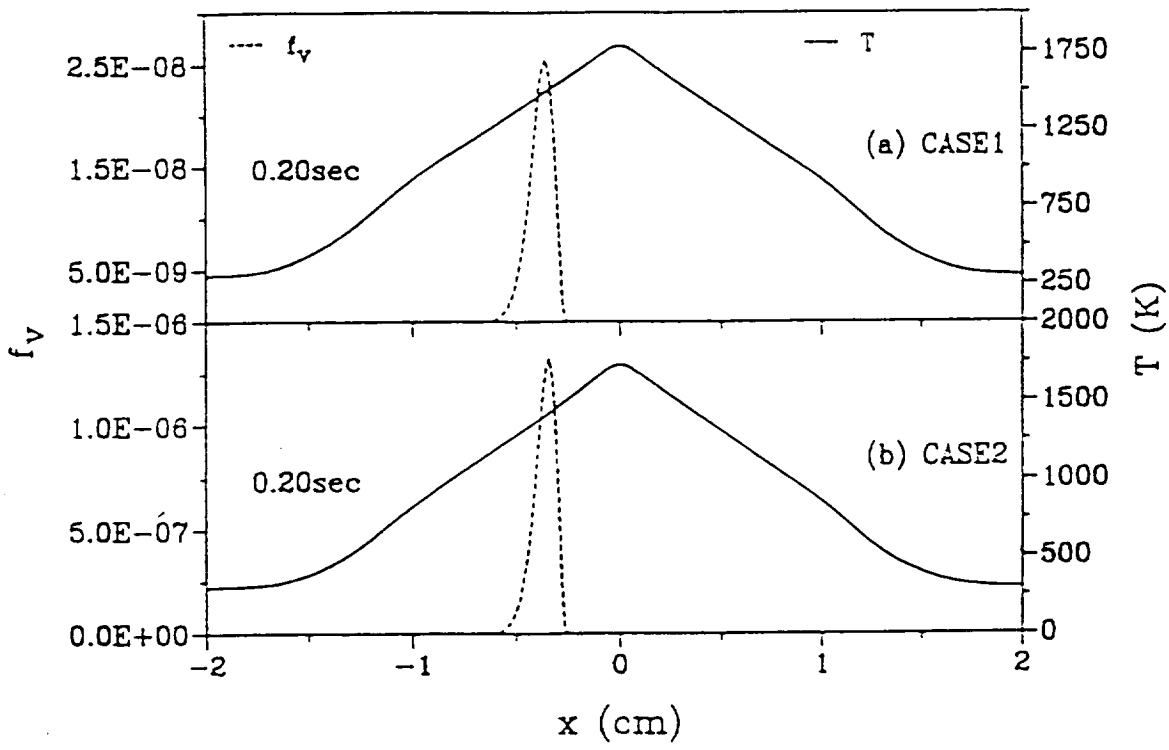

Figure 8: Soot volume fraction and temperature distribution at t= 0.2 seconds. (a) Case 1, less sooty flame, (b) Case 2, very sooty flame

APPENDIX F

A Study of the Effects of Radiation on Transient Extinction of Strained Diffusion Flames

Joint Technical Meeting of Combustion Institute paper, 1995

By

Shamim, T. and Atreya, A.

Central & Western States/Mexican National Combustion Institute Meeting, May 1995

A Study of the Effects of Radiation on Transient Extinction of Strained Diffusion Flames

TARIQ SHAMIM AND ARVIND ATREYA

Combustion and Heat Transfer Laboratory
Department of Mechanical Engineering and Applied Mechanics
The University of Michigan, Ann Arbor, MI 48109-2125

Numerical simulations of transient counterflow diffusion flames were conducted to quantify the low-strain-rate radiation-affected diffusion flame extinction limits. Such limits are important for spacecraft fire safety. The radiative effects from combustion products (CO_2 and H_2O) were considered in the formulation. Employing the Numerical Method of Lines, the governing equations were spatially discretized by using a 4th order central difference formula and temporally integrated by using an implicit backward differentiation formula (BDF). Results show a significant reduction in the flame temperature due to radiation. For flames subjected to small strain rates, this reduction in temperature was found to be sufficient to cause extinction. For methane flame, the extinction occurs for strain rates less than 1 s^{-1}, and the extinguishment time (disappearance of flame chemiluminescence ≈ 1550 K) for most of these strain rates was found to be less than 1 second. A flammability map was plotted to show the maximum flame temperature as a function of the strain rate and the time of radiation induced extinction. Results were compared with an earlier study at zero strain rate and were found to be in excellent agreement.

NOMENCLATURE

a_p	Planck mean absorption coefficient
A	Pre-exponential factor
c_p	constant pressure specific heat of the mixture
D_i	coefficient of diffusivity of species i
h	enthalpy
$h°_{f,i}$	enthalpy of formation of species i
MW	average molecular weight
Le	Lewis number
p	pressure
Q_R	radiant heat loss
Q_{HV}	heat of reaction
R	universal gas constant
T	temperature
t	time
v	axial velocity
Y_i	mass fraction of species i
ε	strain rate
η	similarity transformation variable
λ	thermal conductivity of the mixture
μ	dynamic viscosity of the mixture
ν	mass based stoichiometric ratio

ρ mass density
σ Stefan-Boltzman constant
ψ similarity transformation variable
ω_i mass rate of production of species i

INTRODUCTION

This study was motivated by a need to quantify the low-strain-rate radiation-affected flammability limits. Flammability limits are of practical interest specially in connection with fire safety because mixtures outside the limits of flammability can be handled without concern of ignition. For this reason, extensive tabulations of limits of flammability as limits of composition or pressure have been prepared.[1] However, there are very few studies on radiation-affected flammability limits and diffusion flame extinction limits.

One reason for such a lack of literature is that measurements have indicated that radiant losses from the gas are relatively insignificant for small-scale lab experiments since under normal gravity conditions the excess particulates are simply ejected from the flame tip by the buoyant flow field. But radiant emission may have significant influence on conditions at extinction for larger scales because of the presence of a large number of soot particles and under microgravity conditions because of very low strain rates.

Bonne[2] was the first one who analyzed the problem of diffusion flame extinction with flame radiation. Using the results of a simulated experimental study, he showed that the radiative extinguishment occurs in a zero gravity environment. The existence of a radiative extinction limit at small strain rates was first numerically determined by T'ien[3]. He plotted a flammability map showing the extinction boundaries consisting of blowoff and radiation branches. However, he only considered the radiative heat losses from the fuel surface and neglected gas-phase radiation and absorption.

The radiative effects from soot, CO_2 and H_2O were considered by Kaplan et al.,[4] in their recent study to investigate the effects of radiation transport on the development, structure and dynamics of the flame. Recently, Atreya and Agrawal[5] numerically demonstrated the occurrence of radiative-extinction of a one-dimensional unsteady diffusion flame in a quiescent microgravity environment.

FORMULATION OF THE PHYSICAL PROBLEM

General Governing Equations

A schematic of a counterflow diffusion flame stabilized near the stagnation plane of two laminar flows is shown in Figure 1. In this figure, r and z denote the independent spatial coordinates in the tangential and the axial directions respectively. Using the assumptions of axisymmetric, unity Lewis number, negligible body forces, negligible viscous dissipation, and negligible Dufour effect, the resulting conservation equations of mass, momentum, energy and species may be simplified to the following form:

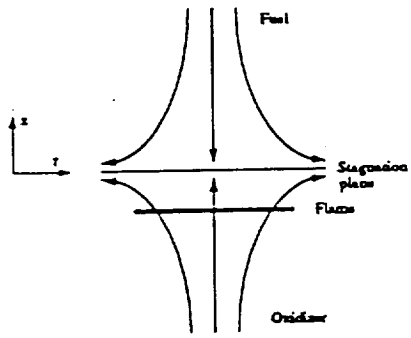

Figure 1 Schematic of counterflow diffusion flame

$$\frac{\partial \rho}{\partial t} + 2\,\rho\,\epsilon\,\psi + \frac{\partial(\rho\, v)}{\partial z} = 0$$

$$\left(\psi - \frac{\rho_\infty}{\rho}\right)\frac{d\epsilon}{dt} + \epsilon\,\frac{\partial \psi}{\partial t} + \left(\psi^2 - \frac{\rho_\infty}{\rho}\right)\epsilon^2 = -\epsilon\, v\,\frac{\partial \psi}{\partial z} - \frac{\epsilon}{\rho}\,\frac{\partial}{\partial z}\left(\mu\,\frac{\partial \psi}{\partial z}\right)$$

$$\rho\left(\frac{\partial h}{\partial t} + v\,\frac{\partial h}{\partial z}\right) = \frac{\partial}{\partial z}\left(\frac{\lambda}{c_p}\,\frac{\partial h}{\partial z}\right) - \sum_{i=1}^{N} \omega_i\,\Delta h_{f,i}^{\circ} - \nabla \cdot Q_R$$

$$\frac{\partial}{\partial t}(Y_i) + v\,\frac{\partial}{\partial z}(Y_i) = \frac{\omega_i}{\rho} + \frac{1}{\rho}\,\frac{\partial}{\partial z}\left(\rho\, D_i\,\frac{\partial Y_i}{\partial z}\right)$$

along with the equation of state:

$$\rho = \frac{p}{\bar{R}\,T}\,\frac{1}{\sum_{i=1}^{N}(Y_i/MW_i)}$$

The symbols used in the above equations are defined in the nomenclature. Note that in the present form the equations do not depend on the radial direction. In this study, the radiative heat flux is modelled by using the emission approximation, i.e., $Q_R = 4\,\sigma\,T^4\,(a_{p,CO_2} + a_{p,H_2O})$; where, σ is the Stefan-Boltzman constant, and a_{p,CO_2} and a_{p,H_2O} are Planck mean absorption coefficients for CO_2 and H_2O respectively. These absorption coefficients were taken from Ref. [6].

Reaction Scheme

The present problem was solved by considering a single step overall reaction which may be written as follows:

$$[F] + v\,[O_2] \longrightarrow (1+v)\,[P]$$

Here, v is the mass-based stoichiometric coefficient. Using second order Arrhenius kinetics, the reaction rate was defined as $\omega = A\,\rho^2\,Y_F\,Y_O\,\exp(-E_R/R\,T)$. The reaction rates for fuel, oxidizer, and product may then be written as $\omega_F = -\omega$; $\omega_O = -v\omega$; and $\omega_P = (1+v)\omega$. The values of the pre-exponential factor A, the activation energy E_R for a methane flame and the other properties were obtained from Ref. [5].

Initial and Boundary Conditions

A solution of these equations requires the specification of some initial and boundary conditions which are given as following:

Initial Conditions:

$\psi(z,0) = \psi_o(z)$

$h(z,0) = h_o(z)$ or $T(z,0) = T_o(z)$

$Y_i(z,0) = Y_{i,o}(z)$ [n conditions or (n-1) conditions + $\rho(z,0)$]

Here subscript 'o' represents the specified initial function.

Boundary Conditions:

The origin of our coordinate system was defined at the stagnation plane.

$\psi(\infty,t) = 1$ $\psi(-\infty,t) = (\rho_+/\rho_-)^{1/4}$

$h(\infty,t) = h_{up}$ $h(-\infty,t) = h_{low}$

[or $T(\infty,t) = T_{up}$ $T(-\infty,t) = T_{low}$]

$Y_i(\infty,t) = Y_{up}$ $Y_i(-\infty,t) = Y_{low}$

$v(0,t) = 0$

The strain rate ε, which is a parameter, must also be specified.

SOLUTION PROCEDURE

The governing equations form a set of nonlinear, coupled and highly stiff partial differential equations. A closed form solution of these equations is very difficult to obtain. Hence, in the present study, the equations were solved numerically. The numerical scheme used is called the *Numerical Method of Lines* (NMOL). In this method, the equations are first discretized by applying a standard finite difference scheme in the spatial direction which transforms PDEs into ODEs. The resulting ODEs in time are then solved by using a time integrator such as Runge Kutta, implicit Adams method, implicit backward differentiation formulas for stiff problems.

In the present study, a 4th order 5-point central difference formula was used to spatially discretize the equations and an implicit backward differentiation formula (BDF) was used to integrate in the temporal direction. In order to carry out the numerical integration, infinity was approximated by a finite length of the order of the length scale of the problem (i.e., $(D/\varepsilon)^{1/2}$). This was confirmed by checking the gradients of all the variables which must vanish at the boundaries.

RESULTS AND DISCUSSION

Figures 2-4 show the results for unity equivalence ratio with T_-=295K, Y_{F-}=0.125, Y_{O-}=0.5 and strain rate ε=0.5 s^{-1}. These results were obtained by dividing the computational domain into 1001 spatial nodes (i.e., the size of spatial node was 0.05 mm). All the profiles shown are at time t= 0.001, 0.01, 0.1, 0.5, and 0.7 second. For these results, constant c_p, equal diffusion coefficients for all gases and $\rho^2 D$=constant were used.

The temperature profiles show a decrease in the maximum flame temperature due to gas radiation. The effect of gas radiation was found to be sufficient to cause extinguishment (defined as disappearance of chemiluminescence =1550 K) in approximately 0.5 second. However, the effect of radiation was found to decrease with an increase in strain rate. Figure 5 shows the steady state temperature profiles for the cases with and without radiation effects for ε=10.0 s^{-1}. The results show that the gas radiation reduces the maximum flame temperature by 175 K without causing any extinguishment.

Figure 6 shows the time variations of maximum flame temperature for various values of strain rates. The plot shows that for flames with strain rates less than 1 s^{-1}, the effect of gas radiation is sufficient to cause extinction.

The results were compared with an earlier study[5] at zero strain rate. Figure 7 shows a comparison of temperature profiles at time t=0.31 s in density distorted coordinates. Both the results were found to be in very good agreement. A small difference at the peak temperature may be attributed to the fact that in Ref. [5], the variation of molecular weight in the calculation of density was not considered.

CONCLUSIONS

A computational model has been developed for an unsteady counterflow diffusion flame to quantify the

low-strain-rate radiation-affected diffusion flame extinction limits. The radiative effects from combustion products (CO_2 and H_2O) were considered in the formulation. A significant reduction in the flame temperature due to radiation was found to occur. This reduction in temperature increases with a decrease in strain rate and was found to be sufficient to cause extinction at low strain rates. For a methane flame, the extinction occurs for strain rates less than 1 s^{-1}. A flammability map was plotted to show the maximum flame temperature as a function of the strain rate and the time of radiation induced extinction. Results were compared with an earlier study at zero strain rate and were found to be in excellent agreement. In the present model, the soot radiation, detailed chemistry and non-unity Lewis number were not considered.

ACKNOWLEDGMENT

Financial support for this work was provided by NASA (under the grant number NAG3-1460) and GRI (under the grant number 5093-260-2780).

REFERENCES

1. F. A. Williams, *Combustion Theory*, Benjamin/Cummings Publishing Co. 2nd Ed. (1985).
2. U. Bonne, *Comb. & Flame*, **16**, 147 (1971).
3. J. S. T'ien, *Comb. & Flame*, **65**, 31 (1986).
4. C. R. Kaplan, S. W. Baek, E. S. Oran, and J. L. Ellzey, *Comb. & Flame*, **96**, 1 (1994).
5. A. Atreya and S. Agrawal, *Comb. & Flame*, (accepted for publication) (1993).
6. M. M. Abu-Romia and C. L. Tien, *J. of Heat Trans.*, **Nov**, 321 (1967).

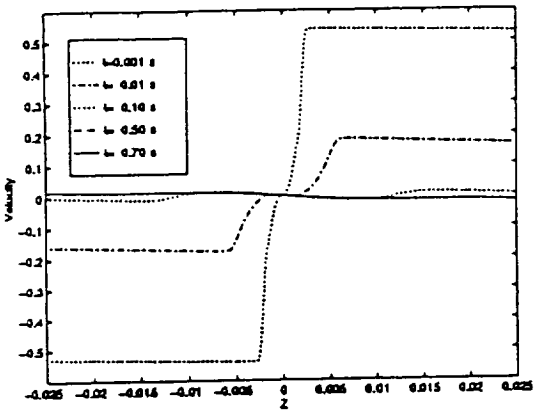

Figure 2 Velocity Distribution
(T_∞=295K, $Y_{F,\infty}$=0.125, $Y_{O,\infty}$=0.5, strain=0.5 s^{-1})

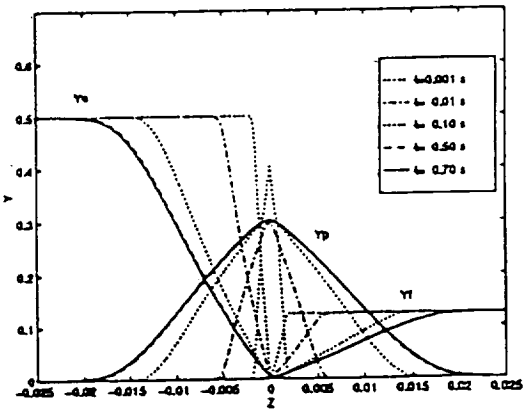

Figure 3 Species Profiles
(T_∞=295K, $Y_{F,\infty}$=0.125, $Y_{O,\infty}$=0.5, strain=0.5 s^{-1})

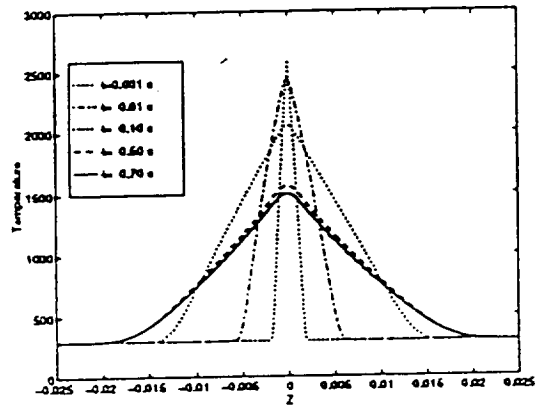

Figure 4 Temperature Distribution
(T_∞=295K, $Y_{F,\infty}$=0.125, $Y_{O,\infty}$=0.5, strain=0.5 s^{-1})

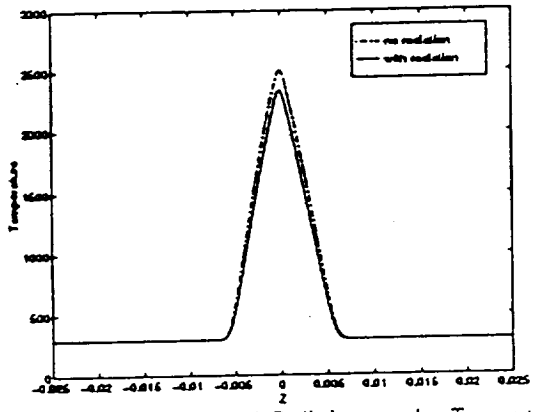

Figure 5 Effect of Radiation on the Temperature Distribution
(T_∞=295K, $Y_{F,\infty}$=0.125, $Y_{O,\infty}$=0.5, strain=10.0 s^{-1})

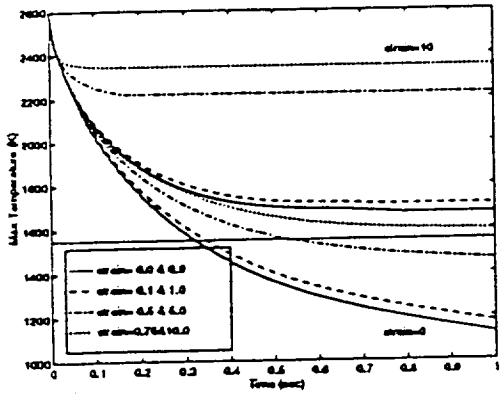

Figure 6 Reduction of Maximum Flame Temperature with Radiation
(T_∞=295K, $Y_{F,\infty}$=0.125, $Y_{O,\infty}$=0.5)

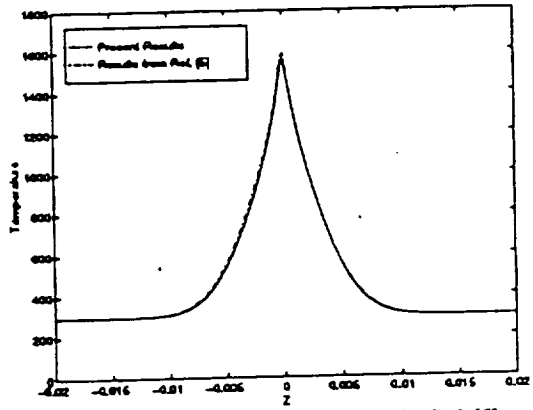

Figure 7 Comparison of the Results with Ref. [5]
(T_∞=295K, $Y_{F,\infty}$=0.125, $Y_{O,\infty}$=0.5, strain=0.0 s^{-1})

APPENDIX G

Numerical Simulation of Radiative Extinction of Unsteady Strained Diffusion Flames

Symposium on Fire and Combustion Systems, ASME IMECE paper, 1995

By

Shamim, T. and Atreya, A.

Symposium on Fire and Combustion Systems, ASME IMECE, 1995

NUMERICAL SIMULATIONS OF RADIATIVE EXTINCTION OF UNSTEADY, STRAINED DIFFUSION FLAMES

Tariq Shamim and Arvind Atreya
Department of Mechanical Engineering and Applied Mechanics
The University of Michigan
Ann Arbor, Michigan

ABSTRACT

In an attempt to fill the existing gap in the literature, time-dependent numerical simulations of axisymmetric counterflow diffusion flames were conducted to quantify the low-strain-rate radiation-affected flammability limits. Such limits are important for spacecraft fire safety. At low strain rates, there is an enhancement of flame radiation due to increased accumulation of combustion products in the flame zone and an increased rate of soot formation. Hence radiative extinction becomes significantly more important.

The model formulation includes the radiative effects from both soot and combustion products (CO_2 and H_2O) as well as soot formation and oxidation. Employing the Numerical Method of Lines, the governing equations were spatially discretized by using a 4th order central difference formula and temporally integrated by using an implicit backward differentiation formula (BDF). Both non-sooty and sooty flames were considered. Results show a significant reduction in the flame temperature due to radiation. The radiation from combustion products was found to play a dominant role. For flames subjected to small strain rates, the radiation-induced reduction in temperature was found to be sufficient to cause extinction. For methane flame, the extinction occurs for strain rates less than 1 s^{-1}, and the extinguishment time (disappearance of flame chemiluminescence = 1550 K (Bonne, 1971)) for most of these strain rates was found to be less than 1 second. A flammability map is presented to show the maximum flame temperature as a function of the strain rate and the time of radiation induced extinction.

INTRODUCTION

The objective of this study is to investigate the effects of radiative heat losses from soot and combustion products (CO_2 and H_2O). This work will lead to the quantification of low-strain-rate radiation-affected diffusion flame extinction limits. Such limits are important for spacecraft fire safety. Although, there has been a growing recognition of the importance of radiative heat losses from flame (Chao and Law, 1993 and Kaplan et al., 1994), there still exists a vast gap in the literature.

One reason for such a lack of literature is that measurements have indicated that radiant losses from the gas are relatively insignificant for small-scale lab experiments since under normal gravity conditions the excess particulates are simply ejected from the flame tip by the buoyant flow field. But radiant emission may have significant influence on conditions at extinction for larger scales because of the presence of a large number of soot particles and under microgravity conditions because of very low strain rates. At low strain rates, there is an enhancement of flame radiation due to increased accumulation of combustion products in the flame zone and an increased rate of soot formation. Hence radiative extinction becomes significantly more important.

Bonne (1971) was the first one who analyzed the problem of diffusion flame extinction with flame radiation. Using the results of a simulated experimental study, he showed that the radiative extinguishment occurs in a zero gravity environment. The existence of a radiative extinction limit at small strain rates was first numerically determined by T'ien (1986). He plotted a flammability map showing the extinction boundaries consisting of

blowoff and radiation branches. However, he only considered the radiative heat losses from the fuel surface and neglected gas-phase radiation and absorption. Recently, Atreya and Agrawal (1993) numerically demonstrated the occurrence of radiative-extinction of a one-dimensional unsteady diffusion flame. But they did not consider the effect of induced strain rates since their formulation was limited to a quiescent microgravity environment.

FORMULATION OF THE PHYSICAL PROBLEM

General Governing Equations

A schematic of a counterflow diffusion flame stabilized near the stagnation plane of two laminar flows is shown in Figure 1. In this figure, r and z denote the independent spatial coordinates in tangential and axial directions respectively. Using the assumptions of axisymmetric, unity Lewis number, negligible body forces, negligible viscous dissipation, and negligible Dufour effect, the resulting conservation equations of mass, momentum, energy, species and the soot mass fraction may be simplified to the following form:

$$\frac{\partial \rho}{\partial t} + 2\,\rho\, e\, \psi + \partial\frac{(\rho\, v)}{\partial z} = 0$$

$$\left(\psi - \frac{\rho_\infty}{\rho}\right)\frac{de}{dt} + e\,\frac{\partial \psi}{\partial t} + \left(\psi^2 - \frac{\rho_\infty}{\rho}\right)e^2 = - e\,\nu\,\frac{\partial \psi}{\partial z} - \frac{e}{\rho}\,\frac{\partial}{\partial z}\left(\mu\frac{\partial \psi}{\partial z}\right)$$

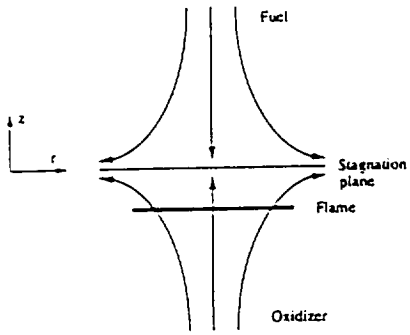

FIGURE 1 SCHEMATIC OF COUNTERFLOW DIFFUSION FLAME

$$\rho\left(\frac{\partial h}{\partial t} + v\frac{\partial h}{\partial z}\right) = \frac{\partial}{\partial z}\left(\frac{\lambda}{c_p}\,\frac{\partial h}{\partial z}\right) - \sum_{i=1}^{N}\omega_i\,\Delta h_{f,i}^{\circ} - \nabla.Q_R + \left(\dot{m}_{s,o} - \dot{m}_{s,f}\right) Q_s$$

$$\rho\left(\frac{\partial Y_i}{\partial t} + v\,\frac{\partial Y_i}{\partial z}\right) = \frac{\partial}{\partial z}\left(\rho\, D_i\,\frac{\partial Y_i}{\partial z}\right) + \omega_i - \delta_i\left(\dot{m}_{s,f} - \dot{m}_{s,o}\right)$$

$$\rho\left(\frac{\partial \phi}{\partial t} + v\,\frac{\partial \phi}{\partial z}\right) = \frac{\partial}{\partial z}(\rho\, v_T\,\phi) + \left(\dot{m}_{s,f} - \dot{m}_{s,o}\right)$$

Here ψ is a similarity transformation variable which is related to the radial velocity by $\psi = u_r/(\varepsilon\, r)$. The above equations are closed by the following ideal gas relations:

$$\rho = \frac{p}{\bar{R}\,T}\,\frac{1}{\sum_{i=1}^{N}(Y_i/MW_i)} \quad \text{and} \quad dh = c_p\,dT$$

The symbols used in the above equations are defined in the nomenclature. Note that in the present form the equations do not depend on the radial direction. The last term in the energy equation represents the energy release by soot oxidation. This term is zero when negative. In this study, the radiative heat flux is modelled by using the emission approximation, i.e., $Q_R = 4\,\sigma\,T^4\,(a_{P,CO_2} + a_{P,H_2O} + a_{P,soot})$; where, σ is the Stefan-Boltzman constant, and a_{P,CO_2}, a_{P,H_2O}, $a_{P,soot}$ are the Planck mean absorption coefficients for CO_2, H_2O and soot respectively. The absorption coefficients for combustion products were taken from Abu-Romia and T'ien (1967) and for soot we have used $a_{P,soot} = 118.6\,f_v\,T\ m^{-1}$ obtained from Siegel and Howell (1981).

The variable δ_i in the species equation is zero for all species except for fuel for which it takes the value of unity. This last term in the fuel conservation equation represents the fuel depletion through soot formation, and is zero when negative. The soot conservation equation includes convection, thermophoretic diffusion and source term. The thermophoretic velocity is defined as:

$$v_T = - 0.55\left(\frac{\eta}{T}\right)\left(\frac{\partial T}{\partial z}\right)$$

The soot mass fraction is related to soot volume fraction by $\phi = f_v\rho_s/\rho$.

Soot Production Model

The source term in the soot conservation equation, i.e., $(\dot{m}_{s,p} - \dot{m}_{s,o})$, is represented by a model developed by Zhang et al., (1992) and Atreya and Zhang (1995) and may be described as following:

$$(\dot{m}_{s,p} - \dot{m}_{s,o}) = A_p f_v^{2/3} \left(\xi_F - \frac{3}{8}\xi_O\right) \exp\left(-\frac{E_s}{RT}\right);$$

$$\text{where} \quad \xi_j = \sum_{i=1}^{N} \left(\frac{AW_i \, a'_{ij}}{MW_i}\right) Y_i$$

In this simplified model, the soot nucleation rate equation is avoided by the use of an average number density. The value of the pre-exponential factor for soot reaction A_p, the soot activation energy E_s, the energy released during soot oxidation Q_s and the soot particle density ρ_s were taken to be 10^{10} kg/m^3.s, 150 kJ/mole, 9×10^3 kJ/kg and 1.86×10^3 kg/m^3 respectively (Zhang et al., 1992 and Atreya and Zhang, 1995).

Reaction Scheme

The present problem was solved by considering a single step overall reaction which may be written as follows:

$$[F] + \nu\,[O_2] \longrightarrow (1+\nu)\,[P]$$

Here, ν is the mass-based stoichiometric coefficient. Using second order Arrhenius kinetics, the reaction rate was defined as $\omega = A\,\rho^2\,Y_F\,Y_O \exp(-E_R/R\,T)$. The reaction rates for fuel, oxidizer, and product may then be written as $\omega_F = -\omega$; $\omega_O = -\nu\omega$; and $\omega_p = (1+\nu)\omega$. For the calculations presented here, the values of various constants and properties were obtained from Atreya and Agrawal (1993).

Initial and Boundary Conditions

A solution of these equations requires the specification of some initial and boundary conditions which are given as following:

Initial Conditions:

$\psi(z,0) = \psi_o(z)$

$h(z,0) = h_o(z)$ or $T(z,0) = T_o(z)$

$Y_i(z,0) = Y_{i,o}(z)$ [n conditions or (n-1) conditions + $\rho(z,0)$]

$\varphi(z,0) = \varphi_o(z)$

Here subscript 'o' represents the specified initial function.

Boundary Conditions:

The origin of our coordinate system was defined at the stagnation plane.

$\psi(\infty,t) = 1$ $\quad \psi(-\infty,t) = (\rho_-/\rho_-)^{1/2}$

$h(\infty,t) = h_{up}$ $\quad h(-\infty,t) = h_{low}$

[or $T(\infty,t) = T_{up}$ $\quad T(-\infty,t) = T_{low}$]

$Y_i(\infty,t) = Y_{up}$ $\quad Y_i(-\infty,t) = Y_{low}$

$v(0,t) = 0$

The strain rate ε, which is a parameter, must also be specified.

SOLUTION PROCEDURE

The governing equations form a set of nonlinear, coupled and highly stiff partial differential equations. A closed form solution of these equations is very difficult to obtain. Hence, in the present study, the equations were solved numerically. The numerical scheme used is called the *Numerical Method of Lines* (NMOL). In this method, the equations are first discretized by applying a standard finite difference scheme in the spatial direction which transforms PDEs into ODEs. The resulting ODEs in time are then solved by using a time integrator such as Runge Kutta, implicit Adams method, implicit backward differentiation formulas for stiff problems.

In the present study, a 4th order 5-point central difference formula was used to spatially discretize the equations and an implicit backward differentiation formula (BDF) was used to integrate in the temporal direction. In order to carry out the numerical integration, infinity was approximated by a finite length of the order of the length scale of the problem (i.e., $(D/\varepsilon)^{1/2}$). This was confirmed by checking the gradients of all the variables which must vanish at the boundaries.

RESULTS AND DISCUSSION

Figures 2-4 show the results for unity global equivalence ratio with T_-=295K, Y_{F-}=0.125, Y_{O-}=0.5 and strain rate ε=0.1 s^{-1}. These results were obtained by dividing the computational domain into 1001 spatial nodes (i.e., the size of spatial node was 0.05 mm). All the profiles shown are at time t= 0.001, 0.01, 0.1, 0.3, and 0.4 second. For these results, constant c_p, equal diffusion coefficients for all gases and $\rho^2 D$=constant were used.

The temperature profiles show a decrease in the maximum flame temperature due to gas radiation. The effect of gas radiation was found to be sufficient to cause extinguishment (defined as disappearance of chemiluminescence =1550 K (Bonne, 1971)) in approximately 0.3 second. However, the effect of radiation was found to decrease with an increase in strain rate. Figure 5 shows the steady state temperature profiles for the cases with and without radiation effects for ε=10.0 s^{-1}. The results show that the radiation reduces the maximum flame temperature by 250 K without causing extinction.

Figure 6 shows the development of soot volume fraction profiles at various time intervals for strain rate of 0.1 s^{-1}. This figure shows that the soot volume fraction initially increases, reaching a maximum value in approximately 0.04 s and then starts

decreasing. The figure also shows a shift of soot formation zone towards the fuel side. The decrease in the soot formation is due to: (i) a reduction in the flame temperature as a result of radiation; (ii) the convection of soot to lower temperature zones; and (iii) an increased rate of soot oxidation. The convection of the soot volume is mainly due to expansion waves generated at the initial stage of ignition (see Figure 2). This convection effect is further assisted by the following two factors: (i) the spread of products of combustion with time increases the OH radical concentration, which in turn increases the soot oxidation in the high temperature zone and thus shifts the soot formation towards low temperature zone; and (ii) the thermophoretic diffusion of soot particle. The latter effect, however, is not very dominant. The convection of soot volume fraction is opposed by the strain induced flow. This opposing effect becomes important at higher strain rates. Results at higher strain rates show a considerable decrease in the soot volume fractions with soot formation in the higher temperature zones.

Figure 7 shows the time variations of maximum flame temperature for various values of strain rates. The plot shows that for flames with strain rates less than 1 s^{-1}, the effect of radiation is sufficient to cause extinction. These results show similar trends as those obtained in our previous study (Shamim and Atreya, 1995), which included the effect of gas radiation only. The effect of soot radiation was obtained by comparing the cases with and without soot radiation. The difference in peak temperatures for these two cases as a function of strain rate at time t=0.05 s is plotted in Figure 8. The figure shows a decrease in the effect of soot radiation with an increase in strain rates. This decrease is due to a decrease in the soot volume fractions at higher strain rates. However, since the radiative losses from combustion products decrease at a faster rate with strain rates, the contribution of soot radiation becomes more significant at higher strain rates.

CONCLUSIONS

In order to quantify the low-strain-rate radiation-affected diffusion flame extinction limits, the effects of radiative heat losses on an unsteady counterflow diffusion flame were numerically investigated. The model formulation includes the radiative effects from both soot and combustion products (CO_2 and H_2O) as well as soot formation and oxidation. Both non-sooty and sooty flames were considered. Results show a significant reduction in the flame temperature due to radiation. This reduction in temperature increases with a decrease in strain rate. The radiation from combustion products was found to play a dominant role, specially at low strain rates. For flames subjected to low strain rates, the radiation-induced reduction in temperature was found to be sufficient to cause extinction. For methane flame, the extinction occurs for strain rates less than 1 s^{-1}, and the extinguishment time (disappearance of flame chemiluminescence = 1550 K) for most of these strain rates was found to be less than 1 second. A flammability map is presented to show the maximum flame temperature as a function of the strain rate and the time of radiation induced extinction. In the present model, detailed chemistry and non-unity Lewis number were not considered.

ACKNOWLEDGMENT

Financial support for this work was provided by NASA (under the grant number NAG3-1460) and GRI (under the grant number 5093-260-2780).

NOMENCLATURE

a^j_i	number of atoms of kind "j" in species "i"
a_p	Planck mean absorption coefficient
A	pre-exponential factor
AW	atomic weight
c_p	constant pressure specific heat of the mixture
D_i	coefficient of diffusivity of species i
E_a	soot activation energy
fv	soot volume fraction
h	enthalpy
h^o_{fi}	enthalpy of formation of species i
$m_{s,p}$	soot production rate
$m_{s,o}$	soot oxidation rate
MW	average molecular weight
Le	Lewis number
p	pressure
Q_R	radiant heat loss
Q_s	heat of reaction for soot oxidation
R	universal gas constant
T	temperature
t	time
u_r	radial velocity
v	axial velocity
v_T	thermopheretic velocity
Y_i	mass fraction of species i
δ_i	variable defined in the species equation
ε	strain rate
η	kinematic viscosity of the mixture
λ	thermal conductivity of the mixture
μ	dynamic viscosity of the mixture
ν	mass based stoichiometric ratio
ξ	variable defined in the soot model

ρ	mass density
σ	Stefan-Boltzman constant
ϕ	soot mass fraction
ψ	similarity transformation variable
ω_i	mass rate of production of species i

REFERENCES

Abu-Romia, M. M., and T'ien, C. L., 1967, "Appropriate Mean Absorption Coefficients for Infrared Radiation of Gases," *Journal of Heat Transfer*, Vol. 11, pp. 321-327.

Atreya, A. and Agrawal, S., 1993, "Effect of Radiative Heat Loss on Diffusion Flames in Quiescent Microgravity Atmosphere," *Combustion & Flame*, (accepted for publication).

Atreya, A., and Zhang, C., 1995, "A Global Model of Soot Formation Derived from Experiments on Methane Counterflow Diffusion Flames," *Combustion & Flame*, (to be submitted) .

Bonne, U., 1971, "Radiative Extinguishment of Diffusion Flames at Zero Gravity," *Combustion & Flame*, Vol. 16, pp. 147-159.

Chao, B. H., Law, C. K., 1993, "Asymptotic Theory of Flame Extinction with Surface Radiation," *Combustion & Flame*, Vol. 92, pp. 1-24.

Kaplan, C. R., Baek, S. W., Oran, E. S., and Ellzey, J. L., 1994, "Dynamics of a Strongly Radiating Unsteady Ethylene Jet Diffusion Flame," *Combustion & Flame*, Vol. 96, pp. 1-21.

Shamim, T., and Atreya, A., 1995, "A Study of the Effects of Radiation on Transient Extinction of Strained Diffusion Flames," *Joint Technical Meeting of Combustion Institute*, paper 95S-104 pp. 553-558.

Siegel, R., and Howell, J. R., 1981, *Thermal Radiation Heat Transfer*, Hemisphere Publishing Corp., Washington, D.C., 2nd ed.

T'ien, J. S., 1986, "Diffusion Flame Extinction at Small Stretch Rates: The Mechanism of Radiative Loss," *Combustion & Flame*, Vol. 65, pp. 31-34.

Zhang, C., Atreya, A., and Lee, K., 1992, "Sooting Structure of Methane Counterflow Diffusion Flames with Preheated Reactants and Dilution by Products of Combustion," *Twenty-Fourth (International) Symposium on Combustion*, The Combustion Institute, pp. 1049-1057.

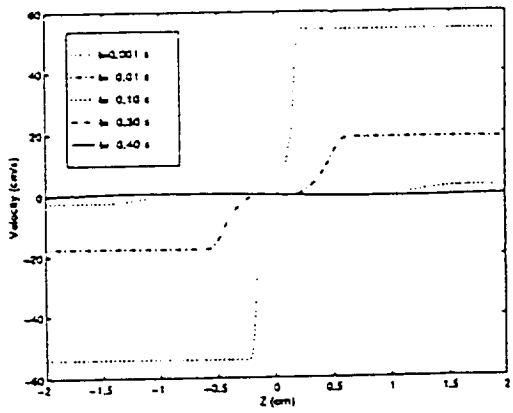

FIGURE 2 VELOCITY DISTRIBUTION
(T_-=295K, Y_{F-}=0.125, Y_{O-}=0.5,STRAIN=0.1 s^{-1})

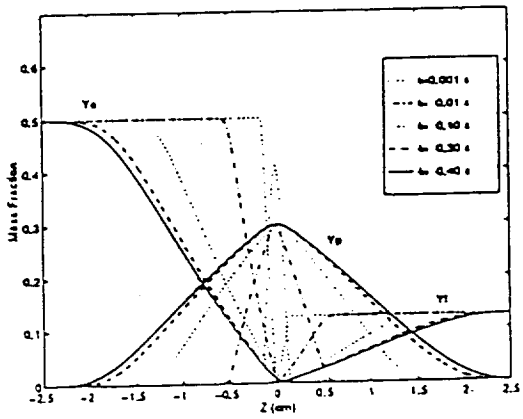

FIGURE 3 SPECIES PROFILES
(T_-=295K, Y_{F-}=0.125, Y_{O-}=0.5, STRAIN=0.1 s^{-1})

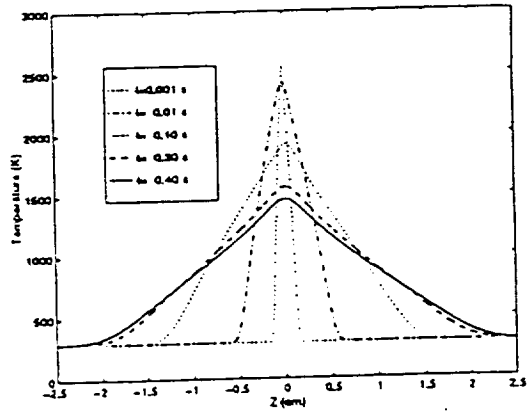

FIGURE 4 TEMPERATURE DISTRIBUTION
(T_-=295K, Y_{F-}=0.125, Y_{O-}=0.5, STRAIN=0.1 s^{-1})

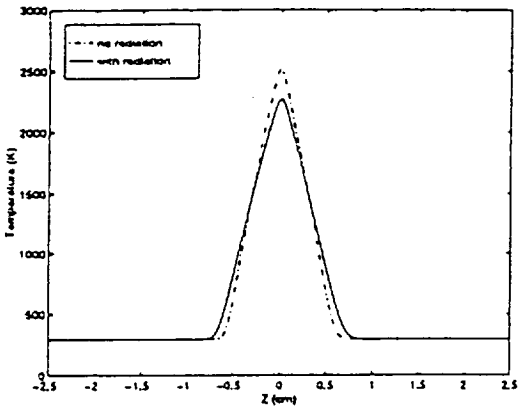

FIGURE 5 RADIATION EFFECT ON TEMP
(T_{-}=295K, Y_{F-}=0.125,Y_{O-}=0.5, STRAIN=10 s^{-1})

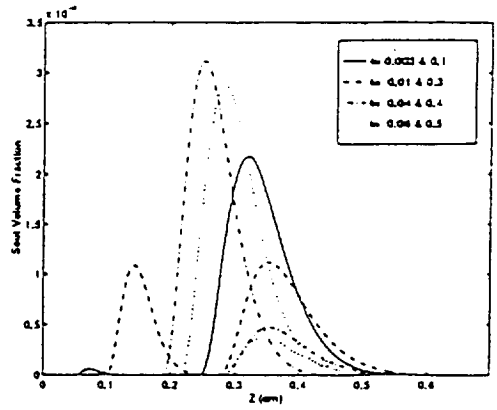

FIGURE 6 PROFILES OF SOOT VOLUME FRACTION
(T_{-}=295K, Y_{F-}=0.125, Y_{O-}=0.5, STRAIN=0.1 s^{-1})

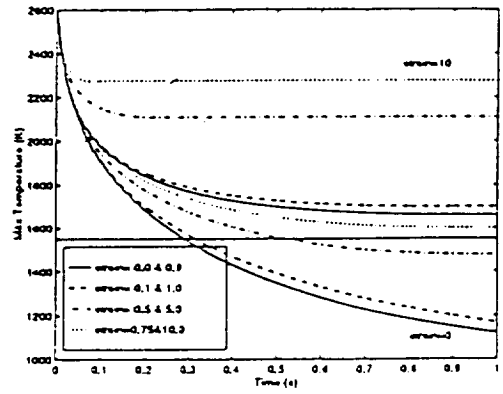

FIGURE 7 REDUCTION OF MAXIMUM FLAME TEMPERATURE WITH RADIATION
(T_{-}=295K, Y_{F-}=0.125, Y_{O-}=0.5)

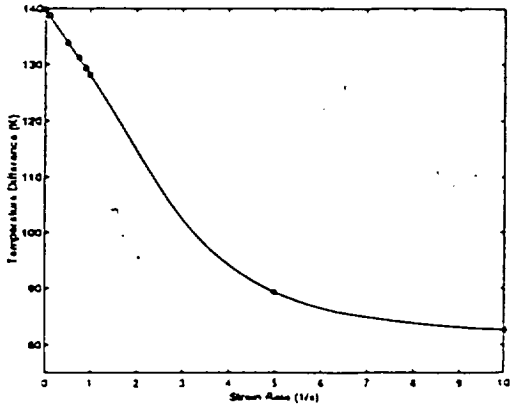

FIGURE 8 EFFECT OF SOOT RADIATION ON THE PEAK TEMPERATURE
(T_{-}=295K, Y_{F-}=0.125, Y_{O-}=0.5, TIME=0.05 s)

APPENDIX H

Experiments and Correlations of Soot Formation and Oxidation in Methane Counterflow Diffusion Flames

Combustion Symposium paper

By

Atreya, A. and C. Zhang

Experiments and Correlations of Soot Formation and Oxidation in Methane Counterflow Diffusion Flames

A. Atreya and C. Zhang
Combustion and Heat Transfer Laboratory
Department of Mechanical Engineering and Applied Mechanics
The University of Michigan
Ann Arbor, Michigan 48109-2125
USA

Telephone: (313) 647 4790
Fax: (313) 647 3170
e-mail: aatreya@engin.umich.edu

A Global Model of Soot Formation Derived from Experiments on Methane Counterflow Diffusion Flames

A. Atreya and C. Zhang
Combustion/Heat Transfer Laboratory
Department of Mechanical Engineering and Applied Mechanics
The University of Michigan
Ann Arbor, MI 48109

ABSTRACT

This paper presents a simple model of soot formation in fuel-rich counterflow diffusion flames. It is derived and tested on extensive measurements of temperature, chemical species, soot volume fraction and particle number density in flames. In order to shed light on a global approach of soot modeling and thereby to admit applications of turbulent flames. Parameters critical to turbulent diffusion flames, such as preheated reactants and dilution by primary products of combustion, were systematically varied in our experiments. It was proposed that the soot formation in a counterflow diffusion flame be modeled by three Arrhenius type reaction equations and one molecular particle coagulation equation (soot nucleation; soot coagulation, soot surface growth and soot oxidation) with constants derived from measurements. The proposed model accounts for the effect of CO_2 and H_2O on soot reduction by using a mixture fraction variable proportional to the unoxidized carbon atom concentration. Soot nucleation rate expression was derived from the homogeneous nucleation theory and soot formation rate was assumed proportional to the soot surface area and the local unoxidized carbon atom concentration. This model, along with SANDIA OPPDIF code, was incorporated into a computation scheme. Comparison of model prediction with our experiments (CH_4 flame) and with those in the literature (C_2H_6 flame) were made and show qualitative agreements. This work has suggested a global approach toward soot modeling aimed for turbulent diffusion flame calculations.

1. Introduction

The process of soot formation is of considerable interest to combustion science because it controls the combustion efficiency, thermal radiation and smoke emission from practical combustion systems. Turbulent diffusion flames used in these systems are known to locally consists of laminar diffusion flamelets [1] and they are often modeled using the flamelet concept [2,3]. Thus, to both understand and model soot formation in turbulent diffusion flames, it is essential to quantify soot formation in a single diffusion flamelet.

During the past several years, there have been many attempts of modeling soot formation. Generally, these efforts fall in two different approaches: reaction chemistry based model and global scheme based model. Frenklach and coworkers [4~7] are using the most detailed chemistry scheme which includes reactions up to large PAH. Similar but simpler approaches were adopted by Lindsdedt [8] and Hall [9] to reduce the complexity by introducing acetylene and benzene as a critical species in soot modeling. On the other hand, Kennedy et al [10], Kent et al [11] and Stewart et al [12] are using a global species (i.e., fuel mixture fraction) to model soot formation.

While considerable progress has been made, adequately but reasonably simplified chemical schemes which accounts for complicated chemical and transport processes in diffusion flames are lacking. Thus, a simpler description of the sooting process which is derived from and backed by extensive experimental measurements seems essential to the success of soot modeling. The present work attempts to explore this unique approach: experiment-based soot modeling. We developed a simple but comprehensive soot formation model based on extensive flame structure measure-ments conducted under different thermochemical environments (i.e. for different degree of reactant preheat and dilution by products of combustion). This work, along with other efforts in the literature, are important toward the development of a soot model used for turbulent flame application.

2. Experiment and Computation

I. apparatus and measurements

The experimental apparatus used is described in detail elsewhere [13].Briefly, a especially constructed ceramic burner with preheating capability is used to establish a flat axisymmetric counterflow diffusion flame approximately 8cm in diameter. The flow rates of fuel and oxidizer streams are determined with critical flow orifices. All the measurements are performed along the axial stream line and one-dimensionality of the flame is confirmed by examining the temperature profile along the radial direction. Temperature is measured using a Pt/Pt-10%Rh (wire diameter 76 μm) thermocouple coated with SiO_2 and is corrected for radiation. Gas compositions are measured by a direct-sampling quartz microprobe and a gas chromatograph. The local soot diameters, number densities and volume fractions are determined by extinction and scattering of a beam from an Argon-ion laser operating at 514.5nm. The soot aerosol is assumed monodispersed with a refractive index of 1.57-0.56i. Visible laser induced fluorescence (VISLIF)distribution was conducted by exciting the flame at 488nm and detecting at 514±10nm. The location of the stagnation plane was also determined by particle track photography.

The experimental conditions that were used are summarized in Table 1, which shows the fuel and oxidizer flow rates and concentrations, the burner preheating temperatures and the various amounts of CO_2 and H_2O that were added to alter the chemical environment of the flame while keeping the thermal environment un-changed. Also shown in Table 1 are two flames by Axelbaum and Vandersburger [14 ,15], these two flames were used to further test our soot model. In our experiments, we used very low strain rates to expand the soot formation zone for accurate spatial measurement.

Detailed temperature, gas species concentrations, PAH and soot profiles were measured for all the flames listed in Table 1. These measured profiles provided the basis for the development of the soot model To enable comparing the sooting structure of various flames, a non-dimensional axial coordinate Zn was employed (Zn=(Z-Zs)/(Zt-Zs), where Z is the vertical distance from the bottom

surface of the burner and Zs and Zt are the locations of the stagnation plane and the peak flame temperature respectively).

II. computation

To ensure the validity of the developed soot model and to compare the soot predictions with the experiments, a detailed reaction mechanism-GRIMECH, along with the code OPPDIF developed by SANDIA [16], was implemented in the present work. The program was run using the specified experimental boundary conditions. It contains 177 elementary reactions and 34 species. The governing equation and solution techniques can be found in Kee [17]. The computation provided chemical and thermal structures of relative flames, which were subsequently compared with the measurements. Conserved scalers (see definitions later) were thus computed and used for the developed soot model to predict soot formation under the relative flame conditions.

III. sooting flame structure

Temperature, velocity and species

Figure 1 shows the measured and computed temperature and velocity profiles for three flames (BA, BB and BC). Figure 2 shows the measured and computed species profiles (BC). The velocity profiles inside these sooting flames could not be measured because of the presence of soot particles, which would affect LDV. Thus, they were calculated by specifying the measured boundary conditions and by using the measured temperature and species profiles. Properties of the multi-component mixture were obtained as a function of temperature from the NASA code [18]. The 1-D continuity and momentum equations employed along with the appropriate boundary conditions may be found in Ref. [19]. The calculated velocity profiles were checked by using the measured locations of the stagnation plane. They matched within the experimental error of ±0.2mm. In these figures, computation results using SANDIA code were also included. It was found that the velocity in the reaction zone ($0 \le Z_s \le 1$) and hence the residence time measured from the flame front was essentially the same for all the flames. However, the flame visible thickness ($Z_t - Z_s$) varied

from 6 to 8mm. Chemical species profile in Figure 2 has shown overall agreement between the measurements and computations in chemical structure.

Soot particle profiles

The measured soot volume fractions and particle number densities are shown in Figure 3 along with computed OH profiles. While the data for other flames could not be presented here, these results are representative. The number density curves in Figure 3 show that the location where the first nuclei appear (inception location) changes considerably with the flame conditions listed in Table 1 (Zn varies from 0.4 to 0.85). The corresponding soot volume fractions peak values also decrease with the shift in the inception location. From Figure 1, one finds that the temperature at the inception location varies from 1400K to 1750K. Thus, it is not possible to conclude that inception occurs at a specified temperature. However, OH profiles (see Figure 3) indicated that an quicker decay of OH from the flame resulted earlier inception (BC). Also, in our experiments, it was found that an increase in the concentrations of CO_2 and H_2O shifts the inception location away from the flame toward the fule side. Thus, one might conclude the critical role played by OH in soot formation, which is critical in modeling the nucleation site of sooting.

Figure 4 shows a comparison of soot volume fraction and number density profiles for the BC flame with those available in the literature. Due to the low strain rates employed in our flames, the residence time (~400ms) is much larger than the literature flame data. Thus, the flight time t was normalized by the maximum residence time to make the results of different flame conditions comparable (tmax, the maximum flight time from the flame, was 18ms for Axelbaum's flame, 16ms for Vandsburger's flame and 96ms for Santoro's flame [20]). It is seen that our results flame are similar to those measured in the cylindrical forward-stagnation counterflow diffusion flames (Vandsburger et al, 1984 and Axelbaum 1988), but the values are slightly lower. This may be due to the difference in fuel concentration and the flame temperature. However, the fact that the two profiles are similar implies that the effect of higher strain rates used by Axelbaum et al. and

Vandsburger et al is essentially to compress the sooting structure rather than to alter the soot nucleation or growth processes. The results of co-annular burner diffusion flame (Santoro [20]) are affected by both soot formation and oxidation. Here, soot number density increase again when the soot volume fraction decreases after t/tmax=0.6 due to oxidation. Later, we will apply our soot models to Vandersburger's and Axelbaum's flames.

Based on the experiments, the structure of fuel-rich counter flow diffusion flame is schematically shown in Figures 5 and 6. H_2 production rate is also included because H_2 is produced by the hydrogen abstraction reactions that occur during soot precursor formation [21]. Essentially a three-color flame was observed which extends from Zn=0.0 toZ n=1.1. While traveling along the central stream line from the oxidizer side to the fuel side, first a light blue zone is encountered in which the peak flame temperature (~1900K) and primary combustion reactions occur. Next, we encounter a bright yellow zone where the temperature is between 1500K and 1800K. Between the blue and the yellow zones there exists a fairly thin dark zone whose origin is unclear to the authors. In the yellow zone, scattering by soot particles was found to be several orders of magnitude smaller than at the stagnation plane. However, soot volume fraction, VIS LIF and other intermediate hydrocarbons were present in this zone. Thus, it seems that in this zone soot precursor are formed. but their concentration is not high enough for nucleation to form measurable size soot particles (>5nm). This is probably because of oxidative attack by OH radicals. The thickness of the yellow zone is approximately equal to the distance between the location of the sharp rise in the number density and the location where the soot volume fraction becomes zero. Between the yellow zone and the stagnation plane, a dark orange zone exists where the temperature is between 1200K and 1600K Soot inception occurs at the diffuse interface between the yellow and the orange zones. Soot particulate scattering and soot volume fraction in the orange zone increase until we reach the stagnation plane.

To summarize the experiments, one would conclude: 1) a reliable sooting flame structure data pool

was established, which reveal the basic sooting processes under various condition. This is very crucial to soot modeling; and 2) while it still awaits detailed flame structure study to clarify the OH and other key radicals' role in soot formation (this work in currently underway in our lab), it is phenomelogically clear that a critical species (or trace species) with enough concentration is essential for soot inception to occur. Our experiments revealed that the concentration of this trace species may increase with (i) increase in the flame temperature; (ii) decrease in oxygen containing species that may, in turn, increase the OH radical concentration; and (iii) increase in the fuel concentration.

Thus far, different approaches have been explored to model the inception species, (e.g., Large PAH, Frenclach[4,7], C_2H_2 and C_6h_6, Lindstedt[8], Gore [9], or arbitrarily assigned, Kennedy[10]). Nevertheless, a universally applicable scheme that can quanti-tatively explain all existing experiments is still lacking. In this work, we attempt to model the inception (nucleation) and growth species with a simple but experimen-tally based global species (the conserved scaler).

Soot model

In the model presented here, the conserved scaler formulation has been used to enable easy application to turbulent diffusion flames. By defining the atomic mass fraction of atom j as:

$$\xi_j = \sum_{i=1}^{n} \left(\frac{M_j \nu_i^j}{M_i}\right) y_i$$

where M_i and y_i denote the molecular weight and mass fraction of species i, M_j denotes the atomic weight of atom j and ν_i^j denotes the number of atoms of j in species i, for an arbitrary control volume in the reaction zone we obtain:

$$\xi_C + \xi_H + \xi_O + \xi_N + \xi_{Ar} + \frac{\rho_s \Phi}{\rho} = 1$$

Here, ρ and ρ_s are the gas and the soot densities (ρ_s taken as 1.86g/cm^3) respective-ly. It is assumed that the fuel is a hydrocarbon and the oxidizer is air. Now, for a non-sooty flame, $\xi_F = \xi_C + \xi_H$ is the fuel mass fraction which is normalized as:

$$Z_F = \frac{\xi_F - \xi_{Fmin}}{\xi_{Fmax} - \xi_{Fmin}}$$

Similarly, the conserved scaler for oxygen is defined as:

$$Z_O = \frac{\xi_O - \xi_{Omin}}{\xi_{Omax} - \xi_{Omin}}$$

However, for a sooty flame, $\xi_F + \rho_s\phi/\rho$ is conserved. Thus, the conserved scaler is defined as:

$$Z = \frac{\rho_s \phi}{\rho} + Z_F \xi_{F-}$$

where

$$\xi_{Fmax} = \xi_{F-} \text{ and } \xi_{Fmin} = 0$$

Here, the subscripts O_-, F_- represent the inlet conditions on the oxidizer and the fuel side respectively. Substituting Z and Z_o in the conservation equation we obtain the soot equation as:

$$\xi_{F-}\rho\vec{V}\vec{\nabla}Z_F - \vec{\nabla}(\rho D_F \vec{\nabla} Z_F) = -\rho_s \rho \vec{V}\vec{\nabla}(\Phi/\rho) - \vec{\nabla}(\rho D_F \Phi \vec{\nabla} T) = \dot{m}'''_{soot}$$

and oxidizer equation as:

$$\rho \vec{v} Z_O - \vec{\nabla}(\rho D_o \vec{\nabla} Z_o) = 0$$

where, $\dot{m}'''_{net}$ is the net soot production rate.

While there were various sheme to define a trace species for soot inception and growth. Fundamental questions still remains. Thus, we introduce a hypothesis for describing soot formation and oxidation:

$$\textit{fuel}\ (C, H \ldots) \Rightarrow \textit{soot}, \quad \textit{soot} + \textit{oxidizer}(O, OH, \text{or } O_2) - \textit{products}.$$

Here, fuel represents unspecified hydrocarbons, fuel fragments and pyrolysis products which are contained in Z_F and the oxidizer represents oxygen or radical species that are contained in Z_O. Now, to quantity $\dot{m}'''_{net}$, first, it is essential to develop a model for the nucleation rate as a function of the thermochemical environment and account for the changes that occur in the particle number density due to coagulation. Then, the soot mass added by surface growth and reduced by oxidation can be calculated.

Nucleation:

In the yellow and orange zones of a sooty flame, the concentration of soot precursors and growth species (large PAHs, C2H2 and other intermediate hydrocarbons) increases toward the stagnation plane. These molecular precursors are of the order of several hundred AMU and may contain between 20 to 50 carbon atoms [22]. As the PAH concentration increases and the temperature decreases toward the stagnation plane, attractive Van der Waals forces between these molecules result in the formation of molecular clusters (The Van der Waals forces for large precursor molecules are substantial and their sticking coefficient is nearly unity [22]). In accordance with the classical homogeneous nucleation theory, it may be assumed that a critical size of these clusters leads to particle inception. It is suggested [22] that the incipient soot particle diameter is about 2nm

(~2000 AMU) and that the average size of condensing precursors is between 200 to 400 AMU. Thus, a cluster of about 6 to 8 large precursor molecules is required to form soot nuclei.

Under supersaturated conditions, the rate at which critical size nuclei are formed by condensation of molecules can be determined from the homogeneous nucleation theory [23] as:

$$\frac{dN_{Nu}}{dt} = p_1^2\left(\frac{1}{kT}\right)^2\left(\frac{\sigma d_p^{*2}}{18\pi g^{*2}}\right)^{1/2} \pi d_p^{*2} \exp\left[-\frac{g^*}{2}\ln S\right]$$

where, d_p^* is the diameter of the critical size particle, g* is the number of large molecules required to form a critical size, p_1 is the partial pressure of precursors, and $S=p_1/p_s$, is the saturation ratio (p_s is the partial pressure of precursor under saturated conditions). Also, k, σ and T are the Boltzmann's constant, the surface tension of the liquid and the absolute temperature respectively. Hence, S must be greater than unity for nucleation to occur.

Assuming σ, g*, d_p^* to be constants, we obtain the nucleation rate as:

$$\frac{dN_{Nu}}{dt} = \left(\frac{p_1}{p}\right)^{(2-g^*/2)} \frac{AP^2}{(kT)^2}\left(\frac{P_s}{P}\right)^{g^*/2}$$

where, p is the total pressure and p_1/p (= χ_1) is the mole fraction of condensing molecules. Also,

$$\frac{p_s}{p} = \exp\left[-\frac{\Delta H_v}{RT}\left(1-\frac{T}{T_b}\right)\right]$$

where, ΔHv is the heat at vaporization of the condensed molecules and T_b is the absolute temperature when the saturation pressure equals the total pressure. Since, $p_s << p$; $T_b >> T$. Thus,

(1-T/Tb) <1. Hence,

$$\frac{dN_{Nu}}{dt} = (\chi_1)^{2-g^*/2}\frac{B}{T^2}\exp(-\frac{\Delta Hg^*}{2RT})$$

In this equation, g*, ΔHv, χ_1 and B are unknowns that must be determined from experiments. Also, B/T^2 may be approximated as a constant for simplicity. Assuming g* ~8 [(2000~3000AMU)/ (200 ~400AMU)] and χ_1 proportional to the carbon available to make soot or unoxidized carbon [i.e. fraction of carbon not in CO_2: (ξ_F-3/8ξ_o). Note that this expression overcorrects for carbon present in CO because of oxygen in H_2O. However, this overcorrection is needed because of the observed strong chemical effect of H2O in delaying soot nucleation]. We can find B and ΔHv from the measured dN_{Nu}/dt by plotting N_{Nu} vs 1/T.

Coagulation:

At high concentration of soot particles, typical of a flame environment, a significant fraction of the observed increase in particle size is due to coagulation . This process is quantitatively described by the equation [24]:

$$N_{Co} = -\frac{6}{5}K_{fr}\phi^{1/6}N^{11/6}$$

with

$$K_{fr} = \frac{5}{12}(\frac{3}{4\pi})^{1/6}(\frac{6kT}{\rho_{soot}})^{1/2}G_c$$

Here, G is a factor that takes into account the dispersion forces between the particles (usually a value of 2 for spherical particles), and α is a function of the particle size distribution, reflecting the

variation in collision rates with different particle sizes. For a monodispersed system α takes the value of $4^{1/2}$. Thus, the generation rate of soot particles is a balance between the nucleation rate and the coagulation rate:

$$N_{net} = N_{\alpha} - N_{Co}$$

Surface Growth:

Most of the soot in a flame is produced by surface growth. In the global model presented here, we assume that the soot formation rate is proportional to the surface area of the soot particles [23] and the local hydrocarbon concentration assumed proportional to the available carbon (ξ_F-3/8ξ_o). This leads to the following Arrhenius equation:

$$m_{\xi} = A_{\xi}(\xi_F - \frac{3}{8}\xi_O)N^{1/3}\phi^{2/3}e^{-E_{\xi}/RT}$$

This equation was derived by assuming the soot aerosol to be monodispersed.

Oxidation:

In these flame, O_2 is not present on the fuel side and the flow is such that the soot particle are convected to the stagnation plane. Thus, oxidation may occur only by OH radicals whose concentration is increased with increase in the local CO_2 and H_2O concentrations. As noted earlier, this process occurs in the yellow zone and significantly affects the concentration of intermediate hydrocarbons that lead to precursor formation and eventually to soot formation. While considerable progress has been made toward developing a fundamental understanding of processes leading to soot inception [24] and a model of soot inception has recently appeared in the literature [4~7], further

work is needed to explain, for example, the effect of CO_2 and H_2O. In the conserved scaler formulation presented here, the details of this zone are by passed by using $(\xi_1 - 3/8\xi_o)$ in both nucleation and surface growth expressions. Hence, for these flames oxidation need not be considered. However, for a typical flamelet in a turbulent flame it is necessary to include soot oxidation. Thus, for the sake of completeness, soot oxidation rate may be expressed as:

$$m''_{ox} = A_o \xi_{ox} Z_o N^{1/3} \phi^{2/3} e^{-E_o/RT}$$

The constants A_O and E_O may be obtained from the literature [25].

In order to experimentally determine the corresponding constants, calculations have been carried out for all the flames listed in Table 1. The overall formation rates for soot volume fraction and soot particle number density were obtained from the global conservation equations which for the counterflow diffusion flame become:

$$\rho v \frac{d}{dz}\left(\frac{\rho_f \phi}{\rho}\right) + \frac{d}{dz}(\rho_f \phi v_T) = m''_{net} = m''_{+} - m''_{ox}$$

and

$$\rho v \frac{d}{dz}\left(\frac{N}{\rho}\right) + \frac{d}{dz}(N v_T) = N_{net} = N_{+} - N_{o}$$

Here, the thermophoretic velocity v_T was calculated from the expression:

$$v_T = -0.55 \frac{\nu}{T} \frac{dT}{dz}$$

To experimentally determine the model constants (A and E/R), measured number densities (which exist only for the orange zone) and soot volume fractions profiles were used along with the above four equations (soot growth, soot oxidation, soot nucleation and soot particle coagulation) to yield formation and nucleation rates. These rates were then normalized according to the relative models. These results are plotted in Figures 7 and 8 defined as:

$$m'''_{\psi}/(N^{1/3}\phi^{2/3}(\xi_F - \frac{3}{8}\xi_O)_P, \text{ and } N'''_{\psi}/(\xi_F - \frac{3}{8}\xi_O)^{-2}$$

Based on the experimentally determined constants (Ap and Ep/R and An and En/R for soot formation and nucleation respectively), the proposed model were finalized and were also plotted along with error margins in these figures.

From these two figures, one could make the following observations: 1) While there is considerable scatter, which was mainly due to differentiation of measured profile data, the trend of soot formation and nucleation rates follow the proposed model; 2) It may be necessary to include a factor in the model, which reflects more accurate effect of OH, and 3) Nevertheless, it is possible to model the complicated soot formation processes in a counterflow diffusion flame with the above three Arrenius type equations and one molecular coagulation equation.

Model test

To enable validation and further refinement of the proposed model, a two-step computation scheme, which incorporates the soot model, was developed. Step 1, SANDIA code OPPDIF was used to compute flame structures with imposed experimental boundary conditions and temperature profiles. This computation would produce the conserved scaler profile for each of the considered flame case. Step 2, a set of ODE equations along with our soot model were numerically solved. The computed soot number density and soot volume fraction profiles were thus compared with

experiments.

The first set of computations involved three flames (BA, BE and BC). These flames were selected because they were less complicated by addition of CO_2 and H_2O. The predicted soot number density and soot volume fraction along with measurements were presented in Figure 9. It is seen that not only did the model correctly predicted the soot particle number and soot mass, but also it reveal the experimentally observed phenomena: as the preheating temperature increased with the reduction in O2 concentration, soot nucleation sites moved toward the flame because of the reduced OH.

The second set of computations were of two counterflow diffusion flames published in the literature (one by Axelbaum, [14] and one by Vandersbuger [15]). It is important to test our model against these two flame because they used different fuel (C_2H_6 as opposed to CH_4). We first used OPPDIF along with experiment conditions to compute the flame structures. Figure 10 compared measured velocity and temperatures with computations, which showed reasonable agreement. In figure 11 and 12, we compare model predicted soot field with measurements. It showed qualitative agreement. Although the model correctly predicted the soot formation process, it slightly underpredicted soot number density and soot volume fraction.

Our computations using different fuel but identical boundary conditions has indicted apparent difference of fuel consumption characteristics in the sooting zone (C_2H_6 consumed far more than CH_4 ahead of the flame). Thus it might be necessary to include another factor in the soot nucleation model at account for this effect.

Conclusions

A simple model of soot formation is developed based on detailed measurements in counterflow diffusion flames. The model formulation incorporates the observed physical and chemical

phenomena pertaining to : (i) Nucleation; which occurs in the orange zone of the three-color (blue-yellow-orange) flame structure and is modeled in accordance with the homogeneous nucleation theory; (ii) Coagulation; which significantly influences the number density in the orange zone. A theoretical expression for this is taken from the literature; and (iii) Surface growth; which is taken proportional to the soot surface area and the local unoxidized carbon concentration. This model is intentionally cast in terms of mixture fraction variables such that it can be easily applied to turbulent diffusion flame calculations. It has been extensively tested against experiments where the thermochemical environment of the flame was changed by changing the preheating temperature and by introducing CO2 and H2O.

The agreement of soot prediction using the model with experiments was very encouraging. However, many issues remain which require attention. Especially, how to account for OH effect , which has been experimentally proved to be crucial in soot formation, and how to account for fuel structure effect. These are precisely the on-going effort in our work. Nevertheless, this work has shed light on a unique approach in soot modeling: experimentally based soot model.

Acknowledgements

This work was supported by the Gas Research Institute under contract number GRI 5087-260-1481 and technical direction of Drs J. N. Kezerle and T. R. Roose and by National Science Foundation under contract number NSF CBT-8552654. The first author would also like to thank Professor G. F. Carrier and Drs F. E. Fendell and H. R. Baum for their interests in this study and several helpful discussions.

REFERENCES

1. Carrier, G. F., Fendell, F. E. and Marble, F. E.: J. App. Math 28(3), 463 (1974)

2. Peters, N.: Prog. Energy Comb. Sci. 10, 319 (1984)

3. Baum, H. R., Rehm, R. G. and Gore, J. P.: 23th Symposium (International) on Combustion, The Combustion Institute, (1990)

4. Frenklach, M., Clary, D. W., Cardiner, W.C., and Stein. S. E. (1985), 20th Symposium (Intl) on Combustion, The Combustion Institute, pp.887-901

5. Frenklach, M., and Warnatz, J. (1987), Combust. Sci. Tech., 51, 265

6. Frenklach, M. (1988). 22nd Symposium (Intl) on Combustion. The Combustion Institute, p1075

7. Frenllach, M. and Wang, H. (1990), 23rd Symposium (Intl) on Combustion, The Combustion Institute. p1559

8. Fairweather, M., Jones, W.P. and Lindstedt, R.P., (1992)., Combust. Flame 89, 45

9. Hall. R.J., Smooke, M.D. and Colket, M.B., (1994) submitted to Combust Sci and Tech

10. Kennedy, I.M., Kollmann. W., and Chen, J., (1990) Combust. Flame 81,73

11. Honnery, D.R., Tappe, M. and Kent, J.H., (1992), Combust Sci and Tech., 83,305

12. Stewart, C.D., Syed, K.J. and Moss, J.B., (1991) Combust Sci and Tech, 75,211

13. Zhang, C., Atreya, A. and Lee, K. (1992) 24th Symposium (International) on Combustion, The Combustion Institute, pp1049-1057

14. Vandsburger, U., Kennedy, I. M. and Glassman, I.: Twentieth Symposium (International) on Combustion, p.1105, The Combustion Institute, (1984)

15. Axelbaum, R. L., Flower, W. L. and Law, C. K.: Comb. Sci. and Tech. 61, 51 (1988)

16. Kee, R.J., Rupley, F.M. and Miller, J.A., (1989) SANDIA report

17. Kee, R. J., Miller, J.A., Evans, G.H. and Dixon-Lewis, G., (1988) 22nd Symposium (International) on Combustion, The Combustion Institute, pp1479-1494

18. Gordon, S. and Mcbride, B. J.: NASA SP-273 (1970)

19 Smooke, M.D., Seshadri.K., and Puri, I.K.: Comb. & Flame 73, p.45 (1988)

20. Santoro, R.J., Miller, J. H.: Langmuir 3, 244 (1987)

21. Smyth, K. C., Tjossem, P. J. H., Hamins, A. and Miller, J. H.: Comb. & Flame 79, 366 (1990)

22 Harris, S.J., and Weiner, A.M., (1988) 22nd Symposium (Interna-tional) on Combustion, The Combustion Institute, p333

23. Friedlander, S. K.: Smoke, Dust and Haze, Wiley, (1977)

24. Haynes, B.S., and Wagner, H. G., (1981) Progress in Energy and Comb. Sci, 7,229

25. Nagle, J. and Strickland-Constable, R. F.: Fifth Conference on Carbon, 154, (1962)

Preheating Temperature (K)	Fuel Composition	Oxidizer Composition	Remarks
300	65%CH_4+35%N_2	16%O_2+84%He	This work, BA flame
300	65%CH_4+15%N_2+12% CO_2+8%He	16%O_2+84%He	This work, IA flame
300	65%CH_4+21%CO_2 +14%He	16%O_2+84%He	This work, MA flame
300	65%CH_4+31.4%N_2+3.6% H_2O	16%O_2+84%He	This work, WAF flame
300	65%CH_4+35%N_2	16%O_2+80.4%He+ 3.6%H_2O	This work, WAO flame
900	65%CH_4+35%N_2	11%O_2+89%N_2	This work, BB flame
900	65%CH_4+15%N_2+12% CO_2+8%He	11%O_2+89%N_2	This work, IBF flame
900	65%CH_4+21%CO_2+ 14%He	11%O_2+89%N_2	This work, MBF flame
900	65%CH_4+35%N_2	11%O_2+69%N_2+12%CO_2 +8%He	This work, IBO flame
900	65%CH_4+35%N_2	11%O_2+54%N_2+21%CO_2 +14%He	This work, MBO flame
1200	65%CH_4+35%N_2	9.7%O_2+90.3%N_2	This work, BC flame
1200	65%CH_4+21%CO_2+ 14%He	9.7%O_2+90.3%N_2	This work, MCF flame
1200	65%CH_4+31.4%N_2+3.6% H_2O	9.7%O_2+90.3%N_2	This work, WCF flame
300	100%C_2H_4	21%O_2+79%N_2	Axelbaum et al
300	100%C_2H_4	18%O_2+82%N_2	Vandersburger et al

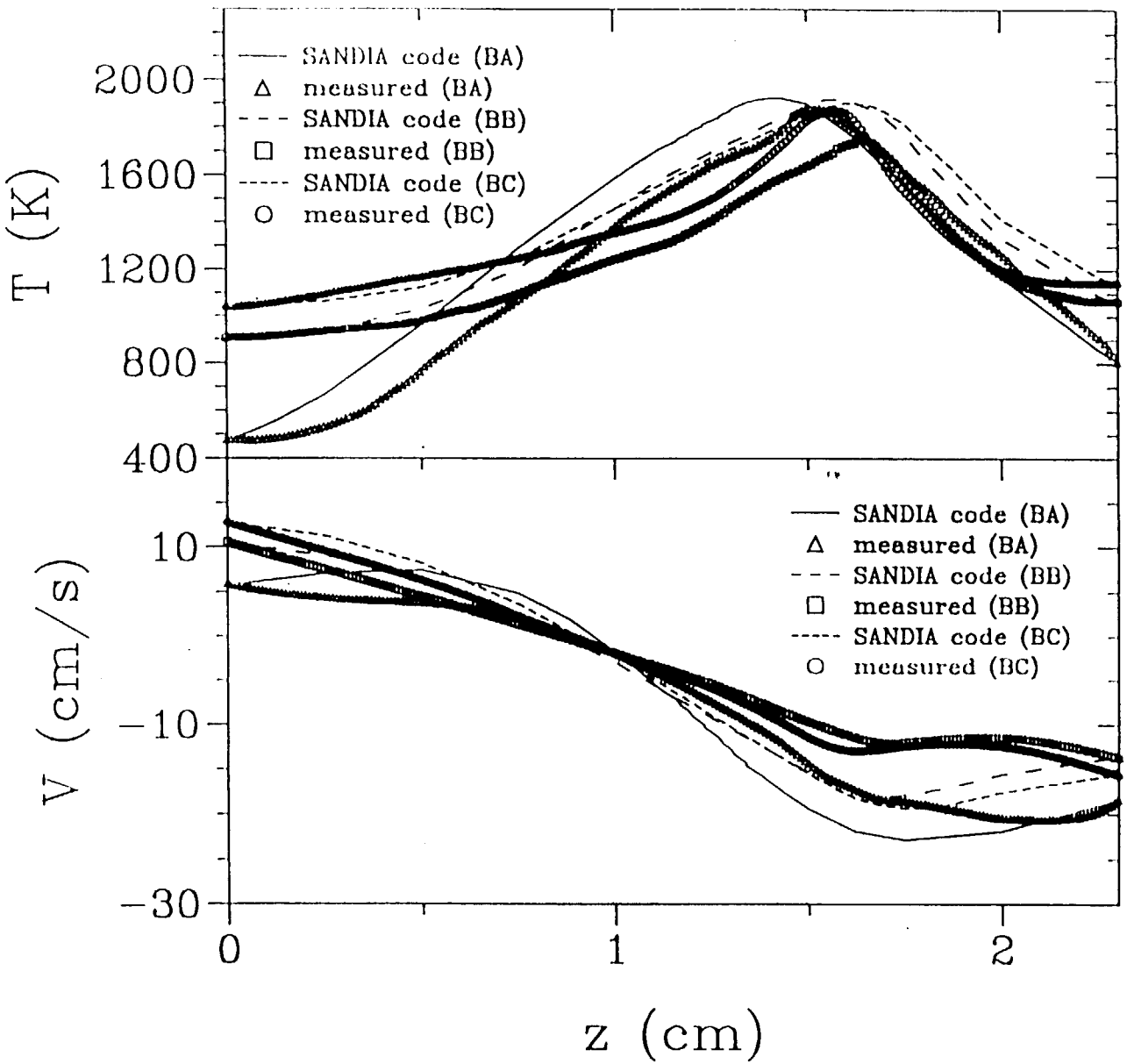
SANDIA code (BA)
measured (BA)
SANDIA code (BB)
measured (BB)
SANDIA code (BC)
measured (BC)
T (K)
2000
1600
1200
800
400
SANDIA code (BA)
measured (BA)
SANDIA code (BB)
measured (BB)
SANDIA code (BC)
measured (BC)
V (cm/s)
10
−10
−30
0
1
2
z (cm)

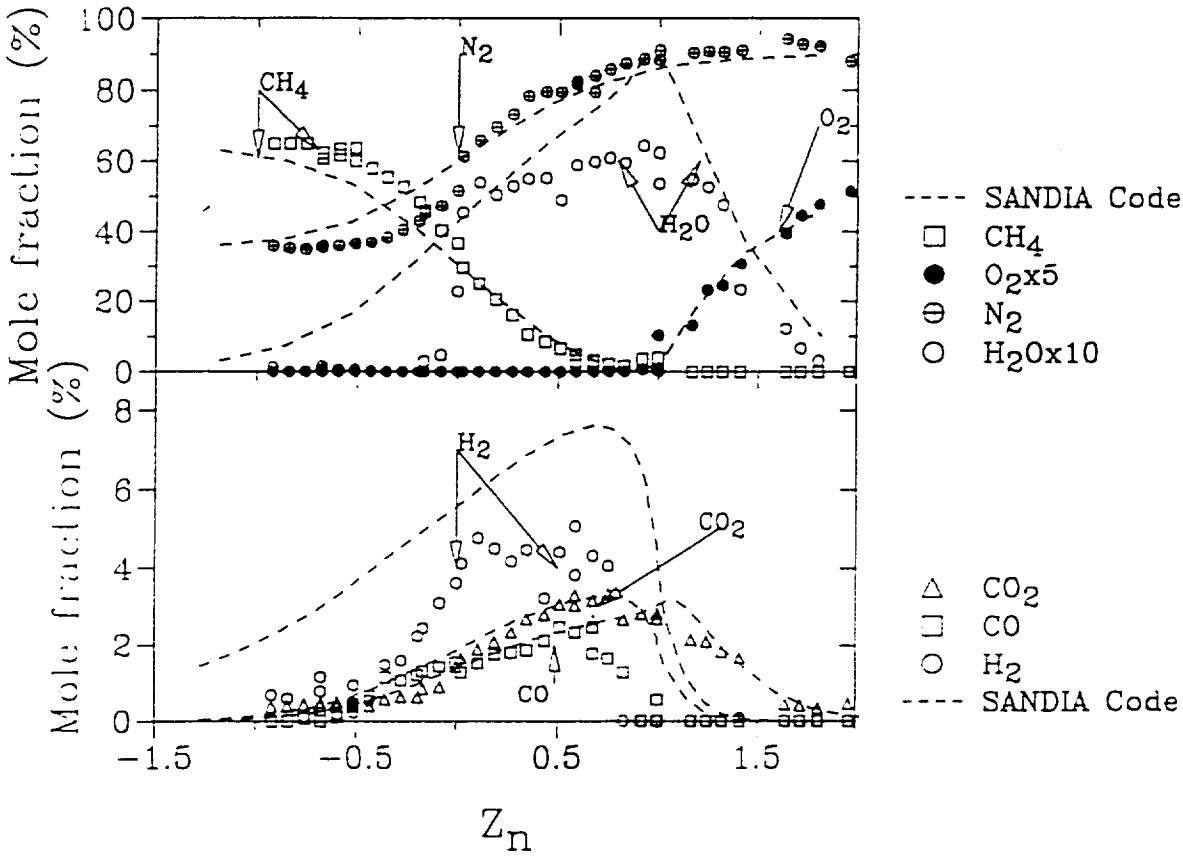
Mole fraction (%)
100
80
60
40
20
0
CH4
N2
O2
H2O
8
6
4
2
0
H2
CO2
CO
−1.5
−0.5
0.5
1.5
Zn
---- SANDIA Code
□ CH4
● O2x5
⊖ N2
○ H2Ox10
△ CO2
□ CO
○ H2
---- SANDIA Code

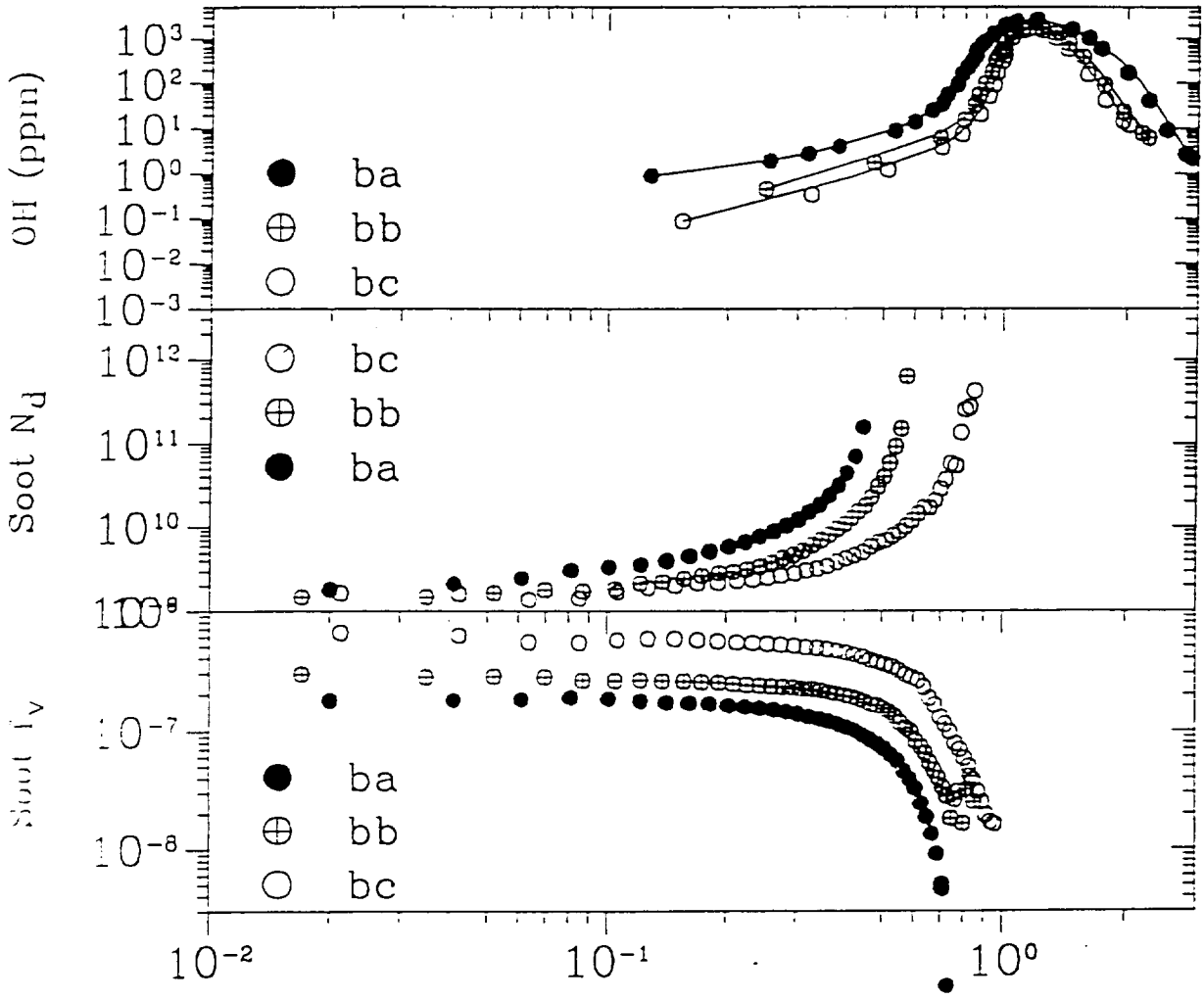
OH (ppm)
Soot N_d
Soot f_v
ba
bb
bc
10^{3}
10^{2}
10^{1}
10^{0}
10^{-1}
10^{-2}
10^{-3}
10^{12}
10^{11}
10^{10}
10^{-7}
10^{-8}
10^{-2}
10^{-1}
10^{0}
Z_n
(Z_n=1,flame location)

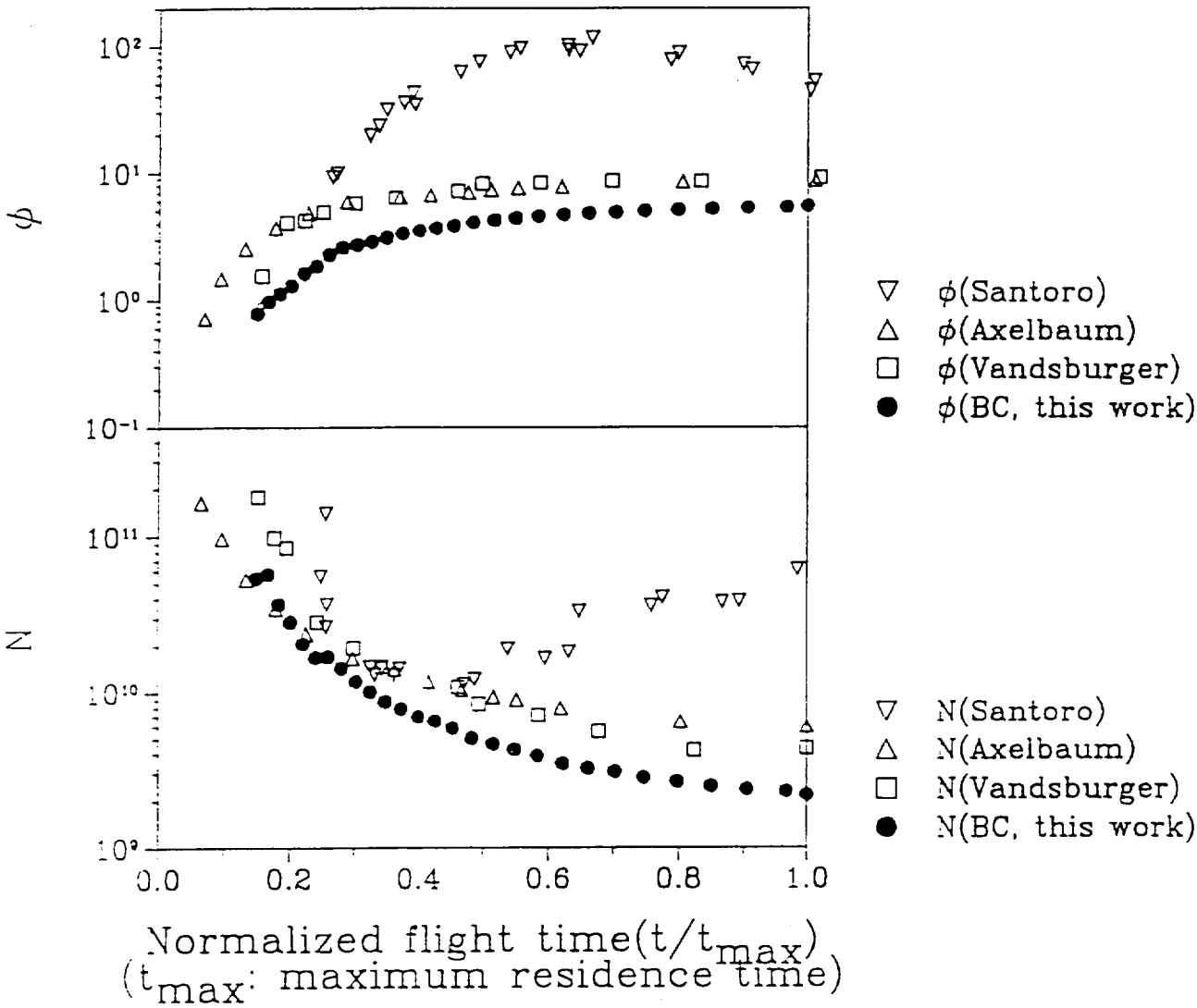
10^2
10^1
10^0
10^{-1}
ϕ
10^{11}
10^{10}
10^9
N
0.0
0.2
0.4
0.6
0.8
1.0
Normalized flight time(t/t_{max})
(t_{max}: maximum residence time)
▽ ϕ(Santoro)
△ ϕ(Axelbaum)
□ ϕ(Vandsburger)
● ϕ(BC, this work)
▽ N(Santoro)
△ N(Axelbaum)
□ N(Vandsburger)
● N(BC, this work)

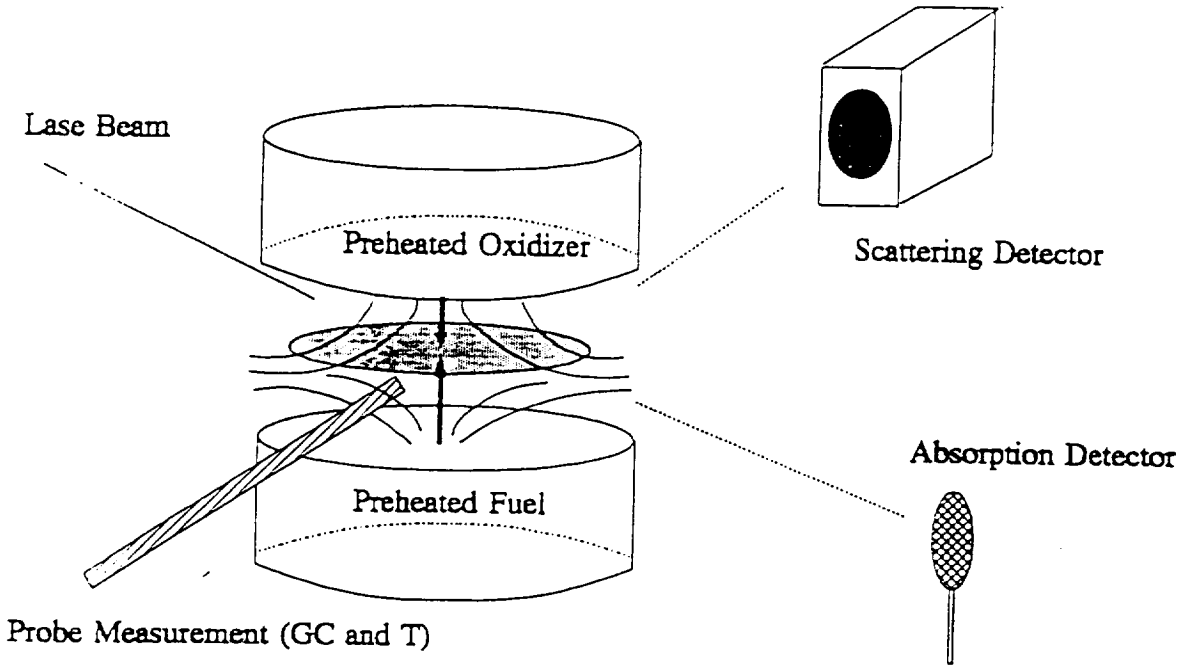

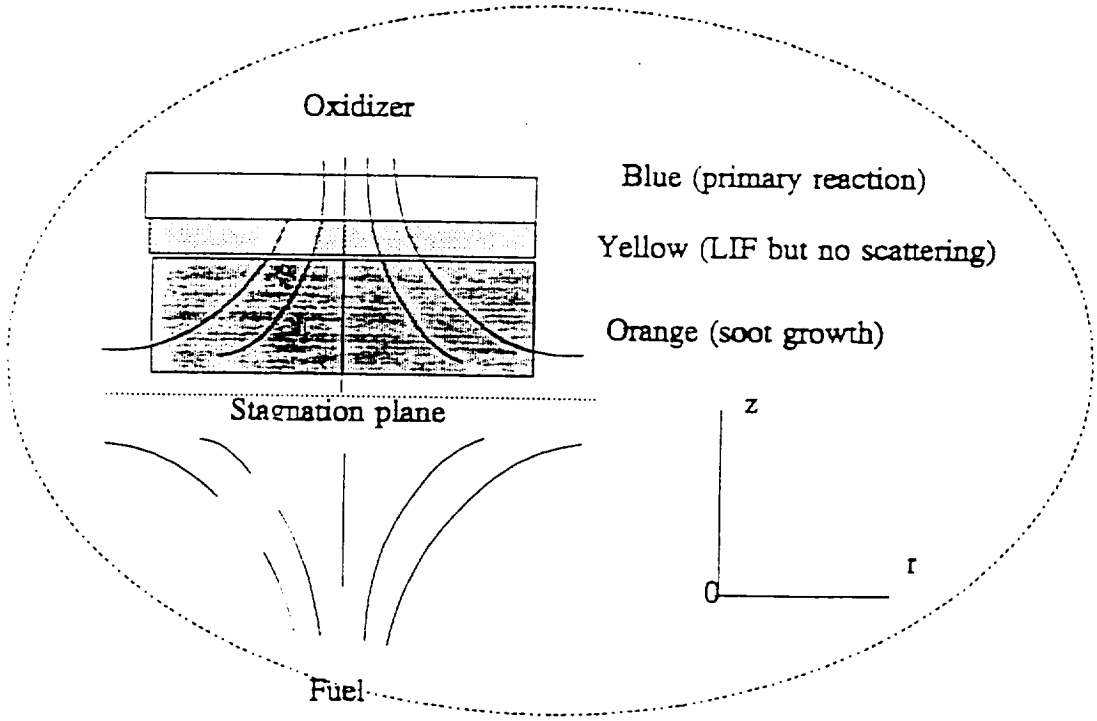

Flame Structure (close-up)

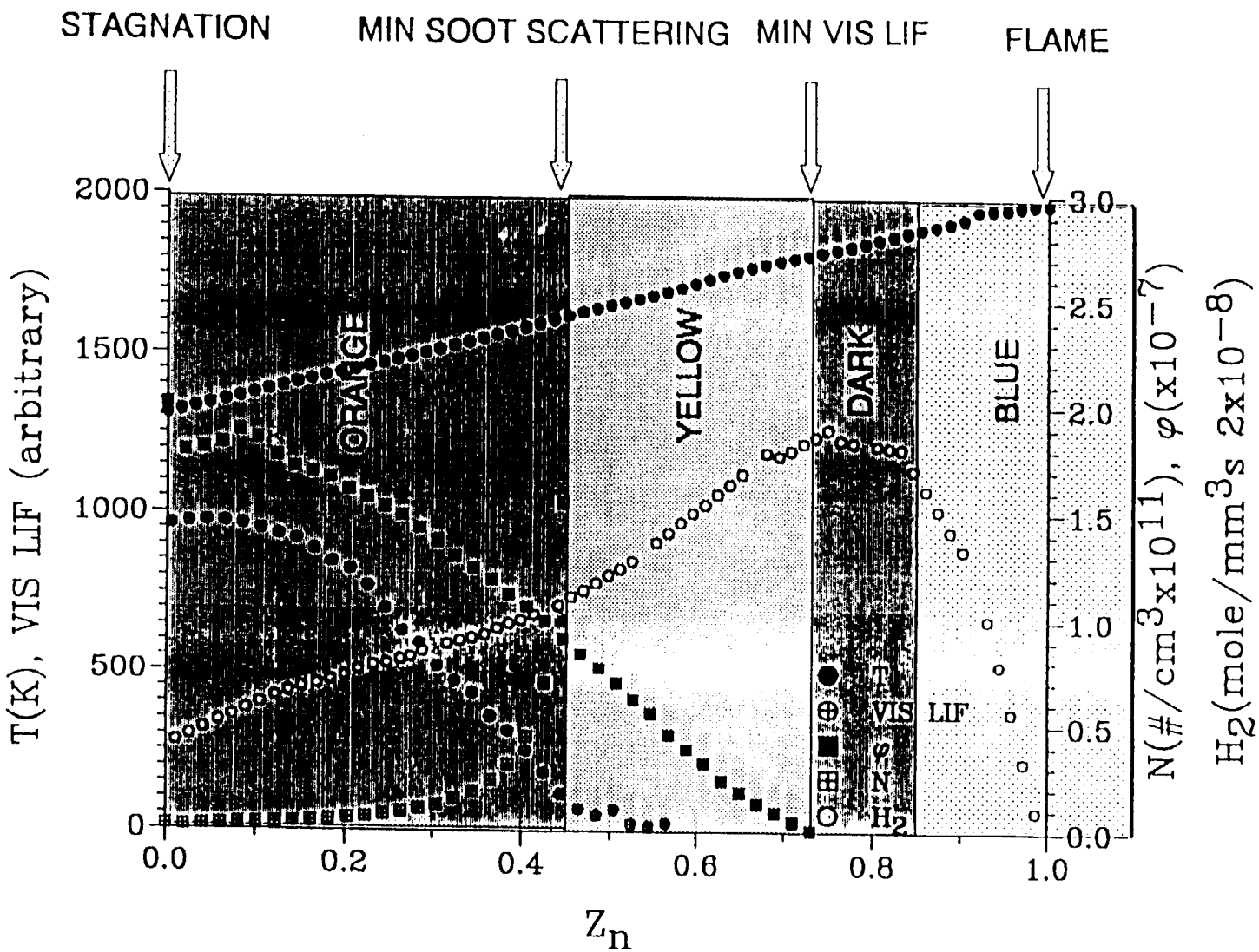
STAGNATION
MIN SOOT SCATTERING
MIN VIS LIF
FLAME
ORANGE
YELLOW
& DARK
BLUE
VIS LIF
T
O
N
H2
T(K), VIS LIF (arbitrary)
2000
1500
1000
500
0
0.0
0.2
0.4
0.6
0.8
1.0
Zn
3.0
2.5
2.0
1.5
1.0
0.5
0.0
N(#/cm3x1011), φ(x10−7)
H2(mole/mm3s 2x10−8)

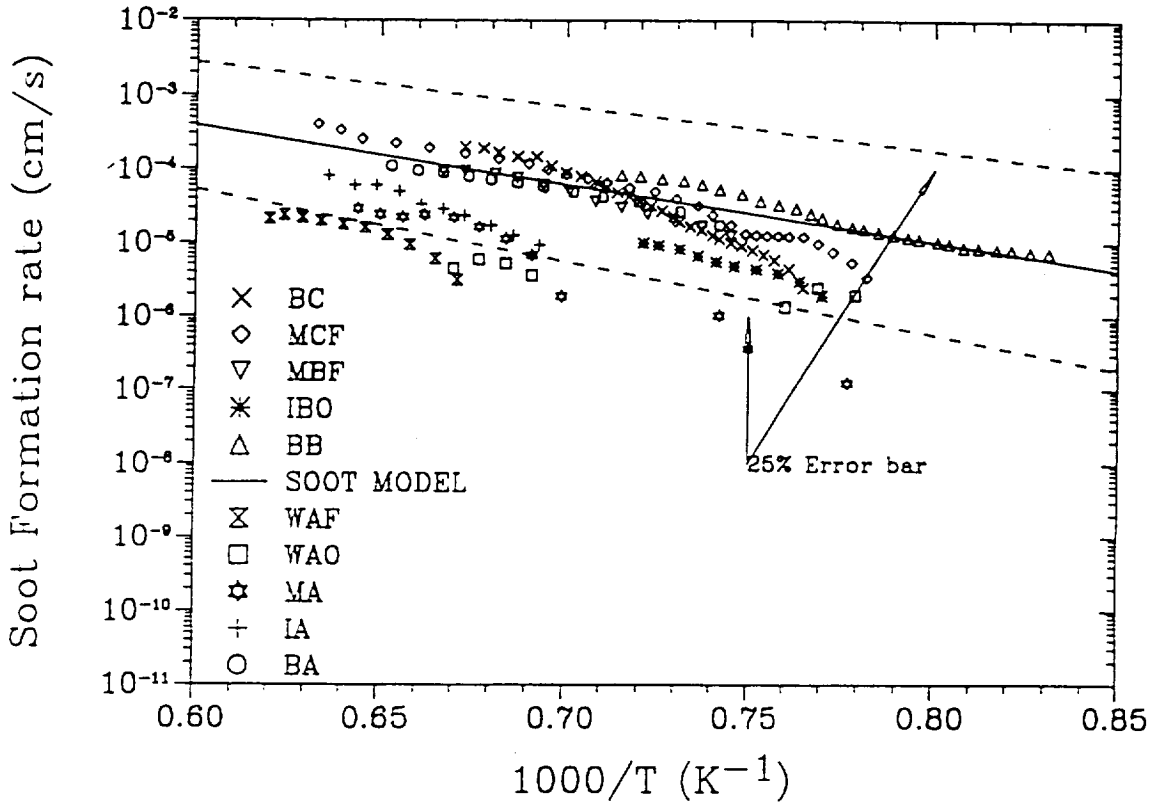
Soot Formation rate (cm/s)
10^-2
10^-3
10^-4
10^-5
10^-6
10^-7
10^-8
10^-9
10^-10
10^-11
0.60
0.65
0.70
0.75
0.80
0.85
1000/T (K^-1)
BC
MCF
MBF
IBO
BB
SOOT MODEL
WAF
WAO
MA
LA
BA
25% Error bar

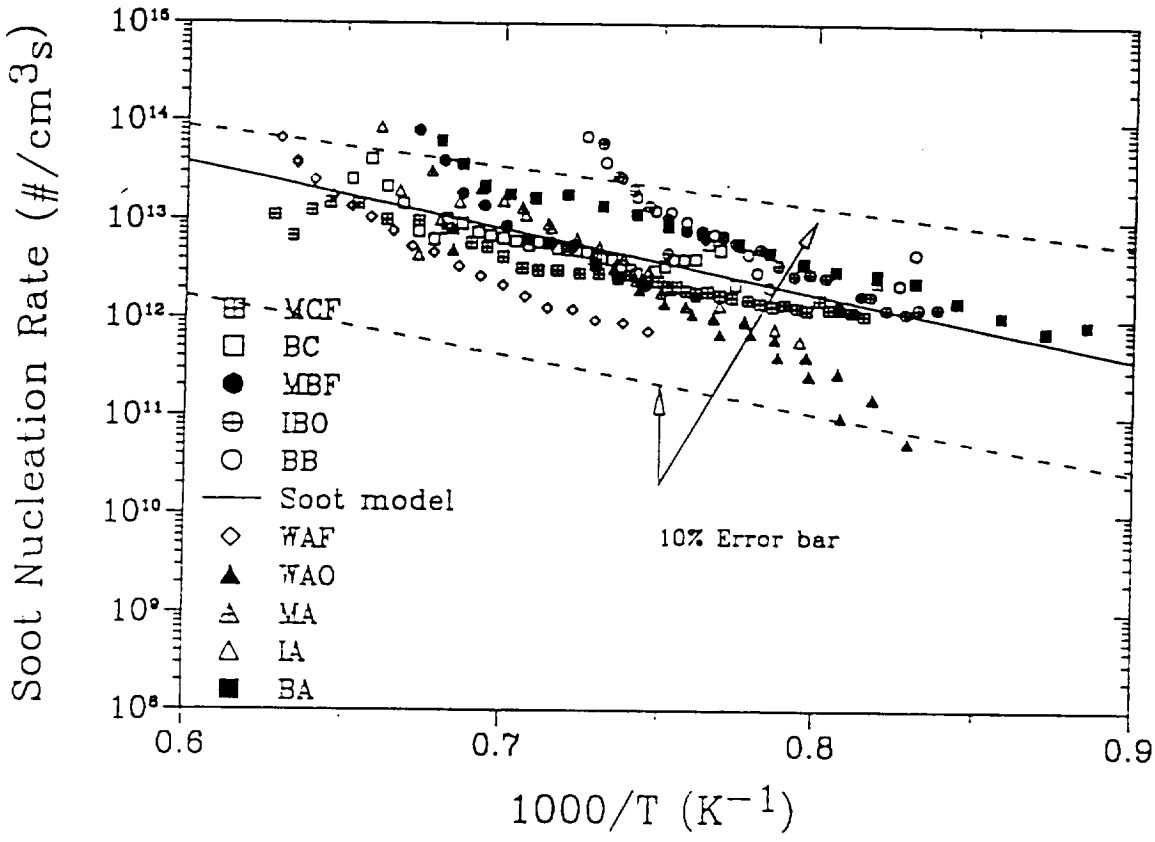
Soot Nucleation Rate (#/cm3s)
10^15
10^14
10^13
10^12
10^11
10^10
10^9
10^8
0.6
0.7
0.8
0.9
1000/T (K^-1)
MCF
BC
MBF
IBO
BB
Soot model
WAF
WAO
MA
IA
BA
10% Error bar

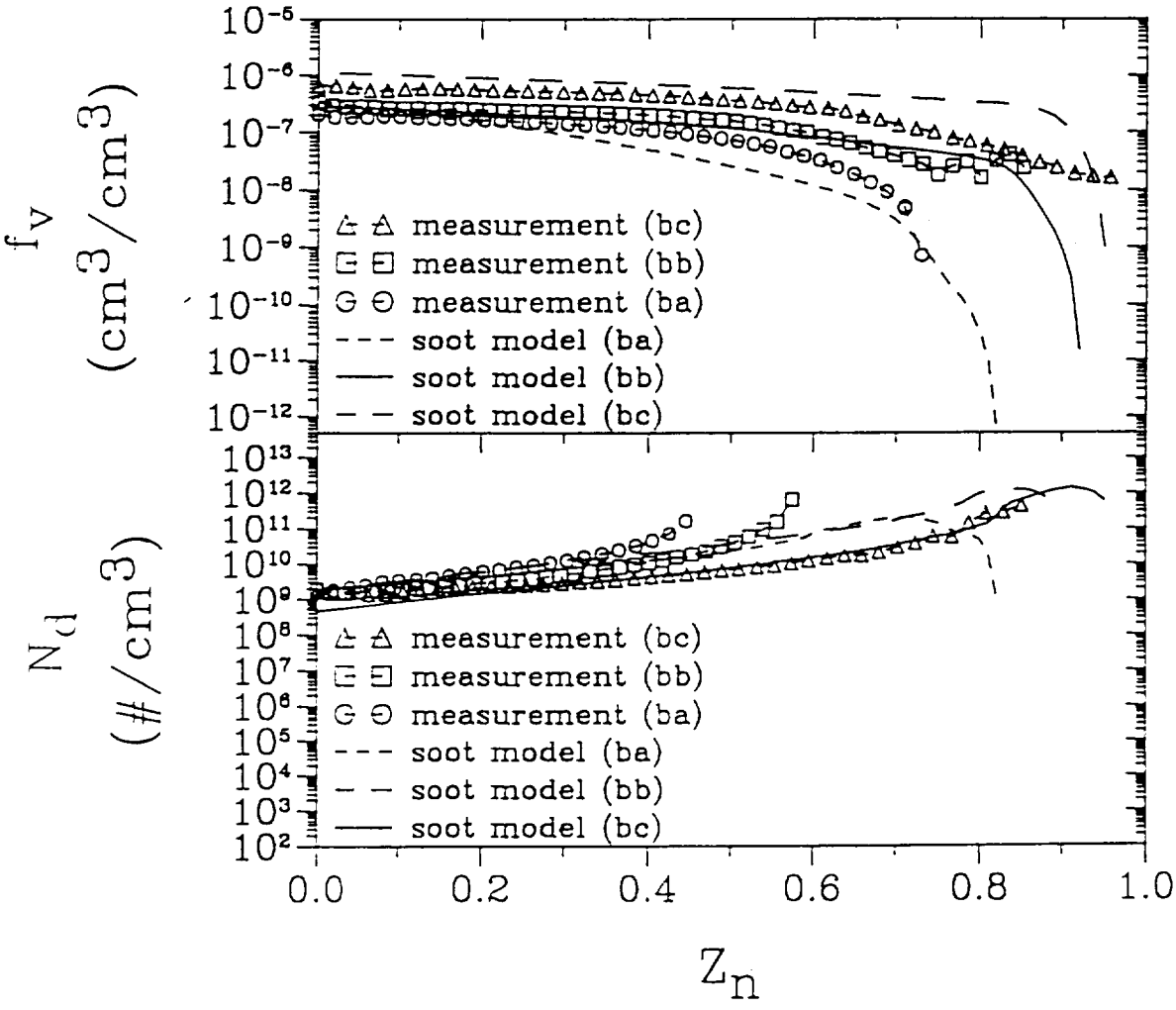
f_v (cm^3/cm^3)
10^{-5}
10^{-6}
10^{-7}
10^{-8}
10^{-9}
10^{-10}
10^{-11}
10^{-12}
measurement (bc)
measurement (bb)
measurement (ba)
soot model (ba)
soot model (bb)
soot model (bc)
N_d (#/cm^3)
10^{13}
10^{12}
10^{11}
10^{10}
10^{9}
10^{8}
10^{7}
10^{6}
10^{5}
10^{4}
10^{3}
10^{2}
measurement (bc)
measurement (bb)
measurement (ba)
soot model (ba)
soot model (bb)
soot model (bc)
0.0
0.2
0.4
0.6
0.8
1.0
Z_n

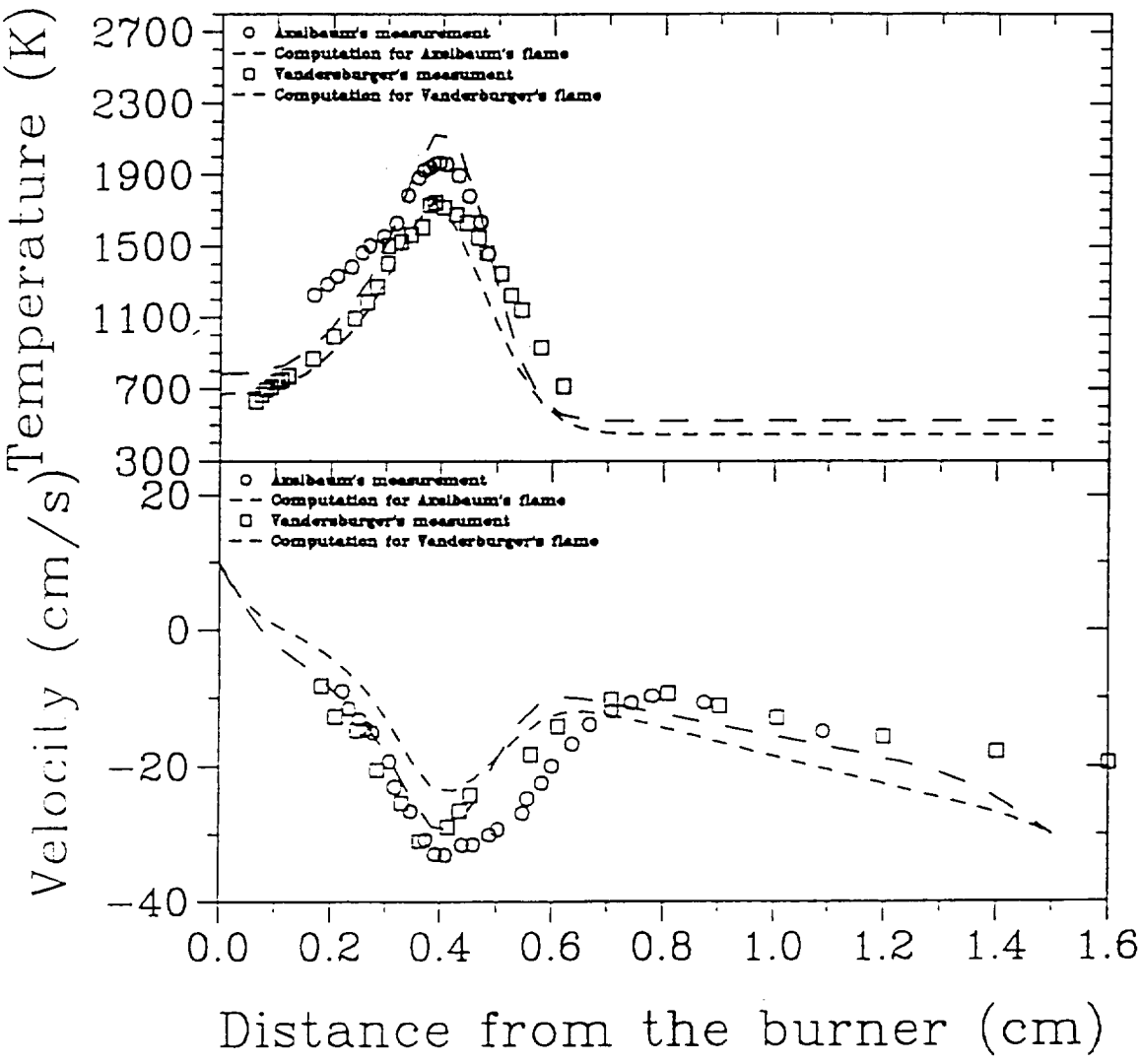
Temperature (K)
2700
2300
1900
1500
1100
700
300
Amalbeam's measurement
Computation for Amalbeum's flame
Vandersburger's measument
Computation for Vanderburger's flame
Velocity (cm/s)
20
0
-20
-40
0.0
0.2
0.4
0.6
0.8
1.0
1.2
1.4
1.6
Distance from the burner (cm)

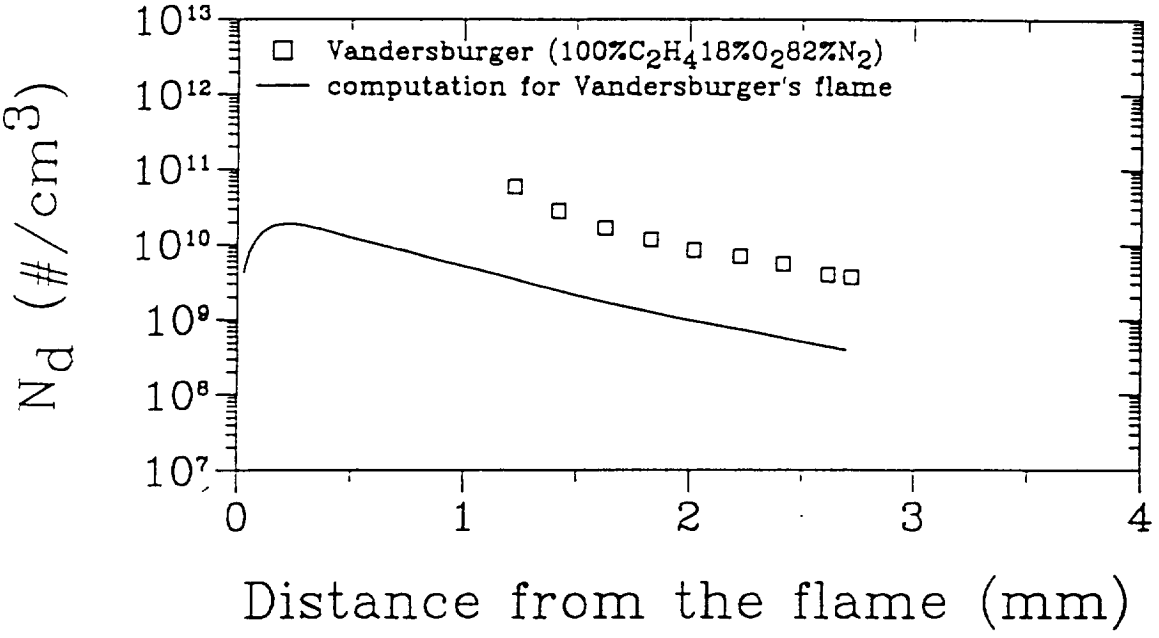
Vandersburger (100%C2H4 18%O2 82%N2)
computation for Vandersburger's flame
Nd (#/cm3)
10^13
10^12
10^11
10^10
10^9
10^8
10^7
0
1
2
3
4
Distance from the flame (mm)

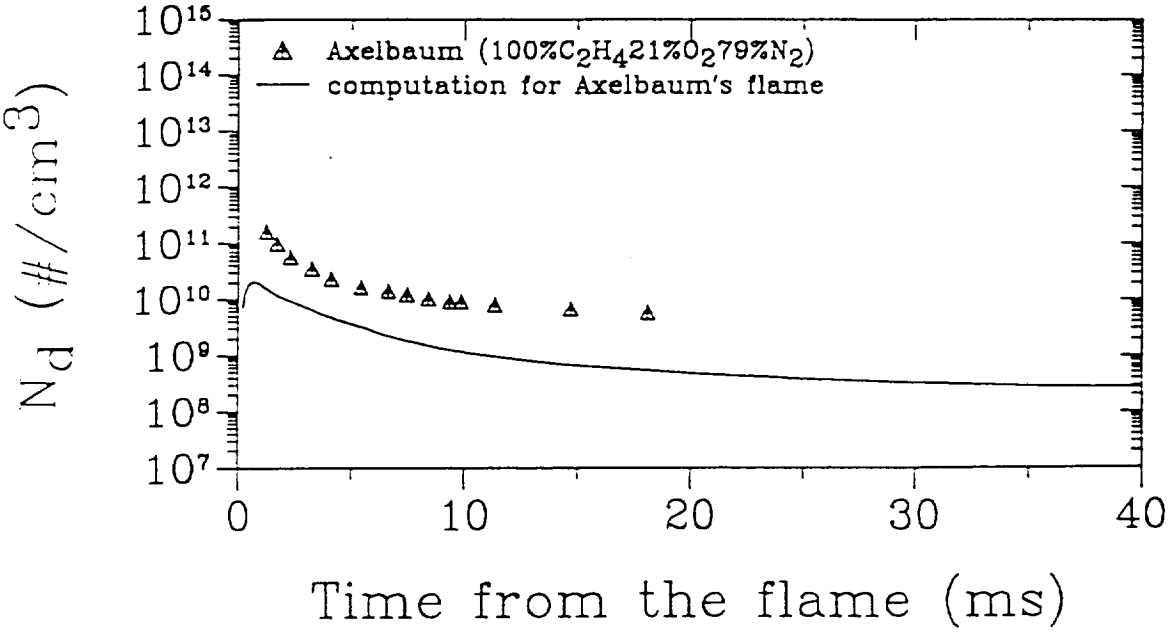
Axelbaum (100%C2H4 21%O2 79%N2)
computation for Axelbaum's flame
Nd (#/cm3)
10^15
10^14
10^13
10^12
10^11
10^10
10^9
10^8
10^7
0
10
20
30
40
Time from the flame (ms)

APPENDIX I

Measurements of Soot Volume Fraction Profiles in Counterflow Diffusion Flames Using a Transient Thermocouple Response Technique

Combustion Symposium paper

By

C. Zhang and Atreya, A.

Measurements of Soot Volume Fraction Profiles in Counterflow Diffusion Flames Using a Transient Thermocouple Response Technique

C. Zhang and A. Atreya

Combustion and Heat Transfer Laboratory

Department of Mechanical Engineering and Applied Mechanics

The University of Michigan

Ann Arbor, Michigan 48109

USA

Telephone: (313) 76-37471

Fax: (313) 74-73170

e-mail: czhang@engin.umich.edu

e-mail: aatreya@engin.umich.edu

paper length

text:	3353 words
equations:	7
figures:	9
table:	1

authors' preference

presentation:	oral
area:	Laminar Flames, Soot and PAH

1996.1.15

Measurements of Soot Volume Fraction Profiles in Counterflow Diffusion Flames Using a Transient Thermocouple Response Technique

C. Zhang and A. Atreya
Combustion and Heat Transfer Laboratory
Department of Mechanical Engineering and Applied Mechanics
The University of Michigan
Ann Arbor, Michigan 48109
USA

ABSTRACT

In this study, the previous work of Rosner et al[1-3] is extended by a simple mathematical model. This new model facilitates determining the profiles of soot volume fraction from measurements of the bead radius and the transient temperature of a soot deposited thermocouple. To demonstrate the feasibility of the developed technique, experiments were performed on a low strain-rate counterflow diffusion flame burner for methane and ethylene flames. Transient temperatures were measured by a Pt/Pt-10%Rh fine-wire thermocouple whose bead size was determined by a microscope. These measurements in conjunction with the model yielded the profiles of soot volume fraction. In addition, the in-situ laser scattering/extinction measurements and the flame spectroscopic analysis were conducted to confirm the thermocouple results. Excellent agreement was found between the two measurement techniques. From this study, it was also found that: (i) Soot deposits on the thermocouple can cause a "dent" in the temperature profile near the flame on the fuel side. This phenomenon persists in yellow flames even to the extent where absorption and scattering by soot is negligible (scattering-limit flame), which seems to support the concept of "transparent particles" recently proposed by D'Anna and D'Alessio[4]; and (ii) The magnitude of the observed temperature "dent" is proportional to the soot loading of different flames. In particular, this "temperature dent" in sooting flames is caused by the combined effect of two competing mechanisms: **soot deposition** due to thermophoresis and **soot oxidation** due to OH attack on soot deposits.

INTRODUCTION

The difficulties of making thermocouple temperature measurements in sooting flames are well documented[1-3,6]. The thermal radiation from the junction of a thermocouple to the surroundings forces the bead surface temperature to fall significantly below that of the adjacent gases. Such a negative temperature gradient will, in turn, drive the surrounding soot onto the thermocouple probe due to thermophoresis. Consequently, a layer of soot develops, which completely shields the bead of thermocouple from the ambient gas. This further reduces the bead temperature as the result of enhanced radiative heat loss due to (i) the higher emissivity of soot; and (ii) the continuous increase in the bead size because of soot deposition (see Fig.1).

While the soot deposition complicates the temperature measurements in sooty flames, the transient response of the thermocouple can be exploited to find the soot deposition rates, and these deposition rates can subsequently be related to local soot loading. Thus, with the aid of an appropriate model, local soot volume fractions can be determined from simple transient temperature measurements. This technique will be very valuable under circumstances where expensive and cumbersome laser diagnostics can not be afforded, such as in microgravity experiments.

Soot deposition has been of interest in many practical combustion systems. Previous work[1,3,7,8,20] have already identified thermophoresis (which is essentially soot particulates transporting "down" a temperature gradient) as the dominant transfer process leading to soot deposition. A recent study by Rosner et al[2] further concludes that thermophoretic properties of soot were essentially insensitive to aggregate size and morphology. Despite the progress made in these work, the emphasis has been

to investigate the mechanism and the rate of soot deposition onto an isothermal surface (combustors, engine walls or cold plates for collecting soot samples from flames). In the present study, we endeavored to extend the previous work of Rosner et al[1-3] by developing a simple mathematical model that facilitates determining the profiles of soot volume fraction in a sooting flame using transient thermocouple response measurements. In addition, we applied the developed technique to exploit further the effect of thermophoresis under various flame conditions, i.e., from a purely blue flame (non-sooty) to a yellow-orange flame (very sooty). Experiments were performed on fuel-rich methane and ethylene counterflow diffusion flames. Transient temperatures inside the sooting zone were measured by a Pt/Pt-10%Rh fine-wire thermocouple (wire diameter~0.2mm) where the bead size was determined by a microscope. Detailed soot volume fraction profiles were deduced from the measured thermocouple bead size as well as the transient temperature history using the model developed. These results were confirmed by the in-situ laser diagnostics and the flame spectroscopic analysis.

THEORETICAL

Based on the preceding discussions, a simple analysis of soot deposition onto a thermocouple bead is performed by assuming that:

(1) The thermocouple bead is simply a sphere and the soot deposition process is spherically symmetric;

(2) Soot particles are spherical droplets with monodispersed distribution;

(3) The emissivity of soot is unity ($\epsilon_s = 1$);

(4) The ambient gas surrounding the thermocouple is locally isothermal and homogeneous

and falls in the low Reynolds number flow regime, thus the Nusselt number is[6]:

$$Nu = \frac{hD}{k} = 2$$

(5) The conversion efficiency of surface collision is 100%, i.e., the particles that collide with the bead of thermocouple are completely absorbed into the soot layer.

(6) Local thermodynamic properties are constant for the thermocouple bead, soot deposits and gases;

(7) The thermocouple bead and the soot deposit layer have negligible thermal "inertia", i.e., the thermocouple instantaneously assumes the steady state temperature for a given bead size; and

(8) Heat transfer proceeds as the radiative heat loss from the "soot-coated" bead to the ambient through a layer of non-attenuating "thin gas" and as the convective heat gain from the ambient gases to the bead.

With these assumptions, we can derive the following equations:

Conservation of soot mass:

$$\frac{d}{dt}\left(\frac{4}{3}\pi R^3 \rho_s\right) = 4\pi R^2 j \qquad (1)$$

where the thermophoretic mass flux can be expressed as[3]:

$$j = -\frac{3\rho f_v \nu}{4(1+\frac{\pi}{8})}\left(\frac{1}{T}\frac{dT}{dr}\right)_{bead\ surface} \qquad (2)$$

Conservation of energy:

$$\sigma(T_R^4 - T_\infty^4) = h(T_g - T_R) \qquad (3)$$

Replacing the temperature gradient in equation (2) and using Nu=2 gives:

$$-\left(\frac{dT}{dr}\right)_{bead\ surface} = \frac{h(T_g - T_R)}{k} = \frac{(T_g - T_R)}{R} \qquad (4)$$

Combining with Eqs. (1) to (4), we get:

$$f_v = \frac{2(1+\frac{\pi}{8})\left(R(t_0)^2 - R(0)^2\right)}{\frac{3v\sigma}{k}\int_0^{t_0}\frac{R(t)(T_R^4(t) - T_\infty^4)}{T_R(t)}dt} \qquad (5)$$

Since R(t) is a slowly varying function of time as compared to $T_R(t)$ in the integrand, it can be further approximated as $(R(t_0)+R(0))/2$ to yield:

$$f_v = \frac{4(1+\frac{\pi}{8})\left(R(t_0) - R(0)\right)}{\frac{3v\sigma}{k}\int_0^{t_0}\frac{(T_R^4(t) - T_\infty^4)}{T_R(t)}dt} \qquad (6)$$

EXPERIMENTAL METHODOLOGY

The experimental apparatus used here is described in detail in our previous paper[5]. Briefly, laminar counterflow diffusion flames were stabilized on a well-designed low-strain rate flame burner. This burner was mounted on an X-Y-Z translating stage system that allows it to be moved relative to the optical measurement system with a resolution of 0.05mm in vertical motion. Flows of gas reactants

were measured with critical orifice flow meters. Flames selected for the present study were summarized in Table 1.

Temperature measurements were made using a Pt/Pt-10%Rh thermocouple with a wire diameter of 0.2 mm. The junction of the thermocouple was formed by butting Pt and Pt10%Rh wires together and coated with SiO_2 to prevent catalytic reaction. The thermocouple probe was made in a triangular configuration to minimize the heat conduction loss and was supported by a ceramic tube. For each experiment, the thermocouple bead size was measured two times under the microscope, prior to and after the soot deposition. The entire thermocouple assembly was mounted on a translating stage whose position was recorded by the computer data-acquisition unit along with the thermocouple temperature data.

Aside from thermocouple measurements, soot was also measured independently using the standard light scattering and extinction techniques. A schematic illustration of the optical apparatus and the burner is shown in Fig.2. Here a 5W Ion laser operating at 355nm, 488nm, 514nm and 1090nm lines was used. The laser beam was modulated using a mechanical chopper to allow for synchronized detection of the transmitted and the scattered light signal at the angles of 0^0 and 90^0 with respect to the incident beam. Additionally, flame emission spectroscopic analysis was conducted using the spectrograph and the ICCD detection system for studying the oxidation of soot deposits by OH attack. Emitted light from the flame was collected at 135^0 with respect to the incident beam by the detection optical fiber. The spatially resolved measurements of flame emission at 306.4nm were made to determine the OH distribution in the flame. However, in this work, these laser diagnostics

were used only for comparison purposes because the quantity of interests is the measurement of soot using thermocouple response technique.

RESULTS

A typical plot of the instantaneous change in the thermocouple bead temperature in response to the process of soot deposition and soot oxidation (burn-up) is shown in Fig.3. This was obtained by quickly inserting a "clean" thermocouple into the sooting zone (to detect soot deposition) and by inserting a "soot-coated" thermocouple into the oxidizing OH zone (to detect soot burn-up). Obviously, these two opposite processes were captured in the transient profiles of thermocouple response. As is seen in Fig.3, soot particles continuously built up on the bead surface, forcing the thermocouple temperature to drop throughout the sampling period. This process of soot deposition was sustained by the negative temperature gradient between the bead and the adjacent gases as a result of the continuous radiative "cooling". In contrast, soot oxidation occurred much fast. Within approximately 20 seconds, soot deposits burned out completely and the thermocouple temperature was stabilized at 1920K.

In order to apply the developed model to the actual soot measurements, we carefully selected two well-defined counterflow diffusion flames suitable for probe measurement. Figs.4 and 5 illustrate the sooting structure of the ethylene flame (a similar structure was also observed for the methane flame). Sandia burner code[9] (OPPDIF), which was modified to include gas radiation with boundary corrections, was used to compute for the flame structure. Soot measurements were performed for comparison with the subsequent measurements the using thermocouple response techniques. As

reported in our previous paper[5]: a blue-yellow-orange sooting flame structure emerged: the bright blue primary reaction zone was on the oxidizer side of the stagnation plane; a thick(3~4mm) yellow-orange sooting zone stayed at the fuel side and was separated from the blue flame by a thin dark zone. Soot inception occurred at the axial position z=15.5mm (measured from the fuel side). The newly formed soot particles were then swept downstream to coagulate and to grow until z=12.2 mm. This relatively thick (3~4mm) and well-defined sooting zone was important for resolving the soot volume fraction profile using a thermocouple whose bead diameter was 0.4mm.

Much work in the literature[10-12,20] has been devoted to collecting soot samples from flames for analyzing soot morphology (i.e., see the recent work by Koylu, Faeth, Farias and Carvalho[20]). To demonstrate the feasibility of measuring soot volume fraction profile using a thermocouple, a series of thermocouple responses taken at different locations inside the sooting zone (flame #1) are examined. Shown in Fig.6 are profiles of the bead temperature reduction and the reduction rate as a result of soot deposition (dT(t,z)/dt and T(t,z)). As was predicted, thermocouple temperature taken at the non-sooty location (flame zone) resulted in a straight line. However, once the thermocouple was placed inside the sooting zone, i.e., from the less-sooty inception location (Δz=1.59mm, measured from the flame) to the soot growth zone (Δz=5.08mm), it not only registered the magnitude but also the rate of bead temperature drop (i.e., Δz=1.59mm, ΔT_{max}~80K, dT/dt_{max} ~0.3 K/S; Δz=5.08mm, ΔT_{max}~130K, dT/dt_{max} ~2.6 K/S). These results confirm: *(1) local soot deposition is proportional to the soot volume fraction and (2) it is technically feasible to determine the soot volume fraction using the thermocouple response techniques.*

Measurements of soot volume fraction using thermocouple response techniques were conducted in two fuel-rich counterflow diffusion flames (flame #1 and flame #2). Eq.(6) was used to determine the soot volume fraction profiles from the measured thermocouple bead size along with the transient temperature data. Results of these measurements and the profiles of "soot-coated" bead size are shown in Fig.7. As is seen, the ethylene flame produced 10 times more soot as compared with the methane flame. Correspondingly, the maximum bead size (soot coated) at the highest soot loading location was 4.5 times that of the "clean" bead while for methane flame it was only about 50% increase in the bead size. Also included in this figure are the soot measurements using in-situ laser scattering and extinction techniques. Despite a relatively lower spacial resolution of thermocouple measurement (which was about 0.4mm in the present experiment) as compared to a much higher resolution of optical method (which was 0.05mm), a good agreement was clearly found in soot measurements between these two techniques, which demonstrated the feasibility of the developed new technique. From the figure, it also seems that the thermocouple measurements overestimate soot volume fraction in the heavy sooting zone. Three factors may have contributed to this discrepancy: (i) The thermophoretic velocity equation (Eq(2)), which was used to derive the soot surface flux, could become less vigorous in the final stage of soot growth where soot can appear as agglomerates; (ii) The constant property assumption (assumption (6)) ; and (iii) The approximation and the quasi-steady assumption used in deriving Eq.(6), which may also over-simplify the process in a heavy sooting zone. Therefore, it will benefit if a simple method could be introduced to measure the R(t) in "real time", which will thus enable removing several assumptions made in the present analysis.

DISCUSSION

The temperature "dent" phenomenon

It has long been known in the literature that temperature profiles normal to a flame can display a "dent" (slope discontinuity). In the past, two hypotheses were introduced to explain the observed phenomenon: (i) the effect of endothermic methane pyrolysis[13] and (ii) the effect of exothermic recombination of radicals onto the platinum thermocouple surface[14]. The second hypothesis deserved more attention here because the phenomenon of temperature "dent" occurred exclusively in those experiments where a thermocouple was used. Similar phenomena were not reported in numerical studies even with a full methane reaction mechanism. In line with the present work, we postulate that the observed "dent" phenomenon, at least in sooting flames, can be attributed to two competing mechanisms: **soot deposition** on the thermocouple due to the effect of thermophoresis and **soot oxidation** due to the effect of OH attack on soot deposits. The physics behind the phenomenon can be perceived as follows: when a thermocouple travels across a sooting zone in the direction of increasing gas temperature (i.e., from "cold" zone to "hot" zone, which favors thermophoresis), the local gas temperature is always higher than that of the bead at each instant. Consequently, soot accumulates on the thermocouple bead thereby reducing the bead temperature. This process can continue until the thermocouple is brought in contact with the high temperature OH pool, where soot deposits burn out (oxidize) via the heterogeneous reaction[15]:

$$C_{soot}\text{-}H(s) + OH \rightarrow products \qquad (7).$$

The depletion of the soot layer previously deposited on the thermocouple immediately reduces the radiative loss thereby bringing up the bead temperature. The combined effect of these two processes

can result in a "dent" in the temperature profile.

Figure 8 illustrates a result of the above-mentioned process. Here, temperature and OH profiles for the ethylene flame are shown. In this experiment, thermocouple was first traversed across the flame from the "hot zone" toward the "cold zone" (thus minimizing the soot deposition due to thermophoresis) to generate a reference profile. Then the direction of thermocouple travel was reversed, i.e., from the "cold zone" toward the "hot zone" (thus maximizing the soot deposition due to thermophoresis). This resulted in the second "soot-loaded" temperature profile. These two temperature profiles were plotted on the same figure and a temperature "dent" was clearly illustrated. Furthermore, this "dent" (the sharp change in the slope of the temperature profile) was found to occur near the peak of OH zone at the fuel side of ethylene flame. Thus, this experiment confirms our hypothesis for a sooty flame. From the results, it may also be inferred that in order to minimize the errors associated with soot deposition during thermocouple temperature measurement, one should traverse the thermocouple through the sooting zone in the direction of decreasing temperature (which is least favorable to soot thermophoresis) to avoid any temperature "dent". Furthermore, the rate of travel of the thermocouple should be as fast as possible but equal to or less than the inherent thermocouple response time. This method was adopted in all our temperature measurements and has been reported in our work[5,21].

Deposition of newly formed soot (d_p<3~4nm)

For soot formation, it is always critical to identify the transition of PAH into soot particles, i.e., soot inception. In our previous paper[5], we found that optically measurable soot exists only in the

orange zone of the blue-yellow-orange sooting flame structure. Indeed, even at the scattering-limit (characterized by varying the flame conditions until the light scattering due to soot is suppressed completely as compared to the background scattering due to gases[1,5]), flames may still emit a dim yellow color. Recently, D'Anna and D'Alessio[4] claimed that soot particles (typically 3~4nm) in their early age are "transparent" (with negligible absorption and fluorescence). An interesting question remained unanswered: *Do these "transparent particles" behave like normal soot particles? i.e., Do they still have thermophoretic properties?* To clarify this issue, we applied the above thermocouple techniques to three different flame conditions (to find the temperature "dent" due to soot): a sooting flame (flame #2), a scattering-limit flame (flame #3) and a yellow-blue transition flame (flame #4 which essentially appears blue). Shown in Fig.9 are the measured temperatures and the UV absorption profiles. It is interesting to note that the "dent" phenomenon persisted even at the scattering-limit flame with negligible UV absorption. It only disappeared when the flame became purely blue (non-sooty case, flame #4). This result seems to support the concept of "transparent" particles: *while soot precursors are optically "transparent" (with negligible absorption), they still have thermophoretic properties.* It further infers that soot inception begins beyond the optically-determined scattering-limit-an interesting issue that requires further exploration.

CONCLUSIONS

In this work, we have extended the previous work of Rosner et al[1-3] by developing a simple mathematical model to resolve the profiles of soot volume fraction using transient thermocouple temperature measurements. Excellent agreement was found between the soot volume fraction profiles determined by the thermocouple technique and those determined by the in-situ laser

scattering and extinction measurements. Thus, the feasibility of this developed technique was demonstrated. It was further found that:

(i) Soot deposits on the thermocouple can cause a "dent" in the temperature profile near the flame on the fuel side. This phenomenon persists in yellow flames even to the extent where absorption and scattering by soot is negligible (scattering-limit flame), which seems to support the concept of "transparent particles" recently proposed by D'Anna and D'Alessio; and

(ii) The magnitude of the observed temperature "dent" is proportional to the soot loading of different flames. In particular, this "temperature dent" in a sooting flame is caused by the combined effect of two competing mechanisms: **soot deposition** due to thermophoresis and **soot oxidation** due to OH attack on soot deposits.

NOMENCLATURE

c_s specific heat of soot

D diameter of thermocouple bead and soot particles.

f_v soot volume fraction

h heat transfer coefficient

I laser power

J' soot mass flux

k thermal conductivity

m_s' soot mass deposition rate

Nu Nussel number

r	radial coordinate
R	radius of the thermocouple bead
Re	Raynold number
T_∞	ambient temperature
T_g	local gas temperature
T_R	thermocouple bead temperature
T	temperature
Z	axial coordinate

Greek letters

ϵ	emissivity
μ	viscosity
ρ	gas density
ν	kinematic viscosity
σ	Stefan Boltzmann constant

ACKNOWLEDGEMENTS

This work was supported by GRI under the contract number GRI 5087-260-1481 and the technical direction of Drs. J.A. Kezerle and R.V. Serauskas; by NASA under the grant number NAG3-1460 and by NSF under the grant number CBT-8552654.

REFERENCES

1. Rosner, D.E. and Seshadri, K., *Eighteenth Symposium (International) on Combustion*, The Combustion Institute. Pittsburgh, 1981, p.1385.

2. Rosner, D.E., Mackowski, D.W. and Ybarra, P.G., *Combust Sci and Tech* 80: p.87, (1991).

3. Eisner, A.D. and Rosner, D.E., *Combust. Flame* 61: p.153, (1985).

4. D'Anna, A., D'Alessio, A. and Minutolo, P., in *Soot Formation in Combustion: Mechanisms and Models* (H. Bockhorn Ed.),Springer-Verlag, 1994, p.83.

5. Zhang, C., Atreya, A. and Lee,K., *Twenty-fourth Symposium (International) on Combustion*, The Combustion Institute. Pittsburgh, 1992, p.1049.

6. Ang, A.J., Pagni, P.J., Mataga, T.G., Margle, J.M. and Lyons, V.J., *AIAA Journal* 26 (3): p323, (1988).

7. Batchelor, G.K. and Shen, C., *J.of Colloid Interface Sci.*107: p.21, (1985).

8. Makel, D.B. and Kennedy, I.M., *Twenty-third Symposium (International) on Combustion*, The Combustion Institute. Pittsburgh, 1990, p.1551.

9. Kee, R.J., Rupley, F.M., Miller, J.A., *Sandia Report*, SAND89-8009B, (1991).

10. Jagoda, J.I., Prado, G. and Lahaye, J., *Combust. Flame* 37: p.261, (1980)

11. Dobbins, R.A. and Subramaniasivam, H., in *Soot Formation in Combustion: Mechanisms and Models* (H. Bockhorn Ed.),Springer-Verlag, 1994, p.290.

12. Smedley, J.M. and Williams, A., in *Soot Formation in Combustion: Mechanisms and Models* (H. Bockhorn Ed.),Springer-Verlag, 1994, p.403.

13. Tsuji, H., *Prog. Energy Combust Sci* 8: p.93, (1982).

14. Madson, J.M. and Theby, E.A., *Combust Sci and Tech* 36: p.205, (1984).

15. Frenklach, M. and Wang, H., *Twenty-third Symposium (International) on Combustion*, The Combustion Institute. Pittsburgh, 1990, p.1559

16. Du, D.X., Axelbaum, R.L. and Law, C.K., *Combst Flame* 102: p.11, (1995).

17. Rosner,D.E., *Transport processes in chemically reaction flow systems*, Butterworth-Heinemann, Stoneham, MA, 1990.

18. Heitor, M.V. and Moreira, L.N., *Prog. Energy Combust Sci* 19: p.259, (1993).

19. Friderlander,S.K., *Smoke, Dust and Haze*, Wiley Interscience, New York, 1977.

20. Koylu, U.O., Faeth, G.M., Farias, T.L. and Carvalho, M.G., *Combust. Flame100*: p.621, (1995).

21. Atreya, A., Zhang, C., Kim. H.K., Shamin, T. and Suh, J., submitted for *Twenty-sixth Symposium (International) on Combustion*, The Combustion Institute. Pittsburgh, 1996.

FIGURE CAPTION

Table 1 Flame conditions.

Figure 1 Sketch of the soot deposition process.

Figure 2 Schematic illustration of the burner and the apparatus.

Figure 3 Thermocouple response to the process of (i) soot deposition and (ii) soot burn-up (oxidation) for the ethylene flame. Note that soot oxidation completes less than 20s. In contrast, soot deposition proceeds continuously.

Figure 4 Profiles of measured temperature (corrected for thermocouple radiation), computed temperature and velocity for the ethylene counterflow diffusion flame. Sooting zone was at the fuel side of the flame.

Figure 5 Profiles of measured soot volume fraction, number density and particle size using

laser scattering and extinction techniques, assuming Rayleigh scatterer model with monodispersed distribution. This well-defined and relatively thick (~3.5mm) sooting zone ensured the feasibility of thermocouple probe measurement.

Figure 6 Profiles of the transient thermocouple bead temperature reduction T(t,z) and the rate of temperature drop dT(t,z)/dt at different locations of sooting zone. In this figure, the location of thermocouple was measured relative to the flame (maximum temperature).

Figure 7 Measurements of soot volume fraction using the thermocouple technique. Shown are the soot volume fraction and the size of "soot-coated" thermocouple bead. Also included are the soot measurements using laser scattering and extinction technique.

Figure 8 Effect of the soot deposition and the soot burn-up (oxidation) on profiles of measured temperature. The temperatures were obtained by traversing the thermocouple across the sooting zone in two directions (F-O: from the soot peak position toward the flame to maximize soot deposition; O-F: from the flame toward the soot peak location to minimize soot deposition). Shown also are the measured and computed OH profiles. Note that the location of the "dent" in temperature profile is coincident with the OH peak.

Figure 9 Effect of soot loading on the temperature profiles. Shown are the measurements of temperature (left), using the same technique as in Fig.8 and the UV absorption (right; the laser was operated at 355nm). They are for three different flames (from top to bottom): Blue flame (no soot); Scattering limit flame (negligible soot particle scattering) and Sooty flame.

TABLE 1
Flame Conditions

Flame #	Reactants Composition	Flow Rates (cold, cm^3/s)	Flame Temp. (uncorrected)	Observations	Max. Soot Loading
1	48.7%C_2H_4 51.3%N_2 84%O_2 16%He	121.0 194.1	1776	soot zone~ 3.5mm soot zone yellow orange	1.534×10^{-6}
2	28.9%CH_4 71.1%He 42.6%O_2 57.4%N_2	171.3 66.2	1864	soot zone~ 3mm soot zone yellow orange	1.010×10^{-7}
3	22.8%CH_4 77.2%He 42.6%O_2 57.4%N_2	231.0 66.2	1834	negligible scattering inception dim-yellow	none
4	15.3%CH_4 84.7%He 42.6%O_2 57.4%N_2	210.4 66.2	1703	non-sooty blue	none

ZHANG & ATREYA

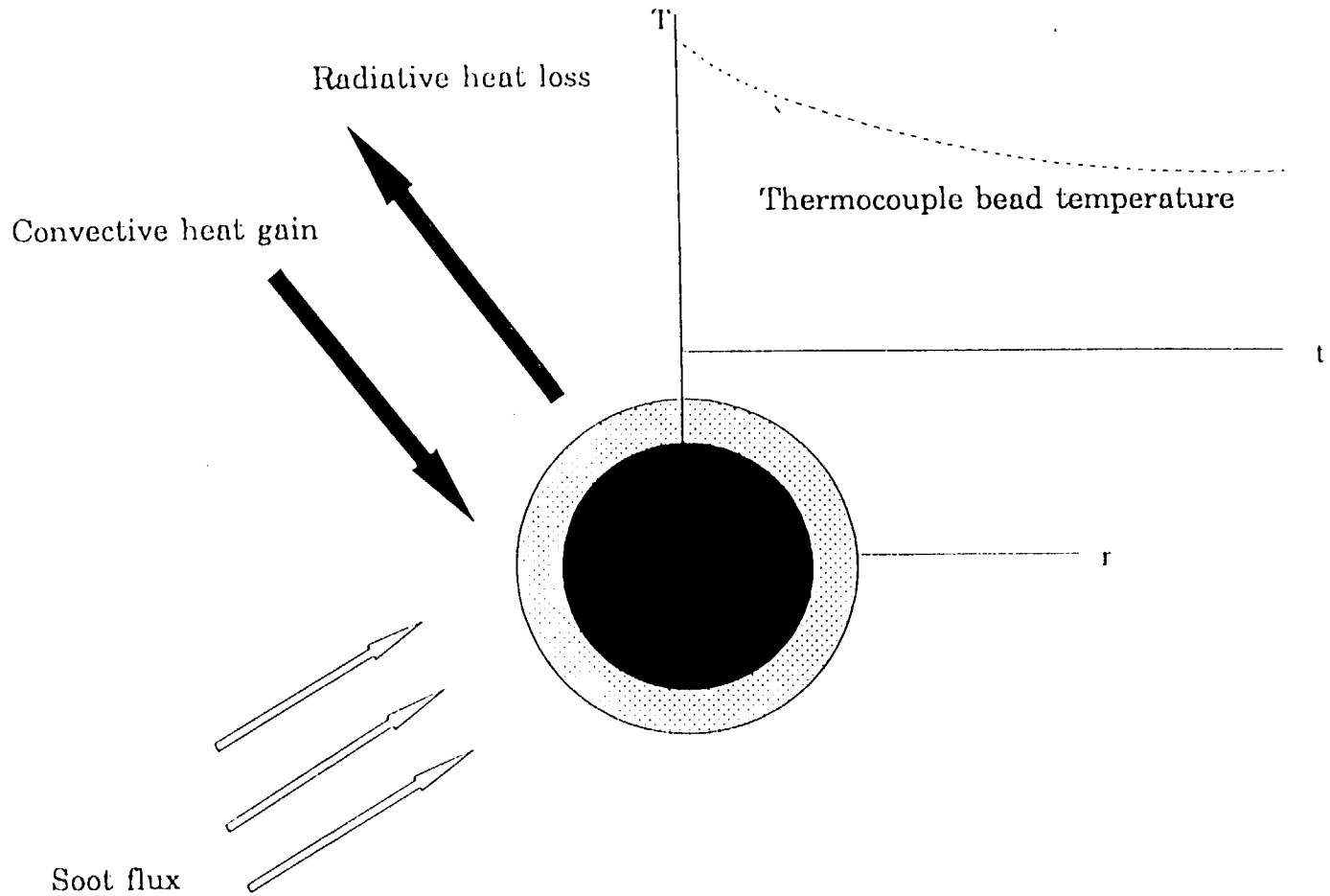

Fig. 1 TRAVIS & ATREYA

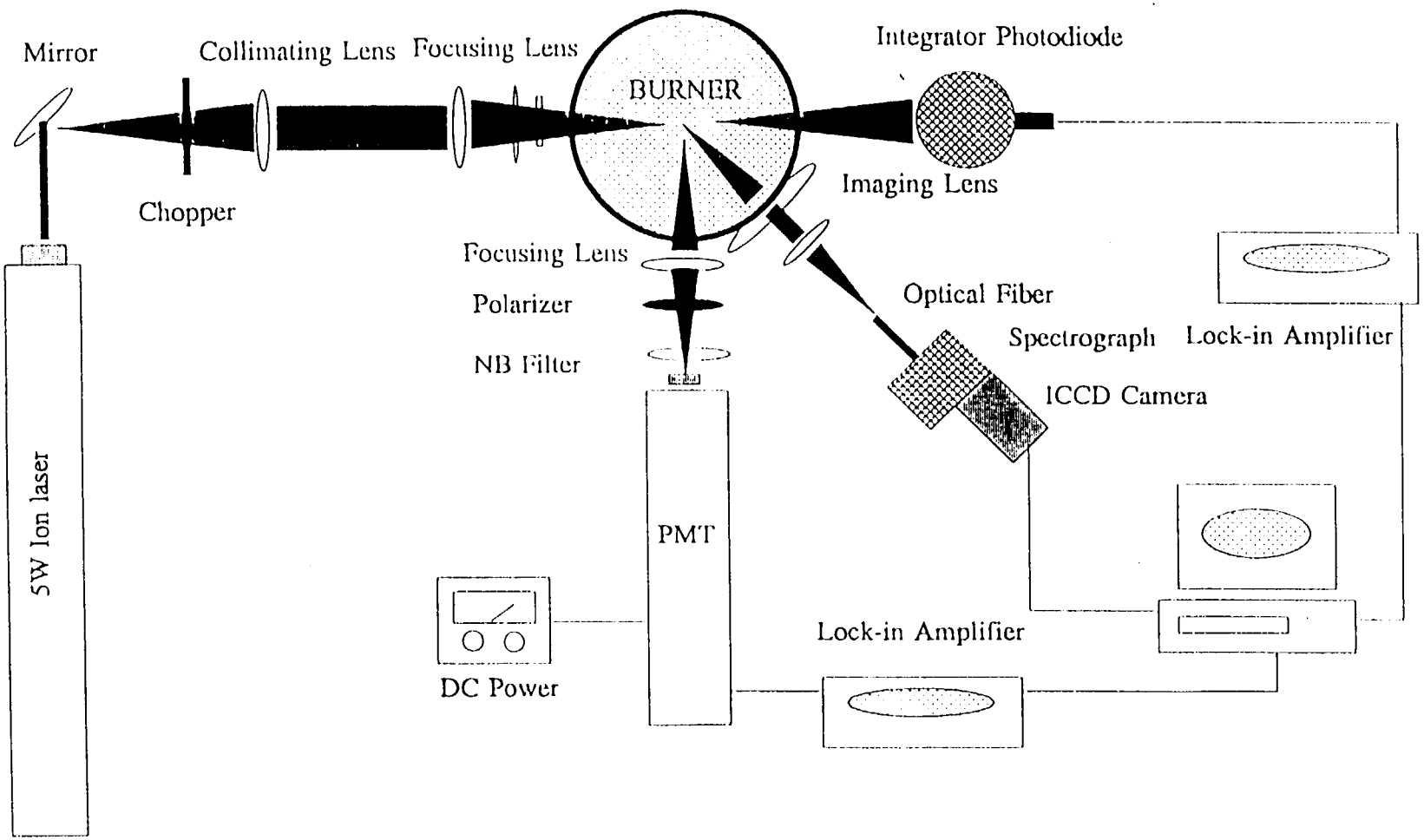

Fig 2 ZHANG & ATREYA

Fig 3 ZHANG & ATREYA

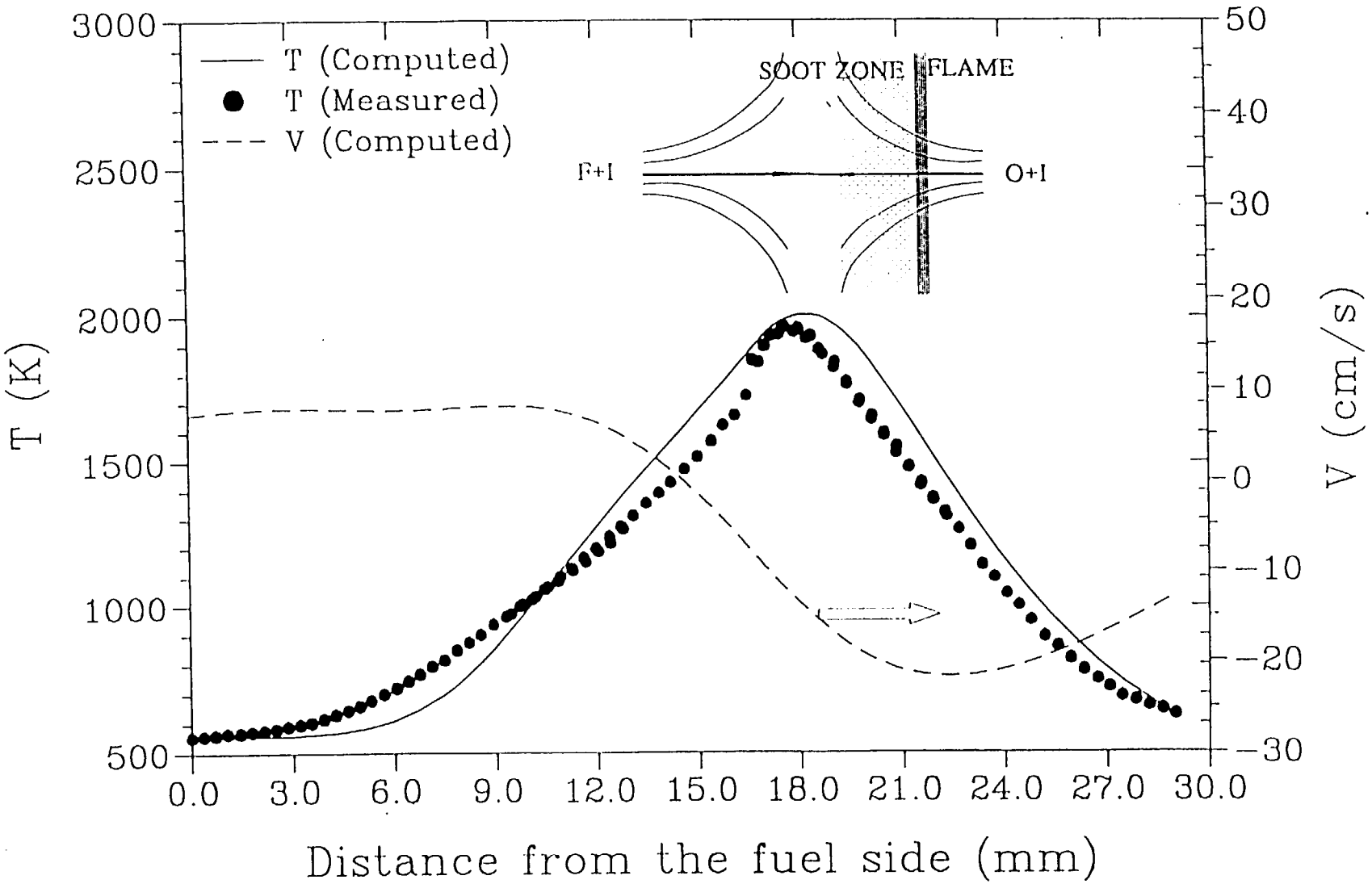
T (Computed)
T (Measured)
V (Computed)
SOOT ZONE
FLAME
F+I
O+I
T (K)
V (cm/s)
Distance from the fuel side (mm)
3000
2500
2000
1500
1000
500
50
40
30
20
10
0
-10
-20
-30
0.0
3.0
6.0
9.0
12.0
15.0
18.0
21.0
24.0
27.0
30.0

Fig. 8 ZHANG

Fig 5 ZHANG & ATREYA

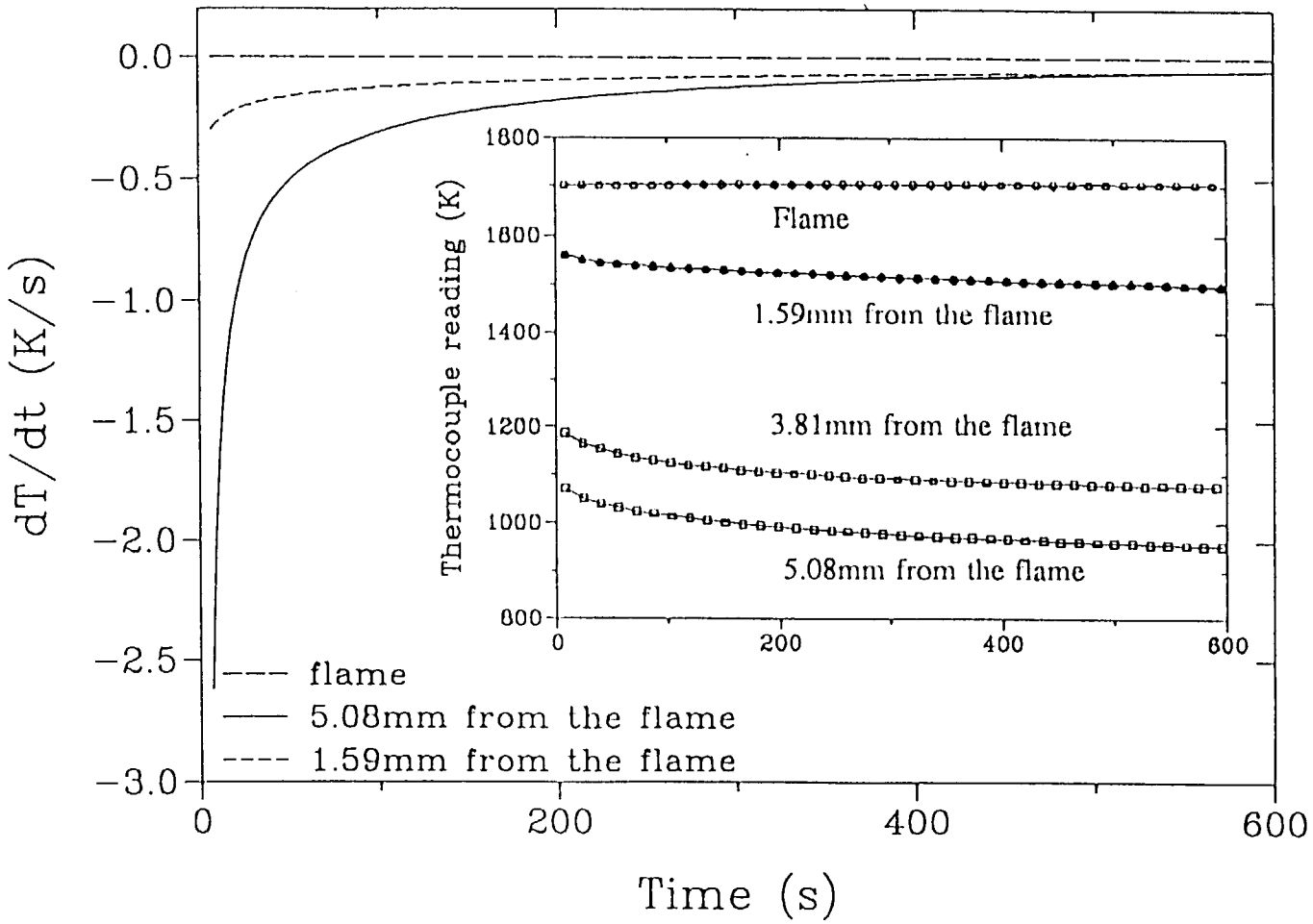

Fig 6 ZHANG & ATREYA

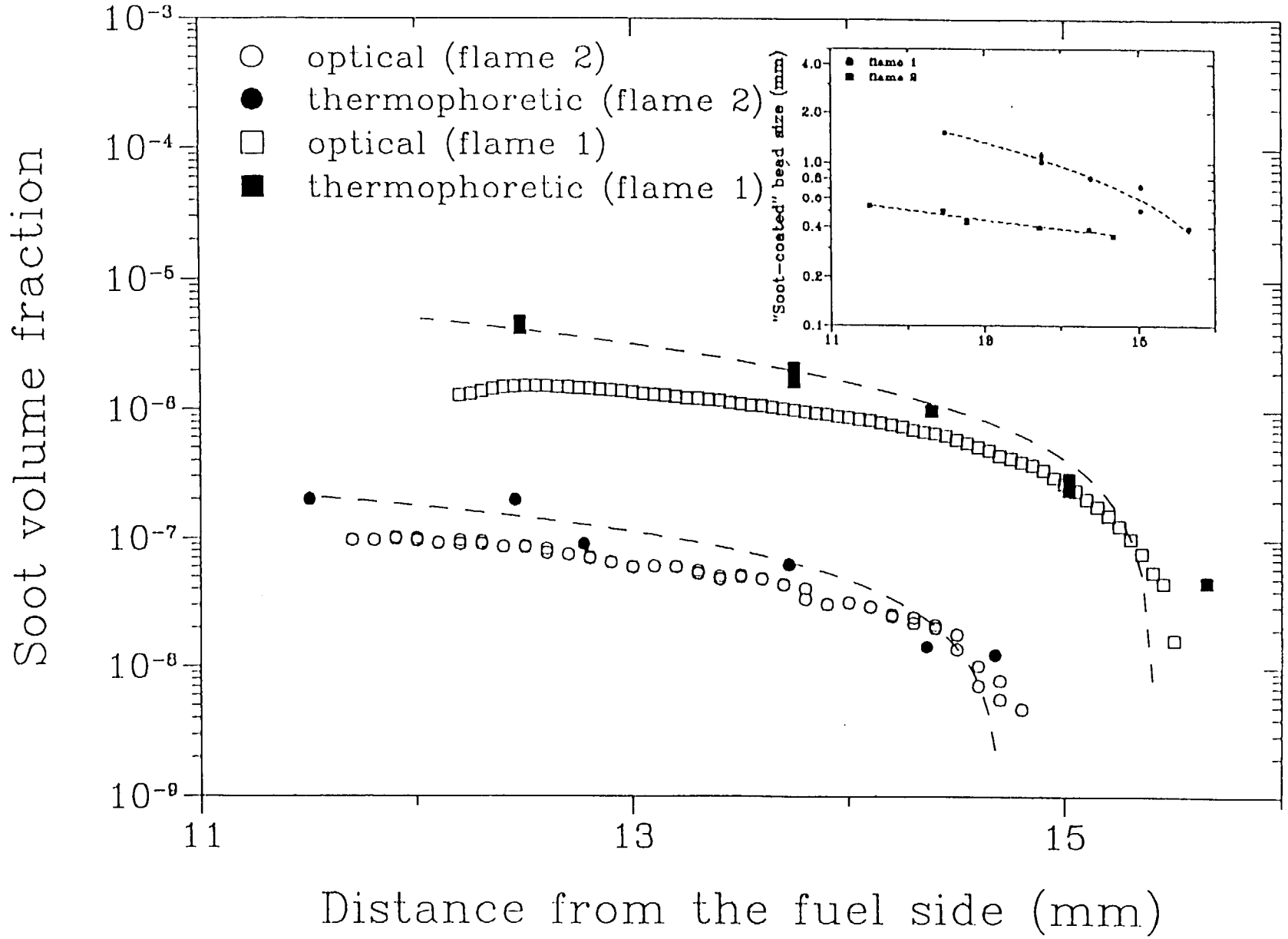

Fig 7 ZHANG & ATREYA

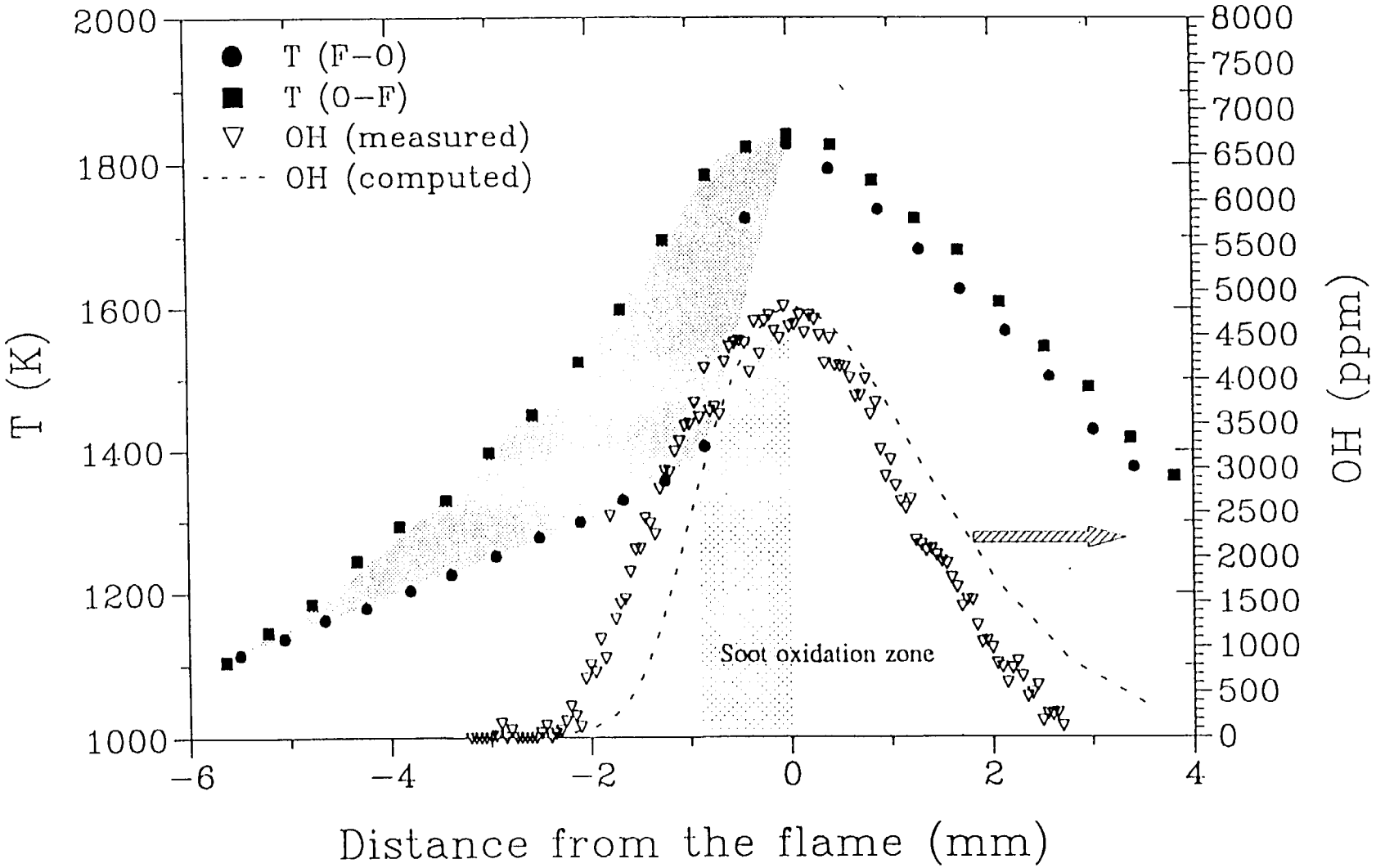

Fig 8 ZHANG & ATREYA

Fig 9 ZHANG & ATKEN

APPENDIX J

The Effect of Changes in the Flame Structure on Formation and Destruction of Soot and NO_x in Radiating Diffusion Flames

Combustion Symposium paper

By

Atreya, A., Zhang, C., Kim, H. K., Shamim, T. and Suh, J.

The Effect of Changes in the Flame Structure on the Formation and Destruction of Soot and NO_x in Radiating Diffusion Flames

A. ATREYA*, C. ZHANG, H. K. KIM, T. SHAMIM & J. SUH
Combustion and Heat Transfer Laboratory
Department of Mechanical Engineering and Applied Mechanics
The University of Michigan
Ann Arbor, MI 48109-2125
USA

Telephone: (313) 747 4790
Fax: (313) 747 3170
e-mail: aatreya@engin.umich.edu

* Corresponding author

1996.1.15

The Effect of Changes in the Flame Structure on the Formation and Destruction of Soot and NO_x in Radiating Diffusion Flames

A. ATREYA, C. ZHANG, H. K. KIM, T. SHAMIM & J. SUH
Combustion and Heat Transfer Laboratory
Department of Mechanical Engineering and Applied Mechanics
The University of Michigan
Ann Arbor, MI 48109-2125

ABSTRACT

In this study, soot and NO_x production in four counterflow diffusion flames with different flame structures is examined both experimentally and theoretically. The distance between the maximum temperature zone and the stagnation plane is progressively changed by changing the inlet fuel and oxidizer concentrations, thus shifting the flame location from the oxidizer-side to the fuel-side of the stagnation plane. One flame located at the stagnation plane is also examined. Detailed chemical, thermal and optical measurements are made to experimentally quantify the flame structure and supporting numerical calculations with detailed chemistry are also performed by specifying the boundary conditions used in the experiments. Results show that as the radical-rich, high-temperature reaction zone is pushed into the sooting zone, several changes occur in the flame structure and appearance. These are: (i) The flames become very bright due to enhanced soot-zone temperature. This can cause significant reduction in NO formation due to increased flame radiation. (ii) OH concentration is reduced from superequilibrium levels due to soot and soot-precursor oxidation in addition to CO and H_2 oxidation. (iii) Soot-precursor oxidation significantly affects soot nucleation on the oxidizer side, while soot nucleation on the fuel side seems to be related to C_2H_2 concentration. (iv) Soot interacts with NO formation through the major radical species produced in the primary reaction zone. It also appears that Fenimore NO initiation mechanism becomes more important when N_2 is added to the fuel side due to higher N_2 concentrations in the CH zone.

INTRODUCTION

The production of soot and NO_x in combustion processes is of considerable practical interest because of the need for controlling pollutant formation. Industrial furnaces that employ non-premixed natural gas burners use several methods of reducing NO_x. These are based upon decreasing the gas temperature and/or controlling the combustion process via staged introduction of fuel or air. Bowman[1] and Sarofim and Flagan[2] present excellent reviews of these NO_x control strategies and their underlying chemical mechanisms. One method of reducing the combustion gas temperature, and hence the NO_x production rate, is via enhanced flame radiation[3]. For industrial furnaces, this method has additional advantages because radiation is the primary mode of energy transfer in these systems. Thus, increasing the flame radiation also increases the efficiency of energy transfer to the objects in the furnace, and hence the furnace productivity.

Enhanced flame radiation can be accomplished by increasing the soot production rate in such a way that it is completely oxidized before leaving the flame zone. Thus, an important question is - *how should the non-premixed flames be configured to increase flame radiation, reduce NO_x and oxidize all the soot and hydrocarbons produced in the process?* In search of such flame configurations, a detailed experimental and theoretical study on a basic unit of a turbulent diffusion flame (a radiating laminar flamelet) was conducted. The objective was to explore the interrelationships between soot, NO_x, transport processes and flame radiation. Experimentally, methane counterflow diffusion flames (CFDF) were used to represent these flamelets and their thermal, chemical and radiation structure was measured and modeled.

Clearly, if soot can be forced into the high temperature reaction zone, then flame radiation will be enhanced and soot and other hydrocarbons will be simultaneously oxidized. Our previous experimental work[4] shows that this can be accomplished by bringing the CFDF to the fuel side

of the stagnation plane (SP). To realize such flame configurations, we note that: (i) In CFDFs all particulate matter (such as soot) is essentially convected toward the SP. Thus, bringing the soot zone closer to the reaction zone implies bringing the peak temperature region closer to the SP. (ii) The location of the SP is determined by momentum balance and the location of the flame is determined by stoichiometry. In an ideal diffusion flame, fuel and oxidizer diffuse into the flame in stoichiometric proportions. Thus, by adjusting the diffusive mass flux of fuel and oxidizer, flame location can be altered relative to the SP. While the diffusive mass flux can be changed by changing the 'ρD' product, the most convenient method is to adjust the inlet fuel and oxidizer mass fractions. To examine the benefits of changing the flame location relative to the SP, comparisons of the detailed flame structure measurements and calculations are needed for flames on the fuel side, on the oxidizer side and at the stagnation plane. While there have been several previous experimental and theoretical studies of CFDF structure[5-8], they have been limited to normal flames that lie on the oxygen side of the SP. Recently, Du and Axelbaum[9] have investigated limiting strain rates for soot suppression in CFDFs as a function of the stoichiometric mixture fraction and numerically examined the structure of two flames on the fuel and the oxidizer side of the SP. Similar studies in coflow flames have also been recently presented by Sugiyama[10] and Faeth and coworkers[11]. However, flame structure measurements and comparisons for sooting flames are not available in the literature. This study provides such measurements and comparisons and investigates the effect of changes in the flame structure on formation and destruction of soot and NO_x.

EXPERIMENTAL METHODS

The experiments were conducted in a unique high temperature, low strain rate CFDF burner. Various diffusion flame conditions were obtained by changing the inlet fuel & oxidizer

concentrations and flow rates. Low strain rates were maintained to facilitate measurements of the flame structure. All measurements were made along the axial streamline of a flat axisymmetric diffusion flame roughly 8 cm in diameter. One dimensionality of scalar variables in the flame was confirmed by radial temperature measurements. All gases used in the experiments were obtained from chemical purity gas cylinders and their flow rates were measured using calibrated critical flow orifices. The complete experimental apparatus including the optical and the gas chromatography setup is described in detail elsewhere[7].

The soot volume fraction and the number density were measured by using an Ar-ion laser. The soot aerosol was assumed monodispersed with a complex refractive index of 1.57-0.56i. These measurements were highly repeatable (within ±3%). OH concentration was measured by laser saturated fluorescence[12,13]. The relative OH measurements were calibrated using detailed chemistry calculations for a non-sooty (blue) methane flame. OH measurements were repeatable to within ±10%.

Other chemical species were measured by gas chromatographs. A quartz microprobe (~100μm dia.) was used for extracting the gas sample from the flame. The gas sample was then distributed via heated lines and valves to the GCs and the NO_x analyzer. Gasses measured were: CO, CO_2, H_2O, H_2, CH_4, He, O_2, and N_2; light hydrocarbons from C_1 to C_6; & PAHs up to C_{18}. The GC and NO_x measurements were accurate to within ±5%, except for H_2O which had variations larger than ±10%.

Temperatures in the flame were measured by a Pt/Pt-10%Rh thermocouple (0.125mm wire diameter). The thermocouple was coated with SiO_2 to prevent possible catalytic reactions on the platinum surface. It was traversed across the flame in the direction of decreasing temperature at a rate fast enough to avoid soot deposition and slow enough to obtain negligible transient

corrections. These temperature measurements were estimated to be accurate to within ±30K after radiation corrections. However, the repeatability was within ±10K.

The experimental flame conditions used for the measurements are summarized in Table I. These flames were measured three times on separate days to check for overall repeatability. This was found to be within the repeatability of the individual measurements. Table I also lists the measured locations of the peak flame temperature (and its value) and the locations of the SP. Note that very low strain rate flames (6-9 sec^{-1}; defined as half the velocity gradient at the SP) were used to facilitate flame structure measurements. In flames 1 and 2, N_2 was used as the diluent for O_2, whereas in flames 3 and 4, N_2 was used as the diluent for CH_4. This was done to simulate the effect of fuel side N_2 on NO formation. Helium was used as the other diluent to help experimentally stabilize these low strain rate flames. Flame 1 was a very sooty flame located significantly on the air side of the SP, whereas, flame 4 was on the fuel side. The mixture fraction 'Z' listed in the table was calculated as the sum of elemental carbon and hydrogen mass fractions[14].

NUMERICAL CALCULATIONS

To better understand the experimental results, numerical calculations with detailed chemistry were performed by specifying the experimental boundary conditions listed in Table I. Experimental burner separation of 29mm was used and the measured boundary temperatures and species mass fluxes were specified as boundary conditions. Like the experiments, the model considers a steady axisymmetric CFDF established between impinging fuel and oxidizer streams. The governing equations for the conservation of mass, momentum, species and energy were solved in the boundary layer form assuming potential flow at the boundary[6]. GRIMECH 2.11 mechanism (276 reaction equations and 50 species) with realistic multicomponent transport was

used in the numerical model. The numerical code used in this work was provided by A. E. Lutz and R. J. Kee[15]. The calculations were done using the measured temperature profiles to eliminate uncertainties caused by the flame radiation model. Some calculations were also done by solving the energy equation without the radiative heat loss term to evaluate the effect of flame radiation on NO_x production.

RESULTS AND DISCUSSION

Detailed flame structure measurements and calculations for the four flames are presented in this section. Figure 1 shows the measured temperature and the measured and calculated NO and OH concentrations for the low strain rate (~6sec^{-1}) blue reference flame. This flame was chosen to represent a typical non-sooty blue flame studied in the literature[5,6] with the hope that the kinetics employed will adequately represent the flame chemistry. The relative OH fluorescence measurements were calibrated using these calculations. The measured and calculated NO results show good agreement, except on the fuel side. The discrepancy on the fuel side appears to be due to the chemical mechanism employed. In sum, this figure represents the expected level of agreement between the measured and calculated NO & OH concentrations. Any significant differences between measurements and calculations for sooting flames could then be attributed to the difference between assumed and real chemistry.

Figures 2, 3, 4 and 5 show flame structure measurements and calculations for the four flames listed in Table I. The upper graph in these figures shows the NO_x structure. It contains data for mole fractions of burner inlet species, temperature and NO concentrations. The bottom graph in these figures shows the sooting structure. Measured soot volume fraction & number density are plotted along with the measured and calculated H_2, CO, and OH concentrations. H_2 and CO were chosen because they are the primary species oxidized by OH. The locations of the

maximum flame temperature (Tmax) and SP are marked on all the graphs. The mixture fraction 'Z' is also plotted to enable conversion from physical distance to mixture fraction coordinate. Individual aspects of this data are compared and discussed below.

Major Chemical Species:

The calculated and measured burner inlet species profiles, presented in the upper graphs of Figures 2-5, show good agreement for all four flames. Since the calculations were done by using measured temperatures and experimental boundary conditions, the differences between measured and calculated CO, H_2, OH and NO profiles may be attributed to the soot formation and oxidation process which is not represented in the chemical mechanism employed. It is expected that the relative rates of soot formation and oxidation will change significantly with the position of the flame relative to the SP. In earlier work[9], similar calculations with C-2 chemistry were used to infer soot nucleation propensity. While Faeth et al's[11] have correlated measured soot nucleation rates with C_2H_2 concentration. Thus, C_2H_2 was chosen for comparison between measurements and calculations. These comparisons are presented in Figure 6 for all four flames. Since the C_2H_2 measurements in the sooting region (which is expected to have the maximum concentration) could not be obtained due to probe clogging difficulties, comparisons with the acetylene concentration on the fuel side (before the sooting region) are meaningful. In this region, flames 1&2 show reasonable agreement, whereas, predictions for flames 3&4 are off by an order of magnitude. Likewise, CO and H_2 measurements (Figures 2-5) also show disagreement. Measured CO and H_2 are higher than calculated for flames 1&2 and lower than calculated for flames 3&4. Note that flames 1&2 were on the oxidizer side, flame 3 was very slightly on the fuel side and flame 4 was substantially on the fuel side. While the reasons for this discrepancy are unclear, it seems to be related to the soot formation and oxidation process

which changes significantly with the location of the flame relative to the SP. These result shows that it is difficult to infer sooting tendencies of diffusion flames with C-2 chemistry.

Sooting Structure:

As these flames were moved closer to the SP, visibly they become very different. Flame 1 had a thick dull-yellow-orange sooting zone, whereas, flames 2, 3 and 4 were very bright yellow with narrow sooting zones. The thickness of the sooting zone can be inferred from Figures 2-5 and the brightness from the average temperature of the sooting zone. Since soot is primarily convected toward the SP, the higher is the temperature at the SP, the brighter the flame becomes. Measured temperatures at SP, listed in Table I, show that this difference can be as large as 800K, making a significant difference in flame radiation. Essentially, as the distance between the flame and SP is changed, soot is constrained between the OH oxidizing zone and the location on the fuel side that satisfies appropriate conditions for soot nucleation. These conditions are not uniquely identified by temperature alone. The temperatures at zero f_v & N on the fuel side vary from 1250K for flame 1 to 1750K for flame 2 to 1600K for flame 3 to 1800K for flame 4.

These flames have very different sooting structures. In flame 1, soot volume fraction (f_v) monotonically increases toward SP and the number density (N) monotonically decreases. In flame 2, while f_v monotonically increases toward SP, N first increases and then decreases, indicating that soot nucleation is severely affected by the presence of OH. For flames 3 and 4, both f_v & N first increase and then decrease and unlike flames 1 & 2 maximum f_v does not occur at the SP. Interestingly, while the maximum value of f_v is about the same in flames 1 & 2, the maximum N in flame 2 is about 3 times larger. While the maximum value of N correlates with the measured C_2H_2 concentration (not the calculated C_2H_2), the maximum value of f_v does not

correlate with the C_2H_2 concentration. Flame 3 shows the largest f_v probably because of the increased residence time in the acetylene rich zone, being close to the stagnation plane.

The most interesting aspect of these flames is that as the radical rich zone (identified by peak temperature & OH concentration) is pushed into the soot zone, large discrepancies between the measured and calculated OH concentration occur. For flame 1, measured and calculated OH shows good agreement and OH is essentially being used to oxidize CO and H_2. As evidenced by monotonically increasing N, there seems to be little soot oxidation. OH, however, does seem to control the soot inception location. This behavior is very different in flames 2 & 3. A considerable reduction in the measured OH occurs signifying that soot competes for OH along with CO and H_2. This is evident from the sharp decrease in N on the oxidizer side. Similar conclusions were obtained by Santoro[16] in coaxial flames, however, a corresponding increase in the CO concentration is not observed in the present flames. In flame 4, soot and OH co-exist perhaps due to larger velocities that carry the soot particles into the OH zone. Also, less reduction in the OH concentration occurs due to lower f_v and N. From these results it appears that OH plays a significant role in determining the soot inception location on the oxidizer side. As noted earlier, the soot inception location on the fuel side seems to be controlled by the C_2H_2 concentration.

NO Structure:

Figures 2-5 show the measured and calculated NO for the four flames. Figures 2-3 correspond to the flames where N_2 was added to O_2, whereas, Figures 4-5 correspond to the flames where N_2 was added to CH_4. However, for flames 1&2, the energy equation was also solved without the radiative heat loss term to determine the effect of flame radiation on NO production. There was approximately a 100K increase in the maximum flame temperature for

the adiabatic calculations which significantly increased the NO concentration (difference between NO^{A} & NO^{T} in figures 2&3). While this difference can be directly attributed to the radiative heat loss, measured NO is still lower than NO^{T} by 70ppm for flame1 and by 40ppm for flame2. Yet, a good comparison was obtained for the blue flame. A possible explanation is the effect of soot on the major radical species produced in the primary reaction zone and their subsequent effect on NO production. In flame2, the OH concentration was significantly reduced due to soot/soot-precursor oxidation. Thus, the O-atom concentration will also be reduced since, at least approximately, partial equilibrium may be assumed[17]. Thus, even if significant contribution to N-atoms comes from the Fenimore initiation reaction[18] ($CH+N_2=HCN+N$), the corresponding contribution from the Zeldovich initiation reaction ($O+N_2=N+NO$) is reduced. Another possibility is that the 40ppm difference for flame2 is due to low N_2 concentration in the primary reaction zone. Calculations show that N_2 concentration difference is responsible for giving peak NO^{T}=75ppm for flame2 and peak NO^{T}=145ppm for flame1 despite about 100K higher temperature for flame2. Thus, it appears that the 70 & 40ppm reduction in NO in flames 1&2 respectively is due to soot-NO interactions through the radicals in the primary reaction zone.

Figures 4-5 show measured and calculated NO for flames 3&4. These flames show much higher NO concentration despite lower peak flame temperatures than flame2. Thus, it seems that the NO formation mechanism has changed. While peak value of flame3 NO is about 50ppm lower than calculations, flame4 shows good agreement. However, a substantial difference exists on the fuel side for both flames. Since this difference is similar to the blue flame, it can not be attributed to the presence of soot. Two questions arise: (i) Why is NO so much higher in flames 3&4? (ii) What are the possible mechanisms? We first note that in flames 3&4 N_2 was added to CH_4, making higher concentration of N_2% available in the fuel rich region. Thus, Fenimore

initiation mechanism is likely to become more effective. To check this hypothesis, calculated N, HCN, CH & O concentrations are plotted in figure 7 for all four flames [Note: these calculations do not contain the effect of soot]. The calculated peak NO concentrations are directly related to the calculated N-atom concentrations and a direct correspondence between CH&N-atom peaks and OH&O-atom profiles exists. While CH-peak for flame2 is higher than flame1, N-peak is lower due to lower N_2% at the CH-peak (~7% N_2 for flame2 and ~35% N_2 for flame1). For flames 3&4, CH-peaks become shorter and broader as the flame moves to the fuel side. However, the N-atom peaks are not substantially affected due to higher N_2% at the CH-peak (~40%). Since large NO is produced by the Fenimore mechanism in flames3&4, the effect of soot is masked. There is, however, a large discrepancy between the measured and calculated OH concentrations for flame3 that makes a substantial difference in the measured and calculated NO concentrations. For flame4, the difference in OH is less and a corresponding difference in NO is also seen. Although more work is needed, it appears that: (i) soot has a large influence on NO through the radical pool in the reaction zone, and (ii) the Fenimore mechanism becomes much more important when N_2 is added to the fuel side due to higher N_2 concentrations. Thus, the relative importance of the Zeldovich mechanism shifts as N_2 is shifted from the O_2 side to the fuel side.

CONCLUSIONS

In this work, soot and NO production in four diffusion flames with different structures was examined both experimentally and theoretically. The distance between the primary reaction zone and the stagnation plane was progressively changed to bring the flames from the oxidizer-side to the fuel-side including one flame located at the stagnation plane. Although more work is needed to understand the soot and NO structure of these flames, following may be concluded:

1) C-2 chemistry does not adequately describe the minor species and radical concentrations in sooting flames. 2) As the radical-rich, high-temperature reaction zone is pushed into the sooting zone, the flames become very bright due to enhanced soot-zone temperature. 3) OH concentration is significantly reduced due to soot and soot-precursor oxidation in addition to CO and H_2 oxidation. 4) The presence of OH significantly affects soot nucleation on the oxidizer side, while soot nucleation on the fuel side seems to be related to C_2H_2 concentration. 5) Significant reduction in NO formation occurs due to reduction in flame temperature caused by flame radiation. 6) It seems that soot interacts with NO formation through the major radical species produced in the primary reaction zone. 7) It appears that Fenimore mechanism becomes more important when N_2 is added to the fuel side due to higher N_2 concentrations in the CH-zone. The relative importance of the Zeldovich mechanism shifts as N_2 is shifted from the O_2 side to the fuel side.

ACKNOWLEDGMENTS

This work was supported by GRI under the contract number GRI 5087-260-1481 and the technical direction of Drs. R. V. Serauskas and J. A. Kezerle; by NSF under the grant number CBT 8552654 and by NASA under the grant number NAG3-1460.

REFERENCES

1. Bowman, C. T. , *Twenty-Fourth Symposium (International) on Combustion,* The Combustion Institute, Pittsburgh, p. 859-878, 1992.
2. Sarofim, A. F. and Flagan, R. C., *Prog. Energy Combust. Sci.*, Vol. 2, p. 1-25, 1976.
3. Turns, S. R. and Myhr, F. H., *Combustion and Flame*, 87, p. 319-335, 1991.
4. Atreya, A., Wichman, I., Guenther, M., Ray, A. and Agrawal, S., *Second International Microgravity Workshop*, NASA Lewis Research Center, Cleveland OH, 1992.
5. Tsuji, H., *Prog. Energy Combust. Sci.*, V. 8, p. 93, 1982.
6. Smooke, M. D., Seshadri, K., and Puri, I.K.: *Comb. & Flame* 73, 45 1988.
7. Zhang, C., Atreya, A. and Lee, K. *Twenty-Fourth Symposium (International) on Combustion,* The Combustion Institute, Pittsburgh, p. 1049, 1992.
8. Axelbaum, R. L., Flower, W. L. and Law, C. K., *Combust. Sci. Technol.* V. 39, p. 263, 1984.
9. Du, J. and Axelbaum, R. L., *Combustion and Flame*, 100, p. 367-375, 1995.
10. Sugiyama, G., *Twenty-Fifth Symposium (International) on Combustion,* The Combustion Institute, Pittsburgh, p. 601, 1994.
11. Sunderland, P. B., Koylu, U. O. and Faeth, G. M. *Combustion and Flame*, 100, p. 310, 1995.
12. Reisel, J. R., Carter, C. D., Laurendeau, N. M., Drake, M. C., *Combust. Sci. Technol.* V. 91, p. 271-295, 1993.
13. Carter, C. D., King, G. B. and Laurendeau, N. M. *Appl. Opt.*, V. 31, p. 1511, 1992.
14. Peters, N., *Twenty-First Symposium (International) on Combustion,* The Combustion Institute, Pittsburgh, p. 1231-1250, 1986.
15. A. E. Lutz, and R. J. Kee, Personal Communications.
16. Puri, R., Santoro, R. J. and Smyth, K. C., *Comb. & Flame* 97, 125, 1994.

17. Smyth, K. C., and Tjossem, P. J. H., *Twenty-Third Symposium (International) on Combustion,* The Combustion Institute, Pittsburgh, p. 1829-1837, 1990.

18. Drake, M. C. and Blint, R. J., *Comb. & Flame* 83, 185, 1991.

FIGURE AND TABLE CAPTIONS

Table 1 Experimental Flame conditions

Figure 1 Measurements and calculations for the non-sooty blue reference flame. Calculations of NO and OH were done using measured (and radiation corrected) temperatures and detailed kinetics (276 reactions & 50 species). The calculated OH concentration was used to calibrate the fluorescence measurements.

Figure 2 Measured and calculated (using measured temperatures) structure of Flame 1. The upper graph shows the mole fractions of burner inlet species, temperature, and measured and calculated NO concentrations. Measured NO represented by *, NO^T - calculated using the measured temperatures, and NO^A - calculated by using the energy equation with zero radiative heat loss. Bottom graph shows the sooting structure. Measured soot volume fraction & number density are plotted along with measured and calculated H_2, CO, and OH concentrations. The locations of the maximum flame temperature (Tmax) and the stagnation plane (SP) are marked on both the graphs. Note that this flame lies on the oxidizer side of the stagnation plane. The mixture fraction 'Z' is also plotted.

Figure 3 Measured and calculated (using measured temperatures) structure of Flame 2. The upper graph shows the mole fractions of burner inlet species, temperature, and measured and calculated NO concentrations. Measured NO represented by *, NO^T - calculated using the measured temperatures, and NO^A -calculated by using the energy equation with zero radiative heat loss. Bottom graph shows the sooting structure. Measured soot volume fraction & number density are plotted along with measured and calculated H_2, CO, and OH concentrations. The locations of the maximum flame temperature (Tmax) and the stagnation plane (SP) are marked on both the graphs. Note that this flame lies on the oxidizer side of the stagnation plane. The mixture fraction 'Z' is also plotted.

Figure 4 Measured and calculated (using measured temperatures) structure of Flame 3. The upper graph shows the mole fractions of burner inlet species, temperature, and measured and calculated NO concentrations. The bottom graph shows the sooting structure. Measured soot volume fraction & number density are plotted along with measured and calculated H_2, CO, and OH concentrations. The locations of the maximum flame temperature (Tmax) and the stagnation plane (SP) are marked on both graphs. Note that this flame lies at the stagnation plane within measurement accuracy. The mixture fraction 'Z' is also plotted.

Figure 5 Measured and calculated (using measured temperatures) structure of Flame 4. The upper graph shows the mole fractions of burner inlet species, temperature, and measured and calculated NO concentrations. The bottom graph shows the sooting structure. Measured soot volume fraction & number density are plotted along with measured and calculated H_2, CO, and OH concentrations. The locations of the maximum flame temperature (Tmax) and the stagnation plane (SP) are marked on both graphs. Note that this flame lies on the fuel side of the stagnation plane. The mixture fraction 'Z' is also plotted.

Figure 6 Calculated and measured concentrations of Acetylene for all four flames. Lines - calculations; Symbols - measurements.

Figure 7 Calculated mole fractions of O & N atoms and CH and HCN radicals in the four flames. Solid lines in the upper graph represent CH for the four flames (F1 - F4), whereas, the solid lines in the bottom graph represent N atoms. These calculations were done using measured temperatures and GRIMECH211.

Table I - Experimental Flame Conditions

Flame Number		Inlet Species Con.(%)		Burner Inlet Conditions		Strain Rate (1/sec) [½Velocity gradient @ S.P.]	Distance from the fuel side (mm)		Comments & Visual Observations (Mix.Fra.)
				Vel. (cm/s)	Temp (K)		S.P. (T)	Tmax (T)	
1	Fuel	CH_4	28.86	11.01	544	5.82	12.2 (1272) K	19.5 (2126) K	Very sooty Flame on O_2 side (Z=0.129)
		He	71.14						
	Oxy	N_2	57.40	4.96	636				
		O_2	42.60						
2	Fuel	He	84.50	15.23	684	8.27	12.2 (1791) K	15.5 (2212) K	Bright Flame on O_2 side (Z=0.297)
		CH_4	15.50						
	Oxy	N_2	18.23	5.42	710				
		O_2	81.77						
3	Fuel	N_2	74.95	7.88	672	9.03	14.5 (2155) K	14.0 (2198) K	Bright Flame at the stagnation plane (Z=0.48)
		CH_4	25.05						
	Oxy	O_2	43.54	10.09	694				
		He	56.46						
4	Fuel	CH_4	21.23	7.78	652	8.49	15.5 (1980) K	12.0 (2201) K	Bright Flame on the fuel side (Z=0.584)
		N_2	78.77						
	Oxy	He	47.82	9.31	670				
		O_2	52.18						

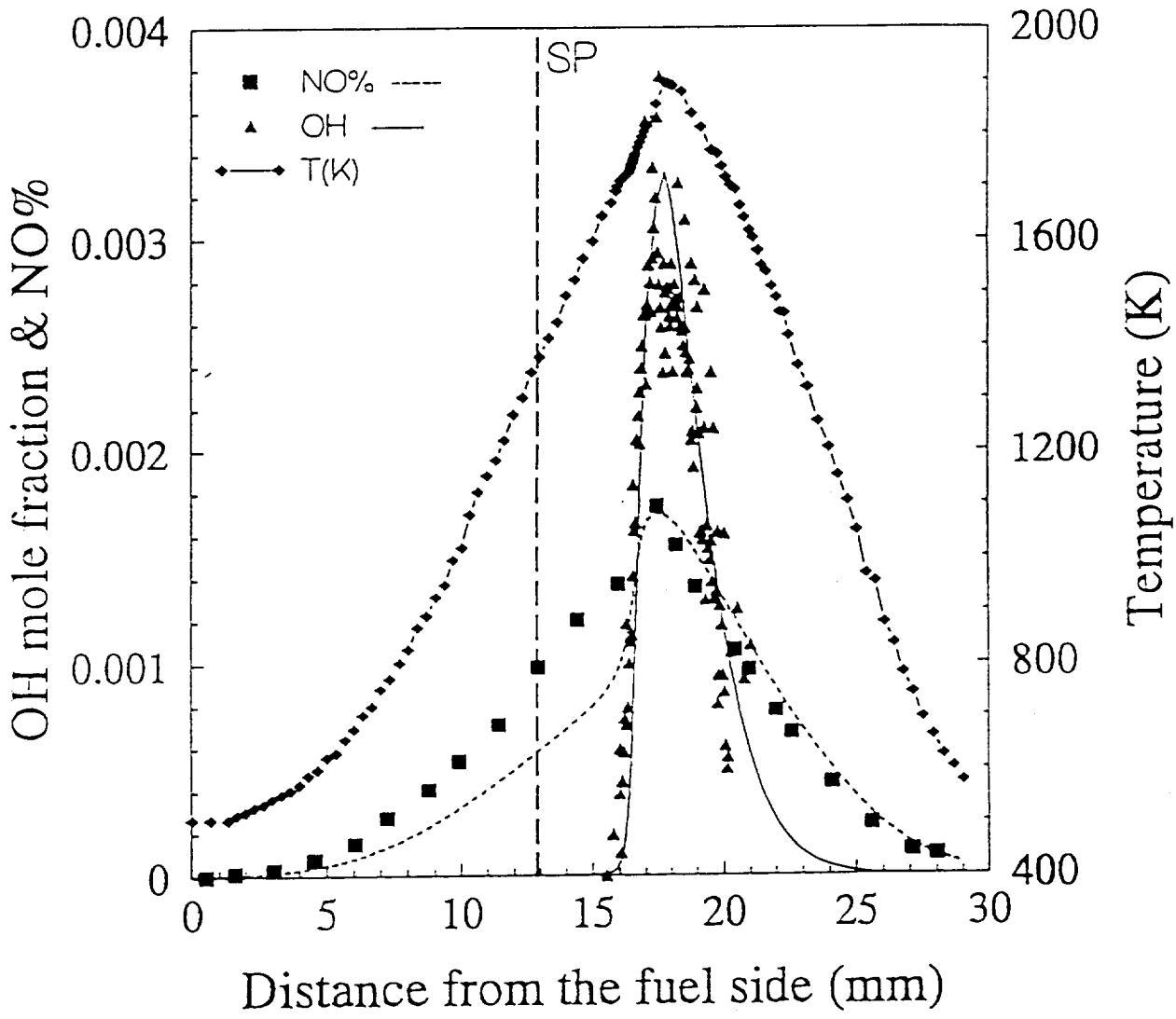
0.004
0.003
0.002
0.001
0
OH mole fraction & NO%
2000
1600
1200
800
400
Temperature (K)
SP
NO%
OH
T(K)
0
5
10
15
20
25
30
Distance from the fuel side (mm)

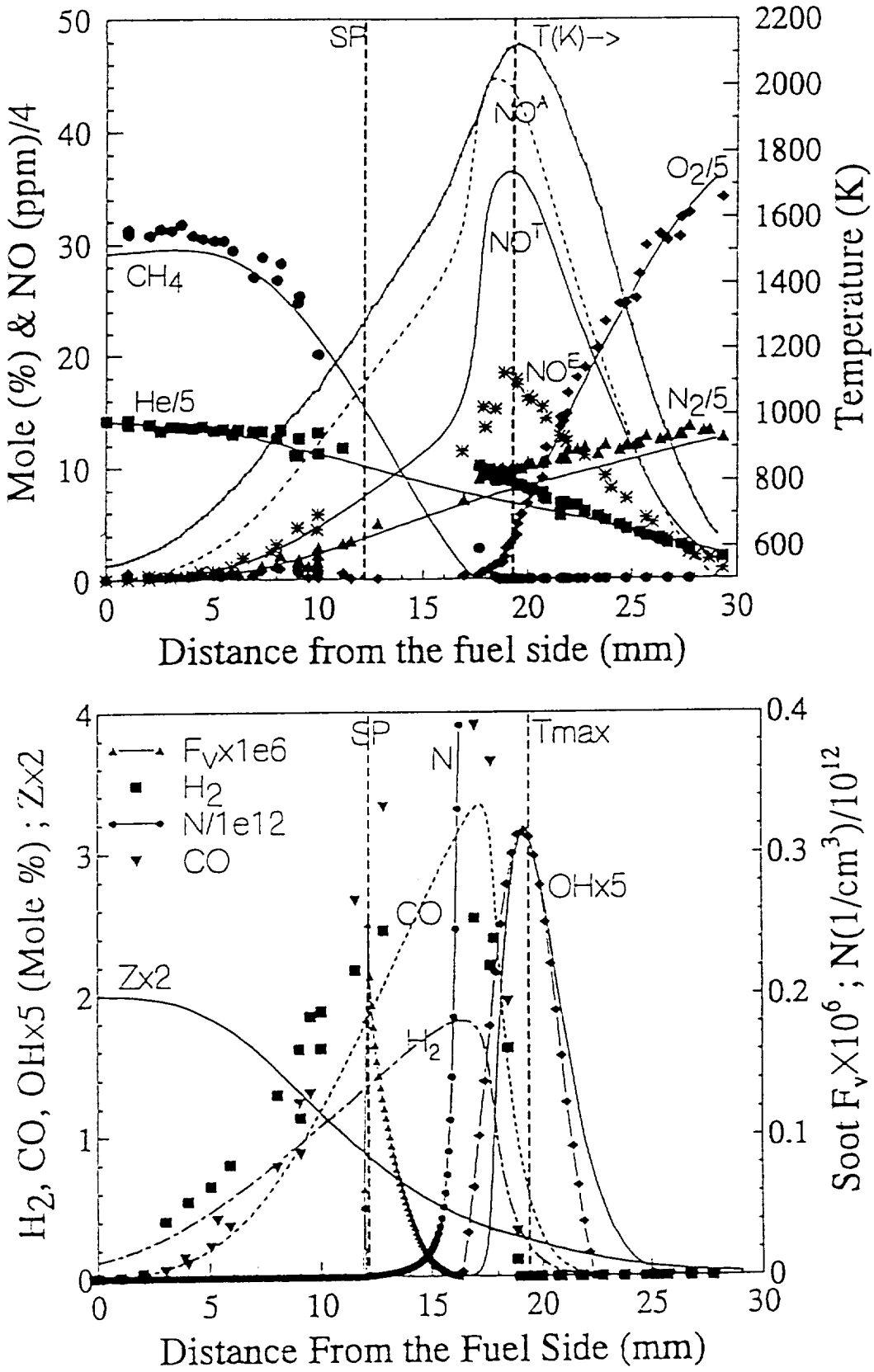
SR
T(K)->
NO^A
NO^T
NO^E
O2/5
N2/5
CH4
He/5
Mole (%) & NO (ppm)/4
Temperature (K)
Distance from the fuel side (mm)
SP
Tmax
FVx1e6
H2
N/1e12
CO
N
OHx5
Zx2
H2, CO, OHx5 (Mole %) ; Zx2
Soot FvX10^6 ; N(1/cm^3)/10^12
Distance From the Fuel Side (mm)

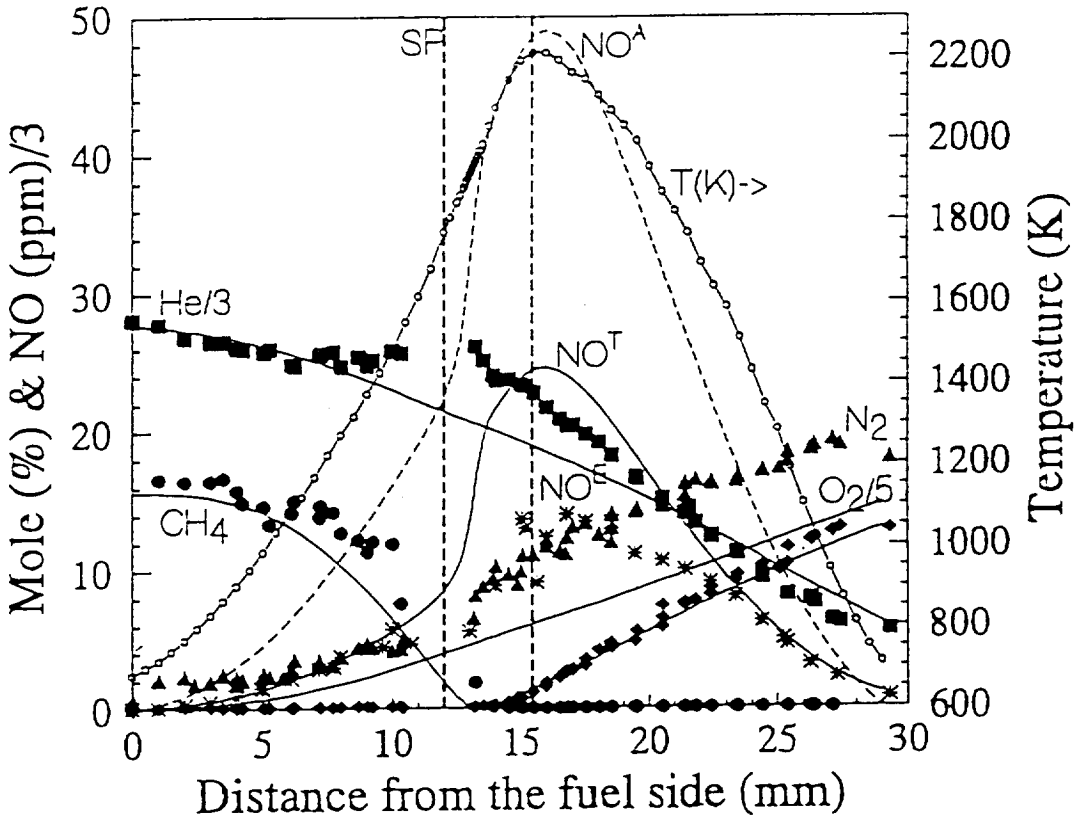
SP
NO^A
T(K)->
He/3
NO^T
N2
NO^E
O2/5
CH4
Mole (%) & NO (ppm)/3
Temperature (K)
Distance from the fuel side (mm)

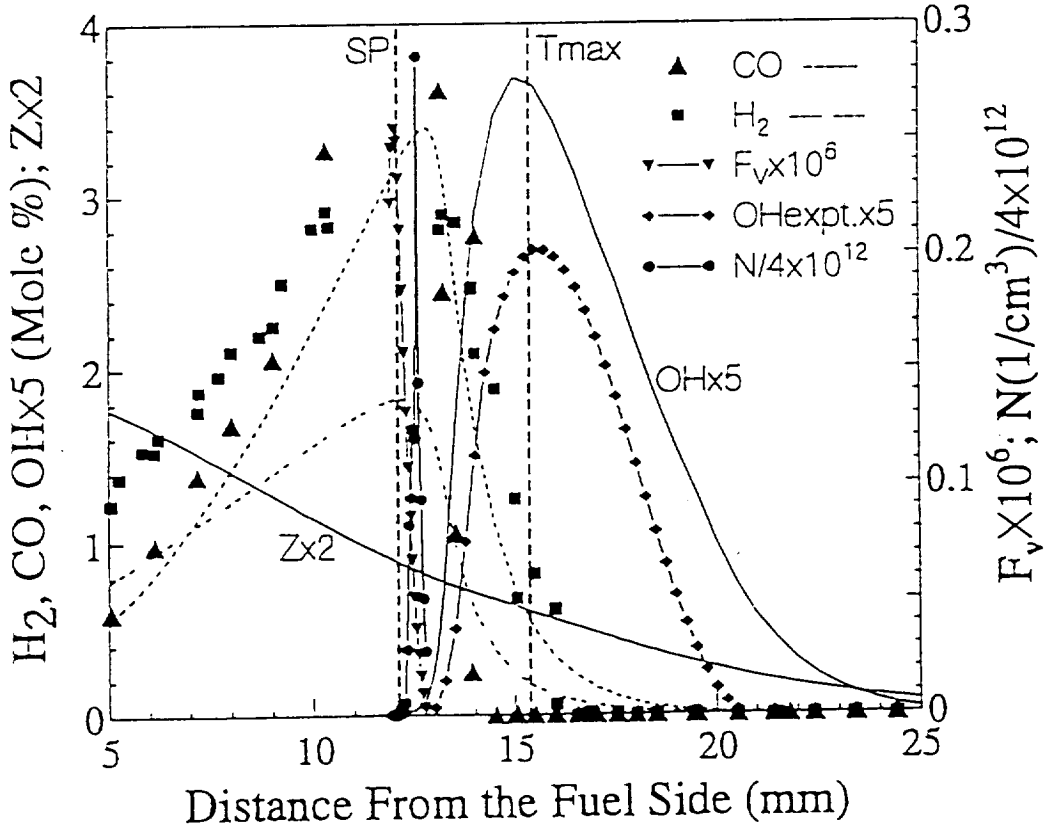
SP
Tmax
CO
H2
FvX10^6
OHexpt.x5
N/4x10^12
OHx5
Zx2
H2, CO, OHx5 (Mole %); Zx2
FvX10^6; N(1/cm^3)/4x10^12
Distance From the Fuel Side (mm)

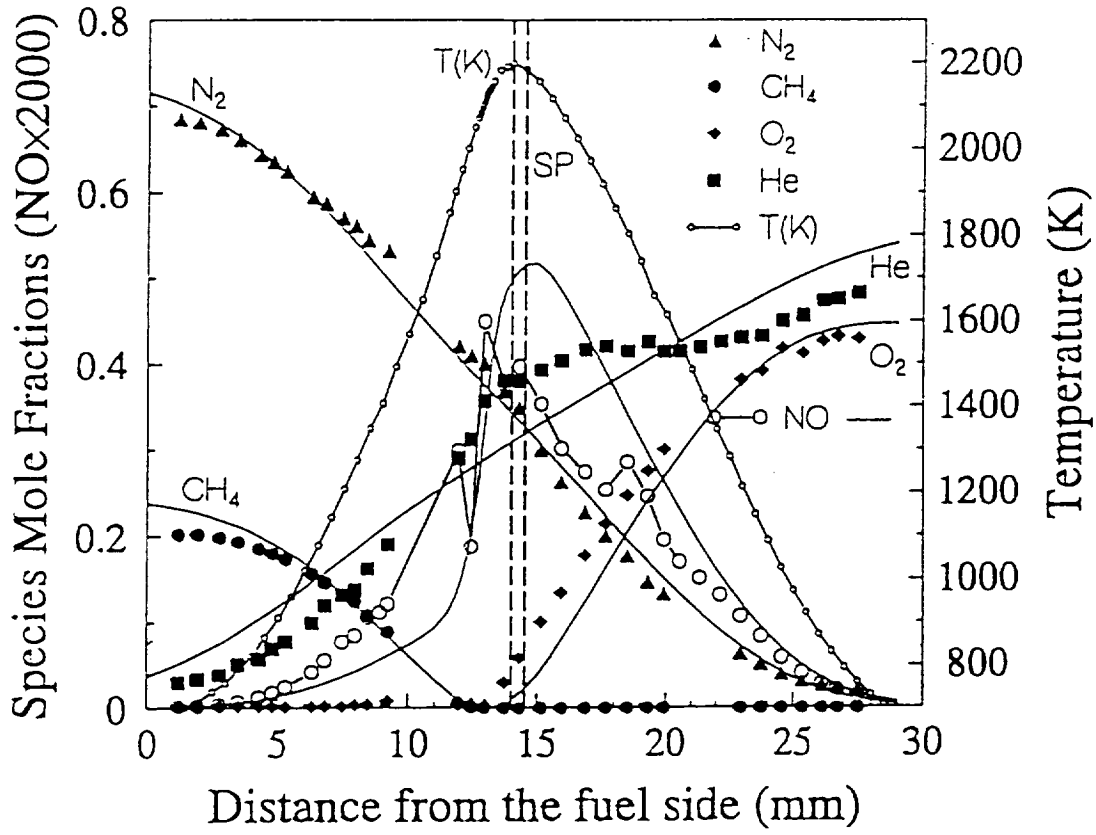
Species Mole Fractions (NOx2000)
Temperature (K)
Distance from the fuel side (mm)
N2
CH4
O2
He
T(K)
NO
SP
0.8
0.6
0.4
0.2
0
2200
2000
1800
1600
1400
1200
1000
800
0
5
10
15
20
25
30

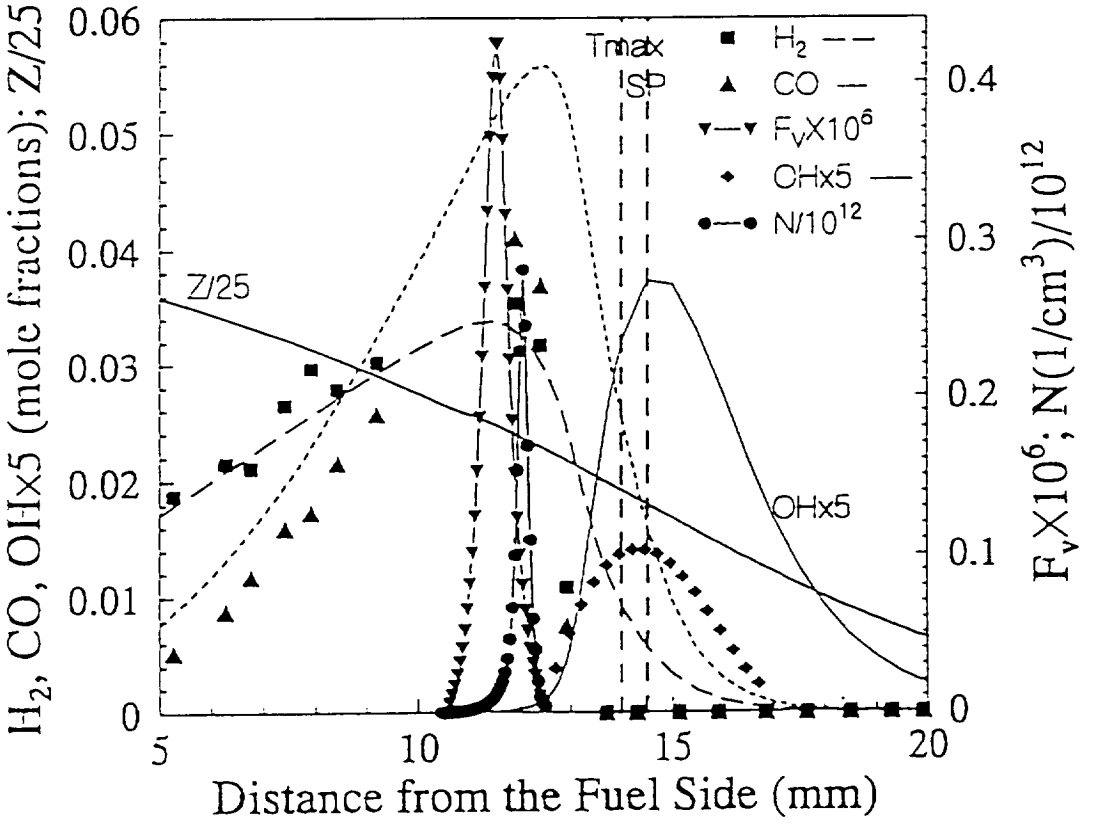
H2, CO, OHx5 (mole fractions); Z/25
FvX10^6; N(1/cm^3)/10^12
Distance from the Fuel Side (mm)
H2
CO
FvX10^6
OHx5
N/10^12
Tmax
Sb
Z/25
OHx5
0.06
0.05
0.04
0.03
0.02
0.01
0
0.4
0.3
0.2
0.1
0
5
10
15
20

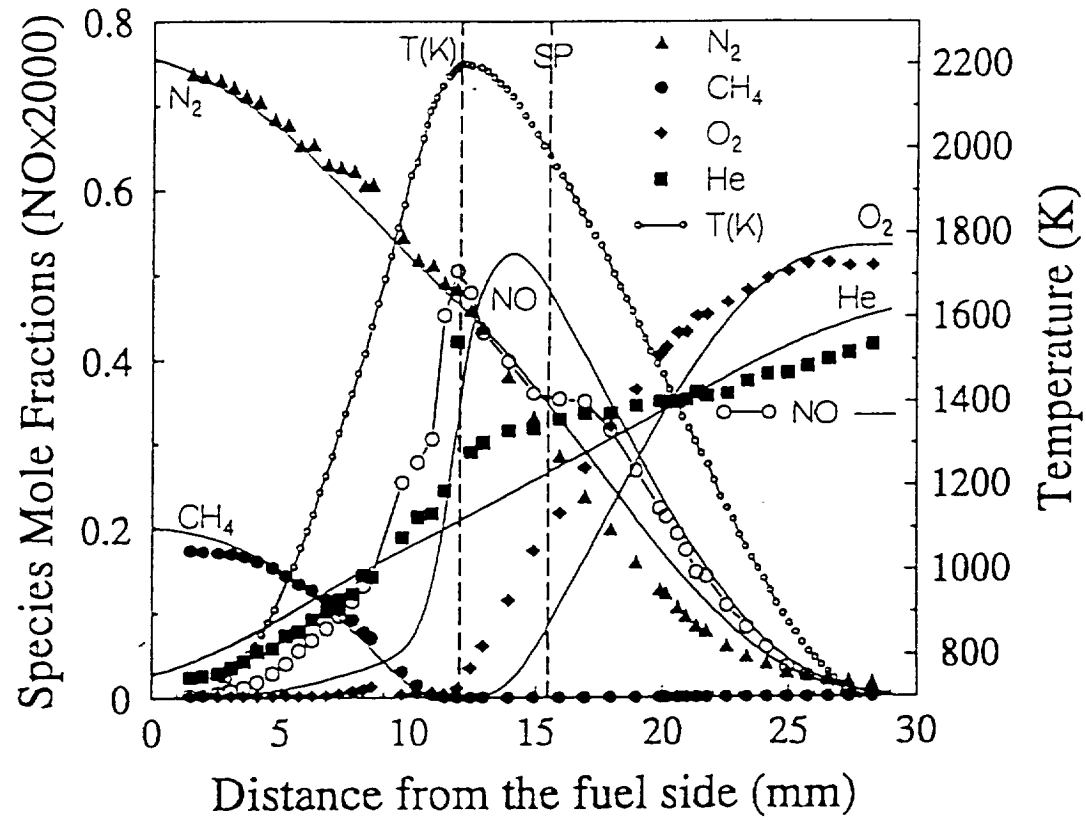
Species Mole Fractions (NOx2000)
Temperature (K)
Distance from the fuel side (mm)
T(K)
SP
N2
CH4
O2
He
NO
0.8
0.6
0.4
0.2
0
2200
2000
1800
1600
1400
1200
1000
800
0
5
10
15
20
25
30

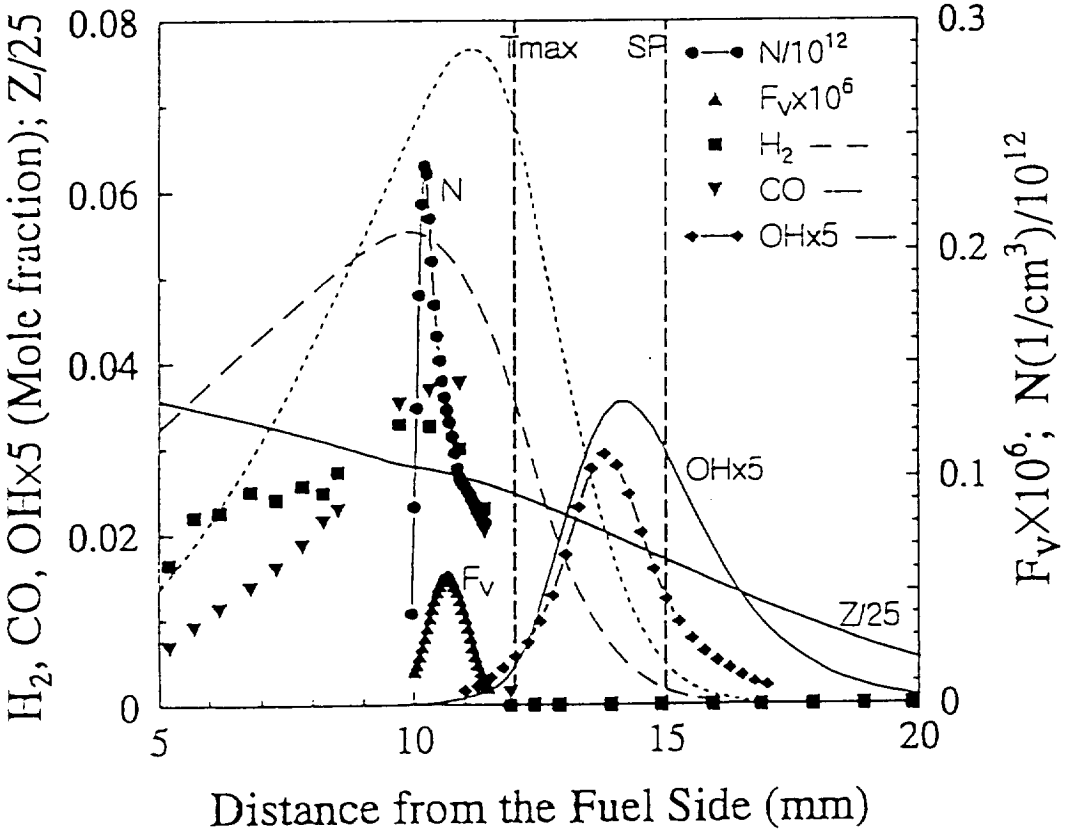
H2, CO, OHx5 (Mole fraction); Z/25
FvX10^6; N(1/cm^3)/10^12
Distance from the Fuel Side (mm)
Tmax
SP
N/10^12
FvX10^6
H2
CO
OHx5
Z/25
N
Fv
0.08
0.06
0.04
0.02
0
0.3
0.2
0.1
0
5
10
15
20

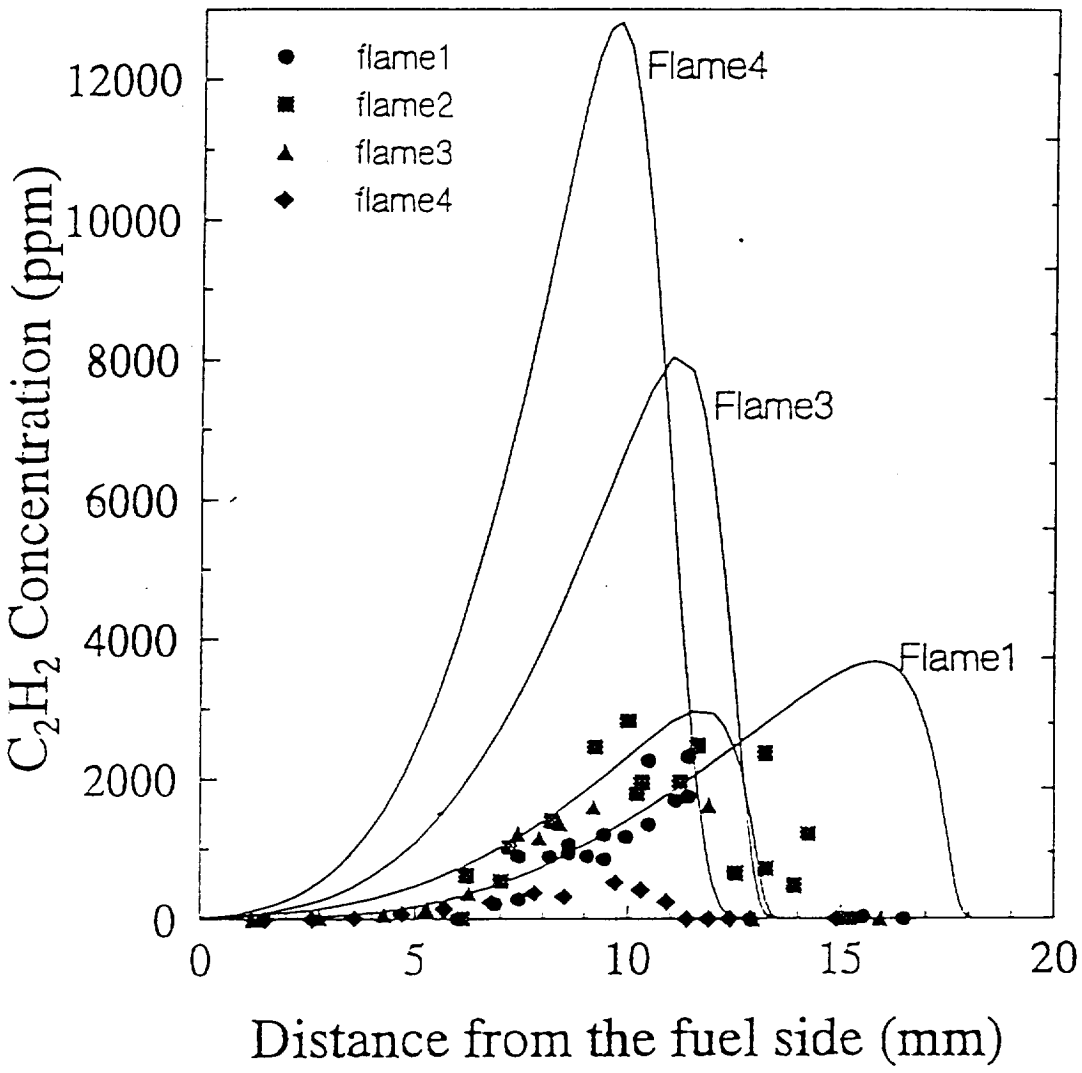
flame1
flame2
flame3
flame4
Flame4
Flame3
Flame1
12000
10000
8000
6000
4000
2000
0
0
5
10
15
20
C_2H_2 Concentration (ppm)
Distance from the fuel side (mm)

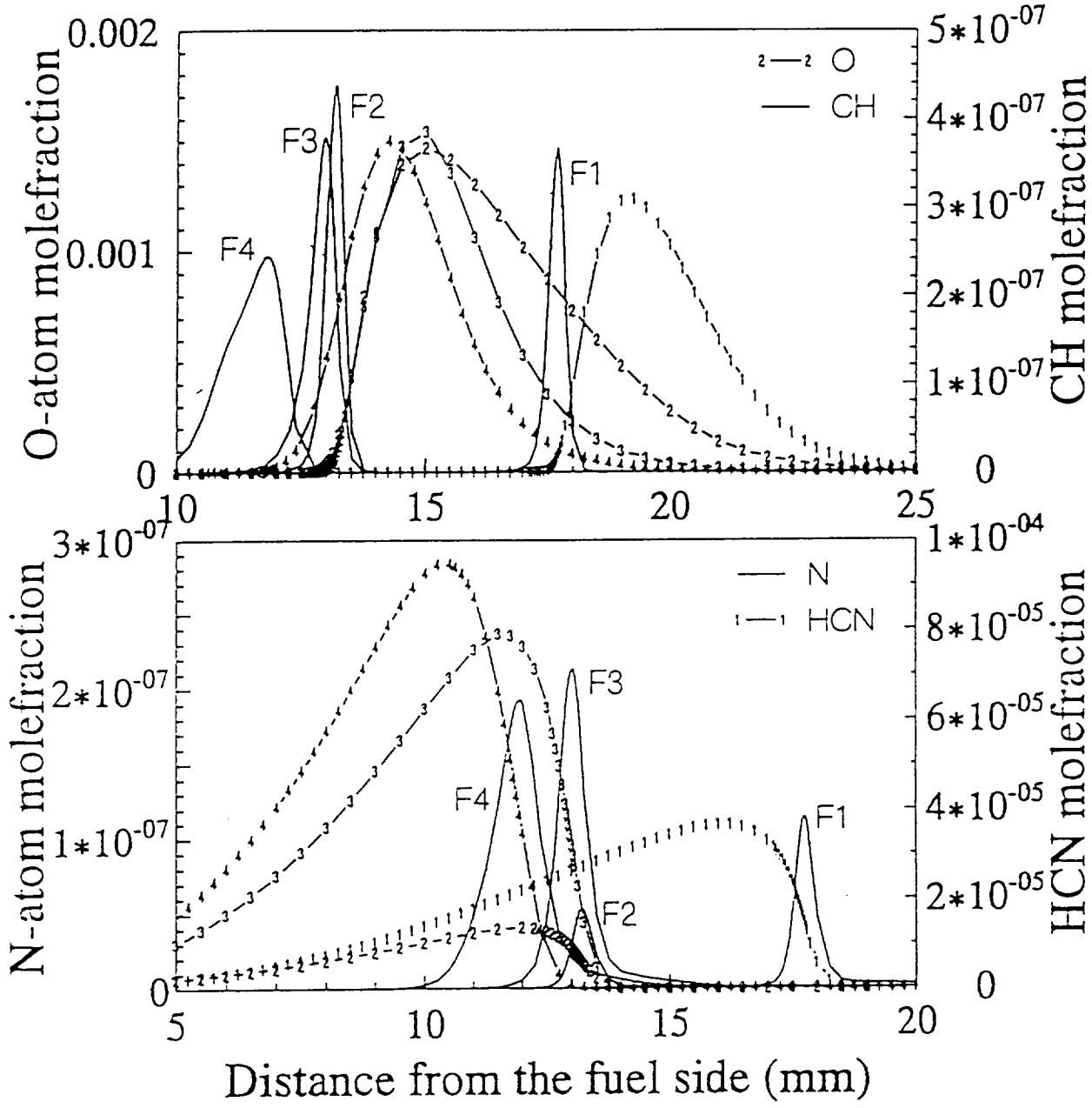
O-atom molefraction
CH molefraction
O
CH
F1
F2
F3
F4
0.002
0.001
0
5*10-07
4*10-07
3*10-07
2*10-07
1*10-07
10
15
20
25
N-atom molefraction
HCN molefraction
N
HCN
3*10-07
2*10-07
1*10-07
1*10-04
8*10-05
6*10-05
4*10-05
2*10-05
5
Distance from the fuel side (mm)

APPENDIX K

The Effect of Water Vapor on Radiative Counterflow Diffusion Flames

Symposium on Fire and Combustion Systems, ASME IMECE paper, 1995

By

Suh, J. and Atreya, A.

Symposium on Fire and Combustion Systems, ASME IMECE, 1995

THE EFFECT OF WATER VAPOR ON RADIATIVE COUNTERFLOW DIFFUSION FLAMES

Jaeil Suh and Arvind Atreya
Department of Mechanical Engineering and Applied Mechanics
The University of Michigan
Ann Arbor, MI

ABSTRACT

The chemical and physical effects of water vapor on the structure of counterflow diffusion flames is investigated both experimentally and theoretically. The experimental flame structure measurements consist of profiles of temperature which are used for computation with detailed C_2 chemistry. This enables describing the flame radiative heat losses more accurately. The flame structure results show that OH radical concentration increases as the water vapor concentration is increased. This increases the flame temperature and the CO_2 production rate and decreases the CO production rate. Additional computations performed for strained radiative counterflow diffusion flames with and without gas radiation show that at low strain rate, gas radiation is important for reducing the peak flame temperature, while it has a negligible effect at high strain rates. Increase in water vapor substitution increases the radiation effect of the water inside the flame at low strain rates.

INTRODUCTION

Water has been, and is, the most important fire suppression agent. Currently, even though we have several other effective chemical fire suppression agents, water is the most prevalent and the only agent for large fires because of its easy accessibility. Water is also non-toxic and is supposed to behave as an inert in a fire. Many other chemical fire suppression agents are known to produce toxic compounds that restricts their usage. However, a large amount of water that is typically used to suppress a fire causes severe water damage which sometimes exceeds the fire damage. To limit the water damage and to minimize the water usage, it is important to understand the mechanisms of fire suppression by water. Recently, there is considerable enthusiasm to use water mist as a replacement for halons. This also requires the knowledge of adequate amount of water to efficiently suppress the fire in the gas phase. Thus, there is a need to quantify the effect of water vapor on flames. Even though water has been used as a suppression agent for a long time, the exact mechanisms of fire suppression by water are not well understood.

Water is known to have two physical effects: (i) cooling of the burning solid by water evaporation and (ii) smothering caused by dilution of the oxidizer and/or the fuel by water vapor. These effects lead to fire suppression when water is applied to the fire. Furthermore, increase of the amount of the water inside of the flame can increase the flame radiation and reduce the flame temperature. However, in addition to these effects, another effect of water that is not well known was observed in our laboratory. This effect is the enhancement of chemical reactions inside the flames by water vapor. Transient experimental results (Crompton, 1995) show an increase in the flame temperature, CO_2 production rate and O_2 depletion rate and a decrease in the CO and soot production rate with water substitution (fuel and oxidizer concentrations were held constant). Furthermore, these results are different from CO_2 substitution which reduced the flame temperatures and suppressed the fire. Thus, water substitution experiments suggest that the chemical reactions inside the flames are enhanced by water vapor. Similar results for premixed flames have been reported earlier by Muller-Dethlefs and Schlader (1976).

In this paper, detailed structure of counterflow diffusion flames with water vapor is measured and calculated to investigate how the reactions occurring inside the flame are enhanced. The counterflow flame configuration was chosen because it represents the local behavior of large turbulent diffusion flames typical of fires. Measured temperature profiles were used for calculation to describe the radiation heat losses from the flame more accurately and the calculations were performed with the full C_2 mechanism. In addition to these, more computations were performed using the energy equation for various strain rates. Two different calculations, with and without gas radiation were conducted for each

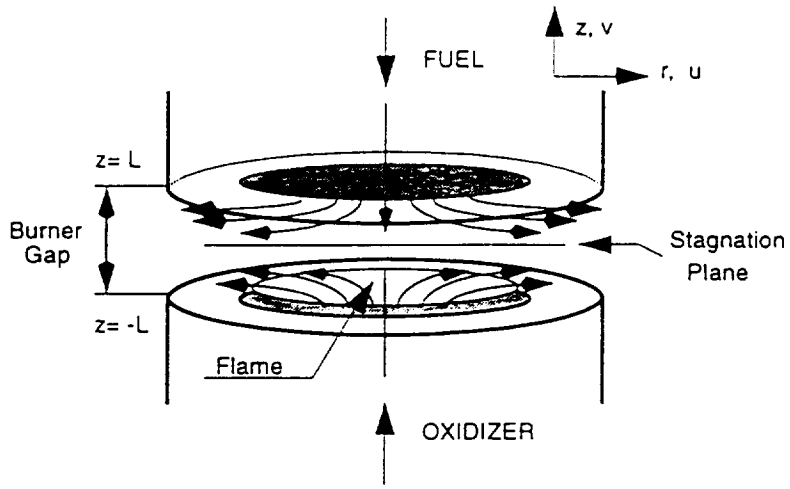

FIGURE 1. SCHEMATIC OF THE COUNTERFLOW DIFFUSION FLAME APPARATUS

strain rate and for each water vapor substitution.

FLAME TEMPERATURE MEASUREMENTS

The counterflow diffusion flame apparatus was used for flame temperature measurement. Schematic of this apparatus is shown in Figure 1. The gap between the fuel side and the oxidizer side was 26mm and the radius of fuel and oxidizer exit was 38.1 mm and 63.5mm respectively. The flow rate of fuel with diluent (nitrogen) through the fuel exit was 2 liter-per-minute, while that of the oxidizer with two different diluents (nitrogen and argon) was 8 liter-per-minute. The input concentration on the fuel side was 75% CH_4 and 25% N_2 and it was maintained constant for various water substitution to the oxidizer side flow. The input concentration on the oxidizer side was changed as water vapor was substituted, holding the molar concentration of O_2 constant at 20%. To maintain the same flow field and the same heat capacity of the oxidizer flow, a mixture of water vapor and argon was substituted for nitrogen. This maintained the same molar flow rate and roughly the same specific heat. Therefore, the amount of oxygen which flowed into the flame was the same for all the experiments (10, 20, 30 and 40% of water vapor substitutions). The flame temperature profile was measured with a coated S-type thermocouple (platinum and platinum with 10% rhodium). Silicone dioxide (SiO_2) coating was used to prevent catalytic reactions.

COMPUTATIONAL METHOD

Numerical modeling of the chemical process is performed using *the Sandia Chemkin-based opposed flow diffusion flame code* (Kee and Miller, 1992). The flame is modeled as a steady state axis-symmetric opposed flow diffusion flame using the experimentally measured center line temperature profile. Pressure is assumed to be constant at 1 atm. The reaction mechanism for methane is the C_2 - mechanism which consists of 177 chemical reactions with 32 species. More chemical reactions will be added later to account for chemical enhancement due to soot disappearance.

Governing Equations

For steady state laminar stagnation point flow in cylindrical coordinates, the mass and the momentum conservation equations are expressed as follows:

Mass

$$\frac{\partial}{\partial r}(\rho u r) + \frac{\partial}{\partial z}(\rho v r) = 0 \qquad (1)$$

Momentum

$$\rho u\frac{\partial u}{\partial r} + \rho v\frac{\partial u}{\partial z} + \frac{\partial p}{\partial r} = \frac{\partial}{\partial z}\left(\mu\frac{\partial u}{\partial z}\right) \qquad (2)$$

Introducing a new function, Ψ, to normalize the r-direction velocity, u, refer to Smooke et al. (1987),

$$\Psi = \frac{u}{u_{\infty}} \qquad (3)$$

where u_{∞} is the free stream tangential velocity at the edge of boundary layer. $u_{\infty} = ar$, where a is the strain rate.
Assuming the transverse velocity, v, density, ρ, and species Y_k to be functions of z-direction only, the following system of boundary layer equations are obtained:

Mass conservation equation

$$\frac{d}{dz}(\rho v) + 2a\rho\Psi = 0 \qquad (4)$$

Momentum equation

$$\frac{d}{dz}\left(\mu\frac{d\Psi}{dz}\right) - \rho v\frac{d\Psi}{dz} + a\left[\rho_{\infty} - \rho(\Psi)^2\right] = 0 \qquad (5)$$

Species equation

$$\frac{d}{dz}(\rho Y_k V_k) + V\frac{dY_k}{dz} - \dot{w}_k W_k = 0, k = 1, 2, \ldots, K \qquad (6)$$

Energy equation

$$\frac{d}{dz}\left(\lambda\frac{dT}{dz}\right) - C_p V\frac{dT}{dz} - \sum_{k=1}^{K} \rho Y_k V_k C_{pk}\frac{dT}{dz} - \sum_{k=1}^{K} \dot{w}_k W_k h_k = 0 \qquad (7)$$

The objective of the numerical method is to find a solution for equations(4-7) using a differential equation solver. In these equations k denotes k-th species, C_p is the specific heat at constant pressure, h_k are species molar enthalpy, W_k are species molecular weights, C_{pk} are constant pressure specific heat for each species and $\dot{w}_k$ are the chemical production rates. Transport properties, viscosity μ, thermal conductivity λ and species diffusion velocities V_k are also introduced.

Boundary Conditions

Boundary conditions for inlet z-direction velocity and the function Ψ at the inlet of fuel and oxidizer streams are specified as follows:

Fuel side: z=L

$$v_f, \qquad \Psi_f = \sqrt{\frac{\rho_o}{\rho_f}}$$

Oxidizer side: z=-L

$$v_o, \qquad \Psi_o = 1$$

The subscripts *f* and *o* denote fuel and oxidizer respectively.

RESULTS AND DISCUSSION

Measured temperature profiles for different water vapor substitutions are shown in Figure 2. The temperature profiles have the same shape except the peak temperature and the width. There is also a small shift in the location of the peak temperature for the 0% water case. We believe that the main reasons of this small shift is measurement error and/or change in the transport properties of the oxidizer side of the flow with water vapor. Interestingly, the maximum temperatures of the flames are increased with increase of water vapor substitution (1914K for 0% to 1960K for 40% water vapor) and the width of temperature profile is also increased. This means that water vapor which is added to the flame has other than a physical suppression effect. Figure 3 shows velocity profiles with different water vapor substitutions. All velocity profiles have nearly the same shape and the same stagnation plane location (8.3mm from the fuel exit), because inerts are substituted with water vapor on the same molar and heat capacity basis. Only in the highest temperature zones, the velocity profiles are different because of different heat release rates and transport characteristics of the mixture. Figures 4 and 5 explains the effect of water vapor

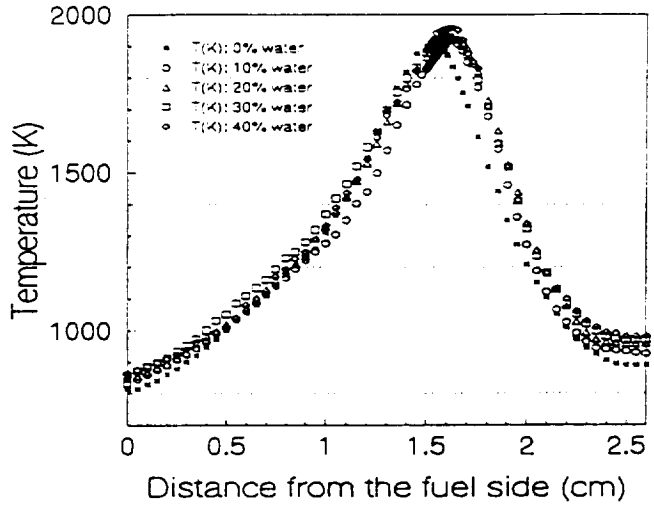

FIGURE 2. MEASURED FLAME TEMPERATURE PROFILES

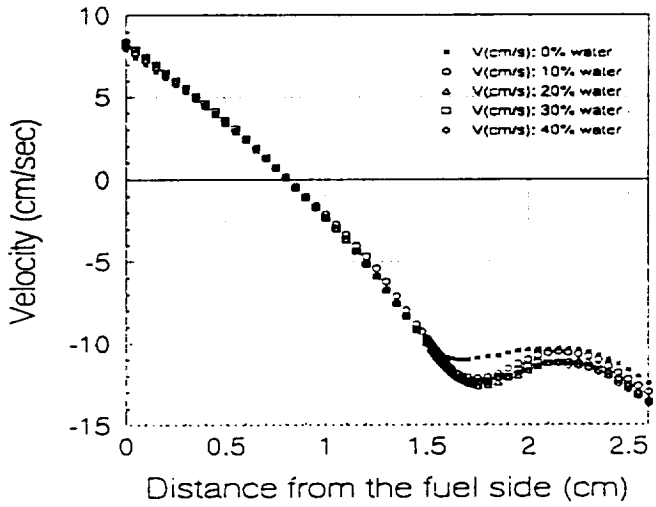

FIGURE 3. CALCULATED VELOCITY PROFILES

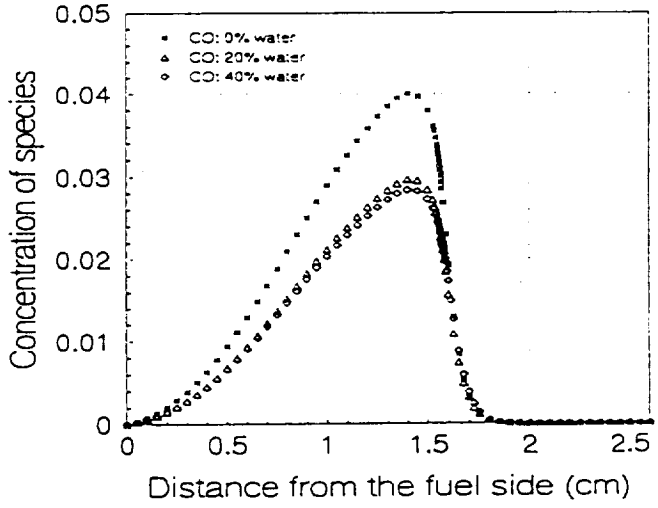

FIGURE 4. CO CONCENTRATIONS

on the reaction of CO and CO_2. The concentration of CO_2 is gradually increased with increase of water vapor addition while the concentration of CO is decreased. The main reaction for CO_2 production with CO is as follows:

$$CO + OH = CO_2 + H$$

Therefore, the increase of CO_2 with decrease of CO means that the active OH radical from water vapor which is produced in the high temperature flame zone enhances the reaction of CO to CO_2. Figure 6 shows the differences in the OH radical concentrations with and without water vapor addition. From Figure 6, it is clear that the presence of water vapor in the flame increases the OH concentration.

In Figure 7, calculated temperatures using the energy equation with and without gas radiation are plotted. These calculations were done using the same input boundary conditions as the experiment for 10% water substitution case and are compared with the experimentally measured temperature. Figure 8 shows similar results for 40% water substitution case. Gas radiation from CH_4, O_2, N_2, CO, CO_2 and H_2O species in the flame was included in the calculations. These results (for 10% and 40% cases) show that locations of the reaction zones (maximum temperature point) are well matched for the experiment and computations. However, the overall temperature profile for the radiation compensated case agrees better with the experimental result than with the adiabatic case. Especially for 40% water vapor substitution case (Figure 8), the radiation compensated computation result is almost the same as the experimental result. The reason is that sooty flames were used for the experiments and when the amount of water vapor substitution was increased, the decease of the soot volume fraction was visually observed. Therefore, in the 10% water vapor substitution case, a fair amount of soot, which was not considered in these calculations, was present and made the difference between the experimental and the calculated results. In the 40% case, however, much less soot was present, thus gas radiation compensated calculation result agrees well with the experimental result. Figure 9 shows the calculated adiabatic flame temperature profiles with various strain rates for the 10% water vapor substitution case, whereas, Figure 10 shows similar results for the 40% water vapor substitution case. Figure 11 shows the calculated radiation compensated flame temperature profiles with various strain rates for the 10% water vapor substitution case while Figure 12 shows those for the 40% water vapor substitution case. In Figures 9 to 12, the lowest strain rate corresponds to the experimental case. As the strain rate is increased, the temperature profile becomes narrow and the location of the maximum temperature moves toward the fuel side for both adiabatic and radiation compensated cases. However, in the adiabatic calculation case, the maximum temperature drops when strain rate is increased while in the radiation compensated calculation case, the maximum temperature is increased up to certain point and then decreased. This result is valid for both 10% and 40% water vapor substitution cases and is mainly due to the radiation from water and other gases. In the low strain field, the flame is wider than that in the high strain field as indicated by the wider temperature profile. Thus, the gas radiation in the flame becomes an important factor to reduce the peak flame temperature in the low strain field. This effect is reduced when the strain rate is increased, i.e., a thin flame sheet can not emit much gas radiation.

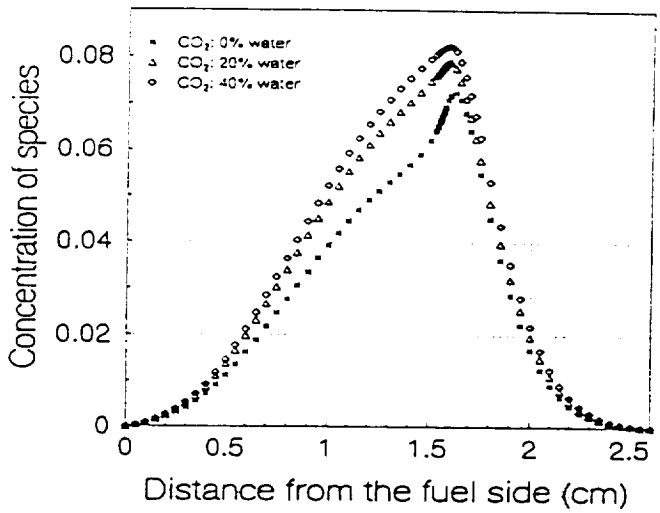

FIGURE 5. CO_2 CONCENTRATIONS

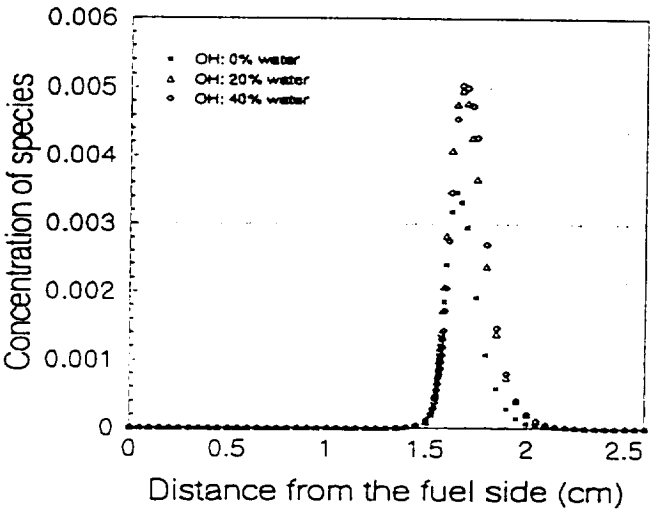

FIGURE 6. OH CONCENTRATION

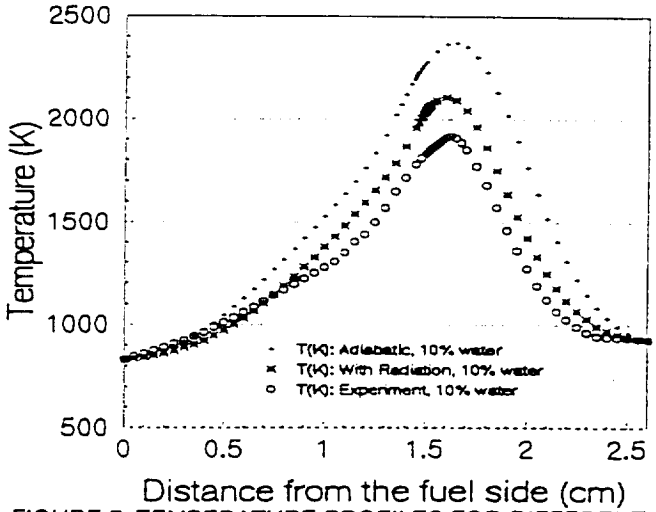

FIGURE 7. TEMPERATURE PROFILES FOR DIFFERENT CALCULATIONS (10% WATER CASE)

Figure 13 shows the maximum flame temperature variation due to increase in the strain rate. At high strain rates, the maximum flame temperatures for adiabatic and radiation compensated calculations are close together, while at low strain rate they are far away for reasons mentioned previously. Increase of water vapor substitution from 10% to 40% enhances the gas radiation inside of the flame. From Figure 13 it can be seen that the maximum flame temperatures for adiabatic cases(10% and 40% cases) are not very different. However, for radiation compensated cases, the 40% water case has more radiation effect than the 10% water case. Therefore, as expected, an increase in water vapor substitution enhances the radiation effect which is more pronounced for low strain rates.

CONCLUSIONS

Computations of flame structure when water vapor is added to the counterflow diffusion flame using experimentally measured temperature profiles are performed for 5 different water vapor concentration cases. Maximum temperature and CO_2 production increased with an increase of water vapor concentration while CO concentration decreased. The concentration of OH radical increases with water vapor addition. This increase in the OH radical concentration explains the increase in the CO_2 concentration and the maximum flame temperature.

Counterflow diffusion flame temperatures are also computed for various strain rates with and without radiation compensation. The radiation compensated calculation results are closer to the experimental results because of the gas radiation from the flame. However, for high strain rate cases, radiation effect is not as much as in low strain rate cases. When water vapor substitution is increased, the effect of water radiation is increased in low strain fields. A soot radiation model is required for more accurate calculations of these sooty flames.

ACKNOWLEDGMENTS

Financial support for this work was provided by NIST (under the grant no. 60NANB3D1440) and NASA (under the grant no. NAG 3-1460).

REFERENCES

Muller-Dethlefs, K., Schlader, A.F., 1976, " The Effect of Steam on Flame Temperature Burning Velocity and Carbon Formation in Hydrocarbon Flames," *Combustion and Flame*, Vol. 27, pp.205-215.

Crompton, T., 1995, "The Physical and Chemical Effects of Water in Larminar Hydrocarbon Diffusion Flames," Master Thesis, University of Michigan, Ann Arbor, MI.

Kee, R.J., Miller, J. A., 1992, "A Structured Approach to the Computational Modeling of Chemical Kinetics and Molecular Transport in Flowing Systems," Sandia National Laboratories Report, SAND86-8841, Livermore, CA.

Puri, I.K., Smooke, M.D. et al., 1987, "A Comparison between Numerical Calculations and Experimental Measurements of the Structure of a Counterflow Methane-Air Diffusion Flame," *Combustion Science and Technology*, Vol.56, pp. 1-22.

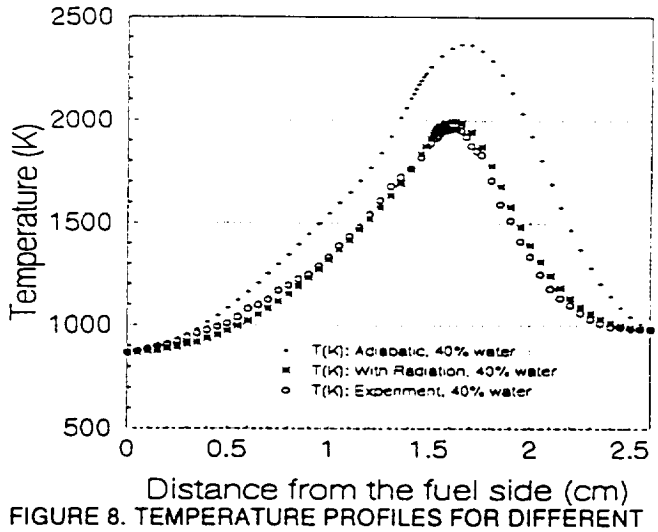

FIGURE 8. TEMPERATURE PROFILES FOR DIFFERENT CALCULATIONS (40% WATER CASE)

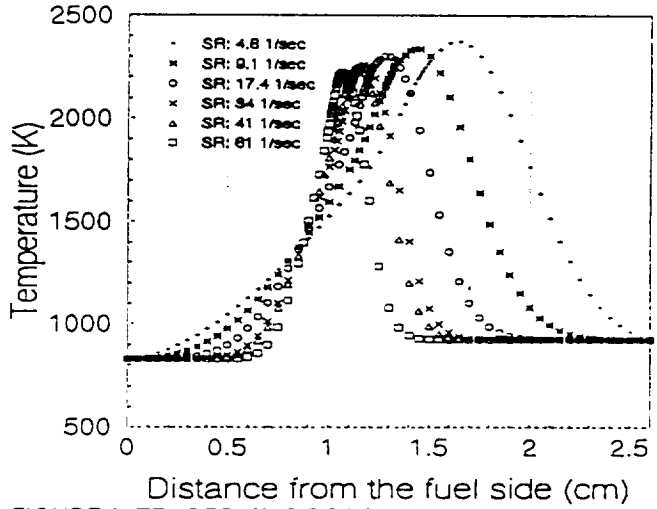

FIGURE 9. TEMPERATURE PROFILES WITH STRAIN RATE VARIATIONS (10% WATER, ADIABATIC)

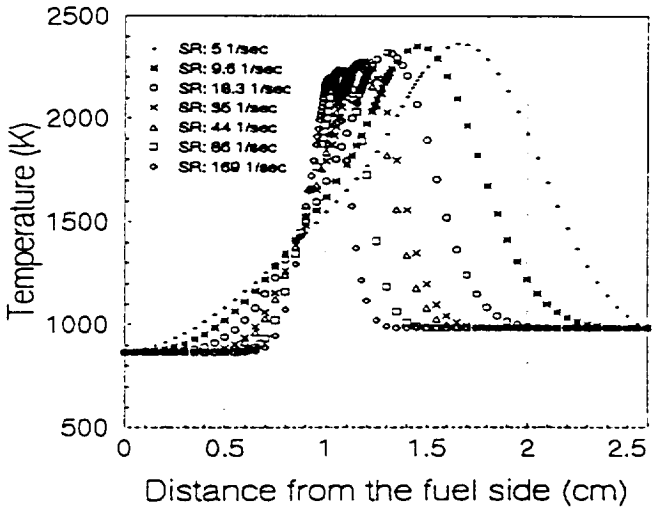

FIGURE 10. TEMPERATURE PROFILES WITH STRAIN RATE VARIATIONS (40% WATER, ADIABATIC)

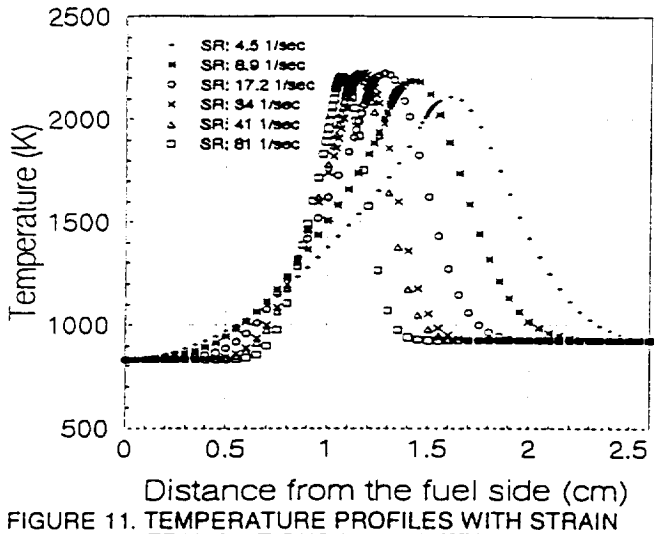

FIGURE 11. TEMPERATURE PROFILES WITH STRAIN RATE VARIATIONS (10% WATER, RADIATION)

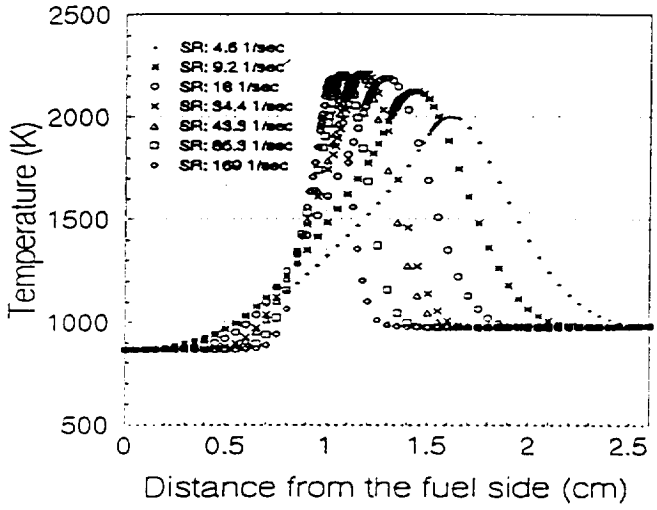

FIGURE 12. TEMPERATURE PROFILES WITH STRAIN RATE VARIATIONS (40% WATER, RADIATION)

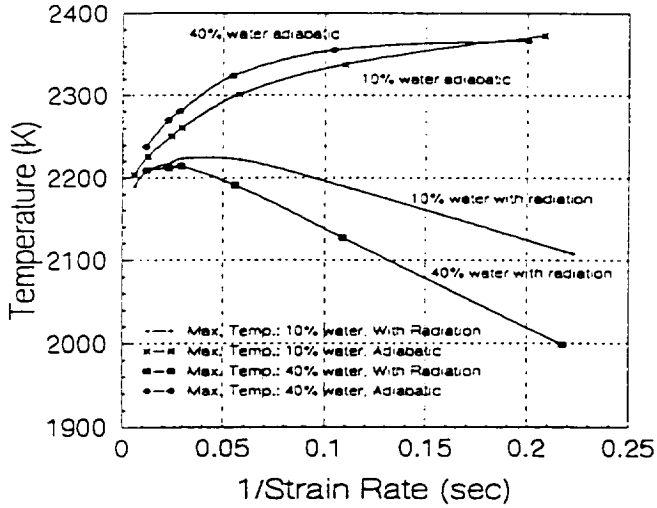

FIGURE 13. MAXIMUM FLAME TEMPERATURES WITH STRAIN RATE VARIATIONS

APPENDIX L

Dynamic Response of Radiating Flamelets Subject to Variable Reactant Concentrations

Proceedings of the Central States Combustion Institute Meeting, 1996

By

Shamim, T. and Atreya, A.

Dynamic Response of Radiating Flamelets Subject to Variable Reactant Concentrations

Tariq Shamim and Arvind Atreya*
Combustion and Heat Transfer Laboratory
Department of Mechanical Engineering and Applied Mechanics
The University of Michigan, Ann Arbor, MI 48109-2125

The effects of reactant (fuel/oxidizer) concentration fluctuations on radiating flamelets using a numerical investigation are reported in this article. The flame response to sinusoidal variations about a mean value of reactant concentration for various values of strain rates is examined. This work will aid in the better understanding of turbulent combustion. The radiative effects from combustion products (CO_2 and H_2O) are also included in the formulation. The maximum flame temperature, heat release rate and the radiative heat loss are used to describe the flame response. The results show that flame responds to fluctuations with a time delay. The effect of the frequency of fluctuation is found to be more important than its amplitude. Low frequency fluctuations bring about a significant flame response causing extinction at large strain rates for high fluctuation amplitudes. At high frequencies relative to the strain rate, rapid concentration fluctuations are distributed closely in space. These are neutralized by the resulting large diffusion gradients. Thus the flame becomes relatively insensitive to fluctuations. The induced fluctuations were found to have more prominent effect on radiation than on the heat release.

Introduction

An investigation of transient effects on flamelet combustion is useful for better understanding of turbulent combustion. The flamelet concept, which was proposed by Carrier et al., [1] and later developed by Peters [2], provides a convenient mechanism to include detailed chemical kinetics into the calculations of turbulent flames. The idea is based on the translation of physical coordinates to a coordinate system where the mixture fraction is one of the independent variables. One can then express all thermochemical variables as unique functions of two variables, the mixture fraction and its dissipation rate by assuming that the changes of thermochemical variables are dominant in the direction perpendicular to the surface of constant mixture fraction [3]. These unique functions have been called "state relationships" [4]. Consequently, the flamelet model can be incorporated into existing turbulent combustion model provided these state relationships are known.

A basic assumption of these flamelet models is that the local structure of the reaction zone may be represented by an ensemble of quasi-steady state strained laminar flame elements which are stretched and convected by the turbulent flow [5]. The validity of this assumption has, however, been questioned in many recent studies by showing that non-steady effects are of considerable importance [5-7]. Consequently, there has been a growing interest in the study of time dependent effects on flamelet combustion [3, 6-13]. However, most of these studies are limited to the effects of time varying strain rate with the exception of the limited study by Clarke and Stegan [14] and Egolfopoulos [15] on concentration fluctuations. Furthermore, the effects of radiative heat losses are not considered by any of these studies with the exception of Egolfopoulos [12].

The present study is an attempt to fill this existing gap in the literature. We investigate the effects of reactant concentration fluctuations on radiating flamelets in this article. The flame response to sinusoidal variations about a mean value of reactant concentration for various values of strain rates is examined.

Mathematical Formulation

General Governing Equations

A schematic of a counterflow diffusion flame stabilized near the stagnation plane of two laminar flows is shown in Figure 1. In this figure, r and z denote the independent spatial coordinates in tangential and axial directions respectively. Using the assumptions of axisymmetric, unity Lewis number, negligible body forces, negligible viscous dissipation, and negligible Dufour effect, the resulting conservation equations of mass, momentum, energy and species may

*Corresponding author
Proceedings of the 1996 Technical Meeting of the Central States Section of the Combustion Institute

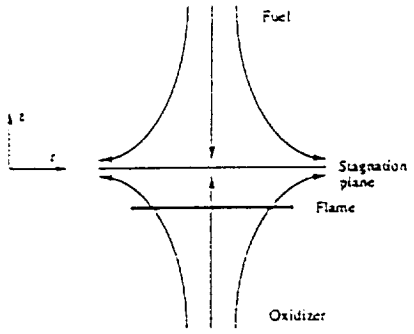

Figure 1 Schematic of Counterflow Diffusion Flame

be simplified to the following form:

$$\frac{\partial \rho}{\partial t} - 2\rho\epsilon\psi - \partial\frac{(\rho v)}{\partial z} = 0$$

$$\left(\psi - \frac{\rho_-}{\rho}\right)\frac{d\epsilon}{dt} - \epsilon\frac{\partial\psi}{\partial t} - \left(\psi^2 - \frac{\rho_-}{\rho}\right)\epsilon^2 = -\epsilon v\frac{\partial\psi}{\partial z} - \frac{\epsilon}{\rho}\frac{\partial}{\partial z}\left(\mu\frac{\partial\psi}{\partial z}\right)$$

$$\rho\left(\frac{\partial h}{\partial t} - v\frac{\partial h}{\partial z}\right) = \frac{\partial}{\partial z}\left(\frac{\lambda}{c_p}\frac{\partial h}{\partial z}\right) - \sum_{i=1}^{N}\omega_i\,\Delta h_{fi}^{o} - \nabla.Q_R$$

$$\rho\left(\frac{\partial Y_i}{\partial t} - v\frac{\partial Y_i}{\partial z}\right) = \frac{\partial}{\partial z}\left(\rho D_i\frac{\partial Y_i}{\partial z}\right) - \omega_i$$

Here ψ is a similarity transformation variable which is related to the radial velocity by $\psi = u/(\epsilon r)$. The above equations are closed by the following ideal gas relations:

$$\rho = \frac{p}{\bar{R}T}\frac{1}{\sum_{i=1}^{N}(Y_i/MW_i)} \quad and \quad dh = c_p\,dT$$

The symbols used in the above equations are defined elsewhere [16]. Note that in the present form the equations do not depend on the radial direction. In this study, the radiative heat flux is modeled by using the emission approximation, i.e., $Q_R = 4\,\sigma\,T^4\,(a_{p,CO_2} + a_{p,H_2O})$; where, σ is the Stefan-Boltzmann constant, and a_{p,CO_2}, a_{p,H_2O} are the Planck mean absorption coefficients for CO_2 and H_2O respectively. The absorption coefficients for combustion products were taken from Ref. [17].

Reaction Scheme

The present problem was solved by considering a single step overall reaction which may be written as follows:

$$[F] + \nu\,[O_2] \rightarrow (1+\nu)\,[P]$$

Here, ν is the mass-based stoichiometric coefficient. Using second order Arrhenius kinetics, the reaction rate was defined as $\omega = A\,\rho^2\,Y_F\,Y_O\exp(-E_R/R\,T)$. The reaction rates for fuel, oxidizer, and product may then be written as $\omega_F = -\omega$; $\omega_O = -\nu\omega$; and $\omega_P = (1+\nu)\omega$. For the calculations presented here, the values of various constants and properties were obtained from Ref. [16].

Initial and Boundary Conditions

A solution of these equations requires the specification of some initial and boundary conditions which are given as following:

Initial Conditions:

$\psi(z,0) = \psi_o(z)$

$h(z,0) = h_o(z)$ or $T(z,0) = T_o(z)$

$Y_i(z,0) = Y_{i,o}(z)$ [n conditions or (n-1) conditions + $\rho(z,0)$]

$\phi(z,0) = \phi_o(z)$

Here subscript 'o' represents the initial steady state solution.

Boundary Conditions:

The origin of our coordinate system was defined at the stagnation plane.

$\psi(\infty,t) = 1$ $\quad \psi(-\infty,t) = (\rho_+/\rho_-)^{1/2}$

$h(\infty,t) = h_{u_2}$ $\quad h(-\infty,t) = h_{u_1}$

[or $T(\infty,t) = T_{u_2}$ $\quad T(-\infty,t) = T_{u_1}$]

$Y_i(\infty,t) = Y_{i,u_2}$ $\quad Y_i(-\infty,t) = Y_{i,u_1}$

$v(0,t) = 0$

The strain rate ϵ, which is a parameter, must also be specified. The reactant concentration is varied by multiplying the boundary value of either fuel or oxidizer concentration by $(1+A^*\sin(2\pi f t))$.

Solution Procedure

The governing equations form a set of nonlinear, coupled and highly stiff partial differential equations. These equations were solved numerically using the *Numerical Method of Lines* (NMOL). A 4th order 3-point central difference formula was used to spatially discretize the equations and an implicit backward differentiation formula (BDF) was used to integrate in the temporal direction. In order to carry out the numerical integration, infinity was approximated by a finite length of the order of the length scale of the problem (i.e., $(D/\epsilon)^{1/2}$). This was confirmed by checking the gradients of all the variables which must vanish at the boundaries.

Results and Discussion

The parameter values used in the present calculations are $T_- = 295$ K, $E/RT_- = 49.50$, pre-exponential constant $A = 9.52 \times 10^9$ ($m^3/kg.s$), $Q_{HV} = 47.465 \times 10^6$ J/kg, $Y_{F-} = 0.125$, and $Y_{O-} = 0.5$. The results were obtained by assuming constant specific heat, equal diffusion coefficient for all gases and $\rho^2 D$ = constant. Results shown in this paper are only for fuel concentration fluctuations but are applicable to both reactants (fuel and oxidizer) since similar findings are obtained for oxidizer fluctuations. Figures 2-5 show the results for strain rate of 10 s^{-1} and sinusoidal variation in fuel concentration of 50% amplitude and 1 Hz frequency.

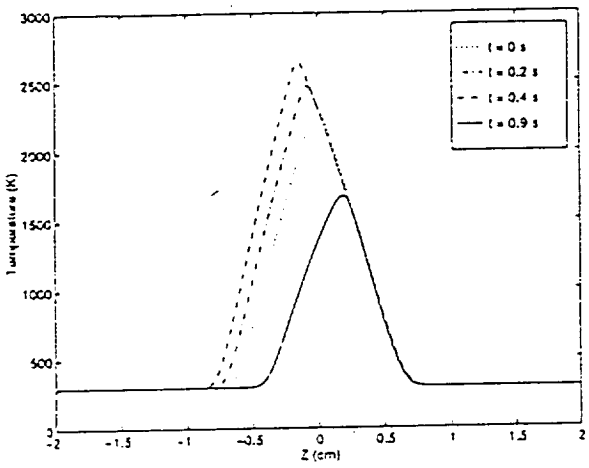

Fig. 2 Temperature Profiles
(Amp = 50%, Freq = 1 Hz, Strain Rate = 10 s^{-1})

Figure 2 shows temperature profiles at various time intervals. The figure shows that the flame which was initially stabilized at the stagnation plane (at 0) begins to move towards the oxidizer side due to an increase in the fuel concentration. After reaching a maximum value, the temperature starts decreasing corresponding to a decrease in fuel concentration and the flame moves back towards the stagnation plane. It crosses the stagnation plane and continues to move towards the fuel side till reaching a minimum temperature. The flame then keeps oscillating back and forth across the stagnation plane between these two temperature limits, which are very close to the steady state values corresponding to the maximum and minimum fuel concentrations. These results show that the flame temperature is substantially affected by fuel concentration fluctuations.

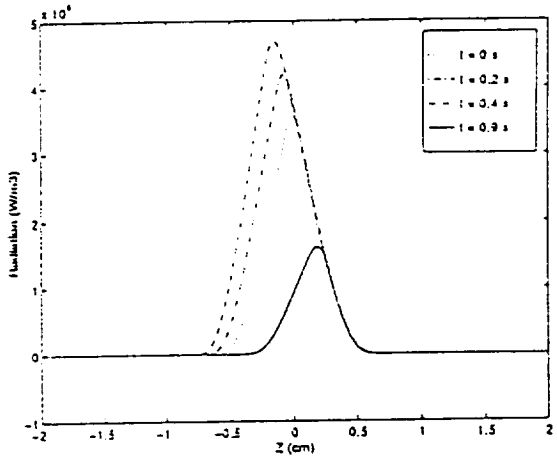

Fig. 3 Radiation Profiles
(Amp = 50%, Freq = 1 Hz, Strain Rate = 10 s^{-1})

Similar trends are observed for the gas radiation profiles. Figure 3 shows that the maximum gaseous radiation per unit volume is increased by 30% corresponding to an increase in the flame temperature and radiating combustion products caused by an increase in the fuel concentration and is decreased by 55% corresponding to a decrease in the flame temperature and radiating combustion products.

In Figure 4, the maximum flame temperature, which is a good indicator of the flame response to the induced fluctuations, is shown as a function of fluctuation time period. The figure shows that the flame responds to fluctuations sinusoidally with a time delay. This delay or phase lag is due to slow transport processes (convection & diffusion) which are responsible for transmitting information from nozzle to the reaction zone. The flame response also shows a slight

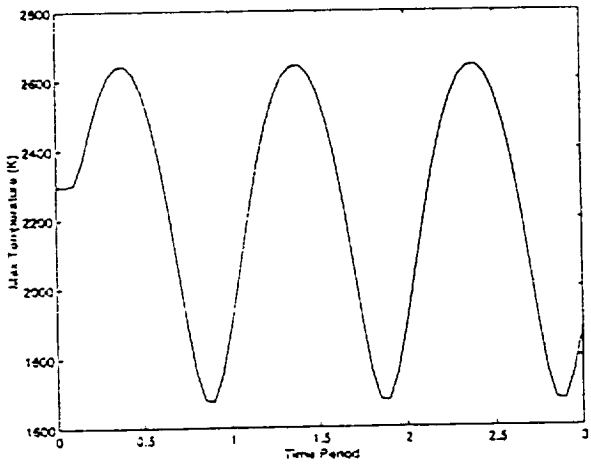

Fig. 4 Maximum Temperature Variations
(Amp = 50%, Freq = 1 Hz, Strain Rate = 10 s^{-1})

asymmetry with respect to the initial maximum temperature, i.e., the mean maximum flame temperature around which the flame temperature oscillates shifts to a lower value.

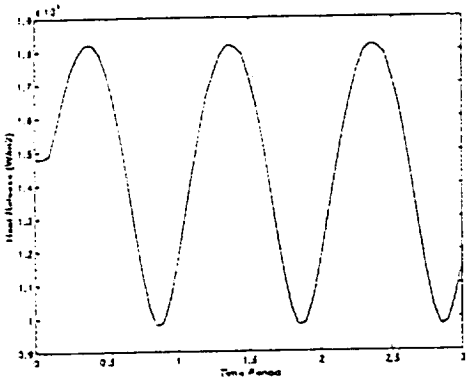

Fig. 5 Variations in Heat Release Rate
(Amp = 50%, Freq = 1 Hz, Strain Rate = 10 s^{-1})

Other indicators of the flame response, such as the heat release rate (or fuel mass burning rate) and the radiative fraction (defined as the ratio of the total heat radiated to the total amount of heat released), show similar trends (Figures 5,6). The increase or decrease in the heat release is due to a corresponding increase or decrease in the fuel burning rate caused by variations in the fuel concentrations. The radiative fraction profile indicates that the fuel concentration fluctuations have more significant effect on radiation than on the amount of heat released. Note that the radiative fraction would remain constant if the radiation fluctuated proportionally to the heat release rate. At the limiting values of fuel concentrations, the change in the total radiation from its mean value is roughly twice more than that in the heat release.

Effect of Fluctuation Amplitude

Figure 7 shows that the variations in the maximum flame temperature as induced by different amplitudes of fuel concentration fluctuations. For these results the induced frequency and strain rate were set at 1 Hz and 5 s^{-1} respectively. The results show that: i) the amplitude of fluctuations has no effect on the time delay in the flame response; ii) the mean maximum temperature around which the flame temperature oscillates decreases with an increase in the fluctuation amplitude; and iii) the amplitude of the flame response increases almost linearly with an increase in the induced fluctuation amplitude. The last conclusion can be drawn more clearly from Figure 8. In this figure, the maximum temperature fluctuations (normalized with the steady state temperature) are plotted as a function of the induced fluctuations (normalized with the steady state fuel concentration). It can be inferred that for larger strain rates at high fluctuation amplitude the extinction will occur.

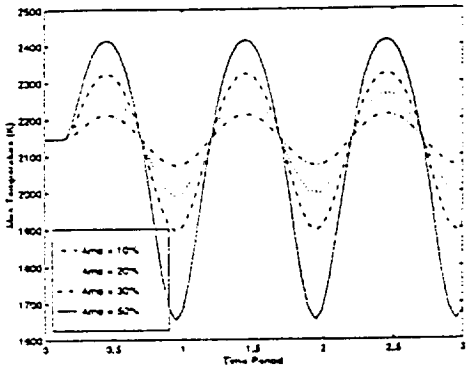

Fig. 7 Variations in Max Flame Temperature for Different Amplitudes (Freq = 1 Hz, Strain Rate = 5 s^{-1})

Effect of Fluctuation Frequency

In Figure 9, the variations in the maximum flame temperature are plotted as a function of time for different frequencies. All these results are for flames subjected to fuel

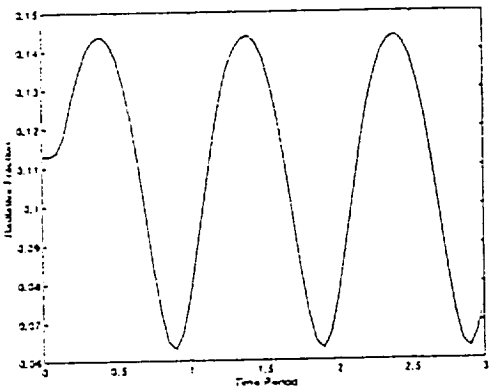

Fig. 6 Variations in Radiative Fraction
(Amp = 50%, Freq = 1 Hz, Strain Rate = 10 s^{-1})

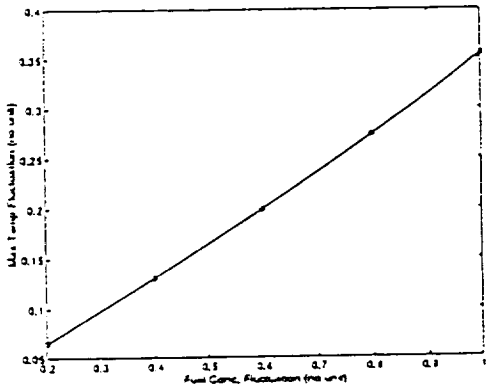

Fig. 8 Effect of Fluctuation Amplitude on Max Flame Temperature (Freq = 1 Hz, Strain Rate = 5 s^{-1})

fluctuations of 50% amplitude and strain rate of 10 s^{-1}. The figure shows that the flame response is maximum at lower frequencies and its amplitude decreases with an increase in frequency. Similar observations are reported in the literature for flames subjected to variable strain rates [7,11, 13]. For the present conditions, the flame becomes relatively insensitive to the induced fluctuations at frequencies higher than 20 Hz as shown in Figure 10. This insensitivity is due to insufficient time available at higher frequencies for transmitting relevant information to the reaction zone. Figure 9 shows that the slow transport processes also cause the phase shift or the time delay in the flame response to increase with an increase in the frequency.

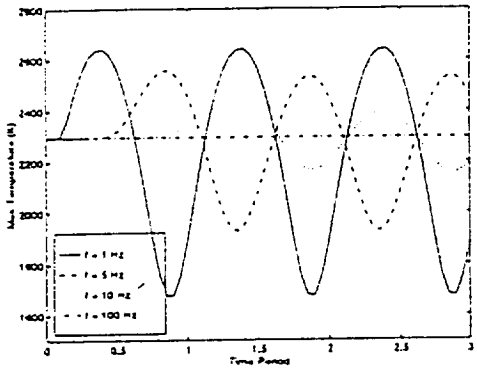

Fig. 9 Variations in Max Flame Temperature for Different Frequencies (Amp = 50%, Strain Rate = 10 s^{-1})

Another observation from Figure 9 can be made about the asymmetric effect in the flame response which decreases with an increase in the induced frequency. Hence the mean maximum flame temperature around which the temperature oscillates increases with an increase in the frequency.

Effect of Strain Rate

The effect of strain rate was investigated by simulating

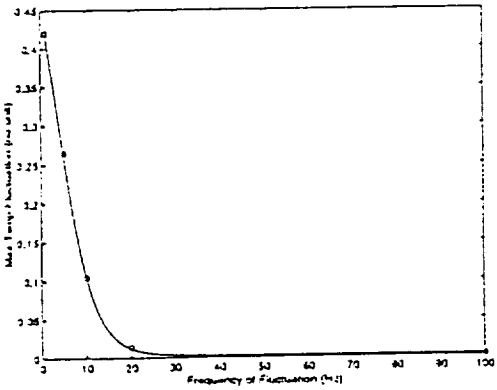

Fig. 10 Max Flame Temperature Fluctuations for Different Frequencies (Amp = 50%, Strain Rate = 10 s^{-1})

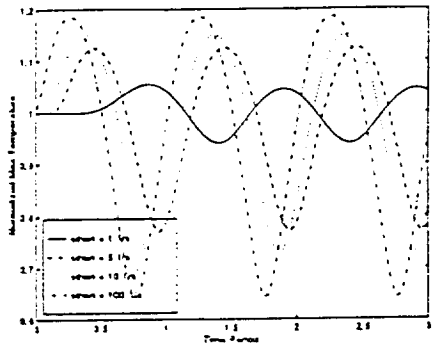

Fig. 11 Variations in Max Flame Temperature (Normalized) for Different Strain Rates (Amp = 50%, Freq = 1 Hz)

flames with different strain rates subjected to similar induced fluctuations. Figure 11 shows the variations in the maximum flame temperature (normalized with steady state temperatures) as a function of time for flames with different strain rates. These flames were subjected to the induced fluctuations of 1 Hz and 50% amplitude. The figure shows that the flame response is more prominent and the amplitude of oscillation is increased at larger strain rates. However, the term large strain rate is a relative one and depends upon the frequency of induced fluctuation. Hence in Figure 12, the maximum normalized temperature fluctuations are plotted as a function of frequency/strain rate (f/ϵ). The figure shows that the flame response is negligible for values of f/ϵ greater than 2 (i.e., low strain rates). Beyond this value, the amplitude of fluctuations increases almost exponentially with a decrease in f/ϵ. This increase in the amplitude can be explained by considering that any information to the reaction zone is transported through convection and diffusion processes. At low strain rates (high f/ϵ), the convection is small and thus the changes at the nozzle cannot be completely transmitted to the reaction zone.

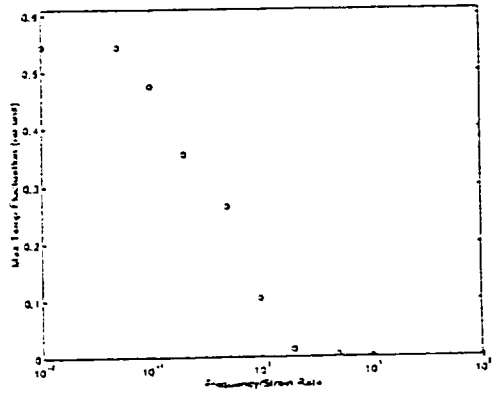

Fig. 12 Max Flame Temperature Fluctuations for Different Frequency/Strain Rate Ratios (Amp = 50%)

Hence the flame response is small. As the strain rate is increased (f/ϵ is decreased), the convection part increases, thereby transporting more information and hence the flame response is increased. Beyond certain strain rate ($f/\epsilon \leq 0.05$), the information propagates instantaneously and the instantaneous flame temperature agrees very closely to the steady state temperature values at the corresponding fuel concentration.

Figure 11 also shows that: i) the increase in the strain rate increases the asymmetry in the flame response; and ii) for a fixed frequency, the phase shift in the flame response decreases with an increase in the strain rate. This later behavior may also be explained based on the previously described argument about the role of the slow convection rates at low strain rates. Other results (not shown here), however, reveal that if the ratio f/ϵ is kept constant, an increase in the strain rate increases the phase lag. This means that the increase in the information transport through convection processes by increasing strain rate is smaller than the increase in fluctuations at the nozzle by a corresponding increase in the frequency.

Conclusions

In this article, we have investigated the dynamic response of radiating flamelet subjected to variable reactant concentrations, using numerical simulations. The reactant concentration was varied sinusoidally and a number of flames with different strain rates were examined. The maximum flame temperature, heat release rate and the radiative heat loss were used to describe the flame response. The results led to the following conclusions:

i) The flame responds sinusoidally with a phase shift to the sinusoidal induced reactant fluctuations.

ii) Low frequency fluctuations bring about a significant flame response causing a possible extinction at large strain rates.

iii) The ratio of frequency over strain rate (f/ϵ) may be used to predict the flame response to the induced reactant fluctuations. The flame response is instantaneous for $f/\epsilon \leq 0.05$ and its amplitude decreases exponentially for $0.05 \leq f/\epsilon \leq 2$, beyond which the flame becomes insensitive to fluctuations. Hence the transient effects must be considered in the flamelet modeling for the critical range $0.05 \leq f/\epsilon \leq 2$.

iv) The effect of the frequency of induced fluctuation is more important than its amplitude.

v) The induced fluctuations have more prominent effect on radiation than on the heat release.

Acknowledgment

Financial support for this work was provided by NASA (under the grant number NAG3-1460) and GRI (under the grant number 5093-260-2780).

References

1. Carrier, G. F., Fendell, F. E., and Marble, F. E., *SIAM J. Appl. Math.*, 28, 463 (1975).
2. Peters, N., *Prog. Energy. Combust. Sc.*, 10, 319 (1984).
3. Chen, J. Y.,Kaiser, T., and Kollmann, W., *Comb. Sc. Tech.*, 92, 313 (1993).
4. Faeth, G. M., and Samuelson, G. S., *Prog. Energy. Combust. Sc.*, 12, 305 (1986).
5. Howarth, D. C., Drake, M. C., Pope, S. B., and Blint, R. J., *Twenty-Second Symposium (International) on Combustion*. The Combustion Institute, Pittsburgh, 1988 (1988).
6. Barlow, R. S., and Chen, J. Y., *Twenty-Fourth Symposium (International) on Combustion*. The Combustion Institute, Pittsburgh, 231 (1992).
7. Ghoniem, A. F., Soteriou, M. C., Kino, O. M., and Cetegen, B., *Twenty-Fourth Symposium (International) on Combustion*. The Combustion Institute, Pittsburgh, 223 (1992).
8. Baum, H. R., Rehm, R. G., and Gore, J. P., *Twenty-Third Symposium (International) on Combustion*. The Combustion Institute, Pittsburgh, 715 (1990).
9. Rutland, C. J., and Ferziger, J. H., *Comb. Sc. Tech.* 73, 305 (1990).
10. Stahl, G., and Warnatz, J., *Comb. & Flame* 85, 285 (1991).
11. Darabiha, N., *Comb. Sc. Tech.* 86, 163 (1992).
12. Egolfopoulos, F. N., *Twenty-Fifth Symposium (International) on Combustion*. The Combustion Institute, Pittsburgh, 1375 (1994).
13. Im, H. G., Law, C. K., Kim, J. S., and Williams, F. A., *Comb. & Flame*, 100, 21 (1995).
14. Clarke, J. F., and Stegan, G. R., *J. Fluid Mech.*, 34, 343 (1968).
15. Egolfopoulos, F. N., *Eastern States Section / Combustion Institute Fall Technical Meeting 1993*. Princeton, NJ, 275 (1993).
16. Shamim, T., and Atreya, A., *Proc. of the ASME Heat Transfer Division*, ASME Int'l Cong. & Exp., San Francisco, CA, HTD Vol. 317-2, 69 (1995).
17. Abu-Romia, M. M., and Tien, C. L., *J. of Heat Trans.*, Nov, 321 (1967).

APPENDIX M

The Effect of Flame Structure on Soot Inception, Growth and Oxidation in Counterflow Diffusion Flames

Proceedings of the Central States Combustion Institute Meeting, 1996

By

Zhang, C, Atreya, A., Kim, H. K., Suh, J. and Shamim, T.

The Effect of Flame Structure on Soot Inception, Growth and Oxidation in Counterflow Diffusion Flames

C. Zhang, A. Atreya[1], H.K. Kim, J. Suh and T. Shamim
Combustion and Heat Transfer Laboratory
Department of Mechanical Engineering and Applied Mechanics
The University of Michigan
Ann Arbor, Michigan 48109

ABSTRACT

This paper presents an experimental investigation into the effect of flame structure on soot inception, growth and oxidation. The experiments were conducted in a low strain rate counterflow burner with the diffusion flame location progressively shifted, via fuel dilution and/or oxygen enrichment, from the oxidizer side to the fuel side of the stagnation plane. Quantitative chemical and physical measurements of temperature, OH, CH, soot, major gas species and intermediate hydrocarbons C_1–C_6 were performed to spatially resolve the sooting structure of four carefully designed sooting flame configurations: Flame I: a basic soot formation case; Flame II: a partially-affected soot formation case, where the flame is pushed closer to the stagnation plane; Flame III: a combined soot formation/oxidation case, where the flame resides at the stagnation plane; and Flame IV: a soot oxidation case, where the flame is on the fuel side of the stagnation plane. From this work, it may be concluded: (1) diffusion flame structure is important in soot inception, growth and destruction, because it is the local conditions (i.e., hydrocarbon concentrations, rich or lean, temperature, etc) that determine the inception and growth of soot; and (2) transport of the incipient soot is crucial because it can either enhance soot growth or lead to soot destruction.

1. Introduction

Injection of a gas fuel jet into a combustor that contains oxidizer is a common practice in many industrial furnaces. Research progress in this front can be found in a recent IGRC proceedings (Dolenc, 1995). Theoretically, the combustion process involves two gas streams (fuel and oxidizer) that react near the interface upon mixing. At different stages from the point of jet initiation, flame can be locally fuel-rich or fuel-lean, depending on the associated equivalence ratios. Consequently, combustion can produce different amount of pollutants (soot, NO etc). Thus, an understanding of the effect of flame configurations on soot formation and destruction is of significance not only for practical burner design but also for pollutant modeling (Du and Axelbaum, 1995, Sugiyama, 1995).

In this work, we are primarily concerned with the influence of flame structure on soot inception, growth and destruction

[1] Corresponding author
Proceedings of the 1996 Technical Meeting of the Central States Section of the Combustion Institute

in a well-defined 1-D planar counterflow diffusion flame. Generally, soot inception occurs on the fuel side of the diffusion flame where the condition that favors nucleation exists. The transport of these newly formed soot particles is very crucial because it can either push soot into the rich intermediate hydrocarbon zone where they grow or it can force soot into the high temperature OH zone where they are oxidized. To shed light on this issue, we experimentally investigated thermal, chemical and sooting structures of four carefully selected flames, whose diffusion flame locations were progressively shifted, via fuel dilution and/or oxygen enrichment, from the fuel side to the oxygen side of the stagnation plane. These experiments enhance our current understanding of soot formation and oxidation.

2. Experimental

2.1 Apparatus

The experiments were conducted in a unique, high temperature, low strain rate counterflow diffusion flame burner (Zhang et al, 1992). This burner was mounted on an X-Y-Z translating stage that allows it to be moved relative to the optical measurement system with a resolution of 0.05 mm in perpendicular to the flame. Flows of gas reactants were measured with critical orifice flow meters.

2.2 Flame conditions

The equation that governs soot transport (the flux of soot particle number) can be expressed as:

$$\vec{N}_{soot} = N(\vec{v}_a + \vec{v}_T) - D\frac{\partial N}{\partial \vec{n}} \quad (1)$$

here, n is the axial coordinate, N is the soot number density, v_a is the gas convective velocity, v_T is the thermophoretic velocity and D is the soot concentration diffusivity. v_T and D are as follows (Friedlander, 1977, Gomez and Rosner, 1994):

$$\vec{v}_T = -\frac{3}{4(1+\frac{\pi}{8})}\frac{\mu}{\rho}\frac{1}{T}\frac{\partial T}{\partial \vec{n}} \quad (2)$$

$$D = \frac{3}{2}\frac{kT}{D_{i,i}\rho\sqrt{\frac{2\pi RT}{\bar{W}}}}\frac{1}{(1+\frac{\pi}{8})} \quad (3)$$

A typical soot transport is illustrated in Fig.1: here the flame is on the oxygen side of the stagnation plane. Soot particle inception occurs near the interface of yellow-orange zone. Once formed, they are pushed toward the rich hydrocarbon zone (between flame and the stagnation) by convection, thermophoresis and soot diffusion (RHS of Eq.(1)). Clearly, one can alter the sign of the convection term in Eq.(1) (i.e., flame at the fuel side) and force the incipient soot particles flow toward the high temperature OH reaction zone where they are oxidized.

In this work, four carefully designed sooting flame configurations were examined: *Flame I* (see Fig.1): a basic

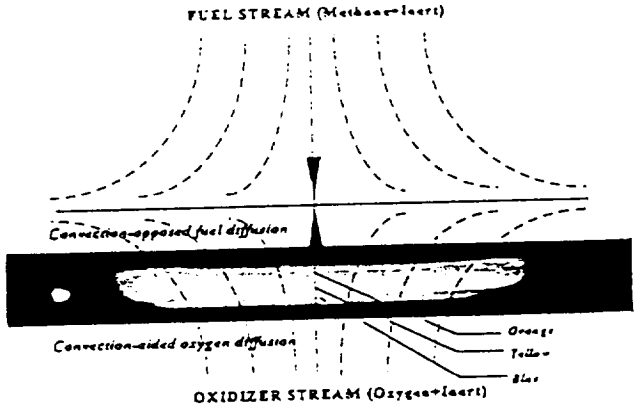

Fig.1 Illustration of a sooting counterflow diffusion flame

soot formation case, where the flame was on the oxidizer side of the stagnation plane with a thick (3–4mm) soot growth zone; *Flame II*: a partially-affected soot formation case, where the flame was pushed closer to the stagnation plane, resulting in a much narrower (~0.8mm) soot growth zone; *Flame III*: a combined soot formation/oxidation case, where the primary reaction zone of the flame resided at the stagnation plane. The convection term of soot transport in eq.(1) changed sign. Thermophoresis and diffusion pushed the newly formed soot particles toward the hydrocarbon zone where they will grow and convection pushed the soot particles into the OH radical zone where they are oxidized; and *Flame IV*: a soot oxidation case, where the flame was on the fuel side of the stagnation plane. Here, gas convection is expected to dominate, forcing the soot particles into the radical-rich flame zone where significant soot oxidation occurs. In addition, a reference flame (blue flame) was also established. The selected flame conditions are summarized in Table 1. The stagnation planes of these flames were confirmed by flow visualization using Titanium iso-proposide ($Ti(OC_3H_7)_4$) and were also confirmed by numerical computations using measured temperatures.

Table 1 Flame Conditions

FL#	Reactants	V (cm/s)	T (K)	flame locat
1	28.9%CH_4+71.1%He	10.1	562	Oxy
	42.6%O_2+57.4%N_2	4.5	649	side
2	15.5%CH_4+84.5%He	13.7	691	Oxy
	81.8%O_2+18.2%N_2	5.2	764	side
3	25%CH_4+75%N_2	6.67	637	on
	43.5%O_2+56.5%He	9.04	699	S.P.
4	21.2%CH_4+78.8%N_2	7.1	669	Fuel
	52.2%O_2+47.8%He	9.4	676	side
Ref	15.3%CH_4+84.7%He	11.2	509	Oxy
	42.6%O_2+57.4%N_2	4.01	573	side

2.3 Measurement techniques

Temperature measurements were made using a Pt/Pt-10%Rh thermocouple with a wire diameter of 0.2 mm. The junction of the thermocouple was formed by butt-welding Pt and Pt10%Rh wires together and coating them with SiO_2 to prevent catalytic reaction. The thermocouple probe was made in a triangular configuration to minimize wire heat conduction loss and was supported by a ceramic tube. The entire thermocouple assembly was mounted on a translating stage whose position was recorded by the computer data-acquisition unit along with the thermocouple temperature data.

A 5W Ar-ion laser operating at 355 nm, 365nm and 514nm lines was used for broadband LIF excitation of PAH and for scattering/extinction measurement of soot. This laser beam was modulated by a mechanical chopper to allow for synchronized detection of the signal. The transmitted laser beam was first collected by an integrating sphere and then measured by the photodiode to minimize possible light deflection due to the density gradients in flames. The scattered light by soot particles and the induced broadband PAH fluorescence were collected by a focusing lens, at 90° with respect to the incident beam, through a band filter and detected by a photomultiplier tube. OH, CH and C_2 emission spectra were collected by a 6:1 imaging optics into an optical fiber coupled Oriel 257 spectrograph (200nm ~800nm) at 135° relative to the incident beam. To ensure the spacial resolution of emission measurements, a thin line(~0.06mm) measuring volume in the flame was achieved by placing a 10-μm slit in front of the optical fiber (nominal diameter of 200μm). The spectrograph then directed the dispersed spectrum (gratings: 600l/mm, 1200l/mm and 2400 l/mm) onto a three-stage cooled, gated-ICCD camera. For OH laser induced fluorescence measurement, a Nd:YAG pumped tunable dye laser was frequency doubled to produce

0.5mJ, 282.5nm, 7ns-pulses. The excited OH LIF was typically sampled with a 100ns gate width. 200 integrations were used to maximize S/N ratio. In these measurements, both the CW and the pulsed laser beams were first collimated and then focused by a 300mm UV coated lens into the burner, which gave an approximate focal diameter of 0.04mm.

Chemical species were measured by gas chromatographs (GC). An uncooled quartz microprobe (~100μm) was used for extracting the gas samples from the flame. The sample withdrawn was located by positioning the microprobe relative to the burner port. The probe was also aligned radially along the streamline to minimize disturbance. The multicomponent sample was extracted and distributed, via a heated vacuum sample line to four GCs for analysis. Gases measured were: CO, CO_2, H_2O, H_2, CH_4, He, O_2 and N_2; light hydrocarbons from C_1 to C_6; and PAH up to C_{18}.

3. Results and Discussion

Counterflow diffusion flame structure

In Figs.2 and 3, the measured temperature, chemical species and CH and OH radical profiles are presented for a blue flame (C_2, PAH and soot were not found). This flame served as a reference for the counterflow diffusion flame structure (the blue flame was used because it posed least uncertainty in modeling and chemical measurements). Also this flame was at the threshold of blue-yellow transition- a slight increase in fuel concentration would lead to a yellow-emission flame. A similar structure (T, V, major species C_1 -C_3 intermediate hydrocarbons but without radicals) was reported in Tsuji's early work on forward stagnant point flow counterflow diffusion flame (Tsuji et al, 1969, 1971).

Here, the measured temperature has been corrected for radiation. OH peaked with the diffusion flame temperature,

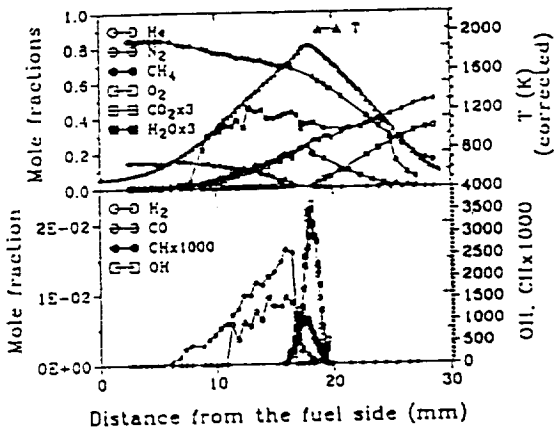

Fig.2 Flame structure I (blue flame)

while CH was slightly off to the fuel side. Both CO and H_2 showed a sharp decrease near the flame on the fuel side where CH existed. This position marked the well-known water-gas shift reaction with strong emission at blue wavelength[2] (Gaydon, 1974). These two species were consumed in the primary reaction zone that produced combustion products H_2O and CO_2. Similar to Tsuji's result, water profile appeared broader but had a larger error in GC measurement.

Intermediate hydrocarbons (C_2-C_6) were shown in Fig.3.

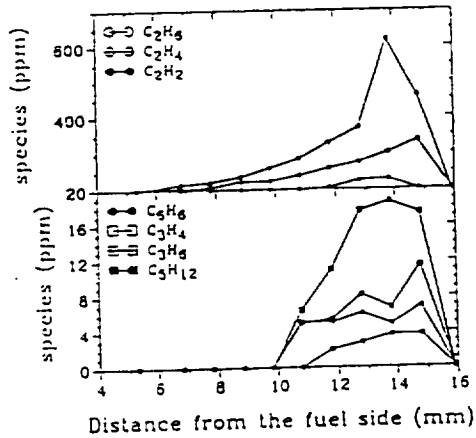

Fig.3 Flame structure II (blue flame)

[2] Blue emission was attributed to either CO combustion or CH emission in the past.

All intermediate hydrocarbons demonstrated similar profiles and peaked at approximately the same location on the fuel side of the flame. C_2 species (C_2H_6 and C_2H_4) existed in a broader zone (Z=7~16mm) while species of C_3 and above existed in a relatively narrower zone (Z=10~16mm). And the magnitude of theses species demonstrated the following trend, indicating a build-up of PAH:

$$C_2 \gg C_3 > C_5 \text{ and } C_6 \quad (4)$$

Similar intermediate hydrocarbon pool structure were found for flames I~IV.

Effect of flame structure on soot formation and oxidation

In Fig.4, OH and soot volume fraction profiles are presented for flames I to IV. Clearly, for the fuel-rich case - *flame on the oxygen side*, once soot inception occurs, it is pushed away from the OH zone. (here, the gas convection, the thermophoresis and the soot diffusion all drive soot particles away from the flame toward the fuel side). Thus, there is little soot oxidation, resulting in a single branch of soot volume fraction profile. It is interesting that flame II yielded higher soot volume fraction despite its lower fuel concentration at the fuel inlet port. This is probably because of the higher temperature to accelerate soot formation.

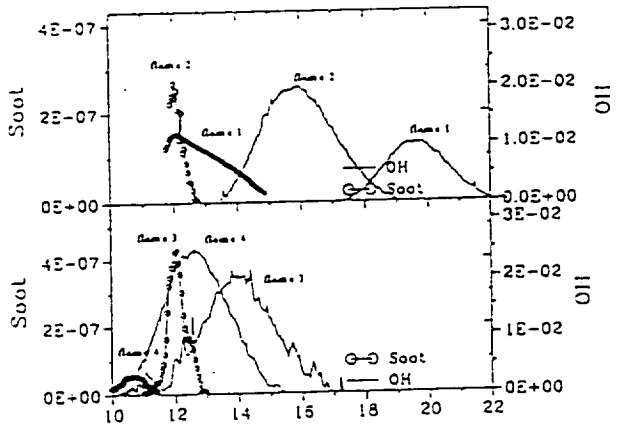

Fig.4 Effect of OH on soot inceprion and growth

Flames III and IV showed very different soot formation picture. Again, soot inception occurred on the fuel side of the flame but very close to the OH reaction zone. However, due to the reversed gas convection, which is the dominant term in Eq. (1), the newly formed soot particles were forced to pass through high temperature OH zone where the oxidation occurred, resulting in a double branched soot profile. For flame III, since the flame resided at the stagnation plane (v_a=0), convection was less dominant than in flame IV, hence the peak soot volume fraction (~4×10^{-7}) was still higher due to its high temperature. In flame IV, the convective term was dominant leaving little time for soot growth. It seems that soot was oxidized immediately after the inception (see Fig.4).

Effect of local equivalence ratio on soot

Soot formation in premixed flames is directly related to the C/O ratio. In the counterflow diffusion flames, however, local C/O ratio varies from zero to infinite. Thus, the flame structure plays an important role. As is seen above, flames I~IV have different peak soot volume fractions, which are not proportional to their inlet fuel concentrations, i.e., flame III produced about 8 times soot higher than flame IV even though its fuel concentrations was only slightly higher. This

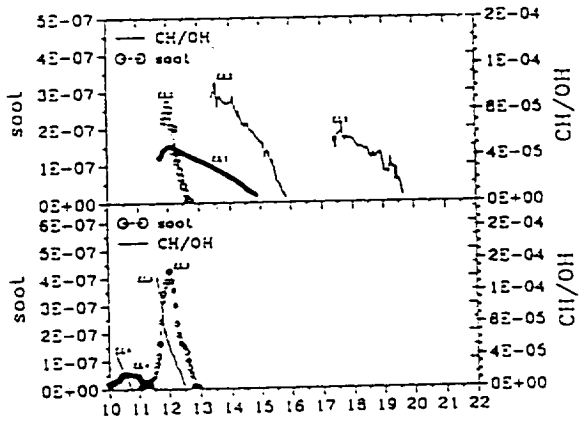

Fig.5 Effect of local condition (CH/OH) on soot

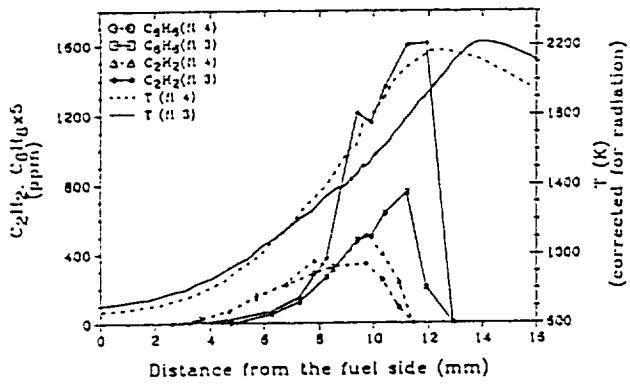

Fig.6 Effect of local conditions (T, C_2H_2, C_6H_6) on soot

suggests that it is the local conditions that determine the peak volume fraction. To further discuss this issue, the local ratio of CH/OH is shown in Fig.5 along with the soot volume fraction. In all cases, the magnitude of peak CH/OH ratio appears to correspond to that of the soot volume fraction profile, which shows the following trend (local soot and CH/OH ratio):

$$soot,\ \frac{CH}{OH}: \quad flame\ III > flame\ II > flame\ I > flame\ IV \quad (5)$$

Similar trend can be observed in intermediate hydrocarbon profiles, i.e., Fig.6 shows that flames III and IV had similar temperature field, but the former flame had higher intermediate hydrocarbons as seen from acetylene and benzene, consequently, it generated more soot.

4. Conclusions

From this work, it may be concluded: (1) diffusion flame structure is important in soot inception, growth and destruction, because it is the local conditions (i.e., hydrocarbon concentrations, rich or lean, temperature, etc) that determine the inception and growth of soot; and (2) transport of the incipient soot is crucial because it can either enhance soot growth or lead to soot destruction.

Acknowledgement

This work was supported by GRI under the contract number GRI 5087-260-1481 and the technical direction of Drs. J.A. Kezerle and R.V. Serauskas; by NASA under the grant number NAG3-1460 and by NSF under the grant number CBT-8552654.

References

1. Dolenc, D.A. ed, Proceedings of the International Gas Research Conference, Cannes, France 1995

2. Du, J. and Axelbaum, R.L., *Combustion and Flame* 100: 367-375 (1995)

3. Sugiyama, G., *Twenty-Fifth Symposium (International) on Combustion*, The Combustion Institute, 1994, p.601

4. Zhang,C., Atreya, A. and Lee,K., *Twenty-fourth Symp. (Intl) on Combustion*, The Combustion Institute, Pittsburgh, 1992, p.1049

5. Friedlander, S.K., *Smoke, Dust and Haze*, Wiley, (1977)

6. Gomez, S. and Rosner, D., *Combust Sci and Tech* 84: p.335 (1993)

7. Tsuji, H. and Yamaoka, I., *Twelfth Symp. (Intl) on Combustion*, The Combustion Institute, Pittsburgh, 1968, p.997

8. Tsuji, H. and Yamaoka, I., *Thirteenth Symp. (Intl) on Combustion*, The Combustion Institute, Pittsburgh, 1970, p.723

9. Gaydon, A.G., *The Spectroscopy of Flames*, Chapman and Hall, London, 1974

APPENDIX N

Measurements of OH, CH, C_2 and PAH in Laminar Counterflow Diffusion Flames

Proceedings of the Central States Combustion Institute Meeting, 1996

By

Zhang, C, Atreya, A., Shamim, T., Kim, H. K., and Suh, J.

Measurements of OH, CH, C_2 and PAH in Laminar Counterflow Diffusion Flames

C. Zhang, A. Atreya[1], T. Shamim, H.K. Kim and J. Suh
Combustion and Heat Transfer Laboratory
Department of Mechanical Engineering and Applied Mechanics
The University of Michigan
Ann Arbor, Michigan 48109

ABSTRACT

In this work, in-situ laser diagnostic methods, flame emission spectroscopy and laser-induced fluorescence, were employed for concentration measurements of four species: OH, CH, C_2 and PAH, in sooting laminar counterflow diffusion flames. Spatially resolved flame emission spectroscopic measurements were performed for OH, CH and C_2 using a 6:1 imaging optics, an optical fiber coupled spectrograph (spectral range of 200nm–800nm) and a gated-ICCD detector. Emission from the 306.4nm band of OH; the 431.5nm band of CH and the 516.5 nm– 595.87nm Swan band system of C_2 were measured. Broadband UV fluorescence (attributed to PAH) was measured by exciting the flame with a CW laser operating at 355nm and 365nm and detecting the fluorescence signal at 452.5±27.5nm. Also, fluorescence from OH was excited at 282.5nm by a Nd:YAG pumped tunable dye laser and detected at bands from 307nm to 318nm. These measurements help identify the progression of the sooting process from the parent fuel to increasingly complex species and finally to soot particles.

1. Introduction

Flame species, such as OH, CH, C_2 and PAH, are important to combustion and soot chemistry. OH has been identified as a dominant oxidizer of soot particles (Neoh et al 1984); CH, on the other hand, has been implicated in the inception stage of soot formation through the chemi-ionization reaction of ground state CH with O and the reaction of electronically excited CH with C_2H_2 (Calcote, 1981); and both C_2 and PAH are known to play an important role in soot nucleation (Gaydon, 1974; Frenklach et al, 1990). Thus, non-intrusive and spatially resolved measurements of these species will help understand and model of soot formation and oxidation in hydrocarbon diffusion flames.

In premixed hydrocarbon flames, emission spectrum from OH, CH and C_2 are prominent (Gaydon, 1974). The well-known C_2 bands, centered at 515nm green line, were first mapped in 1857 by Swan. The visible flame spectrum generally exhibits a strong violet-degraded band in the blue near 431.5nm due to CH and several bands in the ultra-violet ranges due to OH (the strongest is found at 306.4nm). Nevertheless, emission spectroscopy has, in the past, been used primarily for detecting the overall presence of a particular radicals in flames. Because it is a "line of sight" measurement. It had been very difficult to resolve the

[1] Corresponding author
Proceedings of the 1996 Technical Meeting of the Central States Section of the Combustion Institute

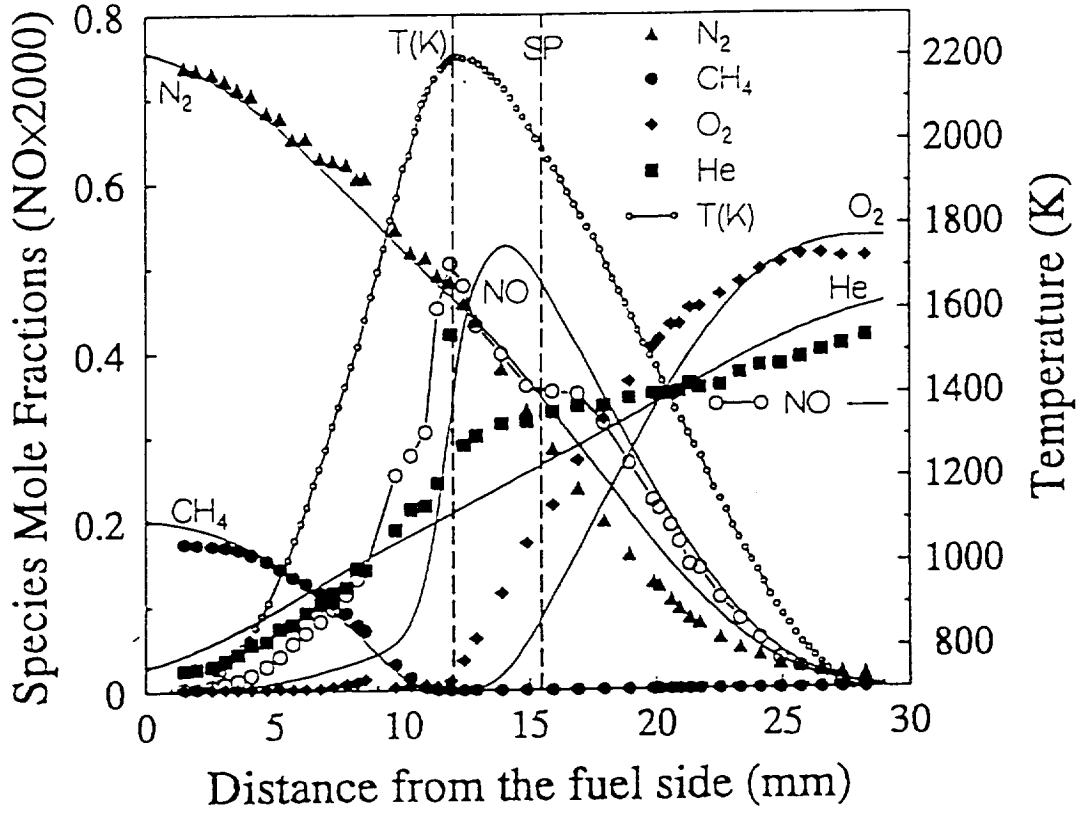
Species Mole Fractions (NOx2000)
Temperature (K)
Distance from the fuel side (mm)
T(K)
SP
N2
CH4
O2
He
NO
0.8
0.6
0.4
0.2
0
2200
2000
1800
1600
1400
1200
1000
800
0
5
10
15
20
25
30

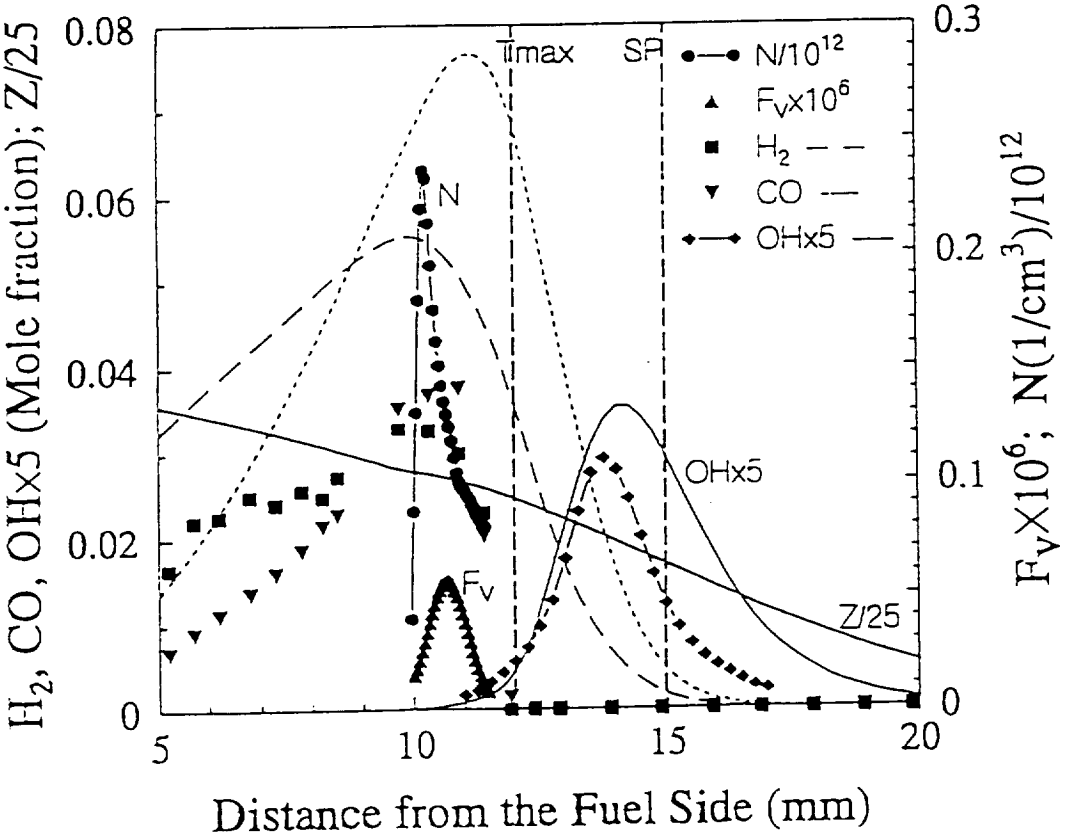
H2, CO, OHx5 (Mole fraction); Z/25
FvX10^6; N(1/cm^3)/10^12
Distance from the Fuel Side (mm)
Tmax
SP
N/10^12
FvX10^6
H2
CO
OHx5
Z/25
N
Fv
0.08
0.06
0.04
0.02
0
0.3
0.2
0.1
0
5
10
15
20

spacial structure of most non-planar flames. Laser induced fluorescence (LIF), on the other hand, has an advantage because the measurement volume is defined by the laser beam. Hence, it has become one of the most widely used technique for probing the radical species profiles (Eckbreth, 1988).

In this work, the collection optics and the detection system have been designed to spatially resolve the emission spectroscopic measurement in a well-defined 1-D planar counterflow diffusion flame. Profiles, normal to the flame, of OH, CH and C_2 were measured. In addition, LIF measurements were also made to measure OH and PAH profiles. These radical and the intermediate hydrocarbon profiles enable us to conceptually examine the progression of the sooting process from the parent fuel to soot particles.

2. Experimental

2.1 Apparatus

The experiments were conducted in a unique, high temperature, low strain rate counterflow diffusion flame burner (Zhang et al, 1992). This burner was mounted on an X-Y-Z translating stage system that allows it to be moved relative to the optical measurement system with a resolution of 0.05mm in perpendicular to the flame. Flows of gaseous reactants were measured with critical orifice flow meters. Flames selected for the present study were summarized in Table 1.

Table 1 Flame Conditions

FL#	Reactants	V (cm/s)	T (K)	comm
1	15.3%CH_4÷84.7%He	11.2	509	blue
	42.6%O_2÷57.4%N_2	4.01	573	flame
2	55.8%H_2÷41.2%N_2	8.21	620	No
	19.2%O_2÷80.8%He	14.0	660	HC
3	28.9%CH_4÷71.1%He	10.1	562	sooty
	42.6%O_2÷57.4%N_2	4.5	649	
4	65%CH_4÷35%N_2	6.8	538	sooty
	16%O_2÷84%He	13.5	662	
5	48.7%C_2H_4÷51.3%N_2	6.8	556	very
	16%O_2÷84%He	13.5	630	sooty

Temperature measurements were made using a Pt/Pt-10%Rh thermocouple with a wire diameter of 0.2 mm. The junction of the thermocouple was formed by butt-welding Pt and Pt10%Rh wires together and coating them with SiO_2 to prevent catalytic reaction. The thermocouple probe was made in a triangular configuration to minimize wire heat conduction loss and was supported by a ceramic tube. The entire thermocouple assembly was mounted on a translating stage whose position was recorded by the computer data-acquisition unit along with the thermocouple temperature data.

A schematic illustration of the optical apparatus and the burner is shown in Fig.1. A 5W Ar-ion laser operating at 355 nm, 365nm and 514nm lines was used for broadband LIF excitation of PAH and for scattering/extinction measurement of soot. This laser beam was modulated using a mechanical chopper to allow for synchronized detection of the signal. The transmitted laser beam was first collected by

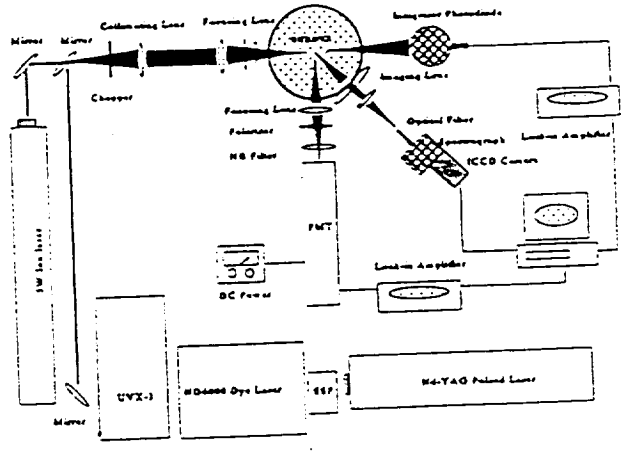

Fig.1 Experimental set-up

an integrating sphere and then measured by the photodiode to minimize possible light deflection due to the density gradients in flames. The scattered light by soot and the induced broadband PAH fluorescence were collected by a focusing lens, at 90° with respect to the incident beam, through a band filter and detected by a photomultiplier tube. While OH, CH and C_2 emission spectrum was collected by a 6:1 imaging optics into an optical fiber coupled Oriel 257 spectrograph (200nm~800nm) at 135°. To ensure the spacial resolution of emission measurement, a thin line (~0.06mm) measuring volume was achieved by placing a 10-μm slit in front of the optical fiber (nominal diameter of 200μm). The spectrograph then directed the dispersed spectrum (gratings : 600l/mm, 1200l/mm and 2400l/mm) onto a three-stage cooled, gated-ICCD camera. For OH LIF measurements, a Nd:YAG pumped tunable dye laser was frequency doubled to produce 0.5mJ, 282.5nm, 7ns-pulses. The excited OH LIF was typically sampled with a 100ns gate width. 200 integrations were used to maximize the S/N ratio. In these measurements, both the CW and the pulsed laser beams were first collimated and filtered and then focused by a 300mm UV coated lens into the burner yielding an approximate focal diameter of 0.04mm.

2.2 Emission and LIF detection schemes

OH

The spontaneous emission bands of OH are due to a $^2\Sigma$-$^2\Pi$ transitions. These bands are degraded to the red and show an open rotational fine structure. In this work, the most prominent (0,0) band of OH at 306.4nm was measured to yield the OH profile across the flame. In addition, LIF from OH was excited with the pulsed laser beam tuned near 283nm and detected from 307nm to 318nm (which covered (0,0) and (1,1) bands).

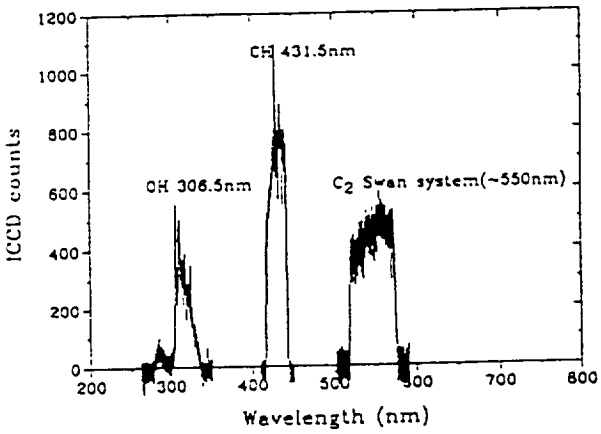

Fig.2 Emission spectrum of OH, CH and C_2

CH

Despite its relative low concentration, CH emission at 431.5 nm is very strong in flames, which is due to (0,0) band of $^2\Delta$ -$^2\Pi$ transition with a fairly open rotational structure. This band was measured to yield CH profile.

C_2

The well-known Swan system consists of a number of bands each with a sharp edge or head on one side and all shaded off or degraded the same way. These bands are due to $^3\Pi$- $^3\Pi$ transition. In this work, Swan bands at 512.9nm to 595.9nm were measured to yield C_2. A typical emission spectrum of OH, CH and C_2 is given in Fig.2.

PAH

The UV induced broadband visible fluorescence is attributed to PAH (Smyth et al, 1985; Beretta et al, 1985). In this work, the broadband PAH fluorescence was excited with a CW laser operating at 355nm and 365nm lines and then detected at 452.5±27.5nm. According to Beretta, PAH fluorescing in this band window may include the following species: *Fluoranthene, Benzperylene, Perylene, Coronene and Anthanthrene.*

2.3 Calibration[3]

Radical concentrations from the measured emission and

[3] calibration were only made for OH and CH.

LIF can be related to measured intensity, I_e and I_a through equations (Gaydon, 1974 and Eckbreth, 1988):

$$[x] = I_e \frac{R_u T}{P} \frac{1}{A \eta_{opt}} = C_e T I_e \quad (1)$$

here A is the Boltzmann distribution relation (generally, flame deviates from the equilibrium conditions, see Smyth, et al., 1990). Likewise, for LIF we have:

$$[x] = const \left[\frac{T_{ref}}{P_{ref}}\right]^{0.5} T^{0.5} \frac{I_A}{E_{21}} = C_f T^{0.5} I_A \quad (2)$$

The Sandia National Laboratories computer code OPPDIF and CHEMKIN-II (Kee, et al. 1989) were extended to include gas radiation and were used for base flame modeling. The present GRIMECH-I mechanism is regarded as quite adequate for a blue methane flame (flame#1, which was not complicated by measured C_3 and higher species or soot). This confidence was based upon comparisons of measured and computed temperature and major chemical species. The computed peak concentrations of OH and CH were used to place the measured OH and CH for the blue flame on the absolute basis. The constants C_e and C_f were then derived to calibrate other flames for OH and CH.

3. Results and Discussion

Comparison of measured OH with model computation

In Fig.3, the measured and computed OH profiles (flame #2 and flame#3) are compared. Here, the solid lines are computed OH profiles and the dashed line is the OH profile of flame#3 obtained by LIF. Good agreement was achieved between measurements of OH using emission spectroscopy and using the LIF. For the hydrogen flame (flame#2), the computed OH is in close agreement with measurement except that the computed profile is broader. In contrast, the computed OH for the sooty flame (flame#3) exhibited a relatively larger error in peak mole fraction, which was due primarily to the fact that flame computations currently lack the capability of handling the rich-combustion and the soot chemistry. These results show that emission spectroscopy can, indeed, be used for resolving prominent radical profiles of OH, CH and C_2.

OH, CH, C_2, PAH and sooting structure

Fig.4 illustrates the sooting structure of flame#3 with relative concentrations of radicals like OH, CH, C_2 and important soot precursor species of PAH (radicals were obtained by using emission spectroscopy and PAH was obtained by using broadband fluorescence measurement). Basically, a blue-yellow-orange sooting flame structure is seen: the bright blue reaction zone, which is characterized by CH emission, was on the oxidizer side of the stagnation plane; CH peaked on the fuel side slightly away from the flame; A relatively thick (~3mm) yellow-orange zone, where significant C_2 was present, was located on the fuel side of the flame and was separated from the blue zone by a very thin dark zone. Soot inception seemed to actually occur at the location where C_2 reached its peak and where PAH profile began to rise. The incipient soot particles were then swept downstream (toward the fuel side) due to the convection and due to the thermophoretic diffusion. Along its path, soot particles grew through coagulation and surface growth. This process ceased at the stagnation plane. With

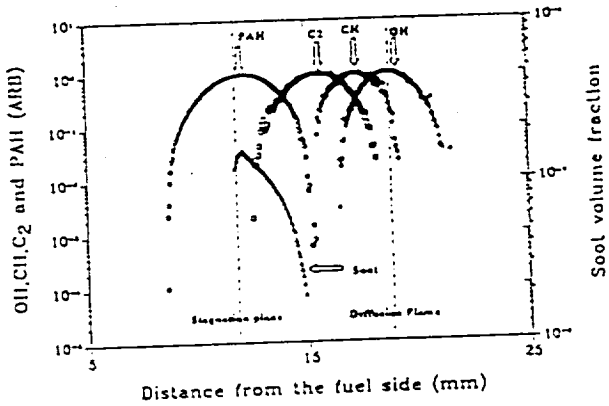

Fig.4 Sooting structure as characterized by OH, CH, C_2 and PAH

negligible soot mass diffusion and weak thermophoretic diffusion, very little soot was present beyond the stagnation plane despite a significant amount of PAH. This emphasizes that little nucleation occurs at or below the stagnation plane and the process is predominantly soot growth controlled.

In light of the sooting processes in premixed flames where the primary fuel breaks down and then builds up to soot in the post flame zone. The above observation may lead to a similar conceptual visualization of the main sooting processes in a fuel-rich counterflow diffusion flame:

(i) Diffusion and convection of radicals such as OH, O and H into the fuel-rich reactant flow[3], resulting in chain-reactions leading to the formation of unsaturated compounds such as acetylene and larger unstable molecules;

(ii) Breakdown of some of the larger molecules, or reactions with radicals like H and CH, to produce C_2 species;

(iii) Continued growth of unsaturated compounds to form ring-structured benzene and large PAH;

(iv) Under certain conditions, nucleation of some PAH into incipient soot particles occurs; and

(v) In accordance with the increase in PAH concentration, soot particles undergo a series of chemical surface reaction, by absorbing species like acetylene, and physical reaction like coagulation;

(vi) In the current flame configuration, soot was eventually transported radially out by convection at the stagnation plane, leaving only little soot that diffused below the stagnation plane. While PAH continued to diffuse towards the fuel side.

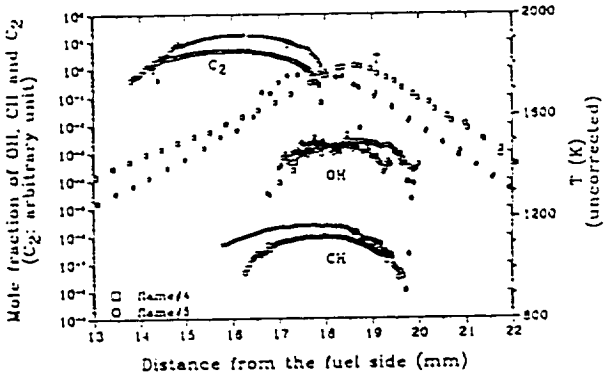

Fig.5 Effect of CH, C_2 and T on soot

C_2, PAH and soot loading

As discussed above, C_2 and PAH are representative of fuel-rich sooting flame, although the definite role of these species under different flame conditions is yet to be elucidated. In Figs. 5 and 6, we further examine the effect of PAH and C_2 on soot loadings in two flames (flames#4 and 5). These two flames had similar thermal and flow field structure (see Fig.5) with a slightly higher flame temperature for the methane flame. Since both flames used the same amount of oxidizer (16%O_2, 13.5cm/s), they had almost same oxidizer concentrations. Nevertheless, the ethylene flame was seen to produce more C_2 and CH. In Fig.6, note that there is 50 times more C_2, 2 times more PAH and 10 times more soot in the ethylene flame. Even though this

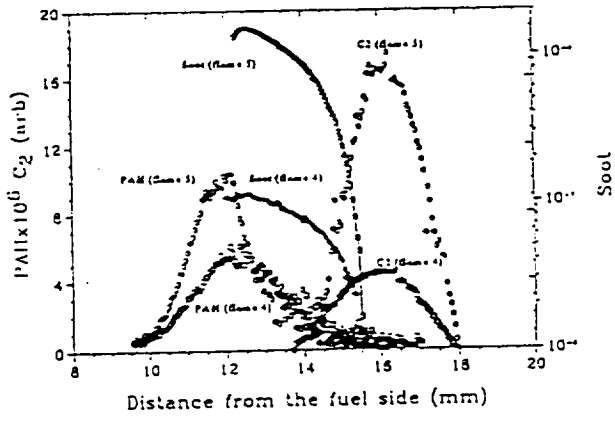

Fig.6 Effect of C_2 and PAH on soot

[3] in the present work, the primary fuel diffused against the gas convection into the flame front which lied at the oxygen side of the stagnation plane

comparison may not be conclusive in a quantitative sense, the result is consistent with the above discussion: given similar thermal and flow structure of two flames, more the available carbon, more the soot is produced.

4. Conclusions

Despite the current progress, flame emission spectroscopy has remained a lesser-used technique for radical profile measurements. In this work, we successfully applied the flame emission spectroscopy to resolve OH, CH and C_2 profiles in a well-defined 1-D diffusion flame. This, in conjunction with LIF measurements and the numerical flame computation, enables us to examine the sooting structure of counterflow diffusion flames as characterized by OH, CH, C_2 and PAH.

From this work, it may be concluded that, similar to premixed flames, sooting path can be derived for diffusion flames: (i) Diffusion and convection of flame produced radicals into fuel stream to form unsaturated hydrocarbon compounds;(ii) Breakdown of large molecules to yield carbon radicals and PAH; (iii) Nucleation of PAH to form incipient soot; and (iv) Soot grow via surface reaction and coagulation.

Acknowledgement

This work was supported by GRI under the contract number GRI 5087-260-1481 and the technical direction of Drs. J.A. Kezerle and R.V. Serauskas; by NASA under the grant number NAG3-1460 and by NSF under the grant number CBT-8552654.

References

1. Neoh, K.G., Howard, J.B. and Sarofim, A.F., *Twentieth Symp. (Intl) on Combustion*, The Combustion Institute, Pittsburgh, 1984,p.951

2. Calcote, H.F., *Comb. & Flame* 42:p.215, (1981)

3. Gaydon, A.G., *The Spectroscopy of Flames*, Chapman and Hall, London, 1974

4. Eckbreth, A.C., *Laser Diagnostics for Combustion Temperature and Species*, Abacus Press, 1988

5.Frenklach, M. and Wang,H., *Twenty-third Symp. (Intl) on Combustion*, The Combustion Institute, Pittsburgh, 1990, p1559

5. Zhang,C., Atreya, A. and Lee,K., *Twenty-fourth Symp. (Intl) on Combustion*, The Combustion Institute, Pittsburgh, 1992, p.1049

6. Smyth, K.C., Miller, J.H., Dorfman, R.C., Mallard, W.G., Santoro, R.J., *Comb. & Flame* 62:p.157, (1985)

7. Beretta, F., Cincotti, V., D'alession, A. and Menna, P., *Comb. & Flame* 61:p.211, (1985)

8. Kee,R.J., Rupley,F.M., Miller, J.M., *Sandia Report*, SAND89-8009B, (1991)

9. Smyth, K.C., Tjossem, J.H., *Applied Physics B* 50:p.499, (1990)

APPENDIX O

Transient Response of a Radiating Flamelet to Changes in Global Stoichiometric Conditions

For Submission to Combustion and Flame, 1996

By

Shamim, T. and Atreya, A.

Transient Response of a Radiating Flamelet to Changes in Global Stoichiometric Conditions

T. Shamim and A. Atreya
Combustion and Heat Transfer Laboratory
Department of Mechanical Engineering and Applied Mechanics
The University of Michigan, Ann Arbor, MI 48109-2125

Corresponding Author

Prof. A. Atreya
Combustion and Heat Transfer Laboratory
Department of Mechanical Engineering and Applied Mechanics
The University of Michigan
Ann Arbor, MI 48109-2125

Phone: (313) 647-4790
Fax : (313) 647-3170
email: aatreya@engin.umich.edu

Transient Response of a Radiating Flamelet to Changes in Global Stoichiometric Conditions

T. Shamim and A. Atreya
Combustion and Heat Transfer Laboratory
Department of Mechanical Engineering and Applied Mechanics
The University of Michigan, Ann Arbor, MI 48109-2125

Absrtact

The effects of changes in global stoichiometric conditions by varying reactant (fuel/oxidizer) concentrations on radiating flamelets using a numerical investigation are reported in this article. The flame response to both step and sinusoidal variations about a mean value of reactant concentration for various values of strain rates is examined. This work will aid in the better understanding of turbulent combustion. The radiative effects from combustion products (CO_2 and H_2O) are also included in the formulation. The maximum flame temperature, heat release rate and the radiative heat loss are used to describe the flame response. The results show that the flame responds to fluctuations with a time delay. The effect of the frequency of fluctuation is found to be more important than its amplitude. Low frequency fluctuations bring about a significant flame response causing extinction at large strain rates for high fluctuation amplitudes. At high frequencies relative to the strain rate, rapid concentration fluctuations are distributed closely in space. These are neutralized by the resulting large diffusion gradients. Thus the flame becomes relatively insensitive to fluctuations. The ratio of frequency over strain rate is identified to predict the flame response to the induced reactant fluctuations. The induced fluctuations were found to have more prominent effect on radiation than on the heat release.

Nomenclature

a_p	Planck mean absorption coefficient
A	Pre-exponential factor
c_p	constant pressure specific heat of the mixture
D_i	coefficient of diffusivity of species i
h	enthalpy
$h^\circ_{f,i}$	enthalpy of formation of species i
MW	average molecular weight
Le	Lewis number
p	pressure
Q_R	radiant heat loss
Q_{HV}	heat of reaction
R	universal gas constant
T	temperature
t	time
v	axial velocity
Y_i	mass fraction of species i
ϵ	strain rate
η	similarity transformation variable

λ thermal conductivity of the mixture
μ dynamic viscosity of the mixture
ν mass based stoichiometric ratio
ρ mass density
σ Stefan-Boltzmann constant
ψ similarity transformation variable
ω_i mass rate of production of species i

Introduction

An investigation of transient effects on flamelet combustion is useful for better understanding of turbulent combustion. The flamelet concept, which was proposed by Carrier et al., [1] and later developed by Peters [2], provides a convenient mechanism to include detailed chemical kinetics into the calculations of turbulent flames. The idea is based on the translation of physical coordinates to a coordinate system where the mixture fraction is one of the independent variables. One can then express all thermochemical variables as unique functions of two variables, the mixture fraction and its dissipation rate by assuming that the changes of thermochemical variables are dominant in the direction perpendicular to the surface of constant mixture fraction [3]. These unique functions have been called "state relationships" [4]. Consequently, the flamelet model can be incorporated into existing turbulent combustion model provided these state relationships are known.

A basic assumption of these flamelet models is that the local structure of the reaction zone may be represented by an ensemble of quasi-steady state strained laminar flame elements which are stretched and convected by the turbulent flow [5]. The validity of this assumption has, however, been questioned in many recent studies by showing that non-steady effects are of considerable importance [5-7]. Consequently, there has been a growing interest in the study of time dependent effects on flamelet combustion [3, 6-13]. However, most of these studies are limited to the effects of time varying strain rate, which is only one of three important parameters that need to be matched in order for the structure of turbulent flamelet to correspond to the structure of the laminar diffusion flame [14]. The effect of the other two parameters, reactant concentration and reactant temperature fluctuations, has not been investigated with the exception of the limited study by Clarke and Stegan [15] (on concentration fluctuations) and Egolfopoulos [15] (on concentration and temperature fluctuations). Furthermore, the effects of radiative heat losses are not considered by any of these studies with the exception of Egolfopoulos [12].

The present study is an attempt to fill this existing gap in the literature. We investigate the effects of reactant concentration fluctuations on radiating flamelets in this article. It is interesting to note that velocity fluctuations, which receive such a wide attention in the recent combustion literature, have a relatively smaller effect on the flame through changes in the flow field and subsequent small changes in the concentration profiles in the reaction zone [17]. The concentration fluctuations, on the other hand, are expected to bring about a more prominent effect on the flame through changes in the equivalence ratio. Such fluctuations are also important in practical combustors which are subjected to various unsteady fluctuations and turbulence. The flame response to step and sinusoidal variations about a mean value of reactant concent-ration for various values of strain rates is examined.

Mathematical Formulation

General Governing Equations

A schematic of a counterflow diffusion flame stabilized near the stagnation plane of two laminar flows is shown in Figure 1. In this figure, r and z denote the independent spatial coordinates in tangential and axial directions respectively. Using the assumptions of axisymmetric, unity Lewis number, negligible body forces, negligible viscous dissipation, and negligible Dufour effect, the resulting conservation equations of mass, momentum, energy and species may be simplified to the following form:

$$\frac{\partial \rho}{\partial t} + 2\,\rho\,\epsilon\,\psi + \partial\frac{(\rho\,v)}{\partial z} = 0$$

$$\left(\psi - \frac{\rho_\infty}{\rho}\right)\frac{d\epsilon}{dt} + \epsilon\,\frac{\partial \psi}{\partial t} + \left(\psi^2 - \frac{\rho_\infty}{\rho}\right)\epsilon^2 = -\,\epsilon\,v\,\frac{\partial \psi}{\partial z} + \frac{\epsilon}{\rho}\,\frac{\partial}{\partial z}\left(\mu\frac{\partial \psi}{\partial z}\right)$$

$$\rho\left(\frac{\partial h}{\partial t} + v\frac{\partial h}{\partial z}\right) = \frac{\partial}{\partial z}\left(\frac{\lambda}{c_p}\,\frac{\partial h}{\partial z}\right) - \sum_{i=1}^{N}\omega_i\,\Delta h_{f,i}^{o} - \nabla.Q_R$$

$$\rho\left(\frac{\partial Y_i}{\partial t} + v\,\frac{\partial Y_i}{\partial z}\right) = \frac{\partial}{\partial z}\left(\rho\,D_i\,\frac{\partial Y_i}{\partial z}\right) + \omega_i$$

Here ψ is a similarity transformation variable which is related to the radial velocity by $\psi = u_r/(\epsilon\, r)$. The above equations are closed by the following ideal gas relations:

$$\rho = \frac{p}{\overline{R}\,T}\,\frac{1}{\sum_{i=1}^{N}\left(Y_i/MW_i\right)} \qquad and \qquad dh = c_p\,dT$$

The symbols used in the above equations are defined in the nomenclature section. Note that in the present form the equations do not depend on the radial direction. In this study, the radiative heat flux is modeled by using the emission approximation, i.e., $Q_R = 4\,\sigma\,T^4\,(a_{P,CO2} + a_{P,H2O})$; where, σ is the Stefan-Boltzmann constant, and $a_{P,CO2}$, $a_{P,H2O}$ are the Planck mean absorption coefficients for CO_2 and H_2O respectively. The absorption coefficients for combustion products were taken from Ref. [18].

Reaction Scheme

The present problem was solved by considering a single step overall reaction which may be written as follows:

$$[F] + v\,[O_2] \rightarrow (1+v)\,[P]$$

Here, v is the mass-based stoichiometric coefficient. Using second order Arrhenius kinetics, the reaction

rate was defined as $\omega = A\,\rho^2\,Y_F\,Y_O \exp(-E_R/R\,T)$. The reaction rates for fuel, oxidizer, and product may then be written as $\omega_F = -\omega$; $\omega_O = -\nu\omega$; and $\omega_p = (1+\nu)\omega$. For the calculations presented here, the values of various constants and properties were obtained from Ref. [19].

Initial and Boundary Conditions

A solution of these equations requires the specification of some initial and boundary conditions which are given as following:

Initial Conditions:

$\psi(z,0) = \psi_o(z)$

$h(z,0) = h_o(z)$ or $T(z,0) = T_o(z)$

$Y_i(z,0) = Y_{i.o}(z)$ [n conditions or (n-1) conditions + $\rho(z,0)$]

$\phi(z,0) = \phi_o(z)$

Here subscript 'o' represents the initial steady state solution.

Boundary Conditions:

The origin of our coordinate system was defined at the stagnation plane.

$\psi(\infty,t) = 1$ $\quad \psi(-\infty,t) = (\rho_\infty/\rho_{-\infty})^{1/2}$

$h(\infty,t) = h_{up}$ $\quad h(-\infty,t) = h_{low}$

[or $T(\infty,t) = T_{up}$ $\quad T(-\infty,t) = T_{low}$]

$Y_i(\infty,t) = Y_{i.up}$ $\quad Y_i(-\infty,t) = Y_{i.low}$

$v(0,t) = 0$

The strain rate ϵ, which is a parameter, must also be specified. The reactant concentration is varied by multiplying the boundary value of either fuel or oxidizer concentration by $(1+A*\sin(2\,\pi\,f\,t))$ for sinusoidal variations and by using a Heaviside function for step changes.

Solution Procedure

The governing equations form a set of nonlinear, coupled and highly stiff partial differential equations. These equations were solved numerically using the *Numerical Method of Lines* (NMOL). A 4th order 3-point central difference formula was used to spatially discretize the equations and an implicit backward differentiation formula (BDF) was used to integrate in the temporal direction. In order to carry out the numerical integration, infinity was approximated by a finite length of the order of the length scale of the problem (i.e., $(D/\epsilon)^{1/2}$). This was confirmed by checking the gradients of all the variables which must vanish at the boundaries. For the calculations presented here, a uniform grid with grid size $\Delta z = 1.6 \times 10^{-2}$ cm and a variable time step of the order of 1 μsec was used. The grid sensitivity was checked by reducing the grid size by half and the results were found to be unaltered.

Results and Discussion

The parameter values used in the present calculations are $T_\infty = 295$ K, $E/RT_\infty = 49.50$, pre-exponential constant $A = 9.52 \times 10^9$ (m^3/kg.s), $Q_{HV} = 47.465 \times 10^6$ J/kg, $Y_{F\infty} = 0.125$, and $Y_{O-\infty} = 0.5$. The results were obtained by assuming constant specific heat, equal diffusion coefficient for all gases and $\rho^2 D$ = constant. Results shown in this paper are only for fuel concentration fluctuations but are applicable to both reactants (fuel and oxidizer) since similar findings are obtained for oxidizer fluctuations.

Flame Response to Sinusoidal Variations in Reactant Concentrations

Figures 2-4 show the results for strain rate of 10 s^{-1} and sinusoidal variation in fuel concentration of 50% amplitude and 1 Hz frequency. Figure 2a shows temperature and velocity profiles at various time intervals. The figure shows that the flame which was initially stabilized at the stagnation plane (at 0) begins to move towards the oxidizer side due to an increase in the fuel concentration. After reaching a maximum value, the temperature starts decreasing corresponding to a decrease in the fuel concentration and the flame moves back towards the stagnation plane. It crosses the stagnation plane and continues to move towards the fuel side till reaching a minimum temperature. The flame then keeps oscillating back and forth across the stagnation plane between these two temperature limits, which are very close to the steady state values corresponding to the maximum and minimum fuel concentrations. These results show that the flame temperature is substantially affected by fuel concentration fluctuations.

Similar trends are observed for the gas radiation profiles. Figure 2b shows that the maximum gaseous radiation per unit volume is increased by 30% corresponding to an increase in the flame temperature and radiating combustion products caused by an increase in the fuel concentration and is decreased by 55% corresponding to a decrease in the flame temperature and radiating combustion products.

In Figure 3a, the maximum flame temperature, which is a good indicator of the flame response to induced fluctuations, is shown as a function of fluctuation time period. The figure shows that the flame responds to fluctuations sinusoidally with a time delay. This delay or phase lag is due to slow transport processes (convection & diffusion) which are responsible for transmitting information from nozzle to the reaction zone. The flame response also shows a slight asymmetry with respect to the initial maximum temperature, i.e., the mean maximum flame temperature around which the flame temperature oscillates shifts to a lower value.

Other indicators of the flame response, such as the heat release rate (or fuel mass burning rate) and the radiative fraction (defined as the ratio of the total heat radiated to the total amount of heat released), show similar trends (Figure 3b). The increase or decrease in the heat release is due to a corresponding increase or decrease in the fuel burning rate caused by variations in fuel concentrations. The radiative fraction profile indicates that the fuel concentration fluctuations have more significant effect on radiation than on the amount of heat released. Note that the radiative fraction would remain constant if the radiation fluctuated proportionally to the heat release rate. At the limiting values of fuel concentrations, the change in the total radiation from its mean value is roughly twice more than that in the heat release.

Effect of Fluctuation Amplitude

Figure 4a shows the variation in the maximum flame temperature as induced by different amplitudes of fuel concentration fluctuations. For these results the induced frequency and strain rate were set at 1 Hz and 10 s^{-1} respectively. The results show that: i) the amplitude of fluctuations has no substantial effect on the time delay (phase lag) in the flame response. The phase lag is found to decrease by only 5° with an increase in the amplitude from 10% to 50%; ii) the mean maximum temperature around which the flame temperature oscillates decreases with an increase in the fluctuation amplitude; and iii) the amplitude of the flame response increases almost linearly with an increase in the induced fluctuation amplitude. The last conclusion can be drawn more clearly from Figure 4b. In this figure, the maximum temperature fluctuations (normalized with the steady state temperature) are plotted as a function of the induced fluctuations (normalized with the steady state fuel concentration). It can be inferred that for larger strain rates at high fluctuation amplitude the extinction will occur.

Effect of Fluctuation Frequency

In Figure 5a, the variation in the maximum flame temperature are plotted as a function of time period for different frequencies. All these results are for flames subjected to fuel fluctuations of 50% amplitude and strain rate of 10 s^{-1}. The figure shows that the flame response is maximum at lower frequencies and its amplitude decreases with an increase in frequency. Similar observations are reported in the literature for flames subjected to variable strain rates [7,11,13]. For the present conditions, the flame becomes relatively insensitive to the induced fluctuations at frequencies higher than 20 Hz as shown in Figure 5b. This insensitivity is due to insufficient time available at higher frequencies for transmitting relevant information to the reaction zone. Figure 5a shows that the slow transport processes also cause the phase shift or the time delay in the flame response to increase with an increase in the frequency.

Another observation from Figure 5a can be made about the asymmetric effect in the flame response which decreases with an increase in the induced frequency. Hence, the mean maximum flame temperature around which the temperature oscillates increases with an increase in the frequency.

Effect of Strain Rate

The effect of strain rate was investigated by simulating flames with different strain rates subjected to similar induced fluctuations. Figure 6a shows the variation in the maximum flame temperature (normalized with steady state temperatures) as a function of time for flames with different strain rates. These flames were subjected to the induced fluctuations of 1 Hz and 50% amplitude. The figure shows that the flame response is more prominent and the amplitude of oscillation is increased at larger strain rates. However, the term large strain rate is a relative one and depends upon the frequency of induced fluctuation. Hence, in Figure 6b, the maximum normalized temperature fluctuations are plotted as a function of frequency/strain rate (f/ϵ). The figure shows that the flame response is negligible for values of f/ϵ greater than 2 (i.e., low strain rates). Beyond this value, the amplitude of fluctuations increases almost exponentially with a decrease in f/ϵ. This increase in the amplitude can be explained by considering that any information to the reaction zone is transported through convection and diffusion processes. At low strain rates (high f/ϵ), the convection is small and thus the changes at the nozzle cannot be completely transmitted to the reaction zone. Hence, the flame response is small. As the strain rate is increased (f/ϵ is decreased), the convection part increases, thereby transporting more information. Consequently, the flame response is increased. Beyond certain strain rate ($f/\epsilon \leq 0.05$), the information propagates instantaneously and the instantaneous flame temperature agrees very closely to the steady state temperature values at the corresponding fuel concentration.

Figure 6b also shows that: i) the increase in the strain rate increases the asymmetry in the flame response; and ii) for a fixed frequency, the phase shift in the flame response decreases with an increase in the strain rate. This latter behavior may be explained based on the previously described argument about the role of the slow convection rates at low strain rates. Other results (not shown here), however, reveal that if the ratio f/ϵ is kept constant, an increase in the strain rate increases the phase lag. This means that the increase in the information transport through convection processes by increasing strain rate is smaller than the increase in fluctuations at the nozzle by a corresponding increase in the frequency.

Flame Response to Step Changes in Reactant Concentrations

Effect of Step Size (Amplitude)

Figure 7a shows the variation in the maximum flame temperature as a function of time to both positive and negative changes in the fuel concentrations for different step sizes (amplitudes). For all these flames the strain rate was kept constant at 10 s^{-1}. The results reveal that: i) as expected, the flame response increases with an increase in the step size; ii) the flame responds with a time delay to a step change and this delay slightly decreases with an increase in the step size; and iii) the effect of a negative step (a decrease in the fuel concentration) is more substantial on the flame than that of a positive step (an increase in the fuel concentration) of similar size.

The time taken by the flame to reach the steady state for different step sizes is shown in Figure 7b. Here, the steady state is defined as the condition when the maximum flame temperature attains 99% of the total change in temperature. The figure shows that, for a similar change in temperature, the flame reaches steady state more rapidly for positive step sizes. Furthermore, the steady state time increases with a decrease in the positive step size whereas the trend is opposite for negative step sizes. It should be mentioned here that a negative step change in fuel concentration moves the flame towards the oxidizer side and a positive step towards the fuel side of the stagnation plane. Hence, the figure shows that the nearer the flame to the reactant side which is subjected to a step change, the more rapidly the flame reaches the steady state.

Effect of Strain Rate

The effect of strain rate on the flame response to step changes in fuel concentrations is similar to that caused by sinusoidal variations in fuel concentrations. Figure 8a displays the maximum flame temperature (normalized with the steady state temperature) profiles for different strain rates. All these flames were subject to a 50% increase in the fuel concentration. These results depict that the higher the strain rate, the greater the flame response. Furthermore, with an increase in the strain rate, the time delay in the flame response decreases and the steady state condition is reached more rapidly (as shown in Figure 8b). The physical reasoning of this behavior is same as described in the earlier section, i.e., the increased role of convection at higher strain rates.

Conclusions

In this article, we have investigated the dynamic response of radiating flamelet subjected to variable reactant concentrations, using numerical simulations. The reactant concentration was varied both sinusoidally and with a step function. A number of flames with different strain rates were examined. The maximum flame temperature, heat release rate and the radiative heat loss were used to describe the flame response. The results led to the following conclusions:

i) The flame responds sinusoidally with a phase shift to the sinusoidal induced reactant fluctuations.

ii) Low frequency fluctuations bring about a significant flame response causing a possible extinction at large strain rates. The effect of the frequency is more important than its amplitude.

iii) The ratio of frequency over strain rate (f/ϵ) may be used to predict the flame response to the induced reactant fluctuations. The flame response is instantaneous for $f/\epsilon \leq 0.05$ and its amplitude decreases exponentially for $0.05 \leq f/\epsilon \leq 2$, beyond which the flame becomes insensitive to fluctuations. Hence, the transient effects must be considered in the flamelet modeling for the critical range $0.05 \leq f/\epsilon \leq 2$.

iv) The induced fluctuations have more prominent effect on radiation than on the heat release.

v) The flame responds to a step change with a time delay. With an increase in the step size, the

response increases and the initial time delay decreases.

vi) For a step change, the steady state time depends upon the final location of the flame and the strain rate; the nearer the flame to the reactant side which is subjected to a change and higher the strain rate, the more rapidly the flame reaches the steady state.

Acknowledgment

Financial support for this work was provided by NASA (under the grant number NAG3-1460) and GRI (under the grant number 5093-260-2780).

References

1. Carrier, G. F., Fendell, F. E., and Marble, F. E., *SIAM J. Appl. Math.*, 28:463 (1975).
2. Peters, N., *Prog. Energy. Combust. Sc.*, 10:319 (1984).
3. Chen, J. Y.,Kaiser, T., and Kollmann, W., *Comb. Sc. Tech.*, 92:313 (1993).
4. Faeth, G. M., and Samuelson, G. S., *Prog. Energy. Combust. Sc.*, 12:305 (1986).
5. Howarth, D. C., Drake, M. C., Pope, S. B., and Blint, R. J., *Twenty-Second Symposium (International) on Combustion*. The Combustion Institute, Pittsburgh, 1988 (1988).
6. Barlow, R. S., and Chen, J. Y., *Twenty-Fourth Symposium (International) on Combustion*. The Combustion Institute, Pittsburgh, 231 (1992).
7. Ghoniem, A. F., Soteriou, M. C., Kino, O. M., and Cetegen, B., *Twenty-Fourth Symposium (International) on Combustion*. The Combustion Institute, Pittsburgh, 223 (1992).
8. Baum, H. R., Rehm, R. G., and Gore, J. P., *Twenty-Third Symposium (International) on Combustion*. The Combustion Institute, Pittsburgh, 715 (1990).
9. Rutland, C. J., and Ferziger, J. H., *Comb. Sc. Tech.* 73:305 (1990).
10. Stahl, G., and Warnatz, J., *Comb. & Flame* 85:285 (1991).
11. Darabiha, N., *Comb. Sc. Tech.* 86:163 (1992).
12. Egolfopoulos, F. N., *Twenty-Fifth Symposium (International) on Combustion*. The Combustion Institute, Pittsburgh, 1375 (1994).
13. Im, H. G., Law, C. K., Kim, J. S., and Williams, F. A., *Comb. & Flame*, 100:21 (1995).
14. Cuenot, B., and Poinsot, T., *Twenty-Fifth Symposium (International) on Combustion*. The Combustion Institute, Pittsburgh, 1383 (1994).
15. Clarke, J. F., and Stegan, G. R., *J. Fluid Mech.*, 34:343 (1968).
16. Egolfopoulos, F. N., *Eastern States Section / Combustion Institute Fall Technical Meeting 1993*, Princeton, NJ, 275 (1993).
17. Egolfopoulos, F. N., *Twenty-Fifth Symposium (International) on Combustion*. The Combustion Institute, Pittsburgh, 1365 (1994).
18. Abu-Romia, M. M., and Tien, C. L., *J. of Heat Trans.*, Nov:321 (1967).
19. Shamim, T., and Atreya, A., *Proc. of the ASME Heat Transfer Division,* ASME Int'l Cong. & Exp., San Francisco, CA, HTD Vol. 317-2:69 (1995).

Figure Captions

Figure 1 Schematic of counterflow flame

Figure 2 Flame subjected to sinusoidal variations in fuel concentrations: a) Temperature and velocity profiles; b) Radiation profiles (Amplitude = 50%, Frequency = 1Hz, Strain rate = 10 s^{-1})

Figure 3 Flame response to the induced sinusoidal fluctuations: a) Variations in maximum flame temperature; b) Variations in heat release rate and radiative fraction (Amplitude = 50%, Frequency = 1Hz, Strain rate = 10 s^{-1})

Figure 4 Effect of fluctuation amplitude: a) Variations in maximum flame temperature (Amplitude = 50%, Frequency = 1Hz, Strain rate = 10 s^{-1}); b) Normalized maximum temperature fluctuations

Figure 5 Effect of fluctuation frequency: a) Variations in maximum flame temperature; b) Normalized maximum temperature fluctuations (Amplitude = 50%, Strain rate = 10 s^{-1})

Figure 6 Effect of strain rate: a) Variations in normalized maximum flame temperature (Amplitude = 50%, Frequency = 1Hz); b) Normalized maximum temperature fluctuations for different frequency/strain rate ratios (Amplitude = 50%)

Figure 7 Effect of step size on the flame response to step changes: a) Variations in maximum flame temperature; b) Steady state times for different step sizes (Strain rate = 10 s^{-1})

Figure 8 Effect of strain rate on the flame response to step changes: a) Variations in normalized maximum flame temperature; b) Steady state times for different strain rates (Step size (amplitude) = 50%)

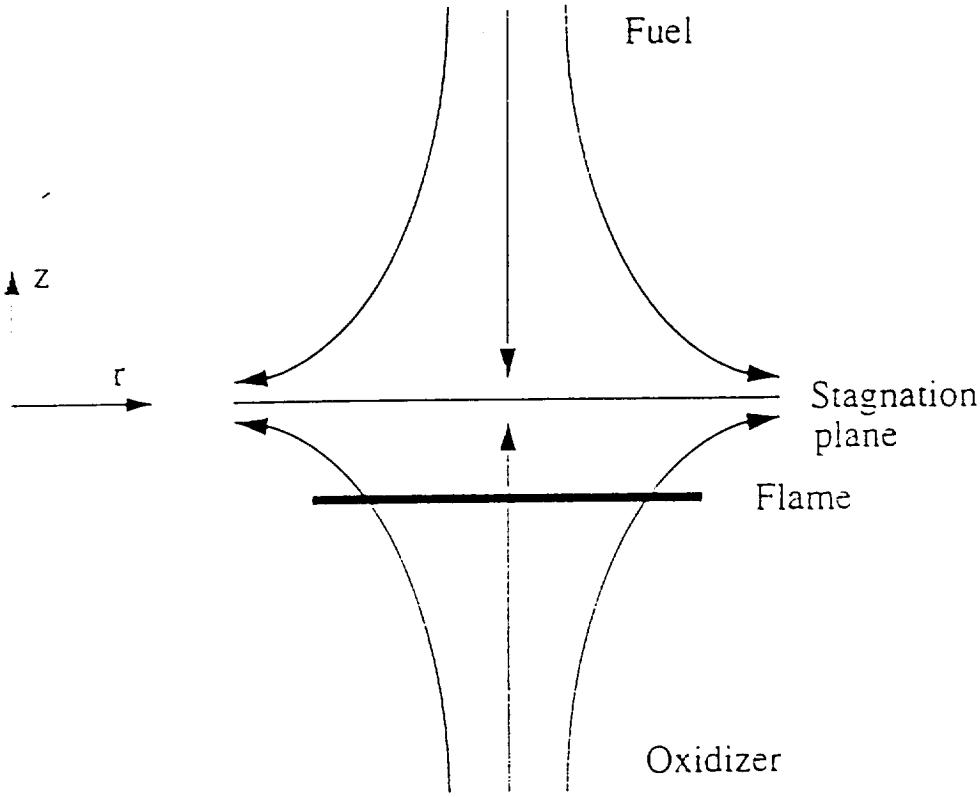
Fuel
z
r
Stagnation
plane
Flame
Oxidizer

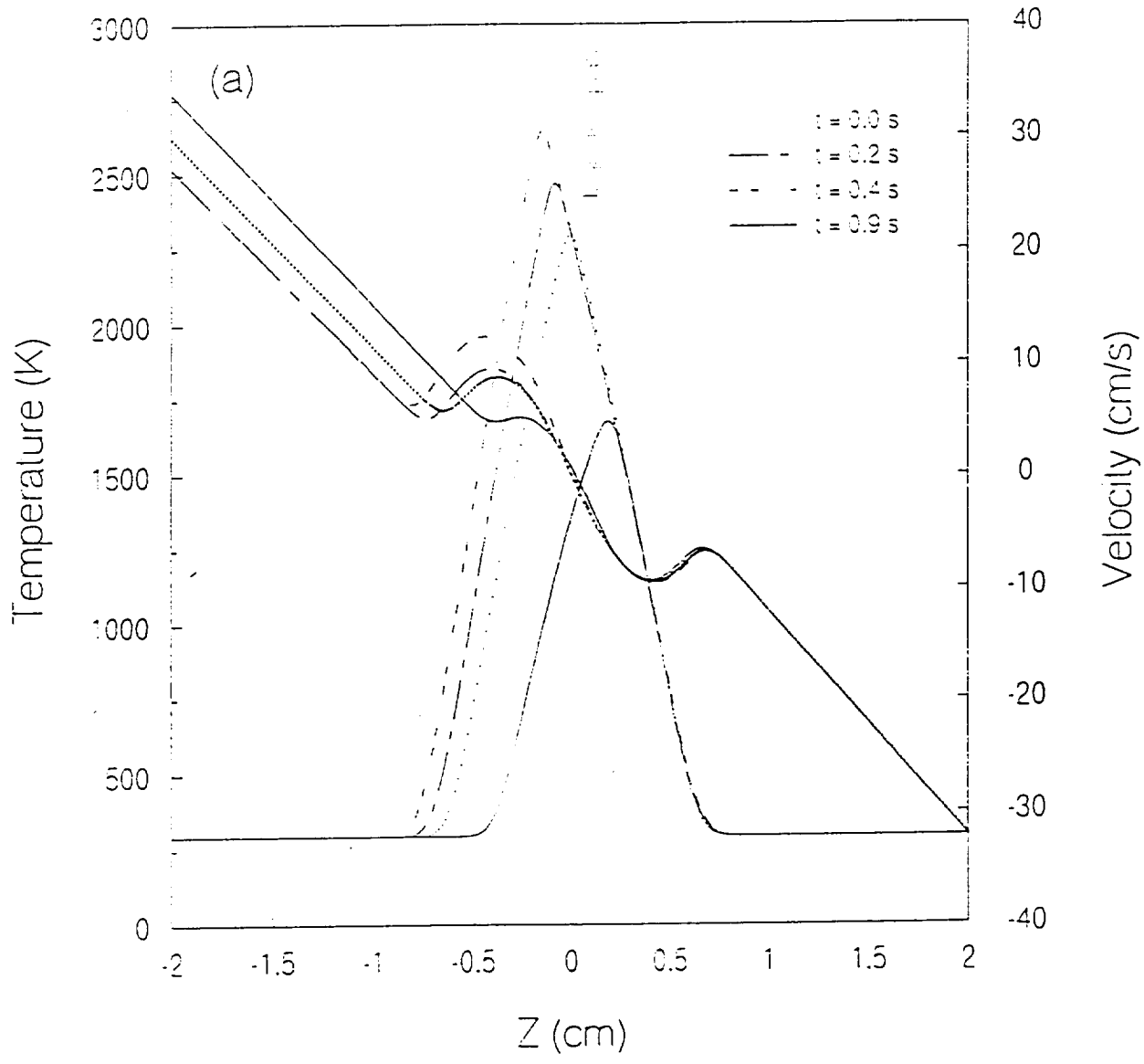
(a)
t = 0.0 s
t = 0.2 s
t = 0.4 s
t = 0.9 s
Temperature (K)
Velocity (cm/s)
Z (cm)
3000
2500
2000
1500
1000
500
0
40
30
20
10
0
-10
-20
-30
-40
-2
-1.5
-1
-0.5
0
0.5
1
1.5
2

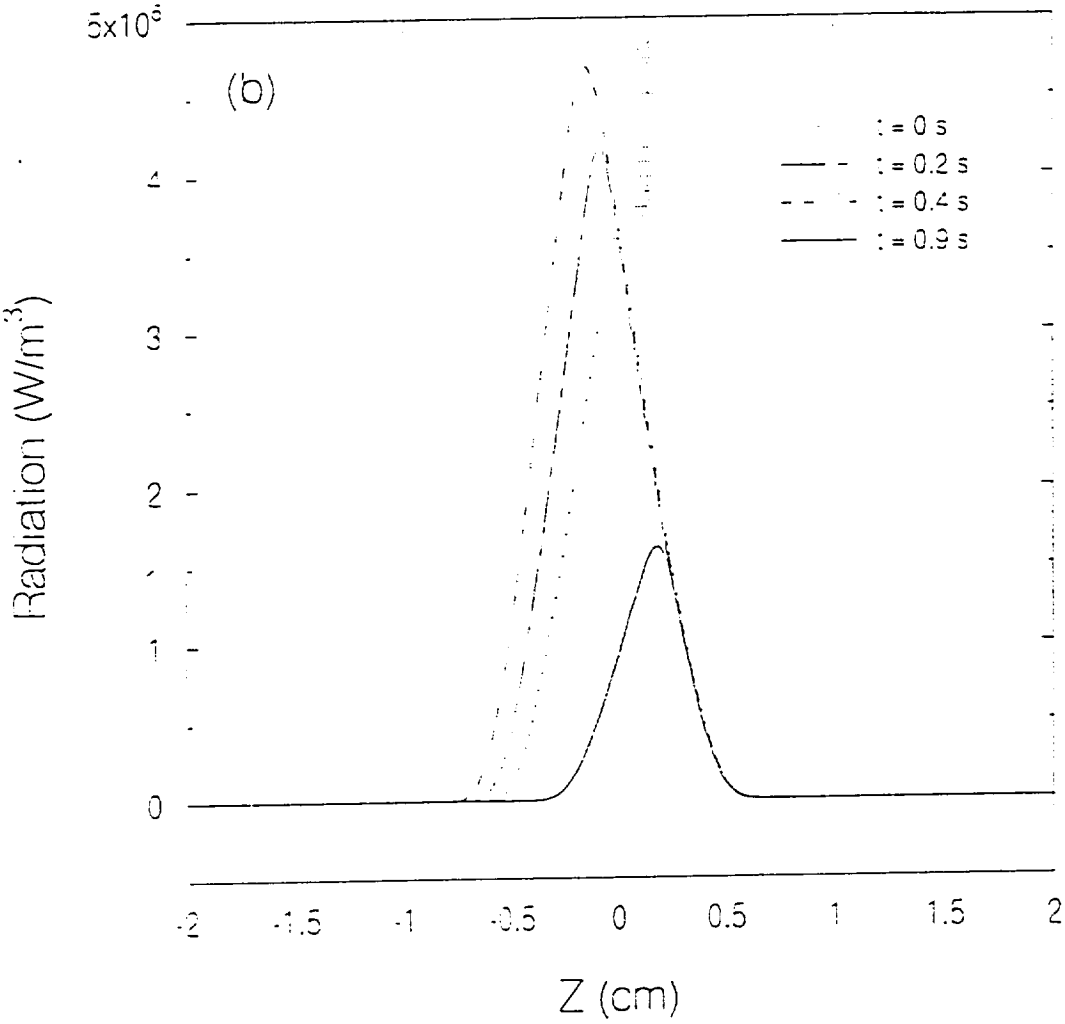
5x10^6
(b)
4
3
2
1
0
t = 0 s
t = 0.2 s
t = 0.4 s
t = 0.9 s
Radiation (W/m^3)
-2
-1.5
-1
-0.5
0
0.5
1
1.5
2
Z (cm)

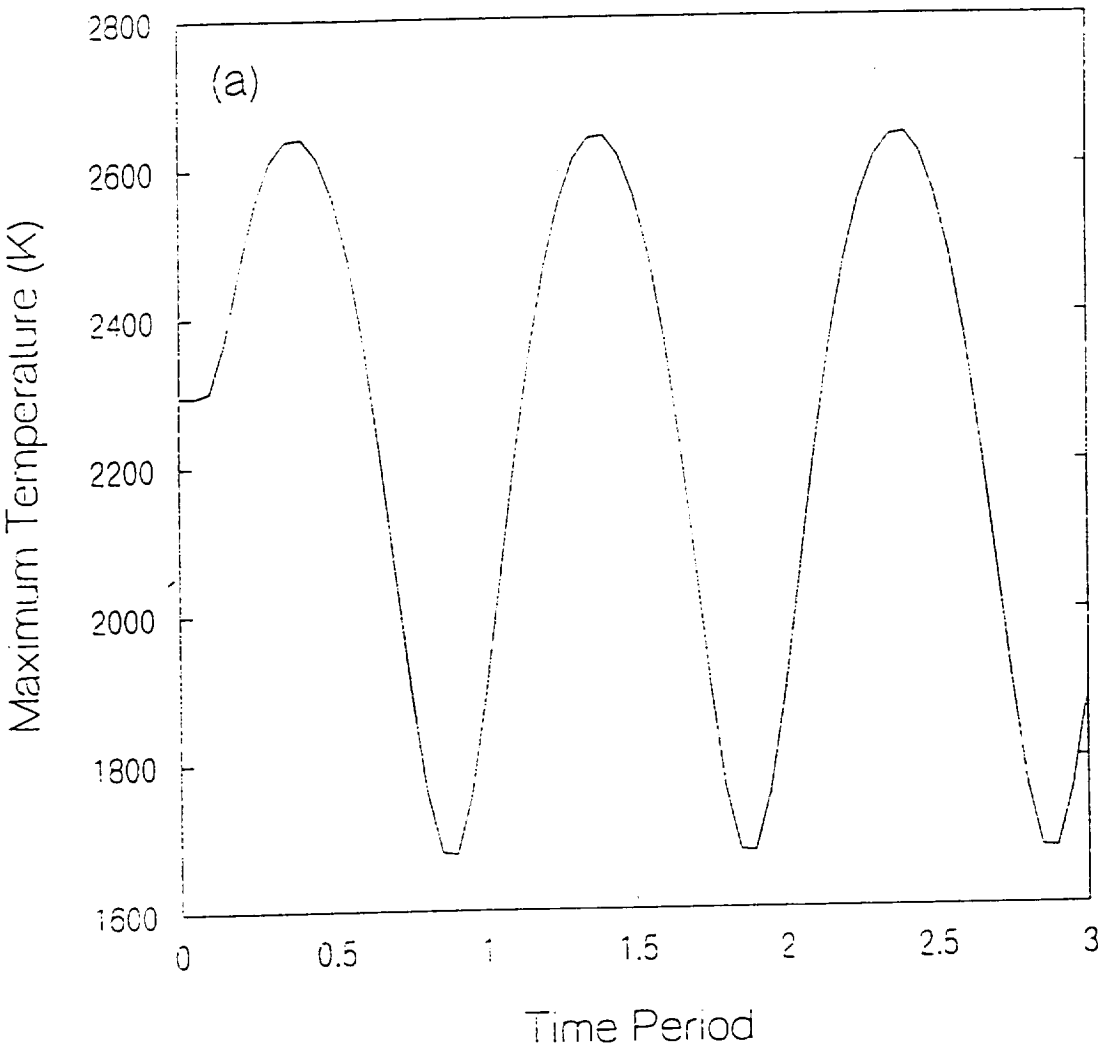
(a)
Maximum Temperature (K)
2800
2600
2400
2200
2000
1800
1600
0
0.5
1
1.5
2
2.5
3
Time Period

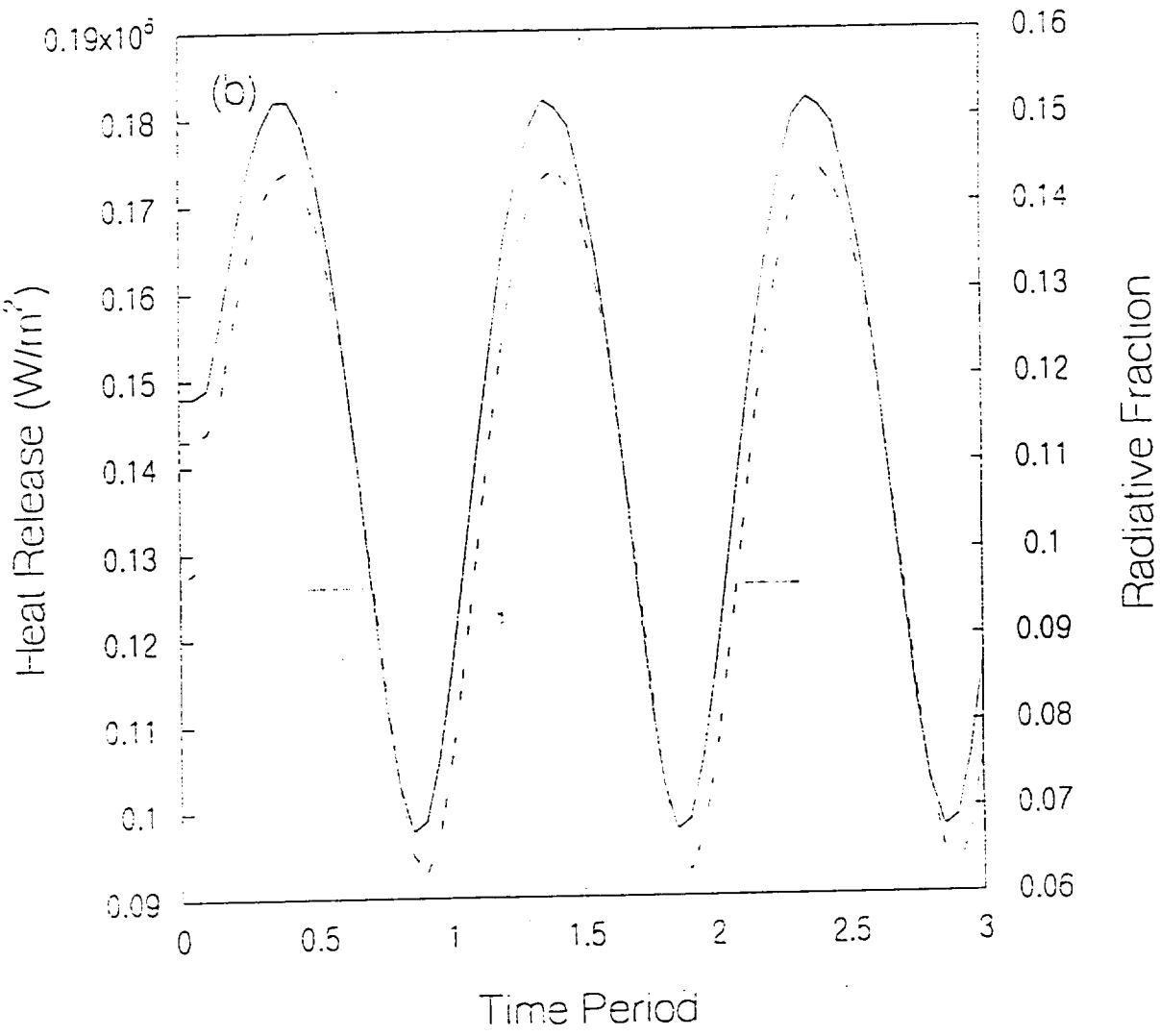
(b)
0.19x10^6
0.18
0.17
0.16
0.15
0.14
0.13
0.12
0.11
0.1
0.09
Heat Release (W/m^2)
0.16
0.15
0.14
0.13
0.12
0.11
0.1
0.09
0.08
0.07
0.06
Radiative Fraction
0
0.5
1
1.5
2
2.5
3
Time Period

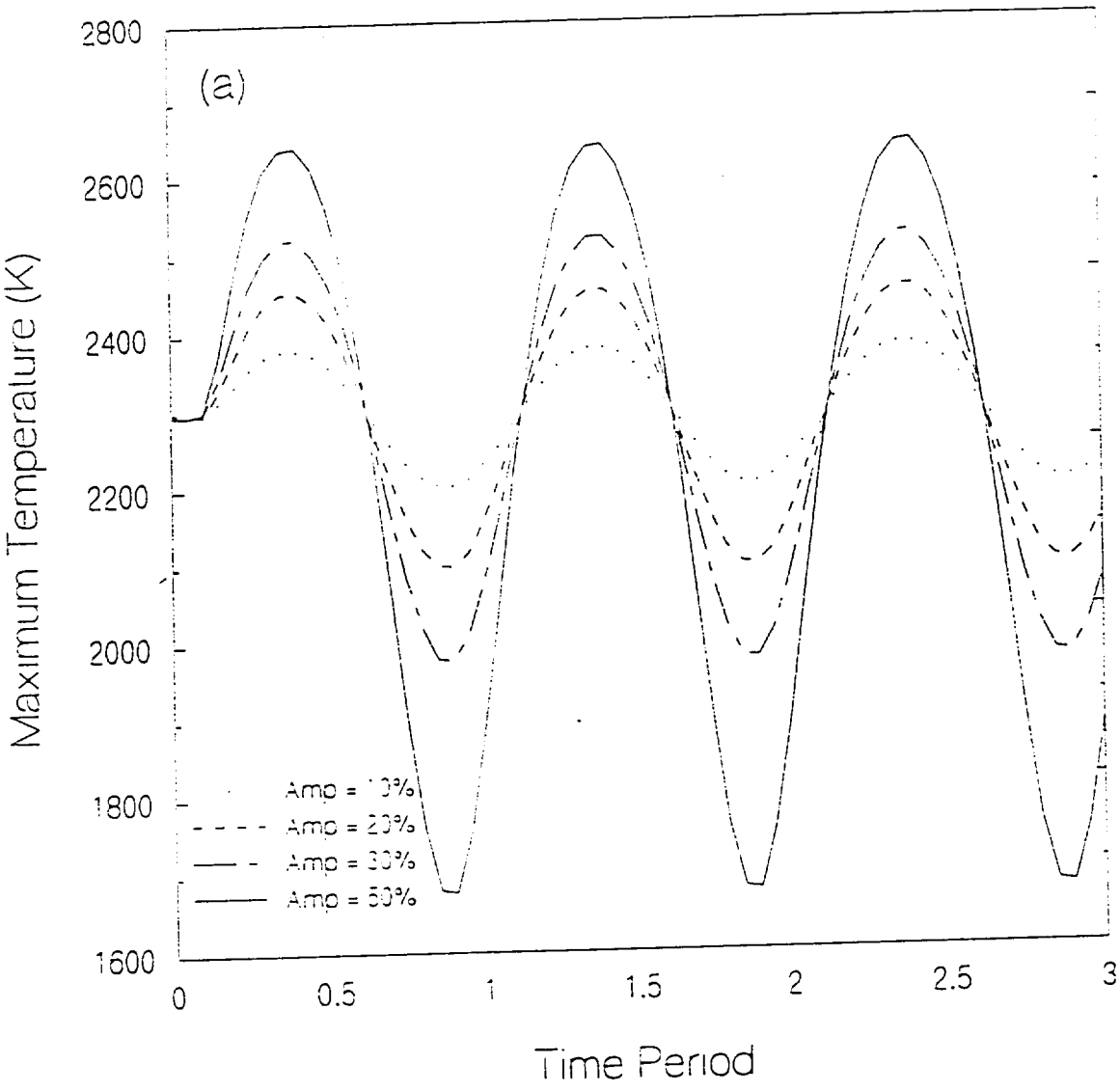
(a)
2800
2600
2400
2200
2000
1800
1600
Maximum Temperature (K)
0
0.5
1
1.5
2
2.5
3
Time Period
Amp = 10%
Amp = 20%
Amp = 30%
Amp = 50%

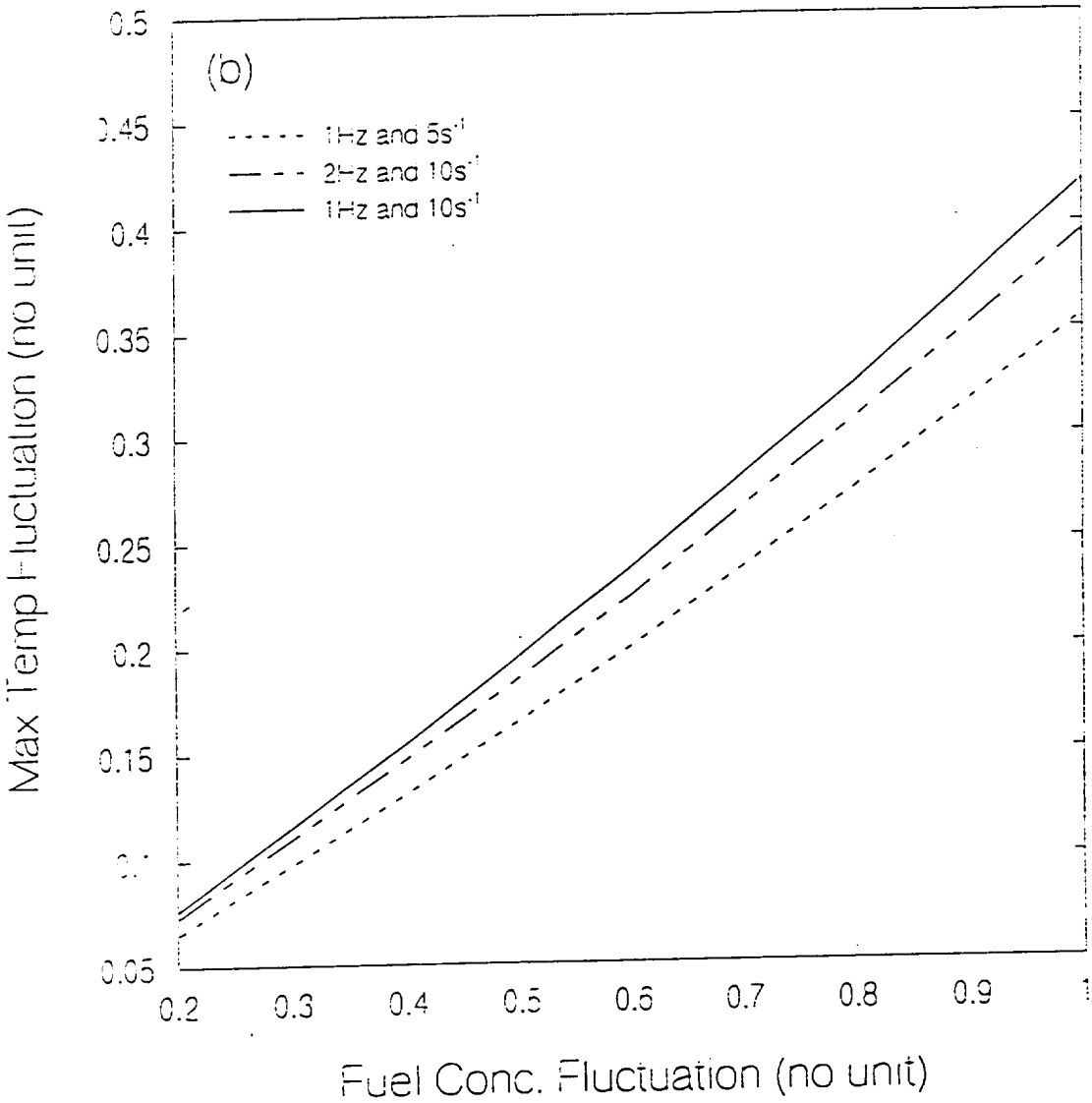
(b)
1Hz and 5s-1
2Hz and 10s-1
1Hz and 10s-1
Max Temp Fluctuation (no unit)
0.5
0.45
0.4
0.35
0.3
0.25
0.2
0.15
0.05
0.2
0.3
0.4
0.5
0.6
0.7
0.8
0.9
Fuel Conc. Fluctuation (no unit)

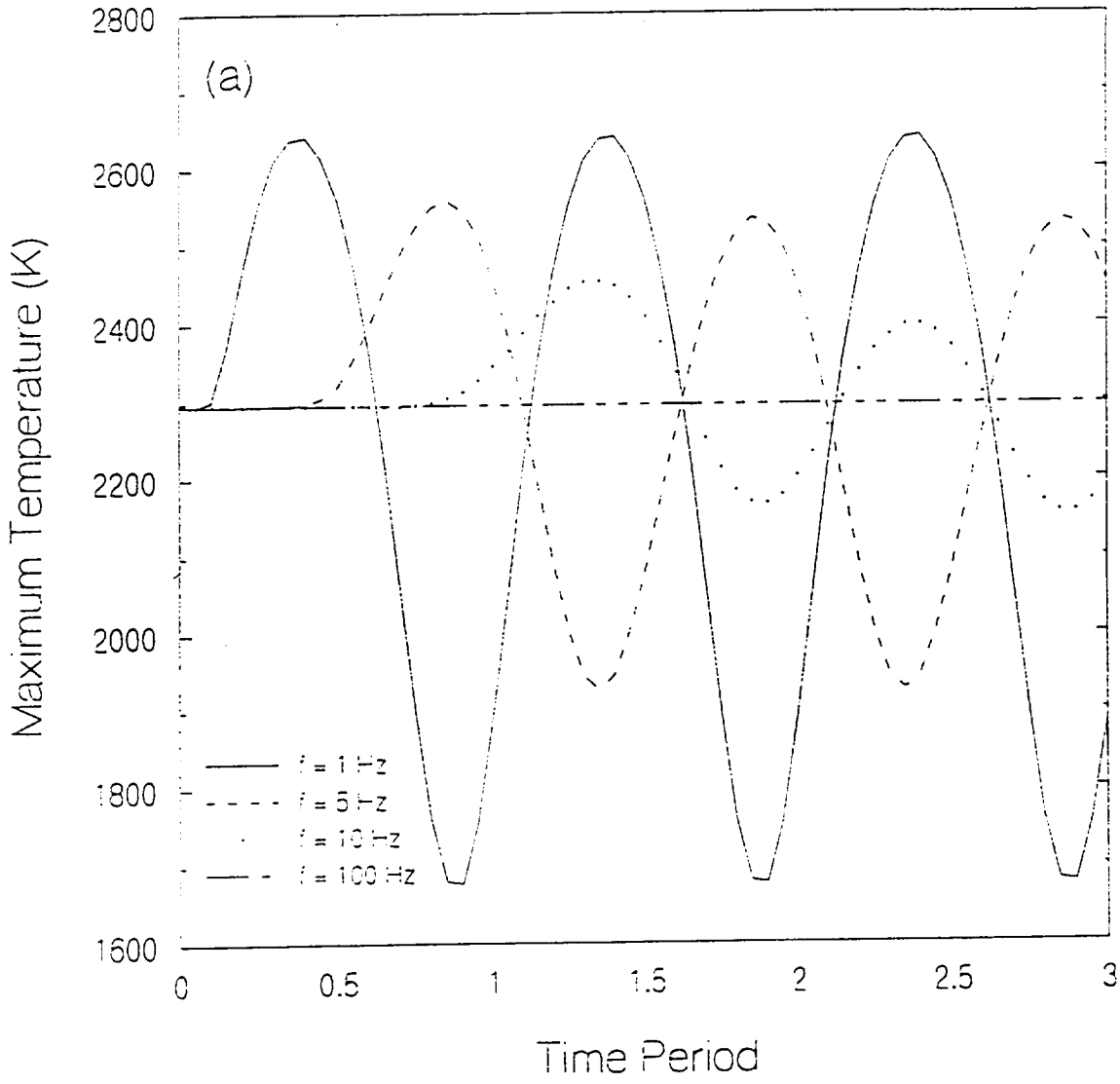
(a)
Maximum Temperature (K)
Time Period
2800
2600
2400
2200
2000
1800
1600
0
0.5
1
1.5
2
2.5
3
f = 1 Hz
f = 5 Hz
f = 10 Hz
f = 100 Hz

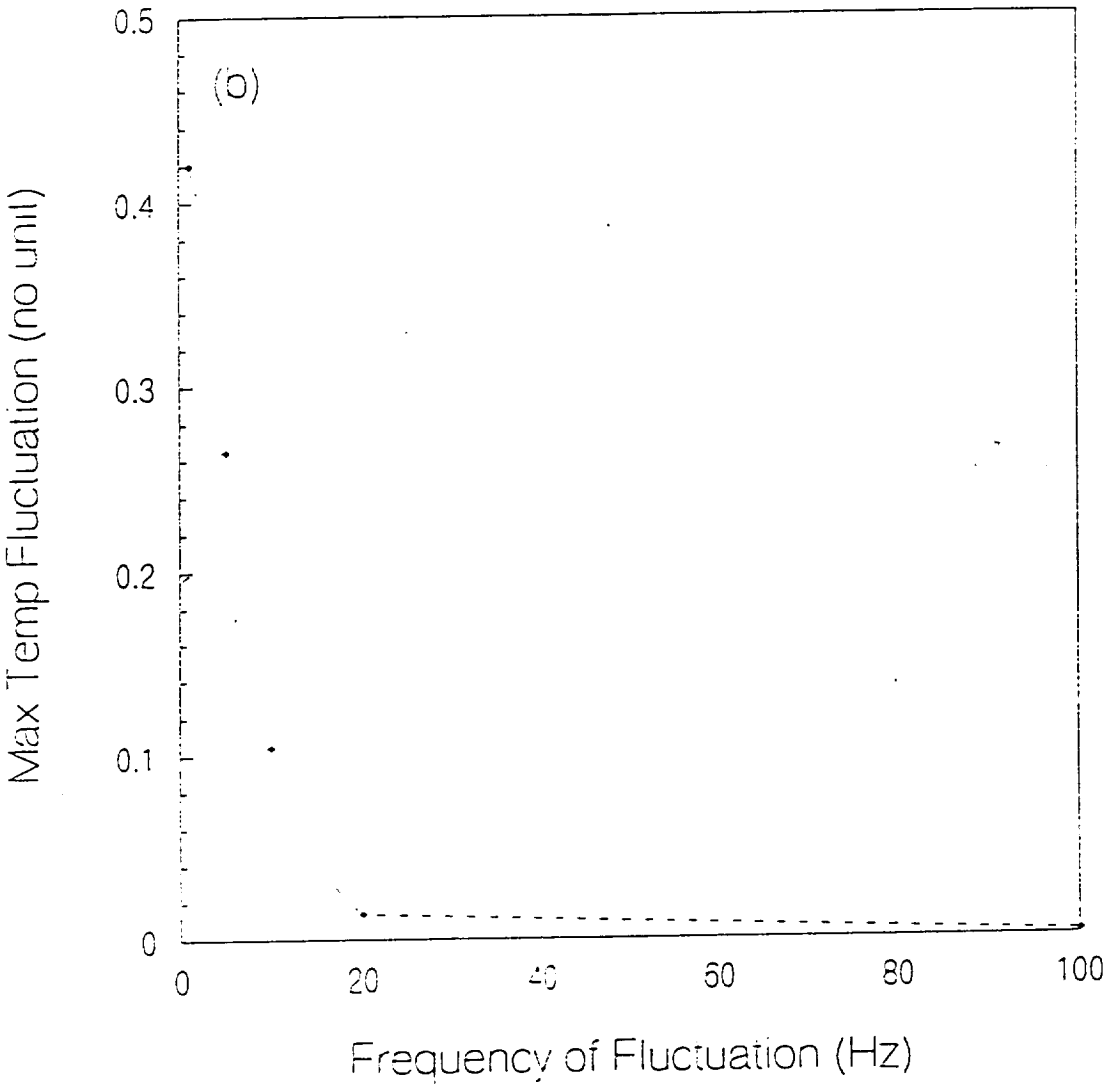
(b)
0.5
0.4
0.3
0.2
0.1
0
Max Temp Fluctuation (no unit)
0
20
40
60
80
100
Frequency of Fluctuation (Hz)

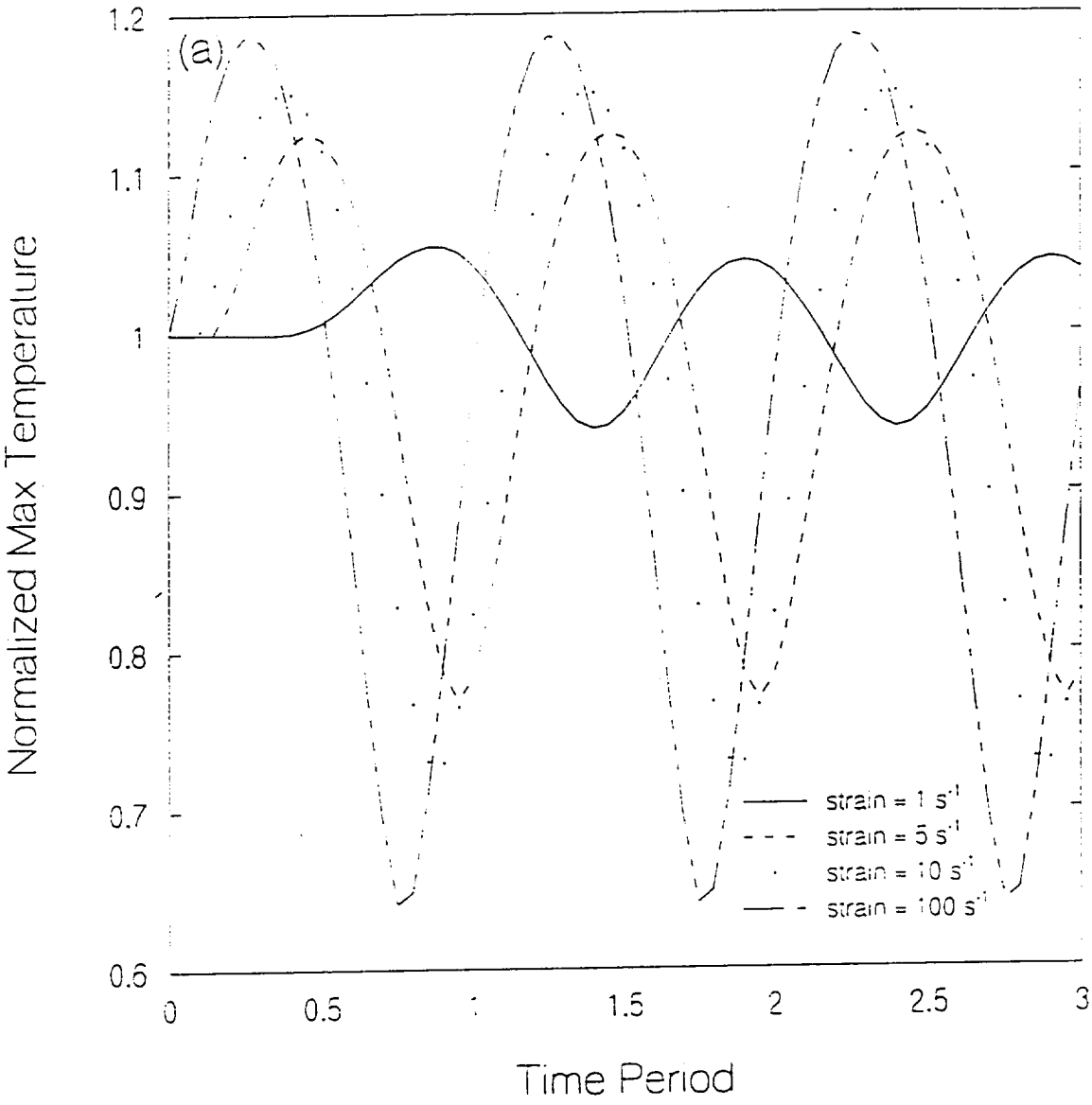
(a)
1.2
1.1
1
0.9
0.8
0.7
0.6
0
0.5
1
1.5
2
2.5
3
Normalized Max Temperature
Time Period
strain = 1 s-1
strain = 5 s-1
strain = 10 s-1
strain = 100 s-1

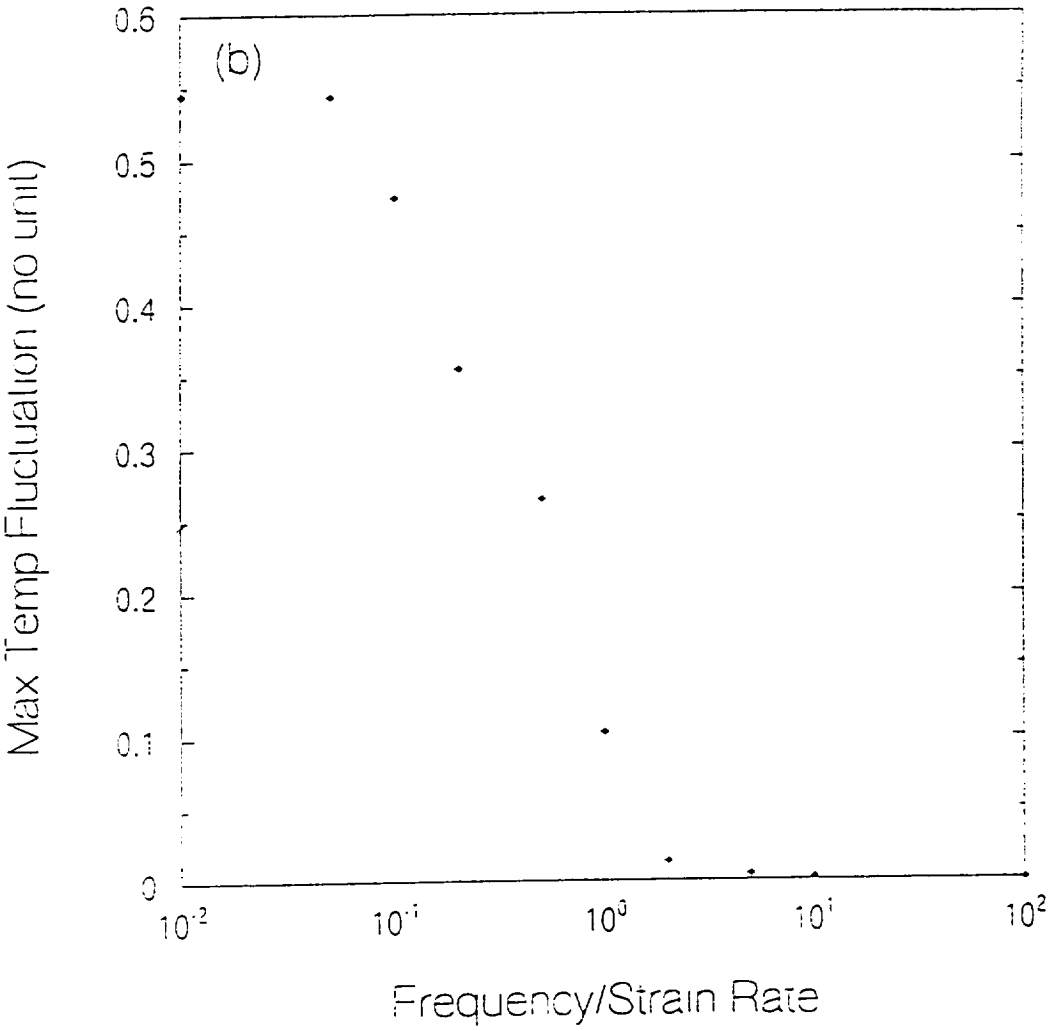
(b)
Max Temp Fluctuation (no unit)
0.6
0.5
0.4
0.3
0.2
0.1
0
10^{-2}
10^{-1}
10^{0}
10^{1}
10^{2}
Frequency/Strain Rate

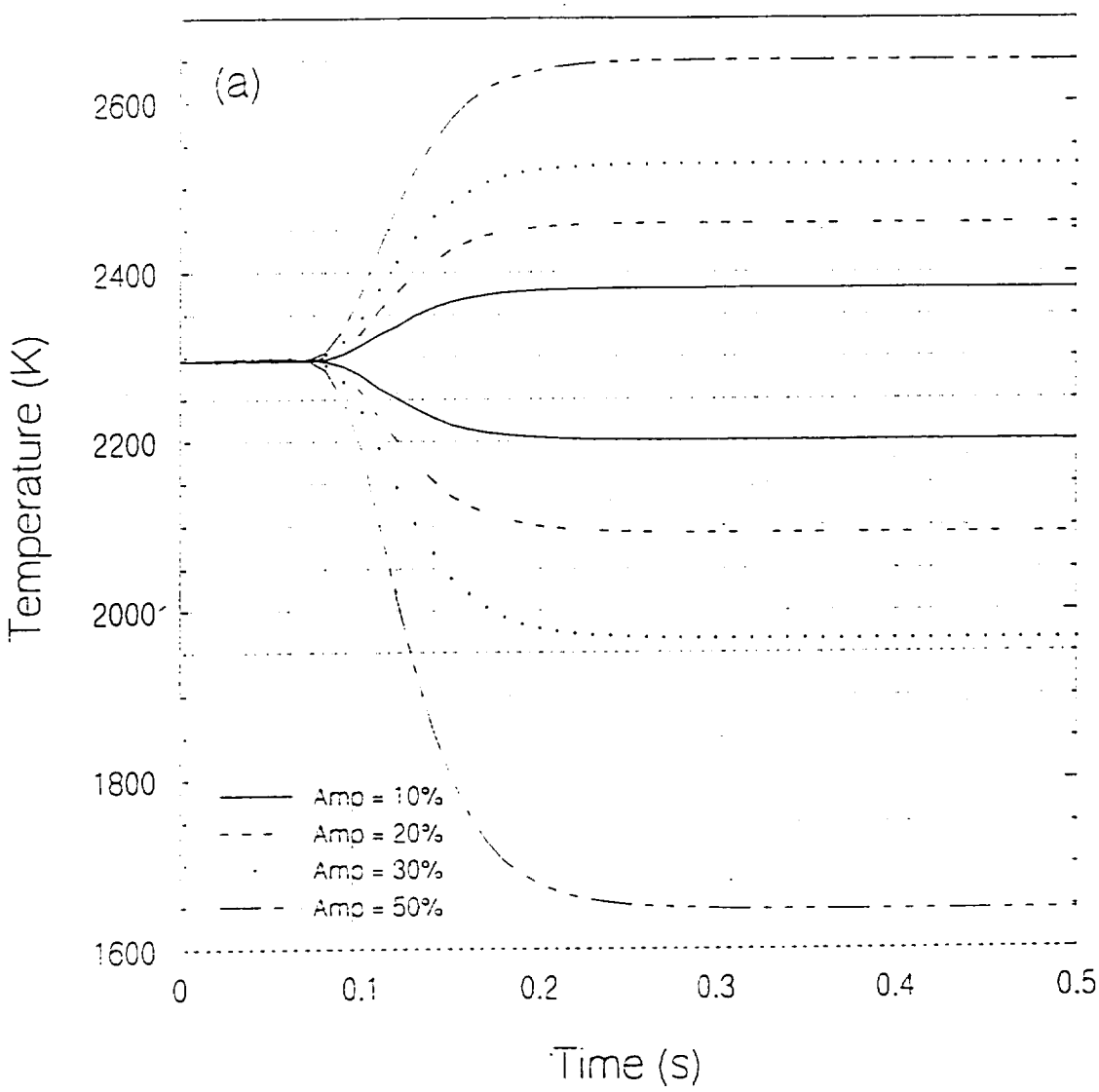
(a)
2600
2400
2200
2000
1800
1600
Temperature (K)
0
0.1
0.2
0.3
0.4
0.5
Time (s)
Amp = 10%
Amp = 20%
Amp = 30%
Amp = 50%

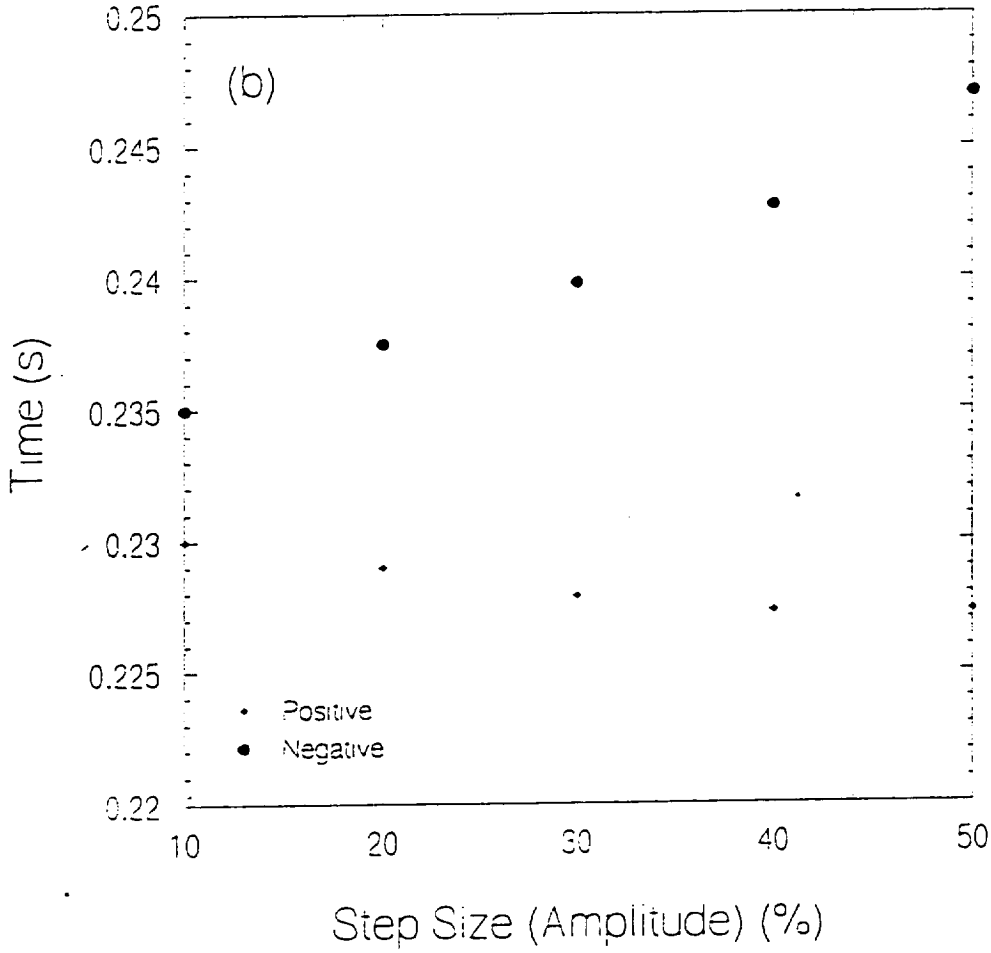
(b)
0.25
0.245
0.24
0.235
0.23
0.225
0.22
Time (s)
Positive
Negative
10
20
30
40
50
Step Size (Amplitude) (%)

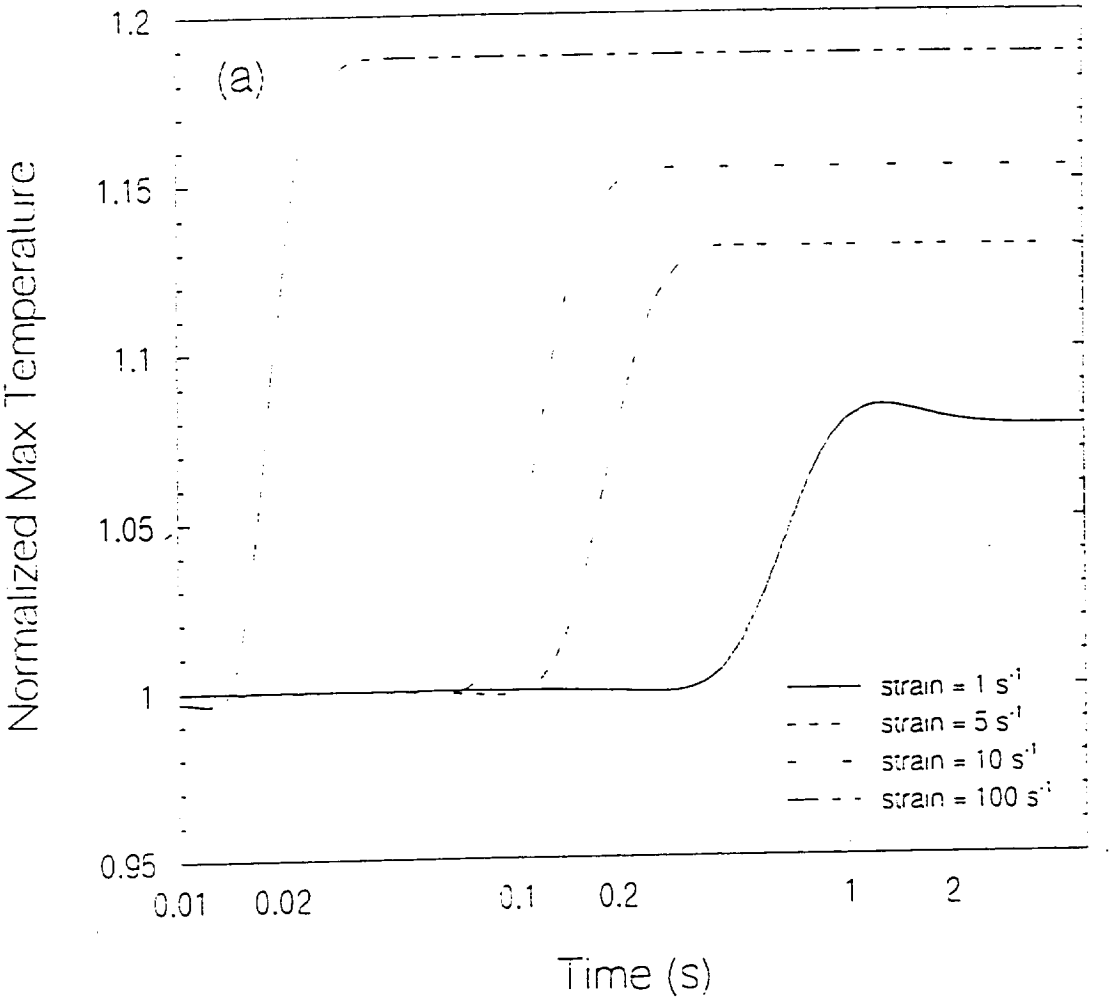
(a)
Normalized Max Temperature
1.2
1.15
1.1
1.05
1
0.95
0.01
0.02
0.1
0.2
1
2
Time (s)
strain = 1 s-1
strain = 5 s-1
strain = 10 s-1
strain = 100 s-1

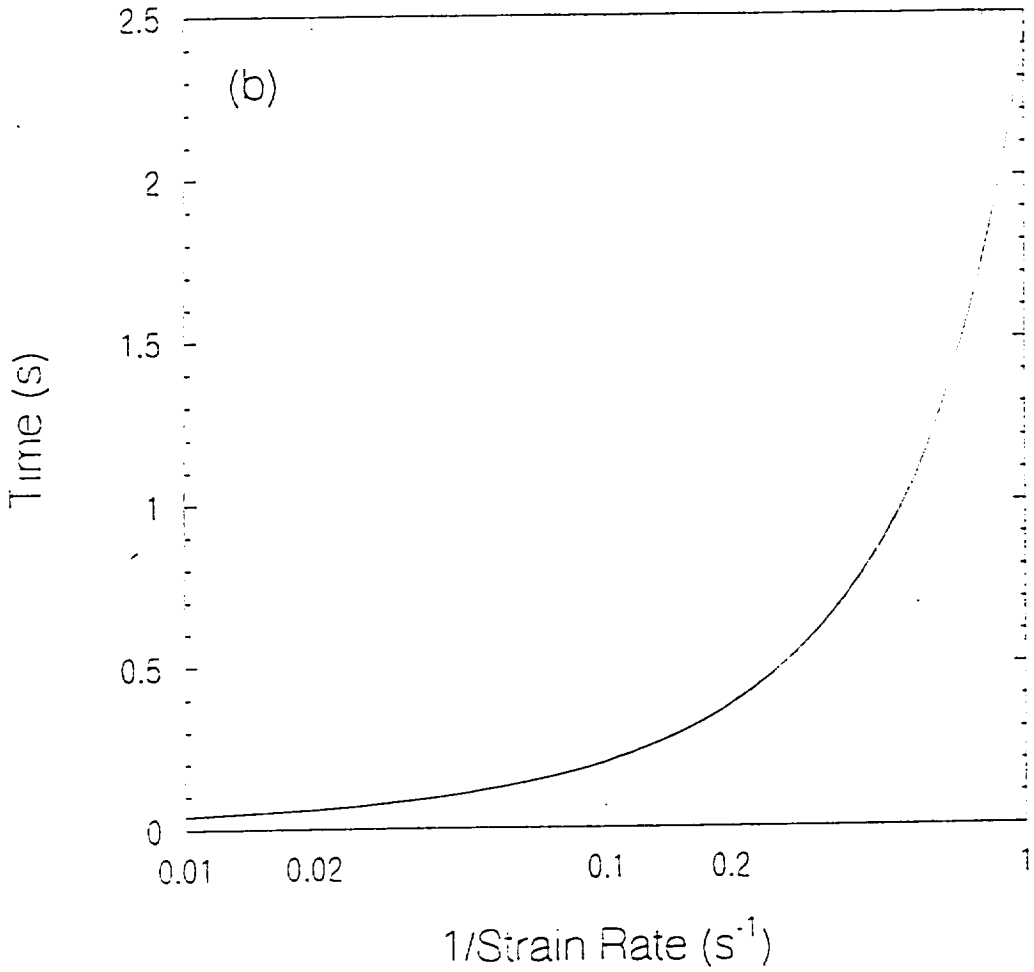
(b)
2.5
2
1.5
1
0.5
0
Time (s)
0.01
0.02
0.1
0.2
1
1/Strain Rate (s-1)